

Biological and Medical Physics, Biomedical Engineering

Igor S. Aranson *Editor*

Physical Models of Cell Motility

EXTRAS ONLINE

 Springer

Physical Models of Cell Motility

BIOLOGICAL AND MEDICAL PHYSICS, BIOMEDICAL ENGINEERING

The fields of biological and medical physics and biomedical engineering are broad, multidisciplinary and dynamic. They lie at the crossroads of frontier research in physics, biology, chemistry, and medicine. The Biological and Medical Physics, Biomedical Engineering Series is intended to be comprehensive, covering a broad range of topics important to the study of the physical, chemical and biological sciences. Its goal is to provide scientists and engineers with textbooks, monographs, and reference works to address the growing need for information.

Books in the series emphasize established and emergent areas of science including molecular, membrane, and mathematical biophysics; photosynthetic energy harvesting and conversion; information processing; physical principles of genetics; sensory communications; automata networks, neural networks, and cellular automata. Equally important will be coverage of applied aspects of biological and medical physics and biomedical engineering such as molecular electronic components and devices, biosensors, medicine, imaging, physical principles of renewable energy production, advanced prostheses, and environmental control and engineering.

Editor-in-Chief:

Elias Greenbaum, Oak Ridge National Laboratory, Oak Ridge, Tennessee, USA

Editorial Board:

Masuo Aizawa, Department of Bioengineering,
Tokyo Institute of Technology, Yokohama, Japan

Olaf S. Andersen, Department of Physiology,
Biophysics & Molecular Medicine,
Cornell University, New York, USA

Robert H. Austin, Department of Physics,
Princeton University, Princeton, New Jersey, USA

James Barber, Department of Biochemistry,
Imperial College of Science, Technology
and Medicine, London, England

Howard C. Berg, Department of Molecular
and Cellular Biology, Harvard University,
Cambridge, Massachusetts, USA

Victor Bloomfield, Department of Biochemistry,
University of Minnesota, St. Paul, Minnesota, USA

Robert Callender, Department of Biochemistry,
Albert Einstein College of Medicine,
Bronx, New York, USA

Steven Chu, Lawrence Berkeley National
Laboratory, Berkeley, California, USA

Louis J. DeFelice, Department of Pharmacology,
Vanderbilt University, Nashville, Tennessee, USA

Johann Deisenhofer, Howard Hughes Medical
Institute, The University of Texas, Dallas,
Texas, USA

George Feher, Department of Physics,
University of California, San Diego, La Jolla,
California, USA

Hans Frauenfelder,
Los Alamos National Laboratory,
Los Alamos, New Mexico, USA

Ivar Giaever, Rensselaer Polytechnic Institute,
Troy, New York, USA

Sol M. Gruner, Cornell University,
Ithaca, New York, USA

Judith Herzfeld, Department of Chemistry,
Brandeis University, Waltham, Massachusetts, USA

Mark S. Humayun, Doheny Eye Institute,
Los Angeles, California, USA

Pierre Joliot, Institute de Biologie
Physico-Chimique, Fondation Edmond
de Rothschild, Paris, France

Lajos Keszthelyi, Institute of Biophysics, Hungarian
Academy of Sciences, Szeged, Hungary

Robert S. Knox, Department of Physics
and Astronomy, University of Rochester, Rochester,
New York, USA

Aaron Lewis, Department of Applied Physics,
Hebrew University, Jerusalem, Israel

Stuart M. Lindsay, Department of Physics
and Astronomy, Arizona State University,
Tempe, Arizona, USA

David Mauzerall, Rockefeller University,
New York, New York, USA

Eugenie V. Mielczarek, Department of Physics
and Astronomy, George Mason University, Fairfax,
Virginia, USA

Markolf Niemz, Medical Faculty Mannheim,
University of Heidelberg, Mannheim, Germany

V. Adrian Parsegian, Physical Science Laboratory,
National Institutes of Health, Bethesda,
Maryland, USA

Linda S. Powers, University of Arizona,
Tucson, Arizona, USA

Earl W. Prohofsky, Department of Physics,
Purdue University, West Lafayette, Indiana, USA

Andrew Rubin, Department of Biophysics, Moscow
State University, Moscow, Russia

Michael Seibert, National Renewable Energy
Laboratory, Golden, Colorado, USA

David Thomas, Department of Biochemistry,
University of Minnesota Medical School,
Minneapolis, Minnesota, USA

Igor S. Aranson
Editor

Physical Models of Cell Motility



Editor

Igor S. Aranson
Argonne National Laboratory
Argonne, IL, USA

ISSN 1618-7210

ISSN 2197-5647 (electronic)

Biological and Medical Physics, Biomedical Engineering

ISBN 978-3-319-24446-4

ISBN 978-3-319-24448-8 (eBook)

DOI 10.1007/978-3-319-24448-8

Library of Congress Control Number: 2015956180

Springer Cham Heidelberg New York Dordrecht London

© Springer International Publishing Switzerland 2016

This work is subject to copyright. All rights are reserved by the Publisher, whether the whole or part of the material is concerned, specifically the rights of translation, reprinting, reuse of illustrations, recitation, broadcasting, reproduction on microfilms or in any other physical way, and transmission or information storage and retrieval, electronic adaptation, computer software, or by similar or dissimilar methodology now known or hereafter developed.

The use of general descriptive names, registered names, trademarks, service marks, etc. in this publication does not imply, even in the absence of a specific statement, that such names are exempt from the relevant protective laws and regulations and therefore free for general use.

The publisher, the authors and the editors are safe to assume that the advice and information in this book are believed to be true and accurate at the date of publication. Neither the publisher nor the authors or the editors give a warranty, express or implied, with respect to the material contained herein or for any errors or omissions that may have been made.

Printed on acid-free paper

Springer International Publishing AG Switzerland is part of Springer Science+Business Media (www.springer.com)

Preface

Multicellular organisms are composed of individual cells that form the tissues, organs, and nervous system. In these organisms, the cells are replaced roughly every 100 days via controlled division and cell death. However, both during organism development and even in the developed organism, there are specialized cells, such as keratocytes, fibroblasts, neutrophils, and others, that show a high propensity to move. The motility of these cells is associated with their specific function within the organism. Motile eukaryotic cells responding to chemical or mechanical stimuli play a fundamental role in tissue growth, wound healing, and immune response. In addition, cell migration is essential for understanding several life-threatening pathologies such as cancer. Beyond the obvious biological and medical relevance, cell motility is also a fascinating example of a self-organized and self-propelled system within the realm of physics. The main difficulty in formulating a comprehensive predictive model of cell motility lies in the extreme complexity of the underlying biological processes associated with the dynamics of moving cells. Correspondingly, a number of conceptually different theoretical approaches were formulated to tackle this formidable problem. This book attempts to give a snapshot of the most recent theoretical and experimental studies in this rapidly developing field. The distinctive feature of this book is that the modeling approaches are based on concepts inspired by contemporary soft matter physics, such as order parameters, phase transitions, reaction-diffusion systems, conservation laws, and force balance conditions.

The structure of the book is as follows. It contains four chapters focused on various approaches to cell movement. Chapter 1 presents a study of cell motility based on the phase field method. This method is especially well suited to treat the moving and deformable boundaries involved in both individual and collective cell motility. It starts with a didactic introduction to a simple model for the movement of an individual cell. Then, it describes how complexity can be added step by step, such as deformability and adhesiveness of substrate, as well as modulations of the substrate properties. Finally, it discusses how the model can be generalized to describe the interactions and the collective movement of many, self-organized cells. Chapter 2 focuses on crawling cell motility driven by spontaneous polymerization

waves. It presents theoretical descriptions of actin dynamics and discusses in detail possible mechanisms for wave generation. Then, the coupling of the actin network to the cell membrane is added. The analysis shows that spontaneous polymerization waves offer a unifying framework for explaining directional and erratic cell motion such as amoeboid motility. Chapter 3 features a modular view of the signaling system regulating chemotaxis. The model describes an excitable network for signal transduction that integrates information from various internal and external cues and signals to the actin cytoskeleton. Simulations using the level set method allow the testing of this model by recreating changes in morphology induced by the signaling network. Finally, Chap. 4 is focused on one-dimensional models of moving cells that are amenable to theoretical treatment. Despite the unavoidable oversimplifications associated with such a representation, the one-dimensional models happen to be useful for understanding the intricate interplay between contraction and protrusion.

This book is written primarily for biophysicists, mathematical biologists, and biomedical engineers entering the field of cell motility and biomechanics. We also hope that experimentalists and theorists already working in the field will find it useful for its comprehensive review of experimental studies of cell movement and survey of the most recent physics-based modeling approaches. It can also serve as supplementary reading material for advanced graduate courses on biological physics and mathematical biology. This book is accompanied by a collection of computational online videos illustrating various aspects of cell motility.

Argonne, IL, USA
June 2015

Igor S. Aranson

Contents

| | | |
|----------|--|----------|
| 1 | Macroscopic Model of Substrate-Based Cell Motility | 1 |
| | Falko Ziebert, Jakob Löber, and Igor S. Aranson | |
| 1.1 | Introduction | 1 |
| 1.1.1 | Basic Mechanisms Involved in the Motility of Eukaryotic Cells | 2 |
| 1.1.2 | Survey of Experimental Facts for Cells Crawling on Two-Dimensional Substrates | 4 |
| 1.1.3 | Main Modeling Approaches | 8 |
| 1.2 | Phase Field Model for a Single Cell | 11 |
| 1.2.1 | Phase Field Description of the Interface | 13 |
| 1.2.2 | Actin Dynamics | 16 |
| 1.2.3 | On Force Balance Versus Explicit Flow | 19 |
| 1.2.4 | Adhesion and Coupling to Substrate Deformation | 20 |
| 1.3 | Dynamics of an Individual Cell | 22 |
| 1.3.1 | Steady Moving Cell | 23 |
| 1.3.2 | Subcritical Onset of Motion | 25 |
| 1.3.2.1 | Analytical Study of Cell Movement in Circular Approximation | 26 |
| 1.3.2.2 | Velocity Branches in Circular Approximation | 27 |
| 1.3.3 | Steady Motion vs. Stick-Slip | 28 |
| 1.3.3.1 | Reduced Description of the Stick-Slip Cycle | 31 |
| 1.3.4 | More Complex Motility Modes | 33 |
| 1.3.5 | Movement on Inhomogeneous Substrates | 34 |
| 1.3.5.1 | Modulation of Substrate Adhesiveness | 36 |
| 1.3.5.2 | Modulation of Substrate Stiffness and Durotaxis | 38 |
| 1.4 | Collective Migration | 39 |
| 1.4.1 | Multiple Phase Fields | 40 |
| 1.4.1.1 | Steric Interaction | 40 |
| 1.4.1.2 | Cell–Cell Adhesion | 41 |
| 1.4.1.3 | Generalization of Actin, Adhesion, and Substrate Dynamics | 42 |

| | | |
|------------|--|-----------|
| 1.4.2 | Binary Interactions of Cells | 43 |
| 1.4.3 | Many Cells: Collective Migration | 45 |
| 1.4.3.1 | Transitions Between Spreading and Collective Motion | 45 |
| 1.4.3.2 | Collective Migration at Moderate Densities | 46 |
| 1.4.3.3 | Collective Migration for Strong Cell–Cell Adhesion and/or High Density | 49 |
| 1.5 | Conclusions | 50 |
| Appendix | | 52 |
| References | | 60 |
| 2 | Cell Crawling Driven by Spontaneous Actin Polymerization Waves... | 69 |
| | Karsten Kruse | |
| 2.1 | Introduction | 69 |
| 2.2 | Spontaneous Actin Waves | 70 |
| 2.3 | Theoretical Descriptions of Cellular Actin Dynamics | 73 |
| 2.3.1 | Actin Polymerization | 73 |
| 2.3.2 | Mechanisms for Generating Spontaneous Actin Waves | 75 |
| 2.3.2.1 | Polymerization Waves in the Absence of Motors | 75 |
| 2.3.2.2 | Cytoskeletal Waves in Presence of Motors | 79 |
| 2.3.3 | Coupling Actin Dynamics to the Membrane | 81 |
| 2.3.3.1 | Sharp Boundary Methods | 82 |
| 2.3.3.2 | Phase-Field Methods | 83 |
| 2.4 | Wave-Driven Migration | 84 |
| 2.4.1 | Phase Diagram | 85 |
| 2.4.2 | Persistent Migration Patterns | 86 |
| 2.4.3 | Erratic Migration Patterns | 88 |
| 2.5 | Conclusions | 89 |
| 2.6 | Supplementary Movies | 90 |
| References | | 90 |
| 3 | A Modular View of the Signaling System Regulating Chemotaxis ... | 95 |
| | Pablo A. Iglesias | |
| 3.1 | Introduction | 95 |
| 3.2 | Motility | 97 |
| 3.2.1 | Random Motility | 97 |
| 3.2.2 | Excitable Behavior | 98 |
| 3.2.3 | Models of Excitable Behavior | 99 |
| 3.2.4 | Coupling EN Activity to Cellular Deformations | 101 |
| 3.2.5 | Viscoelastic Cell Mechanical Model | 102 |
| 3.2.6 | Simulations of Random Motility | 104 |
| 3.3 | Directional Sensing and Adaptation | 104 |
| 3.3.1 | Local Excitation, Global Inhibition | 105 |
| 3.3.2 | Experimental Support for the LEGI Mechanism | 106 |

| | | |
|-----------------------------------|--|------------|
| 3.4 | Coupling Directional Sensing to Motility | 108 |
| 3.4.1 | Response of LEGI-BEN to Spatially Uniform Stimulation .. | 109 |
| 3.4.2 | Response of LEGI-BEN to Spatially Graded Stimulation .. | 111 |
| 3.4.3 | Morphological Changes Induced by LEGI-BEN | 112 |
| 3.5 | Polarization and Directional Persistence | 113 |
| 3.5.1 | Simulations of LEGI-BEN-POL | 115 |
| 3.5.2 | Modeling In Silico Mutants | 116 |
| 3.6 | The Cytoskeletal Oscillatory Network | 119 |
| 3.6.1 | Mathematical Description of STEN-CON | 120 |
| 3.6.2 | STEN-CON Coupling | 121 |
| 3.6.3 | Simulations of Coupled STEN-CON Systems | 122 |
| 3.7 | Discussion and Conclusions | 124 |
| Appendix | | 126 |
| References | | 128 |
| 4 | Cell Locomotion in One Dimension | 135 |
| Pierre Recho and Lev Truskinovsky | | |
| 4.1 | Introduction | 135 |
| 4.2 | Contraction | 139 |
| 4.2.1 | A Toy Model | 140 |
| 4.2.2 | Continuum Thermodynamics | 145 |
| 4.2.3 | Specialization of the Model | 150 |
| 4.2.4 | Non-Local Reformulation | 152 |
| 4.2.5 | Static Solutions | 154 |
| 4.2.6 | Linear Stability | 156 |
| 4.2.7 | Motile Solutions | 158 |
| 4.2.8 | Passive Actin Treadmilling | 162 |
| 4.2.9 | Nonlinear Active Stress | 165 |
| 4.2.10 | Discussion | 167 |
| 4.3 | Protrusion | 167 |
| 4.3.1 | The Model | 168 |
| 4.3.2 | Force Velocity Relation | 171 |
| 4.3.3 | Elastic Regularization | 173 |
| 4.3.4 | Alternative Driving Modes | 176 |
| 4.3.5 | Discussion | 178 |
| 4.4 | Adhesion | 179 |
| 4.4.1 | The Model | 180 |
| 4.4.2 | Contraction Driven Motility | 182 |
| 4.4.3 | The General Case | 185 |
| 4.4.4 | Discussion | 188 |
| 4.5 | Conclusions | 189 |
| References | | 190 |
| Index | | 199 |

Chapter 1

Macroscopic Model of Substrate-Based Cell Motility

Falko Ziebert, Jakob Löber, and Igor S. Aranson

1.1 Introduction

In higher multicellular organisms that are fully developed, the majority of cells are not moving but form the tissues, the organs, the nervous system, etc. The cells are replaced every 100 days or so, by controlled division and cell death (apoptosis). However, both during development as well as in the developed organism, there are specialized cells that show a high propensity to move, subtly connected to their function within the organism. A good example from everyday life are open wounds through the skin (e.g. cuts). The bleeding is stopped rather passively by

Electronic supplementary material The online version of this chapter (doi: [10.1007/978-3-319-24448-8_1](https://doi.org/10.1007/978-3-319-24448-8_1)) contains supplementary material, which is available to authorized users.

F. Ziebert (✉)

Physikalisches Institut, Albert-Ludwigs-Universität Freiburg, Hermann-Herder-Strasse 3,
79104 Freiburg, Germany

Institut Charles Sadron, CNRS-UPR22, 23 rue du Loess, 67034 Strasbourg Cedex 2, France
e-mail: falko.ziebert@physik.uni-freiburg.de

J. Löber

Institut für Theoretische Physik, Technische Universität Berlin, Hardenbergstrasse 36,
EW 7-1, 10623 Berlin, Germany
e-mail: jakob@physik.tu-berlin.de

I.S. Aranson

Materials Science Division, Argonne National Laboratory, 9700 South Cass Avenue,
Argonne, IL 60439, USA

Engineering Sciences and Applied Mathematics, Northwestern University,
2145 Sheridan Road, Evanston, IL 60202, USA
e-mail: aronson@anl.gov

platelets arriving via the blood flow, followed by the coagulation cascade. Then the immune system responds and white blood cells arrive and remove debris and other “junk”. They also chase intruders like bacteria. Then fibroblast cells crawl towards the wound, excrete collagen and thereby recreate the extracellular matrix (ECM). At the same time, the epithelial cells around move collectively to close the wound. Another example is the wiring of the brain and the nervous system, including the extension of neurons. Finally, cancer growth is also an example involving cell motility, where in its late stage, metastasis takes place and malignant cells invade the body.

The ability of cells to move has fascinated biologists for decades. More recently it also captured the attention of physicists and materials scientists. In fact, it is not fully understood how a cell polarizes in order to head in a specific direction, how it maintains its integrity and shape while moving, how it transfers the force to the substrate which may have very different properties in different regions of the organism, and how it is able to move at all. It has been understood by now that cells use their very scaffold, the *cytoskeleton*, which is maintained in a persistent out-of-equilibrium state due to the presence of energy-storing molecules (typically triphosphates), to create the propulsion forces. The question how the motility machinery of cells works in detail has inspired many experimental studies, with the available data rapidly growing. Correspondingly, modeling efforts also acquired pace to rationalize the experimental findings and to place them in a unifying framework.

The construction of models that could incorporate the plethora of mechanisms involved in cellular motion and explain all the observed features in a concise, self-consistent fashion remains an ambitious task. Nevertheless good progress has been recently achieved. In the following we present a brief introduction to the basic facts of cell motility and to the major concepts concerning its modeling. We then describe, in a rather didactic fashion, recent progress in modeling approaches that were able to reproduce many of the experimentally observed features of cells crawling on two-dimensional substrates.

1.1.1 Basic Mechanisms Involved in the Motility of Eukaryotic Cells

Different types of cells show a large variability in their morphodynamics [25, 109]. For example, keratocytes (wound healing cells living in the skin of fish, but also in the cornea of our eye) move persistently with high speed and maintain a crescent-like shape [79]. Fibroblast cells (again a wound-healing cell type) move much slower, have stronger adhesion and develop strong cytoskeletal fibers. Their fan-like shape is more irregular than that of keratocytes [1, 109]. Leukocytes (immune cells) move in an amoeboid fashion with very large shape changes, allowing them to squeeze through tiny gaps in epithelial layers. There is evidence that in addition to crawling, they can also roll along the blood vessels, and even swim [116]. Growth cones of neurons have a microtubules-strengthened stem that later becomes the backbone for nerve signal transport, and an active region at the front. The active

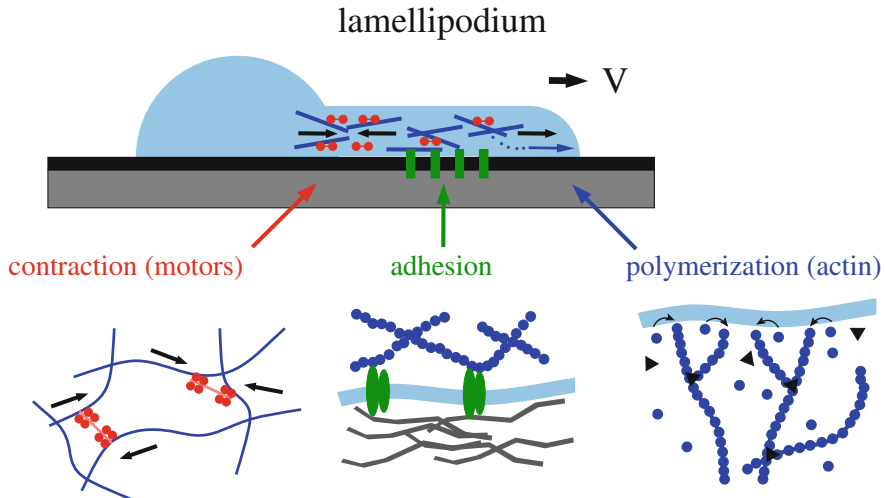


Fig. 1.1 Abercrombie's three step model. Schematics of the three step model of crawling cell motility [1] and sketches of the corresponding microscopic processes: (step 1) ratcheting of actin-polymerization creates a **propulsion** force. (step 2) The force is transmitted to the substrate via **adhesion**. (step 3) Motor-induced contraction of the actin network leads to a **retraction** of the rest of the cell

region is propelled by actin polymerization. There, actin-related filopodia search for other neurons to connect to [40]. Finally, epithelial cells mostly move collectively, linked together by cadherin-based cell–cell adhesion ligands [126, 129], to generate new or to repair old tissue.

In spite of this seeming diversity, the basic mechanism for the actin-based motility of eukaryotic cells has been identified rather early. In the beginning of the 80s, Abercrombie [1] proposed a three step model to rationalize his observations, mainly obtained for fibroblasts. Although different cell types express these ‘steps’ in different ways and specificity, these steps occur more or less for all cell types mentioned above. Abercrombie’s conjecture has been refined later on by Sheetz [147], but we will restrict ourselves here to the simplest version. Let us consider a cell crawling on a flat, two-dimensional substrate as sketched in Fig. 1.1. Typically, the motility is localized in a certain zone called the *lamellipodium*, a thin 100–200 nm layer of actin cytoskeleton surrounded by the cell membrane.

The first step involves a **propulsion** mechanism: due to specific regulation (involving proteins like WASP and Arp2/3), close to the membrane actin (shown in blue) is polymerized involving the hydrolysis of adenosine-triphosphate (ATP). In addition, actin is branched by Arp2/3 (black triangles), leading to a loose actin network, polymerizing together towards the membrane. Details on these complex processes can be found in [28, 128]. It has been rationalized by Oster and coworkers [110, 111, 124] that the ratcheting of actin—new actin monomers can attach between the filament tip and the membrane, if the membrane or the filament itself fluctuates—indeed produces propulsion forces of the order of several pN per filament.

In a second step, the propulsion force has to be transferred to the substrate, which is realized by a complex spatio-temporal orchestration of cellular **adhesion**. Most cells use specialized protein complexes [27, 142] to link the outside, typically the collagen-based ECM, to the internal actin cytoskeleton. Adhesion can be specific, typically integrin-based, as for most epithelial cells or rely on nonspecific adhesion (i.e. friction, as for amoebae like dictyostelium devoid of focal adhesion). Some cells can even switch between both adhesion types, like dendritic cells [135]. Rapidly moving cells like keratocytes typically have only weak intermittent (nascent) adhesion [6, 16, 92], while slower moving cells often exhibit adhesion maturation [142]. This process includes further recruitment of actin and makes use of the mechanosensitivity of the adhesive complex to scrutinize the substrate and to “decide” where to go [170].

Finally, the third step involves the interplay of actin-based molecular motors (myosin) with the actin network. In the presence of ATP, the motor proteins can walk along the filaments in a specific direction, that is determined by the microscopic protein structure [107]. In a crosslinked or entangled network of actin, these local movements translate to contractile stresses, which are used for the **retraction** of the cell body and the detachment of existing adhesive bonds [72, 155]. Interestingly, motors can also be involved in the onset of motion via contraction-induced polarization of cells, as reported by the Theriot group for keratocytes [180].

All three steps are obviously orchestrated by many intertwined, and sometimes for reasons of robustness even redundant, regulatory pathways. Especially, the second main type of cytoskeletal filaments, the microtubules, are known to play a role in motility as they are responsible, for instance, for the directed transport of different regulator molecules [50]. However, only few of these pathways have already been included (and still partially) in modeling approaches. To a large extent, regulation is still beyond the scope of current modeling. We will therefore only focus here on the main physical components of cell movement—actin propulsion, cellular adhesion and motor contraction—and their dynamic interplay in creating cellular motion and shape.

For more details on the three step model we refer to the excellent review by Ananthakrishnan and Ehrlicher [5], which is dedicated to a thorough discussion of their experimental evidence and their repercussions.

1.1.2 Survey of Experimental Facts for Cells Crawling on Two-Dimensional Substrates

The most studied cell type in the context of cell motility are fish skin keratocytes. This is due to the fact that—on homogeneous substrates—these cells preserve their shape while moving, which facilitates both experimental analysis and modeling. In addition, keratocytes move persistently (up to hundreds of cell lengths) and they are not chemotactic (i.e. do not respond to chemical stimuli). The modeling approach reviewed here was originally designed for this cell type. Nevertheless, diverse cell

shapes (see Sect. 1.3.1) and motility modes (see Sects. 1.3.3 and 1.3.4) could be reproduced within the model as well. Therefore, we also review some pertinent experimental results obtained on fibroblast and epithelial cells.

First of all, why should one expect that such a complex system as a moving cell could be amenable to simple modeling approaches? In this context, it has been shown [51, 167] that lamellipodial fragments of cells, that lack the nucleus and most other organelles and hence many of the biological regulation pathways, also display the keratocyte-like motion found for entire cells. This led to the pivotal conclusion that the “motility machinery” works in a *self-organized* way. In other words, gene regulation may not be so crucial for the initialization and continuation of motility, although obviously it is important for the stabilization and coordination of motion in a way that the cell can draw profit from it. Another important result obtained from the study of cell fragments is their inherent *bistability*: they either exist in a symmetric non-moving state, where the actin polymerization forces are completely balanced, or in a polarized state which moves along a specific direction. To induce the motion, a symmetry breaking has to occur, which has to be triggered externally—e.g. by mechanical stimulation—in case of fragments, but usually is self-regulated (‘spontaneous’) in case of the entire cells.

Both findings strongly emphasize the importance of physical aspects in cellular motility: namely, the prevalence of self-organization processes in an out-of-equilibrium system. Consequently, one can hope to capture the *generic features* by rather simple, physical modeling approaches. On the other hand, since detailed regulation pathways are not (yet) modeled, one should always be aware of that physical models of “cells” actually refer rather to cellular fragments or biomimetic “active cytoskeletal droplets” [140, 162] than to genuine biological cells.

We now briefly survey what is known about moving cells.

Typical Scales The cell types considered here have typical sizes (diameters) of 20–40 μm . Typical sizes of the main constituents are fractions of a micron to few microns for the length of the actin filaments and 30–100 nm for the other protein complexes typically involved in motility (myosin, crosslinks, integrins, etc.). Crawling velocities vary from up to 0.5 $\mu\text{m}/\text{s}$ for keratocytes [79] down to 0.2–2 $\mu\text{m}/\text{min}$ for fibroblasts [171]. The time scale of actin turnover is typically of the order of seconds and motor speeds are up to $\sim 1 \mu\text{m}/\text{s}$, corresponding to about 100 steps of step size 5–10 nm/s [68]. The typical life time of a crosslink ranges from seconds to hundreds of seconds [98, 178] and of an adhesive bond from tens of minutes for a fully matured focal adhesion complex [143] down to few seconds for nascent focal contacts in keratocytes. One can hence conclude that cell motility indeed is a complex problem with multiple temporal and spatial scales. Consequently, effective models typically focus on the larger constituents, i.e. the actin filaments, and the processes involving the smaller constituents are modeled in a coarse-grained or effective fashion.

Cell Polarization and Symmetry Breaking A prerequisite for motion is cell polarization, i.e. the presence of a well-defined front and back of the cell. In many practical cases the polarity is established in response to external stimuli, chemical or mechanical ones, which are beyond the scope of simple physical models as

discussed here (see however the recent reviews [71, 112], where the latter focuses on chemotactic cell polarization). As discussed above, however, lamellipodial fragments display a subcritical (i.e. discontinuous or first-order) transition to motion upon simple external perturbations. In another important work, Yam et al. [180] demonstrated that even in the absence of external stimuli keratocytes can self-polarize by motor-induced contraction of the actin network at the place which later becomes the rear of the cell. Finally, when the motile state is fully established, keratocytes form an acto-myosin bundle at the rear that further stabilizes the polarity [167]. Hence current knowledge for keratocytes and their fragments suggests that their polarity is induced by motors.

Cell Shape and Motion It has been demonstrated by Keren et al. [79] that the shape of a moving cell is determined dynamically. In addition, by screening many cells, a relation between cell speed and aspect ratio was conjectured. Although the data was scattered, possible due to comparing cells with different volumes [185], this finding implies an interrelation of polarization and cell speed. Several additional studies focused in more detail on how the local actin distribution [88], the tension of the cell membrane [97], as well as the adhesion to the substrate [16] are involved in determining the shape. Especially, keratocytes move steadily with their well known crescent shape only on substrates with intermediate adhesiveness, while they move more erratically and become either rounded or fluctuating in shape for lower or higher adhesiveness of the substrate, respectively [16]. These findings strongly suggest that the cell shape should not be imposed, as it was done in earlier models [36], but has to be considered self-consistently.

Diverse Motility Patterns Even rather simple cells like keratocytes can display several modes of motion, cf. the dependence on the substrate adhesiveness already discussed above [16]. As another example, bipedal motion has been found in keratocytes [15], i.e. a movement where the rear part of the cell oscillates back and forth normal to the direction of motion. It was explained on a phenomenological level by accounting for intracellular elastic elements [15]. Finally, discontinuous stick-slip-type motion has been found in a variety of cells, e.g. in glioma cells [164], at the front of PtK1 cells [73] and for filopodia [30]. Obviously, there is even more diversity for more complicated cells like fibroblasts and leukocytes, but their understanding and modeling is still at an early stage. Nevertheless the conclusion can be drawn that the cell is a complex dynamical system: the motility pattern is the outcome of an intricate interplay of several components—adhesion, elasticity—that feedback to the overall shape and the propulsion mechanism.

Adhesion and Substrate Deformability In a seminal work, Palecek et al. [119] demonstrated that the speed of a crawling cell is a non-monotonous function of the adhesiveness of the substrate: for too low adhesion (low number of adhesive ligands present on the substrate's surface), the cell speed is low since the force transfer is weak. A maximum is reached for some intermediate adhesion, while for too strong adhesion the cell speed decreases again, due to stalling of actin polymerization. Only the cell's speed was studied in that early work, while later on the concomitant change in shape and motility mode was investigated using keratocytes [16]. A second important parameter is the stiffness of the substrate. A number of studies were

conducted for cells on substrates with varying elastic moduli [121, 152]. Especially, it is now understood that early experiments, using glass slides with elastic moduli in the GPa range, were partially misleading. Rather, a substrate stiffness closer to the value for tissues, i.e. of the order of 10 kPa, should be used to capture the “relevant” phenomenology of crawling cells.

Remarkably, in addition to simply reacting to the substrate stiffness, cells also respond to gradients in stiffness, a phenomenon termed *durotaxis* [100]. In this way, for example, bone marrow stem cells are able to navigate towards substrates with higher stiffness while brain cells head towards softer substrates. The biological function is obvious: the cells aim to join the bone and the brain, respectively. The mechanism is still rather poorly understood. It likely involves substrate deformation/stress sensing via the complex protein cascade involved in adhesion, and a transmission of the signal towards large scale actin orientation to polarize the cell in the right direction.

Force Transmission to the Substrate Intimately related to both adhesion formation and substrate elasticity is the problem of force transmission in moving cells. Efficient force transfer is a crucial prerequisite to motion, since otherwise the actin polymerizing against the membrane would just be transported backwards (which is indeed true to some extent, an effect termed *retrograde flow*) without moving the cell forwards. With the recent advance of traction force microscopy [39, 158, 169] and theories allowing to interpret the data [4, 144], experimental studies on traction force patterns are now rapidly increasing. For keratocytes, the traction force is high close to the front but peaks especially at the sides [55]. In contrast, fibroblasts have very inhomogeneous traction patterns [113], while leukocytes have highest traction at the rear [151]. Although cell modeling efforts incorporating traction patterns are being developed [146, 182], a deep understanding remains elusive and no model exists to date that could account for cell-specific traction patterns. For more information on adherent cells (not necessarily moving) and force transmission, we refer to the excellent review by Schwarz and Safran [143].

Retrograde Flow and Force-Velocity Relation Associated with the actin polymerization at the front and its recycling further away from the membrane is the so-called retrograde flow [165]. It can be directly visualized and measured, for example by particle velocimetry or speckle microscopy. It is known that the retrograde flow affects adhesion and traction force, and also motor contraction [3, 57, 58, 165]. Closely related to this issue is the force-velocity relation of a moving cell, i.e. the dependence of the cell’s velocity on an opposing force. For keratocytes, the velocity is fairly constant at low opposing forces and then drops abruptly close to the so-called stall force [120, 130]. In an important combined experimental and theoretical effort, the force-velocity relation has been rationalized [186], involving additional microscopic processes including actin filament bending and crosslinking.

Perturbing and Confining Cells A plethora of chemical agents is known to interfere with the motility modules (protrusion, adhesion, retraction) of cells. For instance, blebbistatin inhibits myosin motors (via binding to them) and cytocha-

lasin D is inhibiting actin polymerization (via blocking its tips, a process called “capping”). Membrane tension can be reduced by adding deoxycholate [132] (note that recently tension was altered more directly via fusing a crawling cell with a vesicle [97]). In principle, such strategies allow for targeted manipulation [16, 57], but one has to be aware of the fact that in the cell “everything is coupled”. For example, when interfering with actin polymerization, one certainly predominantly affects propulsion, but also adhesion (which needs actin for maturation) and actomyosin retraction. Biochemical perturbations, acting inside the cell, obviously remain important tools today. Nevertheless, a more recent trend uses microfabrication techniques to perturb cells “from the outside”: for example, cells can be confined on adhesive spots [43, 69, 136], that can be stamped on the substrate’s surface (and the remainder of the surface made inert) via microcontact printing. A more detailed study focused on spreading cells in contact with differently shaped adhesive micro-environments [160]. Csucs et al. [35] showed that keratocytes can be perturbed—while still be able to move—via a substrate containing stripe patterns of adhesive ligands. The cells centered with respect to the stripes and moved predominantly along them. Cells can also be perturbed by patterning the stiffness of the substrate, as studied in [163]. There, composite synthetic substrates decorated by micropillar arrays with different dimensions (and hence different elastic moduli) were prepared. This allowed studying the behavior of spreading and moving cells at the boundaries between differently stiff regions. Finally, also the surface topology and the surface chemistry of the substrate can be varied.

1.1.3 Main Modeling Approaches

After cell motility had been identified as an important problem and the mechanism described, mostly in words, by Abercrombie, early modeling efforts focused on distinct processes of the motility apparatus. Since we are mostly interested in macroscopic (whole cell) models, we review only the major aspects of these efforts, followed by a discussion of the state-of-the-art of macroscopic cell modeling.

Propulsion was first rationalized as the ratcheting of actin polymerization [110, 111, 124], including more detailed effects like multiple filaments and bending fluctuations. The main argument in these models is that a sufficiently large fluctuation of the membrane (or a bending fluctuation of the filament, or both) allows the attachment of a new monomer at the growing tip of the actin filament. After the attachment the membrane cannot retract back, hence this process results in directed motion. More recent approaches account for additional relevant processes, such as capping (involving proteins temporarily attaching to the actin tips, hence temporarily excluding them from the pool of growing filaments) and severing (involving proteins cutting actin filaments) [61]. Other recent computational works focused on the two-dimensional structure of the growing actin network, where Arp2/3 complexes induce branching of actin filaments at well-defined angles [141, 172], cf. Fig. 1.1. Also note that alternative motility mechanisms have been proposed

and modeled, like actin polymerization waves [42, 173] (see also Chap. 2 by K. Kruse), as well as motor-generated stresses [29, 133] in absence of polymerization. Although many open questions remain, the actin propulsion is probably the best studied of the three Abercrombie “steps”, and a pool of more detailed models is available.

Interestingly, the experimentally found non-monotonous dependence of the cell speed on **adhesion** [119] was actually a prediction from a model that accounted for viscoelasticity and adhesion, but completely neglected polymerization [41]. A similar velocity-adhesion dependence has been later also found in a model including actin polymerization [62]. The modeling of the adhesion process itself is not yet fully developed (see [143] for a recent review). Microscopic theory started with the work of Bell [17], trying to rationalize cell-cell adhesion. Nowadays, the physical understanding of specific adhesion is advanced mostly on the model system of a vesicle with membrane-bound receptors adhering to a ligand-covered substrate [26, 150], and neglecting most complications arising in cellular adhesion. As far as the coupling between adhesion formation and the cytoskeletal dynamics is concerned, this important issue has just started to be investigated, on the microscopic level in some simple situations [48, 96, 137]. On the macroscopic scale, an analogy between cellular adhesion and wetting has been put forward [139], but typically reaction-diffusion type models are employed [16, 182]. Finally, adhesion maturation is almost exclusively neglected in modeling approaches, though a whole cell model that incorporates this effect has been recently proposed [153].

Specific models of **cell retraction** are practically absent, as this process is mostly an effect in the bulk of the cytoskeleton. A theoretical description of actomyosin and its self-organized contractility is still a topic of ongoing research [49, 95], with the models spanning from microscopic theories for contractile bundles [83, 114, 125] and dilute filament-motor mixtures [184] to macroscopic approaches. The general macroscopic theory has been termed “active gel theory” [76, 84, 85], and has been formulated also for multi-component systems [74], e.g. for actin and cytosol. In brief, the active gel approach is a generalization of the linear irreversible hydrodynamics of polar liquid crystals [24, 127], accounting in addition for the ATP-consuming processes of actin polymerization and contraction. Note that for polar liquid crystals, the relations between microscopic and macroscopic theories have been investigated in some detail [174], while this is less obvious in the case of the active gel [99].

On the level of the **whole cell**, the first models were purely descriptive: the “graded radial extension model” [94] related the shape and the local advancing velocity of the cell to the balance of the propulsive force and the retrograde flow. Refined versions of this model, including a graded actin density and/or adhesion, are still employed today [16, 79] to rationalize experimental data. More physically oriented models typically employ some version of active gel theory. Several one-dimensional approaches for cell motion have been proposed [29, 86, 134] (see also Chap. 4), on either polymerization-related flow or acto-myosin contraction. In the framework of a simplified active gel theory, the onset of motion for a two-

dimensional thin layer of active gel can be calculated analytically [21]. In addition, the difference in motility whether actomyosin creates either a pushing or a pulling force has been thoroughly investigated [133].

Two-dimensional models were first based on some simple rules [64], then on fixed cell shapes [82]. In fact, until the end of the 2000s, progress was hampered by a mostly technical problem in the modeling, which however is at the very heart of cell motility: namely, the occurrence of moving boundaries. It should be noted that the cytoskeletal dynamics and its coupling to the membrane and the substrate is in general nonlinear, and non-local, and in addition heterogeneous (though the latter is mostly neglected in modeling approaches so far). Hence after a model for a motile cell had been formulated, the solution was prohibitively difficult due to the necessity to treat an already very complex nonlinear problem in a *moving and deformable domain*.

Several modern concepts that circumvent this problem—which are all similar in spirit—have been recently adapted from simpler systems to the cell motility problem. The **phase field method** [18, 52, 91] had been originally introduced to model solidification processes, but later on has been applied to a variety of systems including the Saffman–Taylor fingering instability [53, 54], elastic surface instabilities [78] and fracture mechanics [12, 77], the fluidization transition in granular media [9], the crystallization of polymers [179], and finally vesicles (where it also goes under the name “advection field approach”) [2, 18, 45] and growing actin gels [75]. This list clearly demonstrates the versatility of this method, which meanwhile has developed into a standard tool in the vast field of multiphase/composite materials [149]. In the phase field method, extensively reviewed in its application to cell motility in the following sections, the interface is not treated explicitly. Rather, an auxiliary field (the phase field) is introduced that follows a relaxational dynamics in an associated double well potential. This potential has minima for the two “phases”, for example solid vs. melt in solidification, intact material vs. crack in fracture, or for vesicles or cells simply “the inside” vs. “the outside”. The interface is then given by the smooth transition region between the two phases. Forces acting on the interface can be easily accounted for and will result via the dynamics in the phase field potential to a local advance/retraction of the interface.

A related but different approach is the so-called **level set method**, originally developed in the context of incompressible two-phase flow [154]. This method also introduces a continuous field to treat the interface. However, instead of having a potential associated to the interface, a distance function is used. This method has the advantage of describing “featureless” interfaces, i.e. surfaces without interfacial tension or other physical properties, while the phase field method inherently attributes an energy to the interface. A small inconvenience is, however, that often the distance function may be numerically ill-behaved and accumulate errors and therefore typically has to be reinitialized every couple of time steps (see also Chap. 3 in this book on implementation of the level set method).

The phase field method has been successfully applied to model motile cells: from simple models capturing basic features [145, 185] to models focusing on adhesion [146, 182], substrate deformation [102], and amoeboid motility based

on actin waves [44]. Also the effect of a simple signaling pathway on motility has been investigated [106]. A similar approach (albeit not clearly named so) was also used in a series of works on active gel droplets [60, 161], recently also in three dimensions [162]. The level set method is nowadays especially used in image analysis, i.e. for cell tracking [138], but has also been used in modeling [87, 93, 104, 115, 148, 176, 181]. Employing this method, the important point has been made that cell motility mechanisms have a certain redundancy [177]: in that work, different motility mechanisms were studied within the same modeling framework and it was shown that both motility and shapes can be quite similar for different underlying mechanisms.

Both the phase field and the level set method have been recently reviewed, see [46] and the book [118], respectively. In addition, [105] presents an instructive comparison of both methods applied to vesicle dynamics.

In the following we focus on the macroscopic modeling of whole cells using the phase field method. We will not discuss other approaches, like finite element models (see [66] for a state-of-the-art version in three dimensions), models based on a dynamics of the local distance between the cell's center and the membrane [153], or applications of the immersed boundary method [22] to moving cells. In addition, apart from these alternative solution strategies to “physical” models, a plethora of—more heuristic—modeling strategies exists, based e.g. on cellular automata or other discrete rules, like the cellular Potts model [43]. Most of the approaches not discussed here have been recently surveyed in [67]. Readers interested in modeling additional processes involved in determining morphodynamics which we could not discuss here can refer to [47]. Finally, [108] is a review from the biomathematics point of view, while [36] gives a more general overview.

1.2 Phase Field Model for a Single Cell

In this section we overview the computational model for an individual cell crawling on a substrate as developed in [102, 182, 185]. The basic ingredients are illustrated in Fig. 1.2. The model takes into account the main processes involved in substrate-based cell motility, as discussed in the previous section: the **protrusion** via actin filament polymerization at the cell's leading edge, the intermittent formation of **adhesion** sites to transfer momentum to the substrate, and the detachment of adhesion complexes and myosin motor-driven **contraction** at the cell's rear. In addition, the deformable substrate is accounted for, since it interferes with the adhesion turnover. These mechanisms are formulated in terms of (up to) four continuous two-dimensional (2D) fields: the phase field, ρ , the actin polarization field, \mathbf{p} , the concentration of the formed adhesive bonds, A , and the substrate's in-plane displacement field, \mathbf{u} .

Most importantly, the deformable and moving interface—identified with the cell's membrane—is described self-consistently by an auxiliary field, the phase field $\rho(x, y; t)$. Its dynamics is governed by an overdamped motion in a double-well model

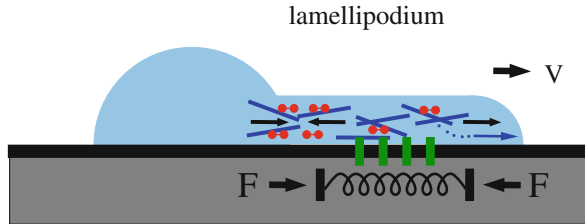


Fig. 1.2 Schematics of the model. The cell moves on a soft deformable substrate, here in positive x -direction with speed V . The propulsion force is due to actin polymerization against the membrane at the front, polarity is maintained by motor-contraction at the rear. Concomitantly, via the formed adhesive bonds, the cell exerts a traction force on the substrate. This force deforms the substrate (that can be modeled either as a single cell-averaged spring, as sketched, or as a 2D elastic displacement field). In turn, the substrate deformation provides a feedback on the adhesion dynamics

free energy that has minima for the two “phases”: the inside of the cell (where $\rho = 1$) and the outside of the cell ($\rho = 0$). The phase field concept is introduced in detail in Sect. 1.2.1.

The propulsion mechanism for the cells considered here (e.g. keratocytes or fibroblasts) is associated with the polymerization of actin filaments against the membrane and the motor-induced contraction of the actin network, both ATP-consuming processes out of thermodynamic equilibrium. The propulsion machinery is therefore modeled by a phenomenological equation for the vector field $\mathbf{p}(x, y; t)$ that describes the local mean orientation of the actin filaments and is explained in Sect. 1.2.2. A more detailed discussion of the propulsion force balance is given in Sect. 1.2.3.

Explicit adhesion, characterized by the local density of adhesive sites $A(x, y; t)$, can be accounted for by making the rate of propulsion dependent on the number of the formed adhesive bonds. The adhesion dynamics itself is governed by a reaction-diffusion equation, where bonds form with a certain rate (that depends e.g. on the actin field \mathbf{p}) and detach when the substrate deformation exceeds a threshold. The substrate can be modeled either by a single cell-averaged elastic spring as shown in Fig. 1.2; its effect is then described by a time-dependent spring extension $U(t)$. Alternatively, one can treat the substrate as a 2D, i.e. height-averaged, viscoelastic medium, governed by an equation for the displacement field $\mathbf{u}(x, y; t)$. The coupling between the cell and the substrate is enabled via the traction force the cell exerts on the substrate; in turn, substrate deformations induce rupturing of adhesive bonds. Details on the implementation of the explicit adhesion and the deformable substrate are described in Sect. 1.2.4.

Before starting the discussion of the model essentials, we would like to point out the main advantages of the approach discussed here: first, in the framework of this model the motion of the cell is indeed *self-organized*: symmetric cells will be stationary, but they can be set into motion by external perturbations, for example a non-symmetric initial condition. This should be compared with the behavior found

experimentally in keratocyte fragments [167], discussed in Sect. 1.1.2. Second, the model can be refined in a step-by-step, modular fashion. This will be exemplified in this section by proceeding from implicit adhesion, to explicit adhesion with a description of the substrate as an elastic-spring, to a full 2D elastic substrate. This makes the modeling and, more importantly, the study of the repercussions of the added processes rather transparent. Last but not least, the phase field method allows for a rather effortless and elegant treatment of the moving cell boundary. In addition it is computationally very efficient: as the phase field is defined everywhere, the problem of a moving cell can be solved on a double-periodic domain, cf. Appendix “Numerical Methods”.

A detailed description of the results for the dynamics of single cells is presented in Sect. 1.3.

1.2.1 Phase Field Description of the Interface

The simplest phase field implementation of an interface is given by the equation

$$\partial_t \rho = D_\rho \Delta \rho - (1 - \rho)(\delta - \rho)\rho, \quad (1.1)$$

for the phase field $\rho(\mathbf{r}, t)$. The first term on the r.h.s. determines the width of the diffuse interface. The second term is the variational derivative, $\frac{\delta F}{\delta \rho}$, of a model “free energy”

$$F(\rho) = \int_0^\rho (1 - \rho')(\delta - \rho')\rho' d\rho'. \quad (1.2)$$

This free energy or “phase field potential” has been chosen such that it has a double well structure with minima at $\rho = 0$ and 1 , cf. Fig. 1.3. These minima correspond to the two “phases”: the inside, defined as $\rho = 1$, and the outside, defined as $\rho = 0$.

From the dynamic equation (1.1) and the functional form of the free energy, Eq. (1.2), it is easy to see that in the homogeneous case, both $\rho = 0$ and $\rho = 1$ are stable fixed points (while $\rho = \delta$, with δ typically chosen close to $\frac{1}{2}$, is unstable). In an inhomogeneous system, there will be hence a competition between these two solutions with smooth transition region(s) which define(s) the interface(s). In fact, in one spatial dimension and for $\delta = \frac{1}{2}$ the stationary solution of Eq. (1.1) is the typical tanh-function

$$\rho_0(x) = \frac{1}{2} \tanh \left(\frac{x - x_0}{2\sqrt{2D_\rho}} \right) + \frac{1}{2} \quad (1.3)$$

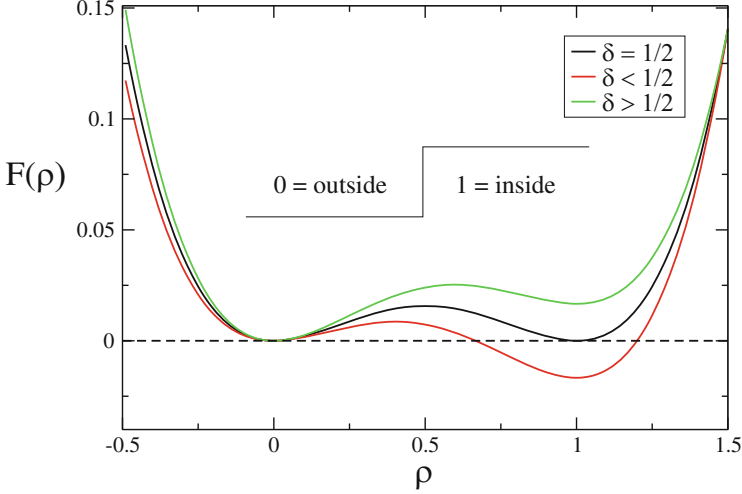


Fig. 1.3 Phase field potential. The free energy $F(\rho)$ associated to the phase field ρ . For $\delta = \frac{1}{2}$ (black curve) both “phases” 0 and 1 (with 1 corresponding to the cell’s interior) have the same energy. Otherwise one of the phases is preferred, resulting in a receding (the outside $\rho = 0$ is preferred, green curve) or advancing motion of the cell (the inside $\rho = 1$ is preferred, red curve)

known from Ginzburg–Landau theory (where we imposed as boundary conditions $\rho(-\infty) = 0$ and $\rho(\infty) = 1$). The not yet specified x_0 is the position of the interface¹ connecting the phases 0 and 1. Clearly, the width of the interface scales with $\sqrt{D_\rho}$.

By construction, the value of the parameter δ determines which of the two “phases” is preferred. For $\delta = \frac{1}{2}$ both phases have the same free energy and hence a *planar* interface is *stationary*, cf. the black curve in Fig. 1.3. If $\delta > \frac{1}{2}$ phase 0 is preferred—it has lower free energy, cf. the green curve in Fig. 1.3—and hence phase 0 will grow at the expense of phase 1: the cell (phase 1) shrinks. The opposite is the case for $\delta < \frac{1}{2}$: now phase 1 will grow. In other words, the cell advances or spreads.

In higher dimensions, the situation is affected by the curvature of the interface. An evolution equation for a circular two-dimensional “droplet” of radius R , large compared to the interface width, i.e. $R \gg \sqrt{D_\rho}$, can be obtained asymptotically by using the front solution given by Eq. (1.3) in polar coordinates (r, θ) . Substituting this solution in the form $\rho_0(x, y, t) = \rho_0(r - R(t))$ into Eq. (1.1), applying the solvability condition with respect to $\partial_r \rho_0$ and using that in polar coordinates the Laplace operator for this front solution $\partial_r^2 + r^{-1} \partial_r \approx \partial_r^2 + R^{-1} \partial_r$, one obtains that the radius of the droplet R evolves according to (cf. the so-called Maxwell rule):

¹Here, the interface position x_0 corresponds to $\rho = \frac{1}{2}$. Alternatively, the interface is also often defined as the maximum of $|\nabla \rho|$.

$$\frac{dR}{dt} = -\frac{D_\rho}{R} - \sqrt{2D_\rho}(\delta - 1/2). \quad (1.4)$$

Thus, if the (small) first term were not present, the droplet shrinks for $\delta > 1/2$ and spreads for $\delta < 1/2$. In fact, the first term is due to the inherent presence of a surface tension Σ , stemming from the free energy associated to the interface² (wall energy in Ginzburg–Landau theory). In turn, also the surface tension of the interface is to some extent tunable by the parameter D_ρ .

The presence of forces (e.g. the polymerization force exerted by the actin cytoskeleton) will effectively tilt the associated phase field free energy and hence interfere with the balance of the two phases. As a simple example of additional forces/constraints, we can implement the fact that keratocytes and many other cells do not change their two-dimensional volume (the cross-section in contact with the substrate) in the course of movement. Such a volume conservation can be easily implemented into the parameter δ as a global constraint:

$$\delta[\rho] = \frac{1}{2} + \mu \left[\int \rho dx dy - V_0 \right]. \quad (1.5)$$

Here μ is the stiffness of the constraint and the term in brackets is the difference between the current volume of the cell

$$V(t) = \int \rho(x, y; t) dx dy \quad (1.6)$$

and the prescribed volume V_0 . If, for instance, the cell is too small, the resulting $\delta < \frac{1}{2}$ will lead to a growth of phase $\rho = 1$ [cf. the red curve in Fig. 1.3 and Eq. (1.4)], i.e. the cell will extend or locally advance to restore the prescribed value V_0 .

The following principal advantages of the phase field approach can be identified: First, any moving boundaries are treated self-consistently, so no re-meshing is needed as in most other methods. Second, as the phase field is defined *everywhere* in the integration domain, the equation(s) can be considered on a two-dimensional double periodic domain, allowing for very effective solutions in the Fourier space, see Appendix “Numerical Methods”. Finally, and most importantly for modular modeling approaches, all couplings between the interface and other relevant fields (e.g. actin, motors, adhesion bonds, regulatory agents, etc.) can be implemented in a simple and elegant way via the phase field and its derivatives: a confinement of constituents to the interior of the cell can be achieved by multiplying the respective densities/terms by ρ (or powers thereof). As $\rho = 0$ outside, these terms then automatically vanish outside. Similarly, a localization of constituents to a region close to the interface can be achieved by using $\nabla\rho$ (or powers thereof), which naturally is peaked around the interface position and vanishes both in the inside and outside homogeneous phases.

² Defining the surface tension as the excess energy due to the interface, one obtains $\Sigma \propto \sqrt{D_\rho}$.

1.2.2 Actin Dynamics

The effect of actin cytoskeleton is described by a vector field, $\mathbf{p}(x, y; t)$. Its direction is the averaged orientation of actin and its absolute value contains both the degree of ordering and the overall actin density (for more information about macroscopic descriptions of polar liquid crystals, cf. [24, 85]). The directionality (“polarity”) of the actin filaments is due to the different polymerization rates at the barbed and pointed ends, as well as due to the directionality of the associated molecular motors such as myosin [68, 128].

From the biological perspective—cf. Sect. 1.1.1—one can identify two major factors that determine the most important coupling mechanisms of the actin polarization field \mathbf{p} to the cell’s membrane: First, the polymerization of actin filaments is governed by proteins that are located close to the membrane, namely nucleators and regulators like WASP and Arp2/3 [28, 128]. Hence the dynamic equation for the actin orientation \mathbf{p} should have a source term located close to the membrane. Second, the existing actin filaments that are polymerizing at the cell’s boundary push against the membrane due to the ratcheting of added monomers [124]. This process can be included via a term describing advection along the direction of already existing \mathbf{p} in the equation for the phase field ρ .

We can hence write

$$\partial_t \rho = D_\rho \Delta \rho - (1 - \rho)(\delta[\rho] - \rho)\rho - \alpha(A) \mathbf{p} \cdot \nabla \rho, \quad (1.7)$$

$$\partial_t \mathbf{p} = D_p \Delta \mathbf{p} - \beta \nabla \rho - \tau_1^{-1} \mathbf{p} - \tau_2^{-1} (1 - \rho^2) \mathbf{p}. \quad (1.8)$$

The last term in the ρ -equation describes the advection of the membrane along polymerizing actin \mathbf{p} , with a rate $\alpha(A)$ that may depend on the distribution of adhesive bonds A , see Sect. 1.2.4. In the \mathbf{p} -equation, we included a diffusion (or elastic) term. The second term describes the creation of actin located at the membrane, with a rate β (note that $\nabla \rho$ is negative when starting from the cell’s interior $\rho = 1$, so this is indeed a source term). The third term describes the degradation of actin, e.g. via depolymerization, with rate τ_1^{-1} where τ_1 is the typical time scale of the actin turnover. As the phase field is zero outside the cell, a non-zero value of \mathbf{p} outside the cell does not affect the dynamics. The last term explicitly suppresses \mathbf{p} outside the cell (note that the rate depends on $(1 - \rho^2)$, which is zero inside the cell and one outside). Alternatively, one could multiply the whole equation by ρ or advect the polarization field \mathbf{p} with the local speed of the cell (cf. Sect. 1.2.3), both being computationally somewhat more expensive.

The model so far describes a cell where actin is nucleated normal to the membrane (due to the direction of $\nabla \rho$ in the source term $\propto \beta$) and continuously pushes [with rate $\alpha(A)$] while being held back by the volume conservation implemented in $\delta[\rho]$, cf. Eq. (1.5). Being completely symmetric, the cell is not able to move, cf. Fig. 1.4a. The symmetry must be broken and the non-symmetric polarized state must be able to sustain itself dynamically. As discussed in Sect. 1.1.2, at least for keratocytes it has been shown [180] that myosin motors are responsible for the

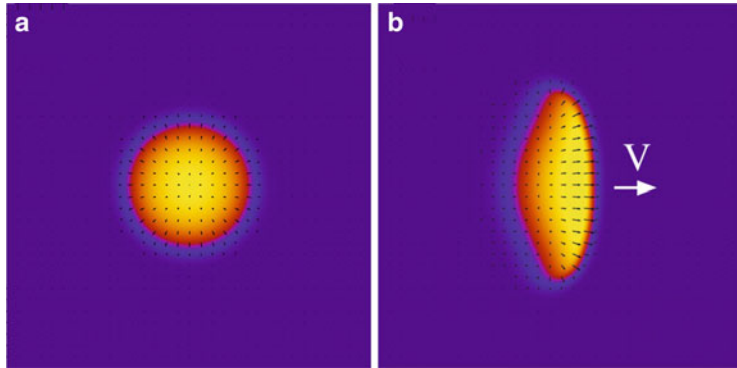


Fig. 1.4 Stationary vs. moving cell. Panel (a) shows a stationary and stable solution of a symmetric immobile cell, while (b) shows a polarized cell moving with a constant speed V . Both are results of Eqs. (1.10), (1.11) for the same parameters. The phase field is color coded (with blue the outside, $\rho = 0$, and yellow the inside, $\rho = 1$), the black arrows show the actin orientation field \mathbf{p} . See also ch1_video1.mpg http://www.physik.tu-berlin.de/~jakob/movies_small//ch1_video1.mpg and ch1_video2.mpg http://www.physik.tu-berlin.de/~jakob/movies_small//ch1_video2.mpg

symmetry breaking, due to two effects: (1) motors induce a local contraction of the actin network; (2) both for keratocytes and their cellular fragments, motors induce the formation of an acto-myosin bundle at the rear.

The first effect, contraction, can be modeled by adding a term $-\sigma|\mathbf{p}|^2$ to $\delta[\rho]$. This term can be motivated by active gel theory [76, 84, 85], which postulates a stress due to myosin motor activity in the form

$$\sigma_{ij} \propto \left(p_i p_j - \frac{1}{2} |\mathbf{p}|^2 \delta_{ij} \right). \quad (1.9)$$

As we do not intend to include another dynamic equation for the stress at this point, $-\sigma|\mathbf{p}|^2$ corresponds to the principal value of this tensor and describes actin contraction by motors with rate σ . In principle, it is possible to refine this description by accounting for the stress field explicitly.

The second effect, motor-induced bundling at the rear, can be modeled by adding a term $-\gamma[(\nabla\rho) \cdot \mathbf{p}] \mathbf{p}$ to the equation for \mathbf{p} , Eq. (1.8). This term can be motivated by a simple motor dynamics [185]. It describes an increased motor activity at the rear that suppresses the polarization \mathbf{p} by formation of an antiparallel bundle: note that, unlike nematic filament order, the polar order described by the vector \mathbf{p} is *reduced* in an anti-parallel, contractile bundle. Macroscopically, the suggested term $-\gamma[(\nabla\rho) \cdot \mathbf{p}] \mathbf{p}$ breaks the $\pm\mathbf{p}$ reflection symmetry. While the bundling effect seems to be keratocyte-specific (and is most probably needed for their crescent-like shape), the contractile term should apply quite generally.

We hence arrive at the following “minimal model”, constituted by the two coupled equations

$$\partial_t \rho = D_\rho \Delta \rho - (1 - \rho)(\delta[\rho] - \sigma |\mathbf{p}|^2 - \rho) \rho - \alpha(A) \mathbf{p} \cdot \nabla \rho, \quad (1.10)$$

$$\partial_t \mathbf{p} = D_p \Delta \mathbf{p} - \beta \nabla \rho - \tau_1^{-1} \mathbf{p} - \tau_2^{-1} (1 - \rho^2) \mathbf{p} - \gamma [(\nabla \rho) \cdot \mathbf{p}] \mathbf{p} \quad (1.11)$$

together with Eq.(1.5) defining $\delta[\rho]$. Either one of the two motor-related terms, contraction $\propto \sigma$ and bundling $\propto \gamma$, can induce stable moving solutions: a representative moving cell (with both motor-related terms present) is shown in Fig. 1.4b. Note that the parameters in Fig. 1.4a, b are the same, only for (b) the *initial condition* was more strongly polarized in the $+x$ -direction. Hence the developed model is bistable, in accordance with the experiments on cell fragments [51, 167] discussed in Sect. 1.1.2.

In addition, the model self-consistently reproduces the phenomenology of the graded radial extension model, proposed as a (purely descriptive) model for keratocytes [94] and discussed briefly in Sect. 1.1.3: there the authors noted that, since the shape does not change, the velocity should be graded with a maximum at the middle of the moving front and decreasing towards the sides of the cell. Examining the distribution of \mathbf{p} in the steady moving state, Fig. 1.4b, and noting that the local velocity is roughly proportional to \mathbf{p} and in the direction of \mathbf{p} , cf. the advective term, shows that this is automatically the case in our model. Table 1.1 summarizes estimates for the main parameters used in the minimal model Eqs.(1.10), (1.11).

Table 1.1 Parameters of the model and estimates

| Parameter | Value | Description |
|---------------|-------------|---|
| D_ρ | 0.2 | Diffusion/elastic coeff. for \mathbf{p} → sets typical length scale to $\simeq 1 \mu\text{m}$ |
| τ_1^{-1} | 0.1 | Degradation of \mathbf{p} inside cell (actin depolymerization rate of 10 s^{-1}) → sets typical time scale to $1 - 10 \text{ s}$ |
| α | 0.5–4 | Advection of ρ by \mathbf{p} |
| β | 0.5–4 | Creation of \mathbf{p} at interface \leftrightarrow actin polymerization velocity $0.1 \mu\text{m s}^{-1}$ |
| γ | 0–1 | Symmetry breaking due to motors, corresponding motor velocity $0.1 \mu\text{m s}^{-1}$ |
| σ | 0–1 | Contractility due to motors |
| D_p | 1 | Determines width of diffuse interface |
| V_0 | πr_0^2 | Overall area of cell [$r_0 = 5 - 18 \mu\text{m}$] |

Summary of the typical (rescaled) values used in the numerical solution of Eqs.(1.10), (1.11) and their correspondence to typical values for the “real” system. Other parameters: stiffness of volume conservation: $\mu = 0.1$; decay of \mathbf{p} outside cell: $\tau_2^{-1} = 0.4$

1.2.3 On Force Balance Versus Explicit Flow

Equation (1.10) relates the normal speed of the interface, \mathbf{V} , with the distribution of the actin polarization. Indeed, upon substituting the front solution, Eq. (1.3), in the form $\rho(\mathbf{r}, t) = \rho(\mathbf{r} - \mathbf{V}t)$ into Eq. (1.10), we obtain after using the solvability condition (cf. Sect. 1.2.1) the following kinematic condition at the interface:

$$\mathbf{V} = \alpha(A)\mathbf{p} - D_\rho \boldsymbol{\chi}, \quad (1.12)$$

where $\boldsymbol{\chi}$ is the local interface curvature.

In order to obtain the force balance condition in the bulk, we can represent Eq. (1.10) as a pure advection equation,

$$\partial_t \rho = \mathbf{v} \cdot \nabla \rho, \quad (1.13)$$

where \mathbf{v} is the local advection velocity of the cell. The equation governing the advection velocity then reads (neglecting for simplicity the contractile term $\propto \sigma$)

$$\zeta \mathbf{v} = \alpha(A)\mathbf{p} - \nabla P. \quad (1.14)$$

In general, on the l.h.s. of Eq. (1.14) a viscous friction coefficient ζ should appear, but it can be absorbed in the parameters on the r.h.s., so we can set³ $\zeta = 1$. P is an effective pressure related to the volume constraint and counter acting the propulsion force $\propto \mathbf{p}$. In turn, in models that incorporate an explicit actin flow, the pressure has to be obtained self-consistently. For example, it can be obtained either from a simple incompressibility condition, $\nabla \cdot \mathbf{v} = 0$, or from a global mass conservation condition for the actin monomers as in [146]. Approaches including flow explicitly are therefore more computationally expensive (and in addition can face problems related to the ill-definedness of two-dimensional hydrodynamics and strong dependencies on the boundary conditions) than just solving the simple Eq. (1.10).

On the level of our model, one can cast the effective pressure gradient P in the form

$$\nabla P = \rho(1 - \rho) \left(\mu \left[\int \rho dx dy - V_0 \right] - \rho \right) \frac{\nabla \rho}{|\nabla \rho|^2}, \quad (1.15)$$

where we used that the terms $D_\rho \Delta \rho - (1 - \rho)(\frac{1}{2} - \rho)\rho$ on the r.h.s. of Eq. (1.10) just define the interface and are passively advected. We note that there is no guarantee that the r.h.s. of Eq. (1.15) is indeed the gradient of some scalar potential. Moreover, the incompressibility condition for the flow velocity $\nabla \cdot \mathbf{v} = 0$ is only approximately

³Actually, already in Eq. (1.1), a time scale for the change in ρ should be included, which was set to one.

fulfilled, which is the price to pay for the simplicity of Eq.(1.10). The argument of force balance given here can in principle be extended to account for the other relevant forces, like contractile stresses inside the cell, or the membrane tension (see e.g. [19]).

1.2.4 Adhesion and Coupling to Substrate Deformation

As discussed in Sect. 1.1, cell adhesion is a multi-stage process involving interactions of several proteins forming complexes that link the internal actin cytoskeleton to the outside, typically the ECM. Moreover, the system is mechanosensitive, i.e. the formation of adhesion sites depends on forces, both external ones and those generated by the cell. Finally, depending on the time scales of motion, nascent adhesion sites may also undergo maturation.

In view of this, we restrict ourselves here to the most basic phenomenology of motility-related adhesion: first, we account for the fact that the rectified actin polymerization, creating a pushing force close to the membrane, can propel the cell forwards *only if* the actin filaments locally adhere. In other words, (part of) the propulsion force has to be transferred to the substrate, as can be observed experimentally by traction force measurements [39, 55]. This fact had already been accounted for in Sect. 1.2.2 by writing the propulsion rate as $\alpha(A)$ with $A(\mathbf{r}, t)$ the local number of formed adhesive bonds. For simplicity we assume a linear dependence $\alpha(A) = \alpha A$, i.e. an increase in the amount of adhesive bonds directly increases the propulsion force. Note, however, that for too strong adhesion, the cell speed decreases again (see [119] and the discussion in Sect. 1.1.2), since breaking the adhesive bonds then takes too much energy. This dependence could be captured by using a nonlinear (non-monotonic) function $\alpha(A)$ instead. Second, we account for a nonlinear attachment of the adhesive bonds and a detachment mechanism that involves the substrate deformation, as detailed below.

A simple continuous equation for the density of adhesive bonds [182] (cf. also [146] for a discrete implementation of adhesion) is given by

$$\partial_t A = D_A \Delta A + \rho (a_0 p^2 + a_n A^2) - (d(u) + sA^2) A. \quad (1.16)$$

The first term describes the diffusion of the proteins forming the adhesive complexes within the membrane. The second term describes two attachment mechanisms, both restricted to the inside of the cell by the common factor ρ : first, a linear attachment rate that is proportional to p^2 , implementing the necessary presence of actin to build an adhesive bridge. Second, an attachment term that is nonlinear in A and models the fact that several mechanisms facilitate the attachment of additional bonds if a bond has been already formed (for instance, locally reduced membrane fluctuations). The last term contains the two dominant contributions limiting the number of adhesive bonds: the first is linear detachment, with a rate d that depends on the substrate deformation u , see below. The second is cubic in A and therefore limits the

total number of adhesive bonds at a given place, i.e. implements excluded volume of the adhesive complexes (alternatively one could, in addition to the engaged bonds, add an equation for the non-engaged bonds; but again this modification will be computationally more expensive).

The detachment rate $d(u)$ of the adhesive bonds depends on the substrate displacement, in general $\mathbf{u}(x, y; t)$ (alternatively, one could also use the stress/force). For simplicity one can assume a step function $d(u) = d\theta(u - U_c)$, where $\theta(x) = 1$ for $x > 0$ and 0 otherwise. For numerical reasons it is better to approximate the step-function via a smooth, e.g. tanh-like dependence

$$d(u) = \frac{d}{2} \left(1 + \tanh(b(|\mathbf{u}|^2 - U_c^2)) \right). \quad (1.17)$$

In both cases U_c determines the critical displacement for rupturing and d the maximum rate of detachment. b is a rather irrelevant parameter introduced for the purpose of smoothing of the step function (the larger b is, the steeper is the transition).

The substrate can be described at different levels. The most detailed approach for now is to derive an equation governing the local substrate displacement $\mathbf{u}(x, y; t)$ by applying a thin layer approximation to a linear viscoelastic model of the substrate. Details on the derivation can be found in [102] and in Appendix “Derivation of the Equation for the Elastic Displacements”. One obtains

$$\eta \partial_t \mathbf{u} = - \left(G \mathbf{u} - \frac{1}{\xi} (\mathbf{T} + h[5\Delta \mathbf{T} + 19\nabla(\nabla \cdot \mathbf{T})]) \right), \quad (1.18)$$

where G is the elastic (shear) modulus of the substrate, η describes dissipation in the adhesive process (e.g. due to bond rupturing) and h is related to the thickness of the deformable layer (see Appendix “Derivation of the Equation for the Elastic Displacements”).

The sources for the substrate deformations are the local traction forces exerted by the cell, which can be written as

$$\mathbf{T} = -\xi A \rho \left(\mathbf{p} - \frac{\langle A \mathbf{p} \rho \rangle}{\langle A \rho \rangle} \right), \quad (1.19)$$

where we introduced

$$\langle \cdot \rangle = \int \cdot dx dy \quad (1.20)$$

as a shortcut for integrals over the whole domain. The traction is proportional to both ρ (restriction to the interior) and more importantly A , since formed adhesive bonds are a precondition for the force transfer. The first contribution is opposite to the local propulsion direction \mathbf{p} , including ξ that describes the efficiency of force transmission [102]. The second contribution is due to frictional dissipation.

Table 1.2 Parameters of adhesion and substrate dynamics

| Parameter | Value | Description |
|-----------|--------------|---|
| a_0 | 0.01–0.1 | Linear attachment rate of adhesive bonds |
| a_{nl} | 1–1.5 | Nonlinear attachment rate of adhesive bonds |
| d | 1 | Detachment rate of adhesive bonds |
| U_c | $\sqrt{0.2}$ | Critical substrate stretch for bond rupture |
| s | 1 | Excluded volume of adhesive bonds |
| D_A | 1 | Diffusion of adhesive bonds |
| G | 0–0.3 | Elastic modulus of the substrate |
| η | 10/3 | Substrate relaxation (dissipation) rate |
| h | 0–0.1 | Thickness of deformable substrate |

Summary of the parameters and the typical (rescaled) values used in Eq. (1.16), and in Eq. (1.18) or (1.21), respectively

Note that the total traction $\langle \mathbf{T} \rangle$ is zero, as it should be for a force-free self-propelled object like a cell crawling on a substrate.

It is possible to simplify the model, for instance in case when a spatial resolution of the traction force is not needed. Namely, one can perform a projection of the displacements on the force dipole in the direction of motion, leading to a single equation for an overall (cell-averaged) substrate displacement (see [182] for the derivation). This procedure results in the substrate being accounted for as an effective spring underneath the cell, as sketched in Fig. 1.2. This spring has an extension $\mathbf{U}(t)$ that is governed by the simple ordinary differential equation (ODE)

$$\eta \frac{d\mathbf{U}}{dt} = -(\mathbf{GU} + \mathbf{V}) . \quad (1.21)$$

Here \mathbf{V} is the center of mass velocity. Clearly, a description of the effects of the substrate deformation in terms of the simple Eq. (1.21) is computationally more efficient. However, as we will show in Sects. 1.3.5.2, 1.3.4, the fully-resolved 2D substrate deformation field \mathbf{u} governed by Eq. (1.18) is necessary to describe durotaxis and bipedal motion of cells, respectively. Table 1.2 lists the additional parameters and their values used, in case adhesion and substrate dynamics are taken into account.

1.3 Dynamics of an Individual Cell

Having set up the model for a single cell, we will now analyze and discuss in detail its behavior. Especially, we will demonstrate how upon increasing the level of detail, the model becomes able to capture most of the experimental facts discussed in Sect. 1.1.2.

1.3.1 Steady Moving Cell

If the symmetry of the cell is broken, and the propulsion is sufficiently strong—we will quantify both statements in the next section—the model allows for cells moving steadily with a constant velocity, as already shown in Fig. 1.4b. Such a solution for the more detailed model, accounting for the adhesion dynamics and substrate displacement, is shown in Fig. 1.5: (a) displays the cell's shape, with the phase field ρ shown color coded and its contour at $\rho = 0.25$ in black, as well as the actin orientation field \mathbf{p} as arrows. Panel (b) shows the traction field \mathbf{T} as described by Eq. (1.19) and panel (c) displays the field of the local substrate displacements \mathbf{u} . In both panels (b) and (c) the absolute values of the force and displacement, respectively, are color coded. One can see that for the selected model parameters, the traction points inwards and is highest at the leading edge. This is a direct consequence of our implementation of the actin dynamics, Eq. (1.11), that generates a pushing force (proportional to α) at the front and accounts for contraction along \mathbf{p} (proportional to σ). The displacement field is maximum in the bulk of the cell and its local orientation is similar to that of the traction pattern. The fact that the displacement is lagging behind is due to the interplay between the movement of the cell over the substrate and the viscoelastic relaxation of the latter.

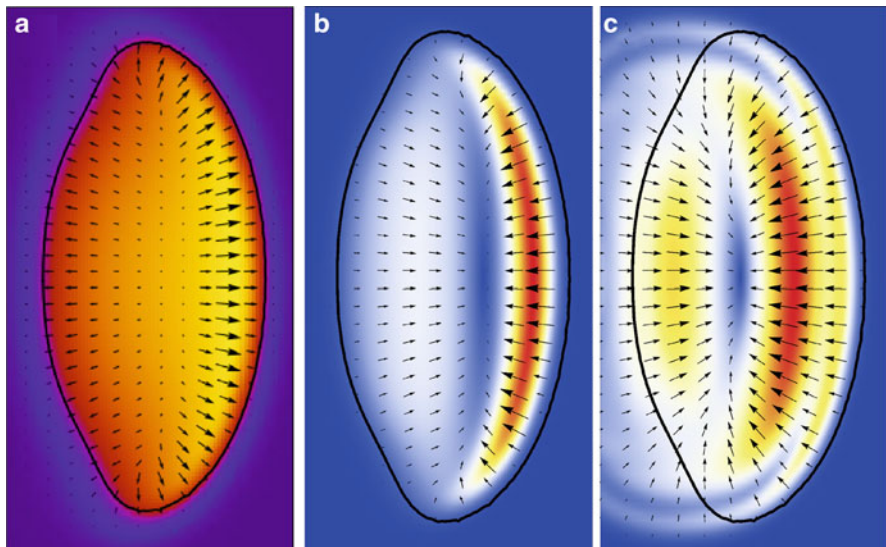


Fig. 1.5 Distributions of various fields for a steady moving cell (motion is to the right). (a) The cell shape (color coded; the *black solid line* shows the contour at $\rho = 0.25$) and the internal actin orientation field \mathbf{p} (arrows). (b) The traction force \mathbf{T} . Red (blue) corresponds to large (small) values of $|\mathbf{T}|$. (c) The displacement field \mathbf{u} . Red (blue) corresponds to large (small) values of $|\mathbf{u}|$. Parameters: $\alpha = 4$, $\beta = 2$, $\gamma = 0.5$, $\sigma = 1.3$, $a_0 = 0.001$, $a_{nl} = 1.5$, $G = 0.25$, $h = 0.1$, others as given in Tables 1.1 and 1.2; initial cell radius $r_0 = 15$

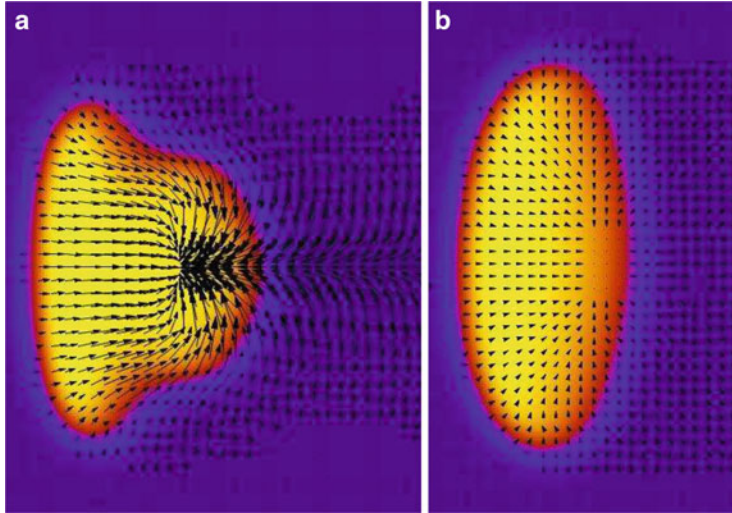


Fig. 1.6 Diversity of shapes and traction patterns. Steady moving cells are shown, direction of motion is to the left. The phase field is color coded and the traction force exerted on the substrate is shown by the *arrows*. Parameters: (a) $\gamma = 0.7$, $\sigma = 0.6$. (b) $\gamma = 0.5$, $\sigma = 1.3$. Other parameters are the same for both: $\alpha = 4.5$, $\beta = 2$, $a_0 = 0.01$, $a_{nl} = 1.5$, $G = 0.05$, $h = 0.1$, cf. also Tables 1.1 and 1.2; initial cell radius $r_0 = 15$

Figure 1.6 shows two steady-moving cells obtained for different model parameters. Note that they are not only differently shaped, but also have different traction patterns, and consequently different force transfers to the substrate: the cell in (a) has high traction at the rear, while the one in (b) has overall small traction of almost homogeneous absolute value.

Let us compare these findings to the experimental facts discussed in Sect. 1.1.2. The forces exerted by cells on the substrate can be obtained experimentally by traction force microscopy. In this method, fluorescent beads are immersed into a soft substrate. The traction forces can be reconstructed from the displacements of the beads during the action of cellular forces by solving an inverse problem [39, 144]. Alternatively, cells can be placed on microfabricated arrays of micro-pillars [158], their deflections directly giving the traction distribution. Since its inception about 15 years ago, traction force microscopy has become a standard tool and has recently been automatized [37], as well as extended to 3D displacement fields [56]. It has been applied to various cell types, e.g. to fibroblasts [39, 113], keratocytes [55], epithelial cells [58], neutrophils [151] and glioma cells [164]. The primary interest of the model, however, rather lies in the generic features of cell motility and cellular force transmission. Hence the obtained traction (and consequently the displacement) distributions are not necessarily applicable to any specific cell type (yet). In fact, from the experiments mentioned above it is known—but not well understood—that different cell types exhibit completely different traction patterns: fibroblast cells have highest traction at the front [39], similar to the case shown in Fig. 1.5b.

Keratocytes have highest traction at the sides, which is most probably a consequence of the self-organized acto-myosin bundles spanning to their sides [55], not yet included into the modeling. Finally, neutrophils have highest traction at the rear [151], similar as shown in Fig. 1.6.

To summarize, modeling of a specific cell type most probably needs to introduce cell-specific processes, e.g. in the actin and adhesion dynamics. Nevertheless, Figs. 1.5 and 1.6 clearly demonstrate that the model is able to capture various shapes of cells, and also various traction patterns.

1.3.2 Subcritical Onset of Motion

The model Eqs. (1.10), (1.11) exhibit a bistability, as already shown in Fig. 1.4: the cell either is symmetric and spreading on the substrate, or it is polarized and moving. Starting from the spreading state, an abrupt onset of motion occurs upon a perturbation for a wide range of the parameters. In most of the simulations shown, the initially round cell was stimulated to move by adding a certain distribution of the polarization to the initial condition. Depending on the model parameters and the initial condition, either the circular symmetric shape was restored, cf. Fig. 1.4a, or the system evolved into a stable moving, polarized, crescent-shape cell as shown in Fig. 1.4b.

To characterize the onset of motion and the propagation velocity, we performed simulations for various parameter ranges. Results are shown in Fig. 1.7a as a function of the parameter γ , describing the asymmetry induced by the molecular motor distribution. We started with a stationary moving cell for a large value of γ and then slowly ramped down γ . As one can see from the figure, the cell's motion stops abruptly at a critical value of $\gamma_c \approx 0.42$, at a minimal velocity of $V_{\min} \approx 0.62$, which of course both depend on the other model parameters.

To quantify also the shape, from the phase field ρ we calculate the aspect ratio h (note that $h = 1$ for a circle) and the two measures for the asymmetry (skewness), ζ and η , as defined in Appendix ‘‘Characterizing the Cell’s Velocity and Shape’’. As shown in Fig. 1.7a the velocity, V , the aspect ratio’s deviation from the circular shape, $h - 1$, and the asymmetry measures all drop to zero for $\gamma < \gamma_c$. Remarkably, one of the asymmetry measures, ζ , increases approaching the transition point, while the second, η , decreases monotonically.

Figure 1.7a illustrates how a moving cell stops abruptly when the parameter γ is reduced. On the other hand, when a stationary circular fragment is perturbed by a small-amplitude noise, it remains stationary for the parameter range shown in that figure. One needs a *finite amplitude* perturbation to trigger the onset of motion, e.g. by choosing a region inside the cell and adding a constant \mathbf{p} . In fact, the onset of cellular motion is a *subcritical* transition, in agreement with the experiments on fragments [167] discussed in Sect. 1.1.2. In these experiments, the keratocyte fragments had to be strongly perturbed to initiate motion, while unperturbed or slightly perturbed fragments stayed immobile. This subcriticality is caused by the

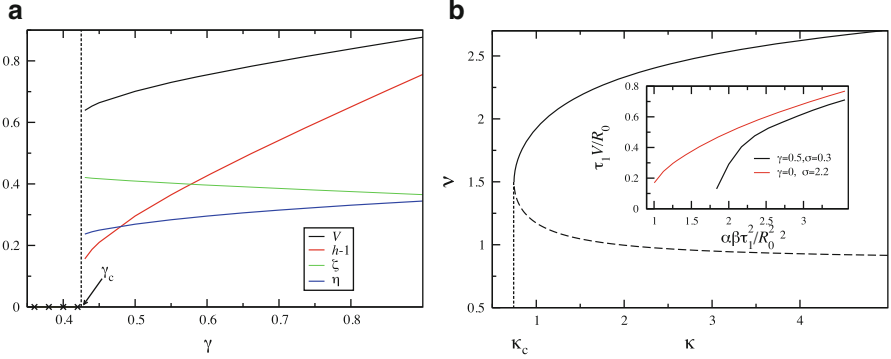


Fig. 1.7 Subcritical transition of stationary vs. moving cells. (a) The cell’s velocity, V , the aspect ratio’s deviation from the circular shape, $h - 1$, and the asymmetry measures ξ, η (cf. Appendix “Characterizing the Cell’s Velocity and Shape”) are shown as a function of γ , the parameter governing the motor-induced asymmetry. The plot was obtained by decreasing γ for a moving solution; for $\gamma < \gamma_c \approx 0.42$ all the quantities vanish and a round, stationary solution ensues (indicated by \times signs). Other parameters: $\alpha = 3$, $\beta = 1.6$, $\sigma = 0.3$, cf. also Table 1.1; initial cell radius $r_0 = 10$. (b) The normalized velocity v vs. the normalized driving force κ . The main plot shows the solutions of Eq. (1.27), the *solid line* corresponding to the stable moving branch and the *dashed line* to the unstable branch. The *inset* shows results obtained by numerically solving the full model for different values of γ and σ as indicated. Other parameters: $\alpha = 4$, $\beta = 2$, constant adhesion $A = 1$, cf. also Table 1.1; initial cell radius $r_0 = 15$

motor-related symmetry-breaking term (proportional to γ), and reflects the fact that a perturbation has to be large enough for the motors to establish a significant asymmetry in their distribution across the cell.

1.3.2.1 Analytical Study of Cell Movement in Circular Approximation

In this and the following section, a reduced analytic description for a steadily moving cell is developed. The main simplification is to assume a fixed round shape of the cell. In spite of this approximation, one should be aware that the cell *must be* polarized and non-circular to move, implying that the distribution of polarization \mathbf{p} is not axi-symmetric. We will also neglect the substrate displacement and consider homogeneous adhesion $A = A_0 = \text{const.}$

The center of mass (c.o.m.) of the cell will be described by $\mathbf{R} = (X, Y)$ and the fixed circular shape is taken, for the sake of simplicity, as a Gaussian $\rho(\mathbf{r}) = \exp(-r^2/R_0^2)$, with R_0 measuring the size of the cell. This choice makes analytic calculations possible.

Focusing on the polymerization dynamics (putting $\gamma = 0, D_p = 0$) the polarization \mathbf{p} for a stationary cell is given to leading order by $\mathbf{p} \approx -\beta\tau_1\nabla\rho$, cf. Eq. (1.11). Similarly, for $\mathbf{V} \neq 0$, Eq. (1.11) yields in the moving frame the condition $-\mathbf{V} \cdot \nabla\mathbf{p} = -\tau_1^{-1}\mathbf{p} - \beta\nabla\rho$. Hence, for small \mathbf{V} we obtain

$$\mathbf{p} \approx -\tau_1 \beta \nabla [\rho + \tau_1 \mathbf{V} \nabla \rho] \approx -\tau_1 \beta \nabla \rho (\mathbf{r} + \tau_1 \mathbf{V}). \quad (1.22)$$

Therefore, to leading order, the polarization field in a moving cell is just given by the gradient field of ρ , shifted in space by the amount $\tau_1 \mathbf{V}$. Correspondingly, the net polarization $\bar{\mathbf{p}} = \int \mathbf{p} dx dy / \pi R_0^2 \neq 0$ for any $\mathbf{V} \neq 0$. Consequently, in spite of the circular approximation for the cell shape, one may obtain non-trivial results due to the non-symmetric distribution of polarization.

1.3.2.2 Velocity Branches in Circular Approximation

Here we show how the velocity of a stationary moving cell can be estimated by means of the circular approximation discussed above. Assuming a solution of the form $\rho = \rho(\mathbf{r} - \mathbf{V}t)$ and multiplying Eq. (1.10) by $\partial_x \rho, \partial_y \rho$, after integration over the entire domain we obtain $V_x = \alpha a_x$ and $V_y = \alpha a_y$ for the components of the center of mass velocity, with (for a round cell)

$$a_x = \frac{2}{\pi} \int A(p_x \partial_x \rho + p_y \partial_y \rho) \partial_x \rho dx dy, \quad (1.23)$$

$$a_y = \frac{2}{\pi} \int A(p_x \partial_x \rho + p_y \partial_y \rho) \partial_y \rho dx dy. \quad (1.24)$$

Let us consider a cell moving along the x -direction. Then $V_y = 0$ and $V_x = \alpha a_x$, where a_x can be explicitly integrated using the expression (1.22) for \mathbf{p} . The integration yields the following expression

$$a_x = \frac{8\beta A_0 \tau_1^2}{81R_0^4} V_x e^{-\frac{2\tau_1^2 V_x^2}{3R_0^2}} (4\tau_1^2 V_x^2 - 3R_0^2). \quad (1.25)$$

As $V_x = \alpha a_x$ this immediately shows that one of the roots is $V_x = 0$, corresponding to the stationary cell. Additional possible roots are given implicitly by

$$\frac{8\alpha\beta A_0 \tau_1^2}{81R_0^4} e^{-\frac{2\tau_1^2 V_x^2}{3R_0^2}} (4\tau_1^2 V_x^2 - 3R_0^2) = 1. \quad (1.26)$$

This equation has non-trivial solutions only for velocities above a certain critical value. To see that, we introduce the dimensionless velocity $v = \tau_1 V_x / R_0$ and the dimensionless parameter $\kappa = 8\alpha\beta \tau_1^2 A_0 / (81R_0^2)$, which is proportional to the driving by actin polymerization α, β . Then Eq. (1.26) assumes a simple dimensionless form

$$\kappa e^{-\frac{2v^2}{3}} (4v^2 - 3) = 1. \quad (1.27)$$

The minimal finite velocity of Eq. (1.27) is $v = 3/2$. For $\kappa > \kappa_c = e^{3/2}/6 \approx 0.746$, two roots exist: Fig. 1.7b shows the two respective branches. The upper

branch (solid curve) is stable and the lower one (dashed) unstable. The result is in qualitative agreement with the numerical solution of the full model: it captures the inherent bistability and the finite velocity gap. However, the numerical values for the dimensionless critical driving parameter κ_c are off by approximately a factor of two due to our approximations, especially due to the assumption of the fixed round shape. For comparison, the inset in Fig. 1.7b presents the cell velocity vs. the propulsion force (both dimensionless again) obtained by direct numerical solution of Eqs. (1.10) and (1.11). The black curve is for keratocyte-like parameters (with $\gamma \neq 0$ mimicking actomyosin bundle formation at the cell's rear). The red curve is without this term, but with a much higher value of σ , describing the overall contraction by myosin [cf. the discussion after Eq. (1.11)]. This demonstrates that also the contractility of motors, proportional to σ , is able to polarize the cell and to create moving states.

1.3.3 Steady Motion vs. Stick-Slip

Cellular motion often is not continuous but rather unsteady. For instance, it has been found that lamellipodia can show periodic contractions that depend on the adhesiveness of the substrate [59]. These contractions later on were interpreted by a stick-slip model [175], i.e. using a mechanical analogy with a system of two rigid objects that are sliding over each other and exhibiting spontaneous jerking motion. Stick-slip-like motion has been found in parts of the lamellipodium, e.g. in osteosarcoma cells [13], as well as in filopodia [30]. Finally, transitions from steady motion to stick-slip and to arrest of motion have been observed in human glioma cells cultured on ECM [164], as well as for other cell types. The transition from steady to stick-slip motion is typically modeled in a simple one-dimensional situation, see e.g. [89]. Stick-slip behavior can also be found in the model at hand: we will now investigate in more detail the consequences of the (still simple) adhesion dynamics and of the substrate deformability, and analyze in detail the occurring motility modes.

First we verify whether the addition of the adhesion dynamics, Eq. (1.16), and the substrate deformation via Eq. (1.21) [or Eq. (1.18)] to the minimal model [Eqs. (1.10) and (1.11) for the interface and the actin orientation], still comprises the phenomenology of the model described previously. This can be easily tested by choosing a relatively high value of the substrate stiffness, since then the spring extension will not play a significant role. Indeed, after a transient the system exhibits a steadily moving state, in agreement with the simple model [185]. The number of the adhesive bonds A and the substrate spring extension U both reach time-independent values. Keeping the substrate stiffness G high and decreasing the value of propulsion α , the motion ceases, again in accordance with the previous results. In that case, the polymerization force is not high enough to sustain the polarized moving state and the cell stops and acquires a radially symmetric shape.

Having this established, one can study the model in a broader range of parameters. One anticipates the occurrence of a stick-slip regime by the following generic mechanism: When the adhesion sites are forming, the cell's velocity increases. By propelling itself forwards, the cell exerts dipolar forces on the substrate⁴ and the substrate deformation increases in absolute value. For low enough substrate stiffness G , the substrate is deformed to an extent that the critical value U_c for bond rupture is reached and the adhesive contacts rapidly break. However, the cell still has to slow down and adjust its shape to the new conditions. As the substrate deformation relaxes, new adhesion sites form again and the cycle restarts. Note that due to the coupling to the shape dynamics, stick-slip oscillations are not necessarily strictly periodic. The average period of the stick-slip cycle increases with a decrease of the attachment rate a_0 , roughly linearly, and the effective stiffness G .

The shape deformations and the local dynamics of the adhesive contacts are shown in Fig. 1.8. This figure illustrates the shape of the cell, the actin orientation

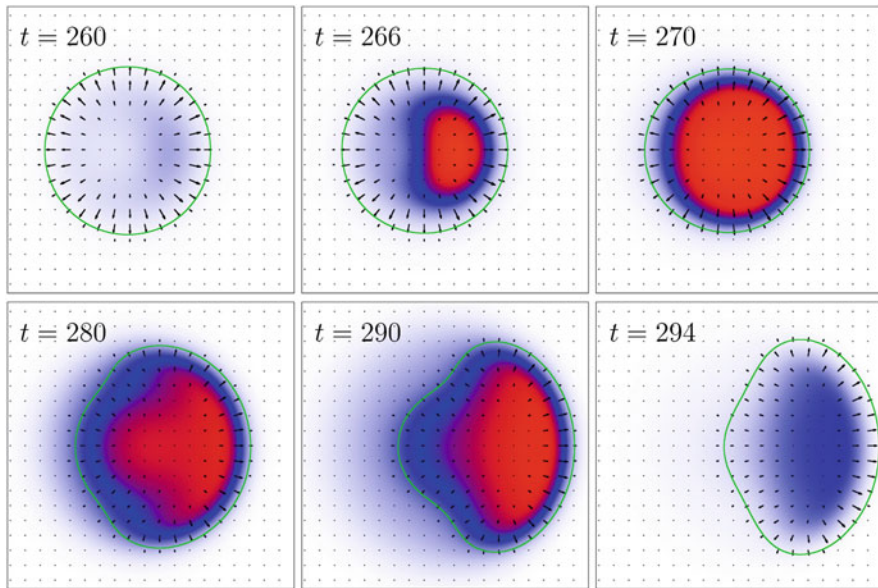


Fig. 1.8 Spatially resolved dynamics during a stick-slip cycle. The cell's boundary is shown as the *green curves*. The *arrows* display the local averaged actin filament orientation. The density of adhesion sites is color coded (with *white color* corresponding to $A = 0$, *blue* to 0.5 and *red* to 1). The direction of motion is to the right. Between $t = 294$ and the next attachment event, the cell will relax to an almost round state, similar to the one displayed for $t = 260$, i.e. the cycle restarts. Parameters: $\alpha = \beta = 2.5$, $\gamma = 0.5$, $\sigma = 0.3$, $a_0 = 0.0025$, $a_{nl} = 1.5$, $U_c = \sqrt{5}$, $G = 0.15$, $\eta = 10$, cf. also Tables 1.1 and 1.2; initial cell radius $r_0 = 15$

⁴Since the cell is self-propelled, the net force exerted by the cell on the substrate, however, is zero.

and the local distribution of adhesive contacts during the stick-slip cycle. At first, there are practically no adhesive contacts and the cell is almost round. In the next panel, adhesion contacts form close to what becomes the leading edge of the cell (the cell is moving to the right), due to the fact that $|\mathbf{p}|$ is still slightly higher there, a remnant from the last cycle. Then adhesive bond formation spreads, either, as for the given parameters, over the entire cell or only partly, close to the front. With the present, rather simple implementation of the adhesion dynamics, this distribution is determined mainly by the time scales of adhesion and substrate dynamics and the value of the diffusion coefficient D_A . Since the distribution of adhesive contacts is not symmetric—they formed earlier close to the leading edge—the cell is able to polarize and begins to move again, until the substrate displacement generated by the cell reaches the critical value and adhesion breaks down. As the propulsion force decreases, the cell slows down and rounds up, i.e. depolarizes, cf. the last panel.

By performing large scale parameter studies, it is possible to obtain dynamic “phase” diagrams for the different modes of cell motion, see Fig. 1.9. In part (a) both the substrate stiffness G and the propulsion parameter α were varied. In agreement with the above discussion, for high enough substrate stiffness and propulsion strength, the cell displays steady-state motion with fixed shape. Decreasing the stiffness, at intermediate values of G a region of persistent stick-slip motion appears, while for still smaller stiffness the cell is unable to move and stops. On the other hand, upon a decrease of the propulsion parameter α , the size of the stick-slip region shrinks until the cell is completely unable to move below a certain critical value α_c .

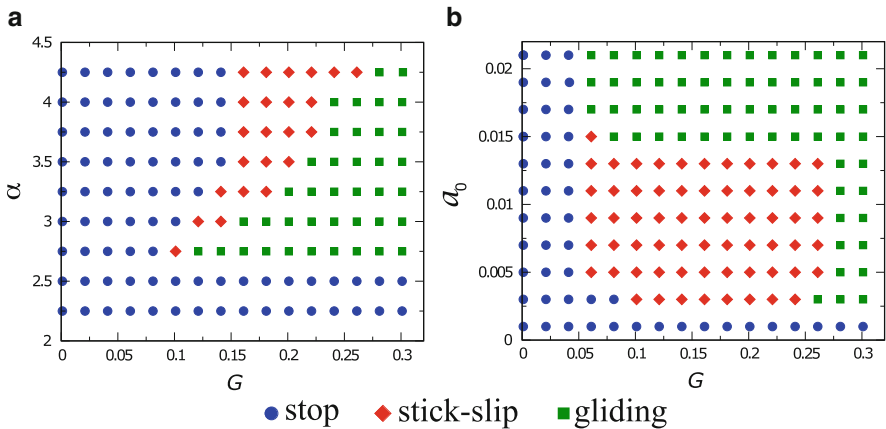


Fig. 1.9 Diagrams of motility modes. (a) The different modes of motility as a function of the propulsion parameter α vs. the substrate stiffness G for $a_0 = 0.01$ and $\beta = \alpha/2$. (b) The different modes of motility as a function of the rate of adhesion formation a_0 vs. the substrate stiffness G for $\alpha = 4$, $\beta = 2$. The other parameters are the same as in Fig. 1.8. In both panels, parameter combinations for which the cell stops after an initial perturbation are marked by *blue circles*, persistent stick-slip motion is marked by *red diamonds* and steady moving states (*gliding*) are depicted by *green squares*

Figure 1.9b displays a similar plot, where the rate of adhesion formation a_0 and the substrate stiffness are varied. Similar as for the propulsion parameter α , there is a threshold value for the adhesion rate below which the cell is not able to move—adhesion is just too weak to transfer the momentum. Increasing a_0 , one obtains a steady motion for high substrate stiffness and stick-slip motion for intermediate values of G . Finally, motion ceases for small stiffness G . The width of the stick-slip region is fairly independent of a_0 , until it abruptly ceases to exist for a second threshold value, above which the adhesive bond formation dominates over the detachment, resulting in steady gliding motion.

This study demonstrates that the motility mode—as well as the cell’s shape—are governed by the interplay of: (1) the motility machinery of the cell (here the propulsion strength α was chosen as a representative, but the behavior is qualitatively similar for the parameters β , σ and γ), (2) the adhesion dynamics (here a_0), and (3) the elastic properties of the substrate (stiffness G), as well as its relaxation time.

Finally we would like to note that the stick-slip motion of cells on a substrate is somewhat different from the classical view of stick-slip motion [122, 168], exemplified by a brick pulled by a soft spring on an adhesive layer: there no motion occurs while the brick is stuck, while the brick moves upon a slippage event after bond breaking. In contrast, for cells crawling on a substrate, the motion is mostly generated upon adhesive contact, where the cell polarizes and momentum from actin polymerization can be effectively transferred to the substrate, while the shape accommodation after the bond breakage has only a minor contribution to motion. Hence instead of stick-slip cycle, a better name for this process occurring in crawling cells would be *propulsion-relaxation* cycle, cf. also Fig. 1.8.

1.3.3.1 Reduced Description of the Stick-Slip Cycle

To obtain a more detailed understanding of the stick-slip motion, one can reduce the full model to two effective ODEs: one for the area-integrated density of adhesive contacts, $A(t) = \langle A(x, y, t) \rangle$, and the second for the extension $U(t)$ of the spring modeling the cell-averaged substrate deformation [we use Eq. (1.21) in this section].

For this purpose we disregard the dynamics of the orientation field \mathbf{p} and assume that the cell is already polarized and able to move. We also neglect all diffusion terms and consider a one-dimensional motion. In this approximation the phase field equation yields a relation between the cell’s velocity $V_x(t)$ and the mean adhesion, $V_x \approx \langle \alpha A(x, y, t) \mathbf{p} \rangle \simeq \bar{\alpha} A$, where $\bar{\alpha}$ is a numerical factor (for a more elaborate description one can go along the lines of Sect. 1.3.2.1). Similarly we obtain $\dot{a}_0 \sim a_0 \langle \rho p^2 \rangle$ and arrive at

$$\begin{aligned}\dot{A}(t) &= \bar{a}_0 - d[U(t)]A(t) + a_{nl}A(t)^2 - sA(t)^3, \\ -\eta \dot{U}(t) &= G U(t) + \bar{\alpha}A(t),\end{aligned}\quad (1.28)$$

where the deformation-dependent detachment rate is still given by Eq. (1.17).

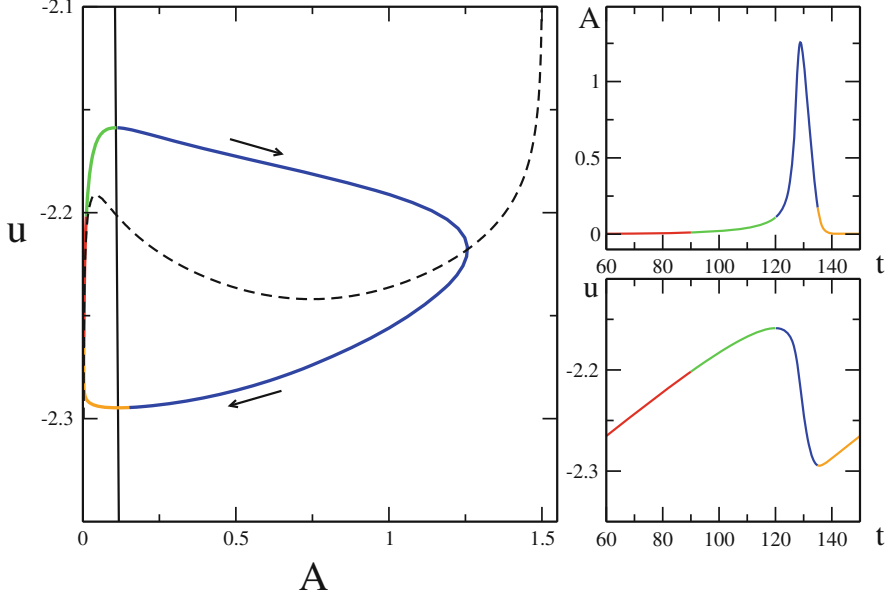


Fig. 1.10 Stick-slip cycle in the reduced ODE model. The main plot shows the nullclines $\partial_t A = 0$ (dashed line) and $\partial_t U = 0$ (solid line) and the limit cycle (with each quarter period marked in a different color) obtained by numerical integration of Eq. (1.28). Starting at the upper part of the blue trajectory, the cell increasingly adheres and U becomes more negative as the cell exerts more and more force on the substrate. When $|U| > U_c$, adhesive contacts break and A rapidly decreases (lower part of the blue trajectory) until the dynamics reaches the A -nullcline (red branch). There U relaxes while A almost stays zero, but in fact slowly grows since at small values of A the cell slows down and adhesion can restart (green trajectory). This is followed again by a rapid attachment (blue trajectory). Parameters: $\bar{\alpha} = 0.2$, $a_0 = 0.0025$, $a_{nl} = 1.5$, $U_c = \sqrt{5}$, $G = 0.01$, $\eta = 10$ as well as $d = 1 = s$, $b = 5$. The two panels on the right show $A(t)$ and $U(t)$ for one period of the stick-slip cycle

Equation (1.28) can be easily integrated numerically. Moreover, within this framework the stick-slip motion can be understood qualitatively from the analysis of the nullclines $\dot{A}(t) = 0$ and $\dot{U}(t) = 0$. Both nullclines [the solid black line for $\dot{U}(t) = 0$ and the dashed black curve for $\dot{A}(t) = 0$] and a typical trajectory are shown in Fig. 1.10. The stick-slip motion corresponds to a limit cycle encircling the unstable fixed point at the intersection of both nullclines.

We can also discuss the dependence on parameters: Increasing the substrate stiffness G (or decreasing the propulsion $\bar{\alpha}$) results in a decrease of the slope of the nullcline $U(A) = -\frac{\bar{\alpha}}{G}A$ (the solid line). At some critical value of G this nullcline will have additional intersections with the second nullcline, resulting in the disappearance of the limit cycle and the creation of a new stable fixed point—corresponding to steady motion of the cell. When starting from the stick-slip regime, the same happens upon decreasing $\bar{\alpha}$, cf. the transition from stick-slip to steady motion upon lowering α in Fig. 1.9a. Finally, upon an increase in a_0 , the maximum

in the dashed nullcline for $\dot{A}(t) = 0$ decreases and is shifted towards higher A values. As soon as the fixed point, i.e. the intersection of the nullclines, is no longer on the descending branch of the dashed curve, steady motion occurs again, cf. the transition from stick-slip to steady motion upon increasing a_0 in Fig. 1.9b.

In addition, Fig. 1.10 displays $A(t)$ and $U(t)$ for a typical trajectory, obtained numerically from Eq. (1.28). The color code splits the period in four. One can see that the attachment-detachment event [cf. the blue peak in $A(t)$] is very rapid. Similar curves can be obtained for the full PDE model, see [182]. However, due to the complete omission of the shape and polarization dynamics—as well as of the subcritical onset of motion—the cycles are perfectly periodic in the simple model given by Eq. (1.28), while not necessarily in the full model.

1.3.4 More Complex Motility Modes

Apart from stick-slip motion of parts of a cell [30] or whole cells [164], more complex motility modes have been reported. An interesting example is the bipedal motion [15, 103] found for keratocytes: due to the coupling of the force-generation to the elasticity (of the substrate and/or of the cell), keratocytes can display lateral out-of-phase oscillations while moving.

The results for the stick-slip motion shown in the last section have been obtained using Eq. (1.21) for the substrate, i.e. using a single effective spring [182]. Obviously this results in a simultaneous rupture of the adhesive bonds in the entire cell, and bipedal motion is not possible. Experimentally, however, it is known that some parts of cells can still adhere while others lose contact [15, 30, 164]. In other words, inhomogeneously distributed forces lead to inhomogeneous adhesion and can provide a feedback on the overall shape and motion, making more complex motility modes possible. To tackle this problem, spatially-resolved local substrate displacements and local traction distribution have to be accounted for, see Eqs. (1.18), (1.19). Indeed, this model generalization leads to the emergence of new dynamic states at the boundaries of the stick-slip region, see Fig. 1.11 (cf. also [102] for more details): (1) breathing motion, where the cell extends periodically in the lateral direction. (2) bipedal motion, where the cell exhibits periodic lateral out-of-phase oscillations but keeps the initial propagation direction and (3) wandering bipedal motion, where the cell veers off the straight path and follows a slightly curved trajectory accompanied by asymmetric shape oscillations. Figure 1.12 shows a representative bipedal motion.

The instability leading to the bipedal and more complex modes of movement is likely related to the coupling between various shape deformation modes and the translational mode. Similar behavior was recently observed in simpler models for self-propelled “soft” deformable particles [80, 117, 159], where based on general symmetry arguments, couplings between various intrinsic modes of shape deformation were considered.

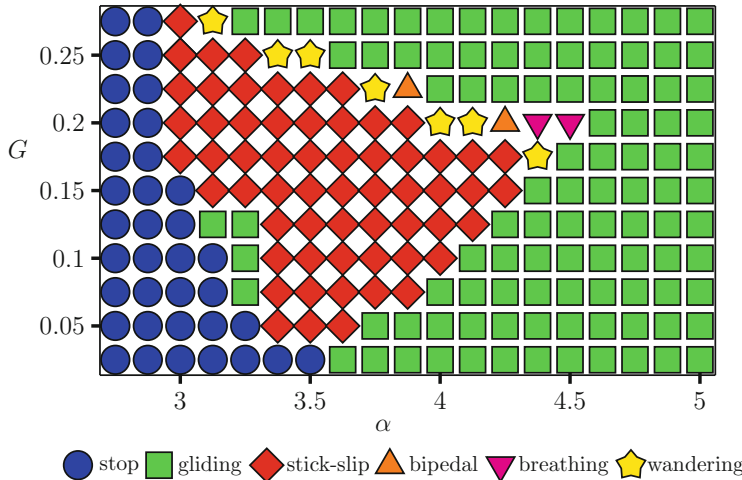


Fig. 1.11 Complex motility modes. Diagram of the motility modes for shear modulus G vs. propulsion strength α . In contrast to Fig. 1.9, the substrate displacement and traction distribution are resolved locally, as described by Eqs. (1.18), (1.19). Parameters are $\beta = \alpha/2$, $\gamma = 0.5$, $\sigma = 1.3$, $a_0 = 0.01$, $a_{nl} = 1.5$, $h = 0.1$, $\eta^{-1} = 0.3$, cf. also Tables 1.1 and 1.2; initial cell radius $r_0 = 15$

In experiments, curved trajectories have also been reported, cf. [15]. Such trajectories, also found in a certain parameter range of our model, are interesting and deserve further investigations. It should be noted, however, that even the very persistently moving keratocyte cells rarely take straight paths for more than several tens of their own length. On a larger scale, they rather explore their environment in a fashion resembling a random walk. Thus, to speculate, the apparent random walk-like changes in direction of keratocytes could in fact be due to the onset of some sort of intrinsic shape instabilities, similar to the wandering bipedal motion (cf. stars in Fig. 1.11).

1.3.5 Movement on Inhomogeneous Substrates

Here we consider the effects of modulated substrate properties, such as adhesiveness and stiffness, on the movement of cells. First of all, this is of high biological relevance since cells typically move in heterogeneous environments—given by other cells, tissue, ECM—that naturally have different elastic and surface properties, adhesiveness etc. Second, as already discussed in Sect. 1.1.2, it is nowadays relatively easy to engineer substrate properties and to study the corresponding cell response, compared to changing the *internal* biochemistry.

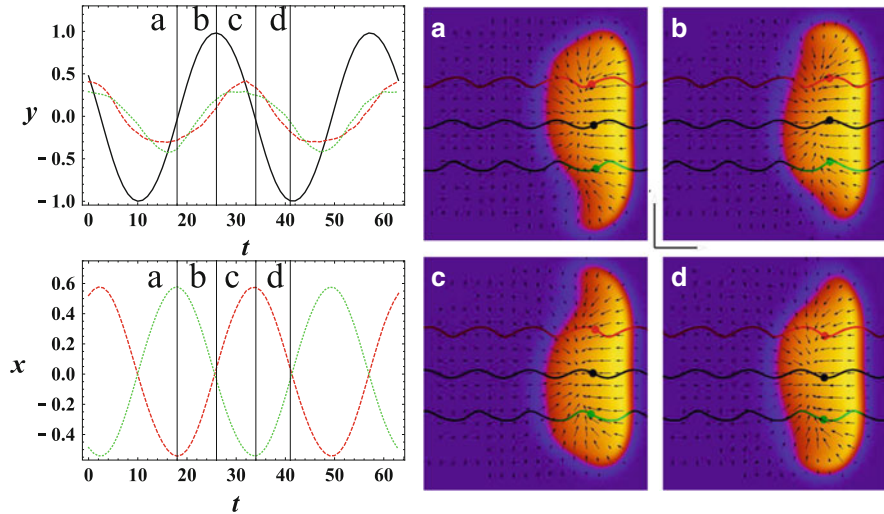


Fig. 1.12 Illustration of bipedal motion. Bipedal motion is an overall straight motion concomitant with out-of-phase oscillations of the lower and upper halves of the cell. Panels (a)–(d) show the shape of the cell and the substrate displacement field. See also ch1_video3.avi http://www.physik.tu-berlin.de/~jakob/movies_small//ch1_video3.avi. The *upper left panel* shows in red dashed (green dotted) the y -component of the center of mass (c.o.m.) of the upper (lower) halves of the cell, which oscillate in-phase, and in black the y -coordinate of the c.o.m. of the entire cell. The *lower left panel* shows the out-of-phase oscillations of the corresponding x -components of the cell's halves. The substrate displacement and traction distribution are described by Eqs. (1.18), (1.19). Parameters are $\alpha = 4.25$, $\beta = \alpha/2$, $\gamma = 0.5$, $\sigma = 1.3$, $a_0 = 0.01$, $a_{nl} = 1.5$, $G = 0.2$, $h = 0.1$, cf. also Tables 1.1 and 1.2; initial cell radius $r_0 = 15$

Experimentally, the adhesiveness can be varied by grafting a high density of integrin ligands (fibronectin or arginylglycylaspartic acid (RGD)⁵) on the substrate while other regions can be made passive, i.e. induce only weak nonspecific adhesion, or repellent. Nowadays, almost any adhesive pattern on the micron scale can be engineered [35, 136] by microcontact printing techniques. Varying the density of ligands in a quantitative way, however, is much more difficult. The substrate stiffness, on the other hand, can be varied in a step-like fashion using soft lithography-fabricated microposts [163], or in a smoother fashion [100], by controlling the crosslink density of the substrate's polymer network.

We will focus on four generic scenarios: (1) a step and (2) a periodic modulation of the substrate adhesiveness, see below. And finally (3) a step and (4) a gradient in the substrate stiffness, as discussed in Sect. 1.3.5.2 on durotaxis.

⁵Fibronectin is the protein of the ECM responsible for the binding to the integrin adhesion receptors. RGD is a peptide sequence of fibronectin, implicated in the attachment.

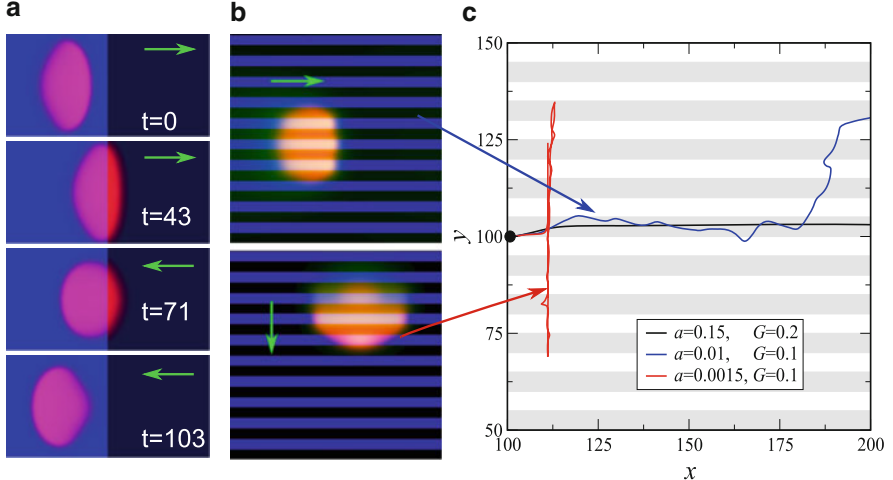


Fig. 1.13 Motility on substrates with modulated adhesiveness. (a) The motion of a cell on a substrate where the adhesive strength is modulated by a step in the rate of adhesion formation a_0 , corresponding to a varying density of adhesive ligands ($a_0 = 0.2$ in the blue region, $a_0 = 0.01$ in the black one; $G = 0.15$ everywhere). The cell prefers to stay on the highly adhesive region and is reflected from the low-adhesion region. See ch1_video4.avi http://www.physik.tu-berlin.de/~jakob/movies_small/ch1_video4.avi. (b) The motion of cells on striped adhesive patterns. Top panel: alternating stripes of $a_0 = 0.15$ (blue) and no adhesiveness, $a_0 = 0$ (black); $G = 0.2$. The cell positions itself symmetrically and moves parallel to the stripes in a steady fashion. See ch1_video5.avi http://www.physik.tu-berlin.de/~jakob/movies_small/ch1_video5.avi. Lower panel: overall low adhesiveness [$a_0 = 0.0015$ (blue) and $a_0 = 0$ (black)]; $G = 0.1$. In contrast to the previous case, after moving initially along the stripes, the cell turns and moves perpendicular to the stripes in a stick-slip fashion. See ch1_video6.avi http://www.physik.tu-berlin.de/~jakob/movies_small/ch1_video6.avi. (c) Select trajectories of the c.o.m. of cells moving on stripe-patterned substrates with different values of a_0 (gray corresponds to high adhesiveness, white to $a_0 = 0$), and for different overall substrate stiffness G . For high G and a_0 , the cell displays persistent steady motion along the stripes (black curve). For intermediate values of a_0 , the predominant motion is along the stripes with excursions into the perpendicular directions (blue curve). Finally, for low adhesiveness the motion is perpendicular to the stripes with reversals. In (a)-(c), all other parameters are as in Fig. 1.8, except for $\alpha = 4$, $\beta = 2.45$.

1.3.5.1 Modulation of Substrate Adhesiveness

The snapshots in Fig. 1.13a illustrate the motion of a cell encountering a step in the adhesion strength, modeled by a step-like spatial variation of the rate of adhesion formation, a_0 . The blue area corresponds to high adhesiveness, the dark one to low adhesiveness. The cell is capable of navigating on the patterned substrate: it bounces off the low-adhesive region, back to the region with higher adhesiveness. This behavior is in qualitative agreement with experiments confining cells in regions of high adhesiveness, cf. e.g. [136].

As a second example we investigated the motion of cells on striped substrates with alternating high/low adhesiveness. This situation was studied experimentally for keratocytes in [35], using microcontact printing of fibronectin corresponding to regions of high adhesiveness and of poly-L-lysine-PEG blockcopolymers corresponding to practically non-adhesive regions. As before, the selective adhesiveness of the substrate can be modeled by a spatial modulation of the rate of adhesive bond formation, a_0 . The upper panel of Fig. 1.13b shows the case of stripes with large values of a_0 . One observes that (1) the cell moves along the stripes and (2) the cell positions itself symmetrically with respect to the stripes (i.e. in the case shown, the center of mass of the cell drifts to the center of a stripe with high adhesiveness). This behavior agrees well with the one experimentally observed [35]. Also in agreement with the experiment, the leading edge of the cells exhibits “protrusion bumps” on the stripes with high adhesiveness and “lagging bumps” on the stripes of low adhesiveness.

Interestingly, a fundamentally different behavior was obtained for cells moving on striped substrates with lower values of the adhesion parameter a_0 , i.e. in the regime where the homogeneous system rather displays stick-slip motion (cf. Sect. 1.3.3). The cell shown in the lower panel of Fig. 1.13b was stimulated by the initial conditions to move along the stripes, exactly as in the case just discussed. However, after some time the cell slowed down, abruptly changed its direction, spread along the stripe in order to maximize contact with the region of high adhesiveness, and started to move perpendicularly to the stripes. This motion is associated with stick-slips, where the cell intermittently almost stops along the adhesive stripe, building up new adhesion strength, and then moves again. In this regime, the cell also randomly reversed its direction. It would be interesting to study whether this behavior can be found in experiments of cells performing stick-slip motion on patterned substrates. Finally, for intermediate values of a_0 we observed a combination of these two modes of motions: for some time the cell moves along the stripes, then it moves perpendicular, then parallel again, etc. Representative trajectories of the cells for all three cases are summarized in Fig. 1.13c.

Experimentally, it is rather difficult to modulate the strength of adhesion in a quantitative matter. It is much simpler to vary the relative width of the adhesive vs. the non-adhesive stripes, while keeping the period of the pattern fixed. We also investigated this situation and observed three different types of motility [182]: (1) for a large width of the adhesive stripe, the cell moves along the stripes in agreement with the previously discussed behavior. (2) Gradually decreasing the width of the adhesive stripes, we observed an instability: the cell exhibits a kind of “rocking motion”, and eventually turns perpendicular to the stripes. The motion is associated with random reversals of direction, similar as on the substrates with low adhesiveness discussed above. (3) For very small widths, however, the reverse trend is observed: the cell stretches in the direction of motion in order to fit between two stripes, and moves again along the stripes. This study suggests that the type of motion is also affected by the commensurability between the size of the cell and the period of the modulation, another prediction that deserves experimental investigations.

1.3.5.2 Modulation of Substrate Stiffness and Durotaxis

Although the substrate's adhesiveness can be modulated rather easily, such a treatment of surface properties often is not very robust. In order to improve the mechanical stability and the resistance to degradation, a possibly better design strategy is the development of synthetic substrates with engineered elasticity. Different strategies have been proposed: microfabricated arrays of microposts (or pillars) allow to modulate the local stiffness via variations of the pillars' dimensions (height, thickness) [163]. However, pillars are not a very natural environment for cells, and alternative methods are currently under development. Examples allowing to tune the elastic properties of a flat substrate are gradient materials [32] and composite materials with alternating stiffness [31].

In view of these developments, we modeled the encounter of a cell with a step in the effective spring constant G of the substrate [182]. A rich variety of different dynamic regimes was observed. To be more close to reality, we show here the results accounting for the local displacement field [102], see Eqs. (1.18), (1.19). Depending on the parameters (we studied mostly the propulsion strength α , and varied the initial conditions), a variety of different scenarios was observed, cf. Fig. 1.14. For cells moving at a certain angle towards a step from a soft substrate to a stiffer one, we observe that the cell passes the step, cf. (a), (c), including a possible deflection of the direction of motion, cf. (a). Moving from stiffer to softer substrates, depending on the initial angle the cell becomes either trapped and moves along the step, cf. panel (b), or is reflected from the step, cf. (d). This behavior is consistent with

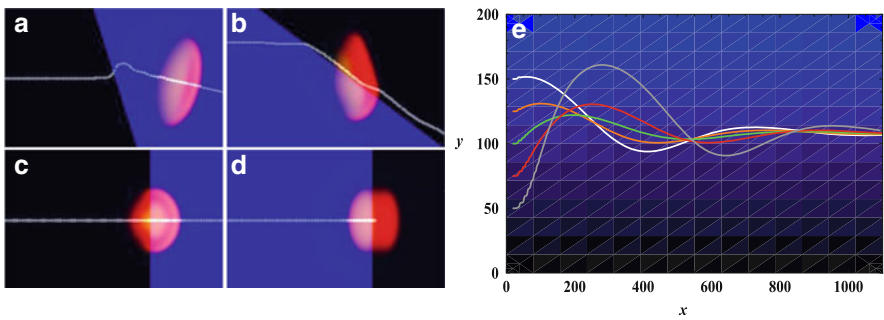


Fig. 1.14 Motility on substrates with modulated stiffness. (a)–(d) Several examples are shown for the behavior of cells colliding with a step in the substrate stiffness (blue: $G = 0.4$, black: $G = 0.05$). The trajectories of the c.o.m. of the cell are shown in white. Top row: $\alpha = 4, \beta = 2$, bottom row: $\alpha = 4, \beta = 1.5$. Other parameters as in Fig. 1.5. (e) Demonstration of durotaxis: a linear gradient in the substrate's modulus G was implemented in the y -direction, from $G = 0$ (black) at the bottom to $G = 0.4$ (blue) at the top. The colored curves show c.o.m. trajectories for cells with different initial positions. They all converge at an optimal value of G . See also ch1_video7.avi http://www.physik.tu-berlin.de/~jakob/movies_small//ch1_video7.avi and ch1_video8.avi http://www.physik.tu-berlin.de/~jakob/movies_small//ch1_video8.avi for two cells starting at different initial values of y . Parameters: $\alpha = 3.8, \beta = \alpha/2$, others as in Fig. 1.5 except $h = 0$

experimental observations of fibroblast cells on microposts assays [163]: there, the cells preferably stayed in the area of high stiffness, while cells coming from the softer side often rotated to migrate perpendicularly to the stiff substrate.

Finally, in order to obtain insights into the cell's mechanosensitivity and durotaxis, we investigated the effect of a gradient in the shear modulus G . For simplicity we considered the thin layer limit $h \rightarrow 0$, where the form of the equation for the substrate displacements, Eq. (1.18), is unchanged (otherwise the gradient in G creates new terms, cf. Appendix “Derivation of the Equation for the Elastic Displacements”). We have found that cells prefer to stay (and to move) on a substrate with optimal stiffness: on very soft substrates, the cells migrate towards stiffer regions, while on very stiff substrates the cells move towards softer areas. This is exemplified in Fig. 1.14e, where a linear gradient of stiffness has been implemented in the y -direction. The differently colored curves are the center of mass trajectories of cells polarized initially in x -direction and starting at different positions. One can nicely see that all trajectories converge, i.e. for the given parameters, the cell prefers a certain value of substrate stiffness.

In conclusion, the model developed here illustrates that the outcome of a cell's “collision” with a step in the substrate parameters—and even more so the outcome of more complex perturbations—depends sensitively on the cell's shape and speed, as well as on the relative differences in adhesiveness and/or substrate stiffness.

1.4 Collective Migration

While in the last decade a significant effort was dedicated to understanding the mechanics, dynamics and motility of individual cells, the processes determining *collective* cell migration still remain elusive to a large extent. There has been a body of experimental work on the motility of cells in monolayers, typically in the context of wound healing [126, 129]. Collective motion of a few individual cells in a small adhesive spot, i.e. not in the context of tissue, was initiated in [69]. Stimulated by the progress in designing patterned synthetic surfaces with controlled adhesive properties, it attracted considerable interest and was followed by detailed studies of collective cell motion in confined adhesive domains [38, 43, 136]. Studies on unbounded substrates, as well as on domains with geometrical constraints, have been undertaken using various cell types like keratocytes and canine kidney cells [7, 8, 156, 166].

In this section we illustrate how the phase-field model for individual cells can be generalized to collective cell migration [101]. With present computer power, one can study the collective motility of up to a hundred cells. The study overviewed in the following reproduces several salient features of cell–cell interactions and makes testable predictions on the role of cell density, cell–cell adhesion and confinement on collective migration.

1.4.1 Multiple Phase Fields

The simplest method to model multiple cells is to assign to every cell i its own phase field ρ_i , with $i \in \{1, \dots, N\}$ and N the total number of cells. Two major types of interactions are dominant between cells: First, steric repulsion that prevents cells from overlapping. And second, cell–cell adhesion that is often responsible for the formation of multi-cellular aggregates. In this section we show that one can write the corresponding phase-field equations as

$$\begin{aligned} \partial_t \rho_i = & D_\rho \Delta \rho_i - \frac{\partial}{\partial \rho_i} F(\rho_i) - \frac{\partial}{\partial \rho_i} W_r(\rho_1, \dots, \rho_N) \\ & - \kappa \left(\sum_{j \neq i}^N \nabla \rho_j \right) \cdot \nabla \rho_i - \alpha \mathbf{p} \cdot \nabla \rho_i. \end{aligned} \quad (1.29)$$

Here F is the usual double well-structured phase field potential, including volume conservation and contraction. W_r is the repulsive steric interaction potential and the advection-type term $\propto \kappa$ models cell–cell adhesion, as discussed below.

1.4.1.1 Steric Interaction

Steric interaction between two different cells i, j can be modeled by an interaction energy $W_r(\rho_1, \dots, \rho_N)$. To avoid interpenetration it must be repulsive, i.e. the two-cell pair potential $W_2(\rho_1, \rho_2)$ should be large and positive if the cells overlap, and zero if not. Candidates for the pair potential are

$$W_2(\rho_1, \rho_2) = \frac{\lambda}{2} \rho_1^m \rho_2^n, \quad (1.30)$$

with $\lambda > 0$ a parameter determining the interaction strength and m, n arbitrary positive exponents. In the sharp interface limit, the interaction is independent of the values of exponents m and n . However, numerically (small) negative values of the phase field may always arise and to avoid an attracting potential in such a case, the exponents should be even. We chose the simplest case, $m = n = 2$, and typically used a value of $\lambda = 30$.

The total interaction potential is the sum over the interactions between all cell pairs, avoiding self-interaction, and can be written as

$$W_r(\rho_1, \dots, \rho_N) = \sum_{j,k < j}^N W_2(\rho_j, \rho_k) = \frac{\lambda}{2} \sum_{j,k < j}^N \rho_j^2 \rho_k^2. \quad (1.31)$$

Considering the fact that Eq. (1.29) includes only the derivative of the interaction potential (1.31) with respect to ρ_i , we can rearrange

$$\frac{\partial}{\partial \rho_i} W_r(\rho_1, \dots, \rho_N) \propto \rho_i \sum_{j \neq i}^N \rho_j^2 = \rho_i \left(\sum_{j=1}^N \rho_j^2 - \rho_i^2 \right) = \rho_i \sum_{j=1}^N \rho_j^2 - \rho_i^3. \quad (1.32)$$

In such a way the sum, $\sum_{j=1}^N \rho_j^2$, has to be computed only once per time step, and can be used for all cells.

1.4.1.2 Cell–Cell Adhesion

In contrast to steric repulsion, cell–cell adhesion is not strictly necessary to model several cells. However, it is known to be present in most cell types and is especially important for epithelial cells. Though a complex subject of its own, for our purpose cell–cell adhesion shares many similarities with cell–substrate adhesion: instead of integrins [70], linking the ECM via the membrane to the actin cytoskeleton, in cell–cell adhesion cadherins [157] link the cytoskeleton of one cell via both membranes to the cytoskeleton of the other cell.

Let us assume that cell–cell adhesion molecules (cadherins) are present on all cell membranes. The concentration of the formed cell–cell bonds of cell i is denoted by $C_i(x, y, t)$ and governed by a reaction-diffusion equation

$$\partial_t C_i = D_C \Delta_{LB} C_i + |\nabla \rho_i| \left(\tilde{\kappa} \sum_{j \neq i} |\nabla \rho_j| - \tau_C^{-1} C_i \right). \quad (1.33)$$

Here τ_C is a relaxation time and Δ_{LB} is (the phase-field equivalent of) the Laplace–Beltrami operator for the diffusion of C_i within the cell membrane,⁶ with D_C the respective diffusion constant. The factor $|\nabla \rho_i|$ ensures that any creation or decay of C_i is restricted to the cell membrane. Adhesion molecules are created with rate $\tilde{\kappa}$ if the membrane of cell j overlaps with the membrane of cell i . For a sufficiently rapid adhesion dynamics we can neglect the diffusion term and the time derivative and approximate Eq. (1.33) by

$$C_i = \kappa \sum_{j \neq i} |\nabla \rho_j|, \quad (1.34)$$

with $\kappa = \tau_C \tilde{\kappa}$.

How should the formed cell–cell bonds C_i feedback to the phase field ρ_i ? The simplest implementation is the following: as a consequence of cell–cell attractive interaction, cell i is advected normal to cell j . The normal vector of cell j (pointing to the inside) is

⁶The Laplace–Beltrami operator should be used instead of the simple Laplace operator, because the cell membrane is a curved surface.

$$\mathbf{n}_j = \frac{\nabla \rho_j}{|\nabla \rho_j|}. \quad (1.35)$$

Thus, we can introduce an additional advection term, with its strength regulated by the formed adhesive bonds C_i , like

$$\partial_t \rho_i \propto C_i \sum_{j \neq i} \mathbf{n}_j \cdot \nabla \rho_i = \kappa \sum_{k \neq i} |\nabla \rho_k| \sum_{j \neq i} \frac{\nabla \rho_j}{|\nabla \rho_j|} \cdot \nabla \rho_i. \quad (1.36)$$

The double sum contains many terms $|\nabla \rho_k| \frac{\nabla \rho_j}{|\nabla \rho_j|} \cdot \nabla \rho_i$, $i \neq j \neq k$ which are only important at space points where three cell membranes meet simultaneously.

Neglecting such terms we arrive at the following simpler equation for the phase field of cell i [which has the same general structure as already given in Eq. (1.29)]:

$$\partial_t \rho_i = D_\rho \Delta \rho_i - \rho_i (\rho_i - \delta_i) (\rho_i - 1) - \lambda \rho_i \sum_{j \neq i}^N \rho_j^2 - \kappa \left(\sum_{j \neq i}^N \nabla \rho_j \right) \cdot \nabla \rho_i - \alpha A \mathbf{p} \cdot \nabla \rho_i, \quad (1.37)$$

where

$$\delta_i = \frac{1}{2} + \mu (\langle \rho_i \rangle - V_{0,i}) - \sigma |\mathbf{p}|^2. \quad (1.38)$$

Note that for purpose of numerical stability we rather use a regularized term for the cell-cell adhesion, $-\kappa \nabla \rho_i \cdot \sum_{j \neq i} f(\nabla \rho_j)$ with

$$f(z) = \frac{z}{\sqrt{1 + \epsilon z^2}}. \quad (1.39)$$

1.4.1.3 Generalization of Actin, Adhesion, and Substrate Dynamics

The equations for the actin polarization \mathbf{p} and the density of adhesive bonds (to the substrate) A remain structurally the same as Eqs. (1.11), (1.16). The only difference is that instead of ρ one has to use $\sum_i \rho_i$:

$$\begin{aligned} \partial_t \mathbf{p} &= D_p \Delta \mathbf{p} - \beta \sum_{i=1}^N f(\nabla \rho_i) - \tau_1^{-1} \mathbf{p} - \tau_2^{-1} \left(1 - \sum_{i=1}^N \rho_i^2 \right) \mathbf{p} \\ &\quad - \gamma \left[\left(\sum_{i=1}^N \nabla \rho_i \right) \cdot \mathbf{p} \right] \mathbf{p}, \end{aligned} \quad (1.40)$$

$$\partial_t A = D_A \Delta A + (a_0 p^2 + a_n l A^2) \sum_{i=1}^N \rho_i - d(|\mathbf{u}|) A - s A^3, \quad (1.41)$$

where we again used the function f for regularization and $d(|u|)$ is still given by Eq. (1.17).

While the fields \mathbf{p} and A are shared by all cells just for reasons of computational efficiency (there should not be too many artefacts, since both fields rapidly tend to zero outside of all cells) the substrate is naturally shared by all cells. Its dynamics is given by Eq. (1.18),

$$\partial_t \mathbf{u} = -\frac{1}{\eta} \left(G \mathbf{u} - \frac{1}{\xi} (\mathbf{T} + h (5 \Delta \mathbf{T} + 19 \nabla (\nabla \cdot \mathbf{T}))) \right), \quad (1.42)$$

where \mathbf{T} is now the sum of all traction forces \mathbf{T}_i ,

$$\mathbf{T} = \sum_{i=1}^N \mathbf{T}_i = -\xi A \sum_{i=1}^N \rho_i \left[\mathbf{p} - \frac{\langle A \mathbf{p} \rho_i \rangle}{\langle A \rho_i \rangle} \right]. \quad (1.43)$$

Note that the traction of each cell vanishes individually, $\langle \mathbf{T}_i \rangle = 0$.

1.4.2 Binary Interactions of Cells

When studying collective behavior, the first step is to investigate the binary interactions between moving cells. Within the model presented in the previous section, a rich phenomenology and dynamics of binary cell interaction has been found. Two distinct cases are shown in Fig. 1.15.

Figure 1.15a shows the interaction (“collision”) of two cells with parameters leading to a “keratocyte-like” behavior (motor asymmetry parameter $\gamma = 0.5$ and contractility parameters $\sigma = 1.3$). Individual cells have a canoe-like shape with a high aspect ratio, they display low intermittent adhesion and move with constant high speed. The interaction between such cells leads to an effective mutual alignment, which is reminiscent of a fully inelastic collision [11]. The center of mass trajectories for different incidence angles reveal that the alignment is more efficient at small incidence angles, Fig. 1.15c: the smaller the incidence angle, the stronger the cells align upon interaction. This nonlinear angle dependence is due to the active cell response in the course of the collision, i.e. due to the self-organized reorganization of the cell’s shape, polarization and adhesion, as well as the substrate deformation. One can anticipate that multiple inelastic collisions will lead to a mutual alignment of the individual cell’s velocity vectors and will promote the onset of collective motion (cf. the next section). Note that a similar mechanism for the onset of collective motion is found in granular-like systems of self-propelled inelastic particles, e.g. for self-propelled discs [65].

Figure 1.15b shows the collision of two cells with parameters leading to a “fibroblast-like” behavior ($\gamma = 0.7$ and $\sigma = 0.6$). For these parameters, well-separated cells are fan-shaped, have strong adhesion (green color) at the rear and a thick region of high actin alignment (blue color) at the front. The cells’ velocity has

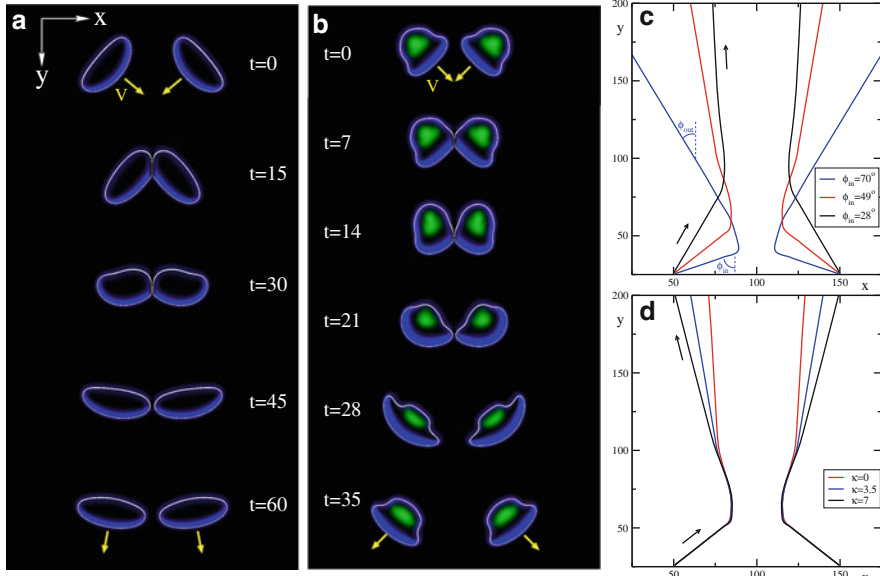


Fig. 1.15 Binary interactions (collisions) of motile cells. (a) A strongly inelastic collision of two canoe-shaped cells ($\gamma = 0.5$, $\sigma = 1.3$), leading to an effective alignment of the directions of motion. See ch1_video9.avi http://www.physik.tu-berlin.de/~jakob/movies_small/ch1_video9.avi. (b) An almost elastic collision of two fan-shaped cells ($\gamma = 0.7$, $\sigma = 0.6$). See ch1_video10.avi http://www.physik.tu-berlin.de/~jakob/movies_small/ch1_video10.avi. In (a) and (b), contours of the cells are given in white, the absolute value of the actin orientation in blue and regions with high adhesion in green. The velocities are indicated as yellow arrows. (c) Effect of the incidence angle on the cells' center of mass trajectories. The red curve corresponds to the snapshots shown in (a). (d) Effect of cell-cell adhesion strength κ on the cells' center of mass trajectories: increasing the adhesion reduces the effective alignment of the cells. In (c) and (d) the direction of motion is indicated by the arrows. Parameters: additional parameters are as in Fig. 1.6, initial cell radius $r_0 = 15$, domain size is 200 (with periodic boundary conditions). For the traction forces exerted by both cell types shown in (a) and (b) see Fig. 1.6b, a, respectively

a small oscillatory component due to stick-slip dynamics of adhesion, cf. Sect. 1.3.3. As seen in Fig. 1.15b, in the course of interaction the “fibroblast-like” cells become severely deformed and exhibit intermittent elongated shapes. Strikingly, the cells’ collision is almost perfectly elastic: the absolute values of the post-collision angles are very close to the respective incidence angles. Consequently, assemblages of such cells are less prone to collective motion than the inelastically colliding cells just discussed: upon repeated collisions the directions of motion of the cells will stay randomized. On the other hand, a cluster of such cells should disperse more efficiently, which may be advantageous for searching strategies or to colonize a given surface.

As our model describes the motility machinery in some detail, it not only captures a variety of different cell types but in addition allows to relate the observed interaction dynamics to intracellular processes. For example, the behavior shown

in Fig. 1.15 indicates that decreasing the contractility σ , i.e. either the activity or the concentration of myosin motors or both, decreases the inelasticity of collisions and, consequently, the propensity of cells to move collectively.

Finally, let us discuss the effect of cell–cell adhesion introduced in Sect. 1.4.1.2. It is believed that cell–cell adhesion promotes collective movement of cells, since the sense of the direction of motion may be transferred more efficiently from one cell to another. Figure 1.15d shows, however, the opposite trend: increasing the cell–cell adhesion parameter κ reduces the effective alignment. This behavior is in accordance to the one found for simpler self-propelled particle models of collective motion that include effects of cohesion [63]: there, the decrease in global orientation upon an increase of cohesion is due to the formation of small, short-lived clusters that continuously merge and break up [123], instead of leading to collective motion on larger scale. We find a very similar dynamics when simulating the collective motion of adhering cells, cf. Sect. 1.4.3.2 and Fig. 1.17.

The only experimental study of the effect of cell–cell adhesion on collective motion we are aware of has been carried out in [43] on canine kidney cells. There, decreasing the cell–cell adhesion was reported to suppress collective motion in cells. However, the cancerous cell lines used there could have, in addition to a reduced adhesion, many other cellular parameters affected as well (e.g. elasticity, propulsion strength). On the other hand, it is also possible that one needs to take internal (visco-)elasticity of the cells into account within the modeling, to capture the transfer of the direction of motion from one cell to the other (which seems to be plausible in principle).

1.4.3 Many Cells: Collective Migration

Having established the basic phenomenology of binary interactions of cells within the proposed modeling framework, we can now move forward and study the dynamics of multiple cells. First, we investigated the consequences of the inherent bistability of the cells—related to their subcritical onset of motion, cf. Sect. 1.3.2—on the collective dynamics. Then we studied how the interactions between multiple cells—steric interaction and cell–cell adhesion—may give rise to the emergence of collective modes of motion, such as collective translational movement in case of an open domain, and collective rotational movement in a confined geometry.

1.4.3.1 Transitions Between Spreading and Collective Motion

As it was discussed in Sect. 1.1.2 and recovered within the model in Sect. 1.3.2, cells are dynamically bistable: for the same conditions, a cell can either be in a symmetric stationary state—corresponding to a rounded cell spreading on the substrate—or in a polarized moving state [167, 185]. Namely, experiments on cellular fragments [167] have shown that, depending on the conditions like incidence angle and speed,

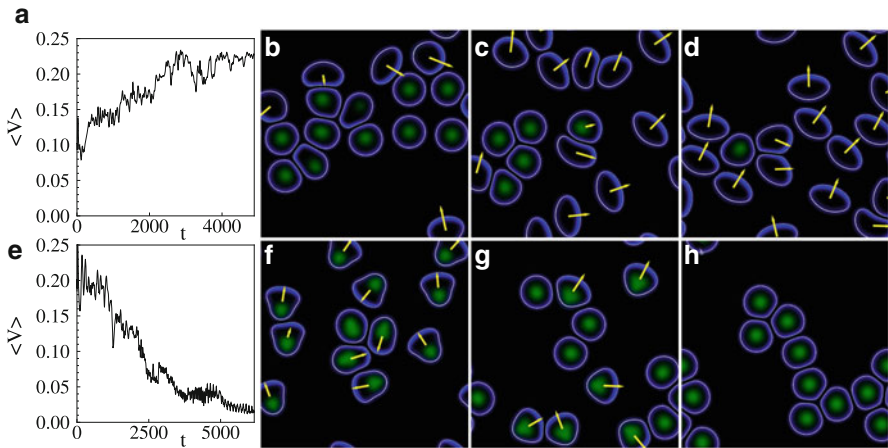


Fig. 1.16 Onset vs. cessation of motion triggered by cell density and environmental conditions. (a)–(d) shows how a few motile cells excite the motion of all cells. See ch1_video11.avi http://www.physik.tu-berlin.de/~jakob/movies_small/ch1_video11.avi. Panel (a) shows the average velocity $\langle V(t) \rangle$ and (b)–(d) a sequence of snapshots. In contrast, (e)–(h) illustrate how initially moving cells come to rest and spread on the substrate. See ch1_video12.avi http://www.physik.tu-berlin.de/~jakob/movies_small/ch1_video12.avi. The values of the parameters are the same in both scenarios, except that in the second case there were fewer cells and the parameter a_{nl} (nonlinear adhesion) was slightly decreased from 1.1 to 1.0

motile cells either can set stationary cells into motion or become stopped by them. How does this intrinsic bistability affect the onset (or cessation) of motion of multi-cell assemblages?

To answer this question, we investigated the effects of collisions in small cell populations; select results are shown in Fig. 1.16. Panels (a)–(d) illustrate a scenario, where a few motile cells manage to set into motion all other cells. In contrast, (e)–(h) illustrates the opposite trend: there, the initially moving cells come to rest due to collisions with other cells and finally all motion ceases and clusters of stationary cells spread on the substrate. Interestingly, the parameters are the same in both scenarios, except that in the second scenario there were fewer cells and the parameter a_{nl} (nonlinear adhesion rate) was slightly decreased from 1.1 to 1.0. The two opposite trends can be quantified by calculating the averaged velocity $\langle V(t) \rangle = \sum_{i=1}^N \mathbf{v}_i(t)$, as shown in Fig. 1.16a, e, respectively.

The observed behavior highlights that transitions between the two states—stationary vs. moving—can be triggered by the environmental conditions (adhesiveness of the substrate), the interactions, as well as by effective parameters like overall cell density and collision probability.

1.4.3.2 Collective Migration at Moderate Densities

We investigated the motility of multi-cell assemblages for varying cell densities. For low cell densities, the emerging behavior should be dominated by binary

interactions. One would hence expect that—for not too high density—fully inelastic collisions, as found in Fig. 1.15a and leading to an alignment of the migration directions of the cells, will induce collective unidirectional motion. We studied two generic situations: First, a system with periodic boundary conditions, corresponding to a cell population that is far from all boundaries, a situation studied experimentally in [156]. Second, we considered a circular confined domain where the cells can adhere (a round adhesive patch), surrounded by a region where adhesion to the substrate is suppressed. This geometry was studied experimentally in [38, 43], where circular domains were prepared by micro-contact printing of adhesive ligands.

Figure 1.17a–c illustrates the emergence of translational collective migration in the periodic domain. To quantify this behavior, one can define an order parameter for the translational collective motion via

$$\phi_T(t) = \frac{1}{N} \left| \sum_{i=1}^N \hat{\mathbf{v}}_i(t) \right|, \quad (1.44)$$

where $\hat{\mathbf{v}}_i$ is the normalized velocity vector of the i th cell. For large cell numbers, the order parameter will vanish if the velocities are random, and it will tend to one if all the cell velocities are aligned. The red curve in Fig. 1.17d clearly illustrates the emergence of a collective unidirectional motion from an ensemble of cells with initially random directions: after a transient (of about $t = 3000$) the order parameter ϕ_T approaches a value close to one.

Figure 1.17f–h shows the emergence of collective motion in the confined circular domain. After a transient of about 4000 dimensionless time units (in both cases, this corresponds to the time needed for the cells to migrate a distance of the order of 50–100 times their own size), all cells perform a counter-clockwise rotation. Again, this behavior can be quantified by an order parameter for rotational collective motion:

$$\phi_R(t) = \frac{1}{N} \sum_{i=1}^N \hat{\mathbf{e}}_{\theta_i}(t) \cdot \hat{\mathbf{v}}_i(t), \quad (1.45)$$

where $\hat{\mathbf{e}}_{\theta_i}$ is the unit vector of cell i in the angular direction. The red curve in Fig. 1.17e shows its evolution for the scenario displayed in (f)–(h), the final value close to one corresponding to counter-clockwise rotation. In the circular domain, the interactions of cells with the boundary (depending on parameters and incidence angle, they can be reflected or trapped by the boundary, cf. Fig. 1.13) force a transition from translational to rotational collective motion, similar to that observed in [43].

As a counter example, we also studied cells with almost elastic collisions (as in Fig. 1.15b), which did not exhibit any collective migration on the considered time scales (up to 8000 time units). One can hence conclude that the simple picture of inelastic collisions inducing the transition—deduced from the binary interactions—is qualitatively correct. Moreover, it prevails up to moderate cell densities as the number density considered here was about 0.4–0.5.

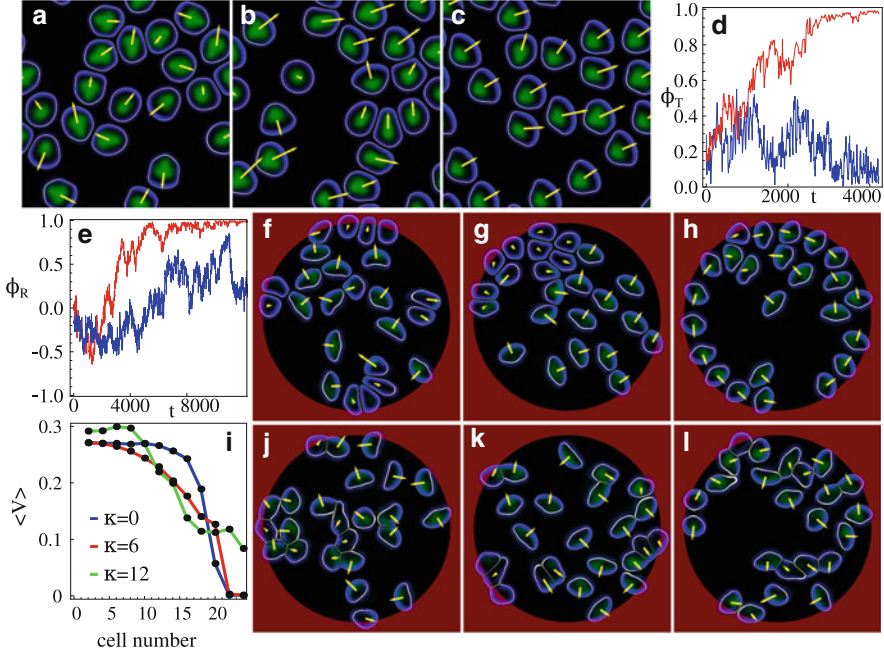


Fig. 1.17 Collective migration of cells. (a)–(c) Emergence of translational collective migration of 20 cells in a periodic domain without cell-cell adhesion, due to the alignment via inelastic collisions as shown in Fig. 1.15. See ch1_video13.avi http://www.physik.tu-berlin.de/~jakob/movies_small//ch1_video13.avi. (d) The order parameter $\phi_T(t)$ for cells without (red, $\kappa = 0$) and with (blue, $\kappa = 6$) cell-cell adhesion. Cell-cell adhesion suppresses collective motion. (f)–(h) Emergence of a rotational collective motion in a circular confined domain (in the red region the adhesive bond formation, a_0 , is reduced by a factor of 9). See ch1_video14.avi http://www.physik.tu-berlin.de/~jakob/movies_small//ch1_video14.avi. Stronger adhesion ($\kappa = 6$) suppresses the collective rotational motion, as shown in j)–l), see ch1_video15.avi http://www.physik.tu-berlin.de/~jakob/movies_small//ch1_video15.avi. This effect can be quantified by the order parameter $\phi_R(t)$ shown in (e) for cells without (red, $\kappa = 0$) and with (blue, $\kappa = 6$) cell-cell adhesion. Large fluctuations of the order parameter occur when cell-cell adhesion is present, indicating transient collective behavior. (i) Average velocity normalized by the total number of the cells moving in a periodic domain, for different cell-cell adhesion strength κ . In all panels, the initial radius of the cells was $r_0 = 10$ and the domain size $L = 100$

So far, cell-cell adhesion was absent, i.e. $\kappa = 0$. Increasing the cell-cell adhesion parameter to moderate values ($\kappa = 6$) leads to a break-down of the collectively rotating state, see Fig. 1.17(j)–(l). This is in accordance with the reduction of the collision inelasticity, see the discussion in Sect. 1.4.2. The order parameters confirm this conclusion for both geometries studied, see the blue curves in Fig. 1.17d, e. Nevertheless, in case of the confined domain, the system displays large fluctuations in the rotational order parameter ϕ_R . This indicates the formation of moving multi-cell clusters, see also Fig. 1.18b, while the whole assemblage displays random reversals of the rotation direction and no trend towards overall collective rotation.

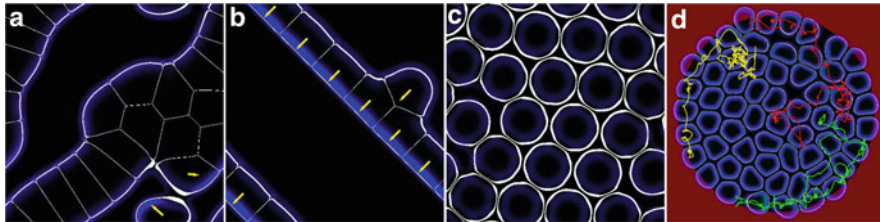


Fig. 1.18 Motion in the regime of strong cell–cell adhesion and/or high cell density. **(a)** Clustering of cells due to strong cell–cell adhesion forces ($\kappa = 12$). A few cells are motile, leave and join the cluster and the cluster changes its shape in time. See ch1_video16.avi http://www.physik.tu-berlin.de/~jakob/movies_small//ch1_video16.avi. **(b)** A traveling band of 8 cells for high adhesion, $\kappa = 12$. Note that the band propagates faster than a single cell (cf. the *green curve* in Fig. 1.17i). See ch1_video17.avi http://www.physik.tu-berlin.de/~jakob/movies_small//ch1_video17.avi. **(c)** Stationary hexagonal arrangement (tissue) of cells for $\kappa = 6$. **(d)** Confined high-density state with 61 cells and no cell–cell adhesion ($\kappa = 0$). The cells compete for voids, thereby moving slowly through the ‘crowded environment’ in a random walk fashion. The *colored curves* show the center of mass trajectories for select cells. See ch1_video18.avi http://www.physik.tu-berlin.de/~jakob/movies_small//ch1_video18.avi

1.4.3.3 Collective Migration for Strong Cell–Cell Adhesion and/or High Density

Further consequences of cell interactions are shown in Fig. 1.18. For strong cell–cell adhesion and increased number density of cells, long-living stationary clusters with a tissue-like arrangement of the cells form. The clusters are surrounded by motile cells which leave/join the clusters in a random fashion, see Fig. 1.18a. At smaller number densities but still high cell–cell adhesion ($\kappa = 12$), cells gather in traveling bands (phalanges) as shown in Fig. 1.18b. In a periodic domain this effect leads to collective motion, while the bands break up and reverse their directions in the case of a circular domain, leading to the high fluctuations in the rotational order parameter.

For very high number densities and adhesion present, all cells stop and form a stationary hexagonal array (a tissue), see Fig. 1.18c. Nevertheless, also in high density states collective motion may still be possible. For larger cell densities, cell contacts become protracted and the behavior becomes increasingly dominated by multiple simultaneous cell collisions. We have found that the average velocity decreases with increasing cell density until a kind of ‘jamming’ transition occurs. This can be inferred from Fig. 1.17i, where the average velocity as a function of the number of cells in the confined domain is shown. The critical density at jamming slightly depends on the parameters, especially it slightly increases with adhesion strength. Close to jamming, cells compete for voids within the ‘crowded environment’: individual cells exhibit a wiggling motion in ‘cages’ formed by the other cells, followed by escapes and random walk-like motion as shown by the trajectories of select cells in Fig. 1.18d. Every ‘escape’ movement of a cell triggers rearrangements of the surrounding cells.

To conclude, the study of collective cell motion presented here has reproduced many experimentally observed regimes, from the activation of non-motile cells by

moving cells due to steric/adhesive interactions [167], the emergence of coherently moving [156] or rotating clusters [43], to the formation of tissue-like stationary clusters. The model suggests also a number of testable predictions. For example, for low cell–cell adhesion, cells move collectively if their interactions are close to inelastic collisions. When increasing the adhesion to moderate values, our study indicates that collective motion is inhibited due to the formation of short-living clusters of a few cells. Until, finally, strong adhesion leads to the formation of densely-packed collectively moving bands. These findings provide additional insight into comparative studies of adhering and weakly adhering cells, as carried out recently by comparing healthy and cancerous cells in [43].

1.5 Conclusions

In this chapter we have discussed a computationally efficient yet very intuitive macroscopic approach to model cell motility. As we have demonstrated, the phase field description for the cell’s moving boundary circumvents one of the major (numerical, but also conceptional) bottlenecks associated with the tracking of the moving domain constituted by the cell. The phase field approach can be easily extended in a modular way [183] to increase the level of detail, e.g. to account for modulations in the substrate properties [182], internal actin (retrograde) flow [146], different propulsion mechanisms like polymerization waves [44], or the effects of chemical signaling [148] and regulation [106]. In the future, the model may be potentially fine-tuned to a specific cell type. For example, it is known that different cell types have different traction signatures—fibroblasts have highest traction at the front, keratocytes at the sides, and neutrophils at the rear—see Sects. 1.1.2 and 1.3.1. We anticipate that one can potentially reproduce realistic, cell type-specific traction distributions by a targeted modification of the model. For example, one has to incorporate a description of the balance of actin fibers between focal adhesion and an effective surface/line tension [20, 109], and possibly also adhesion maturation, to model the overall fan-shape and the arc-like sections at the leading edge of fibroblasts. For keratocytes, the self-organized actomyosin bundle spanning the sides of the cell should be incorporated [55], which most probably causes the high traction forces at the sides.

The phase field model is especially powerful in predicting the modes of cell migration on substrates with modulated properties, such as stiffness or adhesiveness, see Sect. 1.3.5. The model reproduces a broad range of non-trivial cell behaviors, from directed motion along adhesive stripes [182] to the interaction with steps in adhesiveness or stiffness [102] (cells being either able to pass, guided along, or reflected), and the drift towards substrates of optimal stiffness (*durotaxis*, see Sect. 1.3.5.2). Moreover, the model provides testable predictions, such as a transition to a movement perpendicular to the adhesive stripes if the overall adhesiveness or the width of the stripes is reduced [182]. Thus, the phase-field model of cell

movement could become a valuable tool for the design of various bio-medical assays for cell sorting, identification and manipulation, or for the analysis of cell movement through narrow channels in microscopic diagnostic kits.

The generalization of the phase field approach to multiple cells [101] reproduced many experimentally observed regimes as well. The phenomenology includes the activation of non-motile cells by moving cells due to steric/adhesive interactions, the emergence of coherently moving or rotating clusters, and the formation of tissue-like stationary clusters, see Sect. 1.4. In addition, the model hints to an intricate effect of cell-cell adhesion. Namely, cells move collectively if their interactions are close to inelastic collisions and cell-cell adhesion is relatively low. As our study indicated, collective motion is hampered by an increase of adhesion due to the formation of short-living clusters of few cells. Finally, strong adhesion leads to the formation of densely-packed collectively moving bands. These findings provide additional insight into comparative studies of adhesive (healthy) cells and weakly adhering (cancerous) cells [43].

On the other hand, a closer analysis of the binary interactions between cells could provide valuable insights both for the onset of collective migration and for the properties and responses of individual cells. Binary cell interactions, cf. Sect. 1.4.2, may be quantified in terms of an inelastic restitution coefficient, similar to the collisions of macroscopic grains in granular systems [10]. To accumulate sufficient statistics on pertinent cell collision events in experiments, a “cellular collider” could be developed: namely, instead of sampling random (and rather rare) cell collisions on an unconstrained substrate, cells may be guided to collide at desired angles by microcontact printing of adhesive ligands patterns, cf. Sect. 1.3.5. An interesting possible scenario would be a transition from fully inelastic to almost elastic collisions: since cells colliding inelastically have the propensity to move in groups or to form tissues, whereas elastically colliding cells are efficient in dispersing on (and hence exploring) a given area, such a transition would be an interesting manifestation of a cell’s phenotype change.

Another important aspect of the phase-field approach is the inherent bistability of the cells and the related subcritical onset of motion, see Sect. 1.3.2. The bistability affects both individual cells and the collective interactions on many levels. For example, the outcome of a “collision” (that is determining the collective behavior) is the result of the complex interplay between the cells’ shapes and their internal organization (actin polarization, adhesion to the deformed substrate, etc.). Instead of just affecting the directions of motion, however, since collisions can constitute large perturbations they may also stop cells or set stationary cells into motion, see Sect. 1.4.3.1. The bistability, naturally arising in our phase field model is typically *not* present in other simple models. For example, cellular Potts-like models (as employed e.g. to describe the collective rotational motion in [43]), typically model moving cells using a constant propulsion force and a certain persistence time of motion. It is fair to say that the phase field approach is more realistic for non-confluent cells, when the dynamics of individual cells needs to be accurately resolved. In contrast, for confluent cell layers, the phase field approach might be too detailed as the individual effects average out. There, cellular Potts models or

coarse-grained continuum approaches such as [81, 93] may be more suited for the description of the basic features. The phase-field approach for multiple cells could hence also build an important bridge from single cell behavior to confluent layer dynamics and continuum approaches for tissues.

The vast majority of models of cellular motility are so far two-dimensional (i.e. cell height-averaged), and for cells moving on flat substrates. A full three-dimensional description of cell movement is highly desirable, e.g. for cells on substrates presenting topographic features (such as bumps, pillars etc.), and especially in the context of cancer cell proliferation through a tissue. However, even with the existing computing power and employing the efficient phase field model, a comprehensive study of a three-dimensional model seems to be a difficult endeavor. Very recently, a minimal three-dimensional model for an active gel droplet interacting with a flat adhesive substrate was able to capture diverse shapes of crawling cells [162]. Nevertheless significant modeling efforts are still needed to describe the migration of a cell accounting for its internal organization in some detail, and even more so for the movement through a three-dimensional heterogeneous environment, similar to that experienced by cancer cells or leukocytes squeezing through tissues.

Acknowledgements We thank Sumanth Swaminathan (now with W.L. Gore & Associates) for his valuable contribution to the earlier stage of this project. In the course of the model development reviewed here, we enjoyed stimulating discussions with J. Oliver, P. Sens, E. Raphaël, J. Prost, J.-F. Joanny, A. Verkhovsky, H. Chaté and B. Winkler. F.Z. acknowledges funding from the German Science Foundation (DFG) via project ZI 1232/2-1. J.L. acknowledges funding from the German Science Foundation (DFG) within the GRK 1558. I.S.A. was supported by the US Department of Energy (DOE), Office of Science, Basic Energy Sciences (BES), Materials Science and Engineering Division. Part of the numerical work was performed on Northern Illinois University's GPU cluster GAEA.

Appendix

Numerical Methods

To solve the phase field model numerically, especially in the multiple cell case, we developed a highly parallel algorithm implemented on GPUs using CUDA. To avoid (slow) copying between GPU and CPU memory, the algorithm exclusively runs on the GPU (except for the output of data). The code can handle an arbitrary number of cells in single or double precision. Since the phase field keeps track of the cells' boundaries, the problem can be solved on a square domain with periodic boundary conditions. In this case, a pseudo-spectral approach based on the fast Fourier transform (FFT) is the most efficient [131].

Pseudo-Spectral Code To simplify the notations, we illustrate the pseudo-spectral algorithm for an example reaction-diffusion system in one spatial dimension. An extension of the algorithm to higher spatial dimensions is straightforward. We assume a finite domain $0 \leq x < L$ and a system of two coupled equations

$$\partial_t a(t, x) = D_a \partial_x^2 a(t, x) + f(a(t, x), b(t, x)), \quad (1.46)$$

$$\partial_t b(t, x) = D_b \partial_x^2 b(t, x) + g(a(t, x), b(t, x)), \quad (1.47)$$

with periodic boundary conditions

$$a(t, 0) = a(t, L), \quad b(t, 0) = b(t, L). \quad (1.48)$$

The time domain is discretized with time step Δt and the spatial domain is discretized with step size $\Delta x = L/N$, where N is the number of grid points. The discretized fields $a_{j,k}$ and $b_{j,k}$ are then defined as

$$a_{j,k} = a(t_0 + j\Delta t, k\Delta x), \quad b_{j,k} = b(t_0 + j\Delta t, k\Delta x), \quad (1.49)$$

where j enumerates time steps (with t_0 the initial time) and k enumerates the spatial grid points.

In Fourier space (k -space), the wave vectors are then given by $k_n = n\Delta k$ with $\Delta k = \frac{2\pi}{L}$, and the complex exponential in the Fourier transform becomes

$$\exp(i k_n k \Delta x) = \exp\left(2\pi i \frac{nk}{N}\right). \quad (1.50)$$

The FFT of $a_{j,k}$ with respect to the spatial grid points k is defined as

$$\hat{a}_{j,n} = \mathcal{F}[a_{j,k}] = \sum_{k=0}^{N-1} \exp\left(2\pi i \frac{nk}{N}\right) a_{j,k}, \quad (1.51)$$

and the inverse FFT is given by

$$a_{j,k} = \mathcal{F}^{-1}[\hat{a}_{j,n}] = \frac{1}{N} \sum_{n=0}^{N-1} \exp\left(-2\pi i \frac{nk}{N}\right) \hat{a}_{j,n}. \quad (1.52)$$

In spectral methods, it is especially easy to solve the linear part of the equations. In the given example, the discrete equivalent of the second order space derivative $\partial_x^2 a(t, x)$ is easily computed: first, $a_{j,k}$ is transformed to k -space by the forward FFT, then multiplied by $-k_n^2$, and finally transformed back to coordinate space [23]

$$\partial_x^2 a(t, x) \Leftrightarrow \mathcal{F}^{-1}[-k_n^2 \hat{a}_{j,n}] = -\frac{1}{N} \sum_{n=0}^{N-1} \frac{4\pi^2 n^2}{L^2} \exp\left(-2\pi i \frac{nk}{N}\right) \hat{a}_{j,n}. \quad (1.53)$$

For the time stepping of the reaction-diffusion system Eqs. (1.46) and (1.47), we employ the operator-split method [34]:

$$a_{j+1,k} = \mathcal{F}^{-1} \left\{ \exp(-\Delta t D_a k_n^2) [\mathcal{F}(a_{j,n} + \Delta t f(a_{j,n}, b_{j,n}))] \right\}, \quad (1.54)$$

$$b_{j+1,k} = \mathcal{F}^{-1} \left\{ \exp(-\Delta t D_b k_n^2) [\mathcal{F}(b_{j,n} + \Delta t g(a_{j,k}, b_{j,n}))] \right\}, \quad (1.55)$$

where we used the reversed version of $\exp(\Delta t \alpha) = 1 + \Delta t \alpha + \mathcal{O}(\Delta t^2)$ to improve numerical stability [33]. Technically, one calculates an Euler step in real space, transforms to k -space, multiplies by the time evolution operator, and transforms back. The method just described is called pseudo-spectral, since the nonlinear part of the equations (contained in f, g) is evaluated in coordinate space, i.e. not in Fourier space where it would give rise to computationally expensive convolutions.

Combining Scalar to Complex Fields In case of dealing with many equations, the performance of the algorithm can be further improved by exploiting the fact that the FFT of two real fields can be computed more efficiently as a single FFT of a complex field [131]. We hence combine the real fields $a_{j,n}$ and $b_{j,n}$ in a single complex field z via

$$z_{j,n} = a_{j,n} + i b_{j,n}. \quad (1.56)$$

Note that the properties of the FFT imply $\hat{z}_{j,n+N} = \hat{z}_{j,n}$, and especially

$$\hat{z}_{j,n}^* = \sum_{k=0}^{N-1} \exp\left(-2\pi i \frac{nk}{N}\right) (a_{j,k} - i b_{j,k}), \quad (1.57)$$

where z^* denotes the complex conjugate of z . In turn, Eq. (1.57) implies

$$\hat{z}_{j,N-n}^* = \sum_{k=0}^{N-1} \exp\left(2\pi i \frac{nk}{N}\right) (a_{j,k} - i b_{j,k}). \quad (1.58)$$

Consequently, using Eqs. (1.57) and (1.58), we can obtain the FFT of $a_{j,n}$ as

$$\frac{1}{2} (\hat{z}_{j,n} + \hat{z}_{j,N-n}^*) = \sum_{k=0}^{N-1} \exp\left(2\pi i \frac{nk}{N}\right) a_{j,k} = \hat{a}_{j,k}, \quad (1.59)$$

and analogously, the FFT of $b_{j,n}$ as

$$\frac{1}{2} (\hat{z}_{j,n} - \hat{z}_{j,N-n}^*) = i \sum_{k=0}^{N-1} \exp\left(2\pi i \frac{nk}{N}\right) b_{j,k} = i \hat{b}_{j,k}. \quad (1.60)$$

We combine the equations for $a_{j+1,k}$ and $b_{j+1,k}$, Eqs. (1.54) and (1.55), respectively, into a single equation for $z_{j+1,k} = a_{j+1,k} + ib_{j+1,k}$. Using the properties (1.59) and (1.60), this equation can be entirely expressed in terms of z :

$$z_{j+1,k} = \mathcal{F}^{-1} [c_n \hat{w}_{j,n} + d_n \hat{w}_{j,N-n}^*], \quad (1.61)$$

where we introduced the abbreviations

$$\hat{w}_{j,k} = \mathcal{F} [z_{j,n} + \Delta t f (\operatorname{Re}(z_{j,n}), \operatorname{Im}(z_{j,n})) + i \Delta t g (\operatorname{Re}(z_{j,n}), \operatorname{Im}(z_{j,n}))], \quad (1.62)$$

and

$$c_n = \frac{1}{2} (\exp(-\Delta t D_a k_n^2) + \exp(-\Delta t D_b k_n^2)), \quad (1.63)$$

$$d_n = \frac{1}{2} (\exp(-\Delta t D_a k_n^2) - \exp(-\Delta t D_b k_n^2)). \quad (1.64)$$

Compared to Eqs. (1.54)–(1.55), which require four real FFTs (two forwards and two backwards), having expressed the algorithm in terms of a single complex field, Eq. (1.61), requires only two complex FFTs (one forwards and one backwards).

Additional Details on the Implementation of the Algorithm In case of the single cell model, the phase field ρ and the concentration of the adhesive bonds A , as well as the two components of the actin polarization, p_x and p_y , are combined in two complex fields, respectively. For simulations of multiple cells, additional phase fields are combined as complex fields in pairs. For maximum performance, all arrays except the substrate displacement field \mathbf{u} were merged in a single array. Using the CUDA library FFT (CUFFT), this allows to compute all FFTs with a single customized batch FFT. The substrate displacement field \mathbf{u} is treated by a separate CUDA kernel, which calculates the spatial derivatives of the traction field in finite difference approximation.

As already discussed in Sect. 1.4.1.1, sums over phase fields, as e.g. $\sum_{j=1}^N \rho_j^2$ and $\sum_{j=1}^N \nabla \rho_j$, have to be calculated for the cells' interactions. These, as well as the cells' volumes and centers of mass are computed with customized CUDA kernels. The center of mass of each cell is determined as described in [14] to track the position of each cell over time, from which its velocity is readily determined in finite difference approximation. Mean velocities as well as order parameters over time are obtained by summing over all cells. The time-averaged mean velocity was determined by a subsequent averaging over all time steps for sufficiently long time intervals to diminish the contribution of initial transients. We typically use a resolution of 512×512 up to 2048×2048 Fourier modes for a square periodic domain size of $L = 100\text{--}200$. For comparison, the initial cell radii typically used were $r_0 = 10\text{--}15$.

Derivation of the Equation for the Elastic Displacements

The stress tensor for an isotropic homogeneous incompressible visco-elastic solid (often called Kelvin–Voigt material) is given by [90]

$$\sigma_{ik} = \tilde{G}(u_{i,k} + u_{k,i}) + \tilde{\eta}(\dot{u}_{i,k} + \dot{u}_{k,i}) - p\delta_{ik}, \quad (1.65)$$

where $u_i = u_i(x, y, z; t)$, $i \in \{x, y, z\}$ are the components of the displacement field. $p = p(x, y, z; t)$ is the pressure field ensuring the incompressibility. \tilde{G} , $\tilde{\eta}$ are the shear modulus and viscosity, respectively. Assuming overdamped motion ($\ddot{u}_i = 0$) the force balance $\nabla \cdot \sigma$, i.e. $\sigma_{ik,k} = 0$, yields

$$\begin{aligned} \tilde{G}\nabla^2\mathbf{u} + \tilde{\eta}\nabla^2\dot{\mathbf{u}} &= \nabla p, \\ \nabla \cdot \mathbf{u} &= 0. \end{aligned} \quad (1.66)$$

We assume the deformable elastic body to be periodic in the x - and y -direction (with period L). At the lower boundary ($z = 0$), we assume vanishing displacements, corresponding to the elastic body sticking on a non-deformable surface,

$$\mathbf{u}(x, y, z = 0, t) = 0. \quad (1.67)$$

At the upper boundary ($z = H$), the cell exerts a two-dimensional traction force $\mathbf{T} = (T_x, T_y, 0)$, but zero normal force on the elastic body

$$\begin{aligned} \sigma_{xz}(x, y, z = H, t) &= T_x(x, y, t), \\ \sigma_{yz}(x, y, z = H, t) &= T_y(x, y, t), \\ \sigma_{zz}(x, y, z = H, t) &= 0. \end{aligned} \quad (1.68)$$

Nonlinearities arising from the free boundary at $z = H$ are neglected. Eqs. (1.66) are equivalent to a biharmonic equation for $\mathbf{w} = \tilde{G}\mathbf{u} + \tilde{\eta}\dot{\mathbf{u}}$ and Laplace's equation for p . After Fourier transforming in x - and y -direction and introducing the wavenumber $k^2 = k_x^2 + k_y^2$, these equations become

$$\partial_z^4\mathbf{w} - 2k^2\partial_z^2\mathbf{w} + k^4\mathbf{w} = 0, \quad (1.69)$$

$$\partial_z^2p - k^2p = 0. \quad (1.70)$$

Six out of the necessary 14 boundary conditions for Eq. (1.69) are given as before by $\mathbf{w}(x, y, z = 0, t) = 0$ and Eq. (1.68). The remaining eight boundary conditions are obtained by evaluating Eq. (1.66) at the boundaries.

The assumption of a vertical substrate layer height H much smaller than its horizontal extension L , $H \ll L$, allows a long wavelength expansion ($k_x, k_y \ll 1/H$) of the solution to Eq. (1.69). We will keep terms up to second order in k_x, k_y ,

corresponding to retaining spatial derivatives up to second order of the traction force \mathbf{T} . Finally, integrating the result over z from $z = 0$ to $z = H$ leads to Eq. (1.18) given in Sect. 1.2.4.

In case of an inhomogeneous substrate stiffness, $\tilde{G} = \tilde{G}(x, y, z)$, one can easily see that the force balance, $\sigma_{ik,k} = 0$, creates a plethora of additional terms in Eq. (1.66), involving all kinds of first order derivatives of \tilde{G} . However, we can neglect these terms if the long wavelength expansion is truncated at the lowest order and assume no dependence on the vertical direction, $\tilde{G} = \tilde{G}(x, y)$. Hence for simplicity, in all computations involving a space-dependent substrate stiffness G we used Eq. (1.18) in the limit $h \rightarrow 0$ [note that the parameters in that equation are related to the ones introduced here via $h = \frac{H^2}{12}$, $G = \frac{2\tilde{G}}{\xi H}$ and $\eta = \frac{2\tilde{\eta}}{\xi H}$ with ξ the efficiency of traction force transmission, see Eq. (1.19)] and substituted $G \rightarrow G(x, y)$.

Characterizing the Cell's Velocity and Shape

To extract the velocity, the center-of-mass position \mathbf{x}^c is determined according to

$$x_i^c = \int x_i \rho(x, y) dx dy, \quad i = 1, 2. \quad (1.71)$$

The aspect ratio was determined via the corresponding 2×2 variance matrix I_{ij}

$$I_{ij} = \int (x_i - x_i^c)(x_j - x_j^c) \rho(x, y) dx dy. \quad (1.72)$$

Its eigenvalues $\lambda_{1,2}$ were calculated and their ratio

$$h = \sqrt{\lambda_1 / \lambda_2} \quad (1.73)$$

is a measure for the aspect ratio of the cell. For a cell moving in x -direction ($i = 1$), the off-diagonal elements vanish, $I_{12} = I_{21} = 0$, and the aspect ratio is simply given by $h = \sqrt{I_{22}/I_{11}}$. Since a circular shape has aspect ratio $h = 1$, in Fig. 1.7 we trace $h - 1$.

The asymmetry of moving cells, namely the deviation from reflection symmetry, can be described via the skewness tensor G_{ijk}

$$G_{ijk} = \int (x_i - x_i^c)(x_j - x_j^c)(x_k - x_k^c) \rho(x, y) dx dy. \quad (1.74)$$

Obviously, for an ellipse $G_{ijk} = 0$. For a cell with an asymmetric shape moving in x -direction ($i, j, k = 1$), only 4 elements of the skewness tensor are non-zero: $G_{111} \neq 0$, and $G_{122} = G_{212} = G_{221} \neq 0$. Hence one can define the following relative asymmetry measures

$$\zeta = \frac{|G_{111}|^{1/3}}{\sqrt{I_{11} + I_{22}}}, \quad (1.75)$$

$$\eta = \frac{|G_{122}|^{1/3}}{\sqrt{I_{11} + I_{22}}}. \quad (1.76)$$

For an ellipse, $\zeta, \eta = 0$; for the asymmetric moving cells obtained by our simulations one has $\zeta, \eta \neq 0$, see Fig. 1.7.

Supplementary Movies

1. Bistability I (ch1_video1.mpg) http://www.physik.tu-berlin.de/~jakob/movies_small//ch1_video1.mpg. The movie shows a round spreading cell that is perturbed by adding a small polarization pointing to the right. The perturbation is insufficient to set the cell into motion. Cf. also Fig. 1.4.
2. Bistability II (ch1_video2.mpg) http://www.physik.tu-berlin.de/~jakob/movies_small//ch1_video2.mpg. The movie shows a round spreading cell that is perturbed by adding a small polarization pointing to the right. This perturbation leads to the onset of motion. Cf. also Fig. 1.4.
3. Bipedal motion (ch1_video3.avi) http://www.physik.tu-berlin.de/~jakob/movies_small//ch1_video3.avi. Bipedal motion is an overall straight motion concomitant with out-of-phase oscillations of the lower and upper halves of the cell. Shown is the shape of the cell and the substrate displacement field (Fig. 1.12a–d).
4. A cell bounces off a step in adhesion (ch1_video4.avi) http://www.physik.tu-berlin.de/~jakob/movies_small//ch1_video4.avi. The motion of a cell on a substrate where the adhesive strength is modulated by a step in the rate of adhesion formation a_0 , corresponding to a varying density of the adhesive ligands ($a_0 = 0.2$ in the blue region, $a_0 = 0.01$ in the black one; $G = 0.15$ everywhere). The cell prefers to stay on the highly adhesive region and is reflected from the low-adhesion region (Fig. 1.13a).
5. Motion of cells on striped adhesive patterns I (ch1_video5.avi) http://www.physik.tu-berlin.de/~jakob/movies_small//ch1_video5.avi. The alternating stripes have a value of high ($a_0 = 0.15$, blue) and no adhesiveness ($a_0 = 0$, black); $G = 0.2$. The cell positions itself symmetrically and moves parallel to the stripes in a steady fashion (Fig. 1.13b top).
6. Motion of cells on striped adhesive patterns II (ch1_video6.avi) http://www.physik.tu-berlin.de/~jakob/movies_small//ch1_video6.avi. Overall low adhesiveness ($a_0 = 0.0015$, blue) and no adhesiveness ($a_0 = 0$, black); $G = 0.1$. After moving initially along the stripes, the cell turns and moves perpendicular to the stripes in a stick-slip fashion (Fig. 1.13b bottom).
7. Durotaxis I (ch1_video7.avi) http://www.physik.tu-berlin.de/~jakob/movies_small//ch1_video7.avi. A cell moving in a linear gradient in the substrate's modulus G [varying along the y -direction from $G = 0$ (black) at the bottom

- to $G = 0.4$ (blue) at the top]. Independently of the initial conditions, the cell approaches a trajectory with an optimal value of G (Fig. 1.14e).
- 8. Durotaxis II (ch1_video8.avi) http://www.physik.tu-berlin.de/~jakob/movies_small//ch1_video8.avi. A cell moving in a linear gradient in the substrate's modulus G [varying along the y-direction from $G = 0$ (black) at the bottom to $G = 0.4$ (blue) at the top]. Independently of the initial conditions, the cell approaches a trajectory with an optimal value of G (Fig. 1.14e).
 - 9. Inelastic collision of cells (ch1_video9.avi) http://www.physik.tu-berlin.de/~jakob/movies_small//ch1_video9.avi. A strongly inelastic collision of two canoe-shaped cells, leading to an effective alignment of the directions of motion (Fig. 1.15a).
 - 10. Elastic collision of cells (ch1_video10.avi) http://www.physik.tu-berlin.de/~jakob/movies_small//ch1_video10.avi. An almost elastic collision of two fan-shaped cells (Fig. 1.15b).
 - 11. Transition from stationary to moving cells (ch1_video11.avi) http://www.physik.tu-berlin.de/~jakob/movies_small//ch1_video11.avi. Initially, only few cells move, while cells which adhere strongly to the substrate (those with green spots inside) are stationary. Repeated collisions between moving and stationary cells set all cells into motion (Fig. 1.16a–d).
 - 12. Transition from moving to stationary cells (ch1_video12.avi) http://www.physik.tu-berlin.de/~jakob/movies_small//ch1_video12.avi. Initially moving cells come to rest and collect in stationary clusters (Fig. 1.16e–h).
 - 13. Translational collective migration (ch1_video13.avi) http://www.physik.tu-berlin.de/~jakob/movies_small//ch1_video13.avi. Alignment of propagation directions due to collisions between cells in a domain with periodic boundary conditions. Cells do not adhere to each other (Fig. 1.17a–d).
 - 14. Rotational collective migration (ch1_video14.avi) http://www.physik.tu-berlin.de/~jakob/movies_small//ch1_video14.avi. Emergence of rotational collective motion in a circular confined domain (in the red region, the rate of nonlinear adhesive bond formation to the substrate is reduced by a factor of 9) (Fig. 1.17e–h).
 - 15. Suppression of rotational collective migration by cell–cell adhesion (ch1_video15.avi) http://www.physik.tu-berlin.de/~jakob/movies_small//ch1_video15.avi. Adhesion between cells prevents the emergence of collective rotational motion (Fig. 1.17j–l).
 - 16. Clustering of cells (ch1_video16.avi) http://www.physik.tu-berlin.de/~jakob/movies_small//ch1_video16.avi. Clustering of cells due to strong cell–cell adhesion forces. A few cells are motile and the cluster changes its shape in time. Cells leave and join the cluster (Fig. 1.18a).
 - 17. Traveling band of cells (ch1_video17.avi) http://www.physik.tu-berlin.de/~jakob/movies_small//ch1_video17.avi. A band of cells strongly adhering to each other is moving in a domain with periodic boundary conditions (Fig. 1.18b).

18. Cells competing for voids (ch1_video18.avi) http://www.physik.tu-berlin.de/~jakob/movies_small//ch1_video18.avi. Confined high-density state without cell-cell adhesion. Cells compete for voids, thereby moving slowly through a “crowded environment” in a random walk fashion (Fig. 1.18d).

References

1. M. Abercrombie, The crawling movement of metazoan cells. Proc. R. Soc. Lond. B **207**, 129–147 (1980)
2. S. Aland, S. Egerer, J. Lowengrub, A. Voigt, Diffuse interface models of locally inextensible vesicles in a viscous fluid. J. Comp. Phys. **277**, 32 (2014)
3. A.Y. Alexandrova, K. Arnold, S. Schaub, J.M. Vasiliev, J.J. Meister, A.D. Bershadsky, A.B. Verkhovsky, Comparative dynamics of retrograde actin flow and focal adhesions: formation of nascent adhesions triggers transition from fast to slow flow. PLoS ONE **3**, e3234 (2008)
4. D. Ambrosi, Cellular traction as an inverse problem. SIAM J. Appl. Math. **66**, 2049 (2006)
5. R. Ananthakrishnan, A. Ehrlicher, The forces behind cell movement. Int. J. Biol. Sci. **3**, 303–17 (2007)
6. K.I. Anderson, R. Cross, Contact dynamics during keratocyte motility. Curr. Biol. **10**, 253 (2000)
7. T.E. Angelini, E. Hannezo, X. Trepat, J.J. Fredberg, D.A. Weitz, Cell migration driven by cooperative substrate deformation patterns. Phys. Rev. Lett. **104**(16), 168104 (2010)
8. T.E. Angelini, E. Hannezo, X. Trepat, M. Marquez, J.J. Fredberg, D.A. Weitz, Glass-like dynamics of collective cell migration. Proc. Natl. Acad. Sci. U.S.A. **108**(12), 4714–4719 (2011)
9. I.S. Aranson, L.S. Tsimring, Continuum description of avalanches in granular media. Phys. Rev. E **64**, 020301 (2001)
10. I.S. Aranson, L.S. Tsimring, Patterns and collective behavior in granular media: theoretical concepts. Rev. Mod. Phys. **78**, 641 (2006)
11. I.S. Aranson, L.S. Tsimring, *Granular Patterns* (Oxford University Press, Oxford, 2009)
12. I.S. Aranson, V.A. Kalatsky, V.M. Vinokur, Continuum field description of crack propagation. Phys. Rev. Lett. **85**, 118 (2000)
13. Y. Aratyn-Schaus, M.L. Gardel, Transient frictional slip between integrin and the ECM in focal adhesions under myosin-II tension. Curr. Biol. **20**, 1145 (2010)
14. L. Bai, D. Breen, Calculating center of mass in an unbounded 2D environment. J. Graph. GPU Game Tools **13**(4), 53–60 (2008)
15. E. Barnhart, G. Allen, F. Jülicher, J. Theriot, Bipedal locomotion in crawling cells. Biophys. J. **98**(6), 933–942 (2010)
16. E.L. Barnhart, K.-C. Lee, K. Keren, A. Mogilner, J.A. Theriot, An adhesion-dependent switch between mechanisms that determine motile cell shape. PLoS Biol. **9**, e1001059 (2011)
17. G.I. Bell, Models for the specific adhesion of cells to cells. Science **200**, 618 (1978)
18. T. Biben, C. Misbah, Tumbling of vesicles under shear flow within an advected-field approach. Phys. Rev. E **67**, 031908 (2003)
19. T. Biben, K. Kassner, C. Misbah, Phase-field approach to three-dimensional vesicle dynamics. Phys. Rev. E **72**(4), 041921 (2005)
20. I. Bischofs, S. Schmidt, U. Schwarz, Effect of adhesion geometry and rigidity on cellular force distributions. Phys. Rev. Lett. **103**, 048101 (2009)
21. C. Blanch-Mercader, J. Casademunt, Spontaneous motility of actin lamellar fragments. Phys. Rev. Lett. **110**(7), 078102 (2013)
22. D.C. Bottino, L.J. Fauci, A computational model of ameboid deformation and locomotion. Eur. Biophys. J. **27**, 532 (1998)

23. J.P. Boyd, Chebyshev and Fourier spectral methods, revised 2nd edn. (Dover Publications, Mineola, 2001)
24. H.R. Brand, H. Pleiner, F. Ziebert, Macroscopic dynamics of polar nematic liquid crystals. *Phys. Rev. E* **74**, 021713 (2006)
25. D. Bray, *Cell Movements: From Molecules to Motility* (Garland Publishing, New York, 2001)
26. F. Brochard-Wyart, P.G. de Gennes, Adhesion induced by mobile binders: dynamics. *Proc. Natl. Acad. Sci. U.S.A.* **99**, 7854–7859 (2002)
27. K. Burridge, M. Chrzanowska-Wodnicka, Focal adhesions, contractility, and signaling. *Ann. Rev. Cell Dev. Biol.* **12**, 463 (1996)
28. M.F. Carlier, D. Pantaloni, Control of actin assembly dynamics in cell motility. *J. Biol. Chem.* **282**, 23005–23009 (2007)
29. A.E. Carlsson, Mechanisms of cell propulsion by active stresses. *New J. Phys.* **13**, 073009 (2011)
30. C.E. Chan, D.J. Odde, Traction dynamics of Filopodia on compliant substrates. *Science* **322**, 1687 (2008)
31. S.-Y. Chou, C.-M. Cheng, P.R. LeDuc, Composite polymer systems with control of local substrate elasticity and their effect on cytoskeletal and morphological characteristics of adherent cells. *Biomaterials* **30**, 3136 (2009)
32. K.U. Claussen, R. Giesa, T. Scheibel, H.-W. Schmidt, Learning from nature: synthesis and characterization of longitudinal polymer gradient materials inspired by mussel byssus threads. *Macromol. Rapid Commun.* **33**, 206 (2012)
33. S. Cox, P. Matthews, Exponential time differencing for stiff systems. *J. Comp. Phys.* **176**(2), 430–455 (2002)
34. M. Cross, H. Greenside, *Pattern Formation and Dynamics in Nonequilibrium Systems* (Cambridge University Press, Cambridge, 2009)
35. G. Csucs, K. Quirin, G. Danuser, Locomotion of fish epidermal keratocytes on spatially selective adhesion patterns. *Cell Motil. Cytoskeleton* **64**(11), 856–867 (2007)
36. G. Danuser, J. Allard, A. Mogilner, Mathematical modeling of eukaryotic cell migration: insights beyond experiments. *Annu. Rev. Cell Dev. Biol.* **29**, 501–528 (2013)
37. T. Das, T.K. Maiti, S. Chakraborty, Traction force microscopy on-chip: shear deformation of fibroblast cells. *Lab Chip* **8**, 1308 (2008)
38. M. Deforet, V. Hakim, H. Yevick, G. Duclos, P. Silberzan, Emergence of collective modes and tri-dimensional structures from epithelial confinement. *Nat. Commun.* **5**, 3747 (2014)
39. M. Dembo, Y.L. Wang, Stresses at the cell-to-substrate interface during locomotion of fibroblasts. *Biophys. J.* **76**, 2307 (1999)
40. E.W. Dent, F.B. Gertler, Cytoskeletal dynamics and transport in growth cone motility and axon guidance. *Neuron* **40**, 209–227 (2003)
41. P.A. DiMilla, K. Barbee, D.A. Lauffenburger, Mathematical model for the effects of adhesion and mechanics on cell migration speed. *Biophys. J.* **60**, 15–37 (1991)
42. K. Doubrovinski, K. Kruse, Cytoskeletal waves in the absence of molecular motors. *Europhys. Lett.* **83**(1), 18003 (2008)
43. K. Doxzen, S.R.K. Vedula, M.C. Leong, H. Hirata, N.S. Gov, A.J. Kabla, B. Ladoux, C.T. Lim, Guidance of collective cell migration by substrate geometry. *Integr. Biol.* **5**(8), 1026–1035 (2013)
44. A. Dreher, I.S. Aranson, K. Kruse, Spiral actin-polymerization waves can generate amoeboidal cell crawling. *New J. Phys.* **16**(5), 055007 (2014)
45. Q. Du, X.Q. Wang, Simulating the deformation of vesicle membranes under elastic bending energy in three dimensions. *J. Comp. Phys.* **212**, 757 (2006)
46. H. Emmerich, Advances of and by phase-field modelling in condensed-matter physics. *Adv. Phys.* **57**, 1 (2008)
47. M. Enculescu, M. Falcke, Modeling morphodynamic phenotypes and dynamic regimes of cell motion. *Adv. Exp. Med. Biol.* **736**, 337–358 (2012)
48. T. Erdmann, U.S. Schwarz, Stochastic dynamics of adhesion clusters under shared constant force and with rebinding. *J. Chem. Phys.* **121**, 8997 (2004)

49. J. Etienne, J. Fouchard, D. Mitrossilis, N. Bufl, P. Durand-Smet, A. Asnacios, Cells as liquid motors. Mechanosensitivity emerges from collective dynamics of actomyosin cortex. *Proc. Natl. Acad. Sci. U.S.A.* **106**, 2740–2745 (2015)
50. S. Etienne-Manneville, Microtubules in cell migration. *Annu. Rev. Cell Dev. Biol.* **29**, 471–499 (2013)
51. U. Euteneuer, M. Schliwa, Persistent, directional motility of cells and cytoplasmic fragments in the absence of microtubules. *Nature* **310**, 58 (1984)
52. G. Fix, Phase field methods for free boundary problems, in *Free Boundary Problems: Theory and Applications*, ed. by A. Fasano, M. Primicerio (Pitman, Boston, 1983), p. 580
53. R. Folch, J. Casademunt, A. Hernandez-Machado, L. Ramirez-Piscina, Phase-field model for Hele-Shaw flows with arbitrary viscosity contrast. I. Theoretical approach. *Phys. Rev. E* **60**, 1724 (1999)
54. R. Folch, J. Casademunt, A. Hernandez-Machado, L. Ramirez-Piscina, Phase-field model for Hele-Shaw flows with arbitrary viscosity contrast. II. Numerical study. *Phys. Rev. E* **60**, 1734 (1999)
55. M.F. Fournier, R. Sauser, D. Ambrosi, J.-J. Meister, A.B. Verkhovsky, Force transmission in migrating cells. *J. Cell Biol.* **188**, 287 (2010)
56. C. Franck, S.A. Maskarinec, D.A. Tirrell, G. Ravichandran, Three-dimensional traction force microscopy: a new tool for quantifying cell-matrix interactions. *PLOS One* **6**, e17833 (2011)
57. T. Fuhs, M. Goegler, C.A. Brunner, C.W. Wolgemuth, J.A. Kaes, Causes of retrograde flow in fish keratocytes. *Cytoskeleton* **71**, 24–35 (2014)
58. M.L. Gardel, B. Sabass, L. Ji, G. Danuser, U.S. Schwarz, C.M. Waterman, Traction stress in focal adhesions correlates biphasically with actin retrograde flow speed. *J. Cell Biol.* **183**, 999 (2008)
59. G. Giannone, B.J. Dubin-Thaler, H.-G. Döbereiner, N. Kieffer, A.R. Bresnick, M.P. Sheetz, Periodic lamellopodial contractions correlate with rearward actin waves. *Cell* **116**, 431 (2004)
60. L. Giomi, A. DeSimone, Spontaneous division and motility in active nematic droplets. *Phys. Rev. Lett.* **112**, 147802 (2014)
61. A. Gopinathan, K.-C. Lee, J.M. Schwarz, A.J. Liu, Branching, capping, and severing in dynamic actin structures. *Phys. Rev. Lett.* **99**, 058103 (2007)
62. M.E. Gracheva, H.G. Othmer, A continuum model of motility in ameoboid cells. *Bull. Math. Biol.* **66**, 167–193 (2004)
63. G. Grégoire, H. Chaté, Y. Tu, Moving and staying together without a leader. *Physica D* **181**(34), 157–170 (2003)
64. H. Grimm, A. Verkhovsky, A. Mogilner, J. Meister, Analysis of actin dynamics at the leading edge of crawling cells: implications for the shape of keratocyte lamellipodia. *Eur. Biophys. J.* **32**, 563 (2003)
65. D. Grossman, I. Aranson, E.B. Jacob, Emergence of agent swarm migration and vortex formation through inelastic collisions. *New J. Phys.* **10**(2), 023036 (2008)
66. M. Herant, M. Dembo, Form and function in cell motility: from fibroblasts to keratocytes. *Biophys. J.* **98**, 1408 (2010)
67. W.R. Holmes, L. Edelstein-Keshet, A comparison of computational models for eukaryotic cell shape and motility. *PLoS Comput. Biol.* **8**, e1002793 (2012)
68. J. Howard, *Mechanics of Motor Proteins and the Cytoskeleton* (Sinauer, Sunderland, 2001)
69. S. Huang, C.P. Brangwynne, K.K. Parker, D.E. Ingber, Symmetry-breaking in mammalian cell cohort migration during tissue pattern formation: role of random-walk persistence. *Cell Motil. Cytoskeleton* **61**, 201–213 (2005)
70. R.O. Hynes, Integrins: versatility, modulation, and signaling in cell adhesion. *Cell* **69**(1), 11–25 (1992)
71. P.A. Iglesias, P.N. Devreotes, Biased excitable networks: how cells direct motion in response to gradients. *Curr. Opin. Cell Biol.* **24**, 245–253 (2012)
72. P.Y. Jay, P.A. Pham, S.A. Wong, E.L. Elson, A mechanical function of myosin II in cell motility. *J. Cell Sci.* **108**, 387–393 (1995)

73. L. Ji, J. Lim, G. Danuser, Fluctuations of intracellular forces during cell protrusion. *Nat. Cell Biol.* **10**, 1393–1400 (2008)
74. J.F. Joanny, K. Kruse, F. Jülicher, J. Prost, Hydrodynamic theory for multi-component active polar gels. *New J. Phys.* **9**, 422 (2007)
75. K. John, P. Peyla, K. Kassner, J. Prost, C. Misbah, Nonlinear study of symmetry breaking in actin gels: implications for cellular motility. *Phys. Rev. Lett.* **100**, 068101 (2008)
76. F. Jülicher, K. Kruse, J. Prost, J.F. Joanny, Active behavior of the cytoskeleton. *Phys. Rep.* **449**, 3 (2007)
77. A. Karma, W.-J. Rappel, Quantitative phase-field modeling of dendritic growth in two and three dimensions. *Phys. Rev. E* **57**, 4323 (1998)
78. K. Kassner, C. Misbah, A phase-field approach for stress-induced instabilities. *Europhys. Lett.* **46**, 217 (1999)
79. K. Keren, Z. Pincus, G.M. Allen, E.L. Barnhart, G. Marriott, A. Mogilner, J.A. Theriot, Mechanism of shape determination in motile cells. *Nature* **453**(7194), 475–480 (2008)
80. H. Kitahata, K. Iida, M. Nagayama, Spontaneous motion of an elliptic camphor particle. *Phys. Rev. E* **87**(1), 010901 (2013)
81. M.H. Köpf, L.M. Pismen, A continuum model of epithelial spreading. *Soft Matter* **9**(14), 3727–3734 (2013)
82. M.M. Kozlov, A. Mogilner, Model of polarization and bistability of cell fragments. *Biophys. J.* **93**, 3811 (2007)
83. K. Kruse, F. Jülicher, Self-organization and mechanical properties of active filament bundles. *Phys. Rev. E* **67**, 051913 (2003)
84. K. Kruse, J.F. Joanny, F. Jülicher, J. Prost, K. Sekimoto, Aster, vortices, and rotating spirals in active gels of polar filaments. *Phys. Rev. Lett.* **92**, 078101 (2004)
85. K. Kruse, J.F. Joanny, F. Jülicher, J. Prost, K. Sekimoto, Generic theory of active polar gels: a paradigm for cytoskeletal dynamics. *Eur. Phys. J. E* **16**, 5 (2005)
86. K. Kruse, J.F. Joanny, F. Jülicher, J. Prost, Contractility and retrograde flow in lamellipodium motion. *Phys. Biol.* **3**, 130 (2006)
87. E. Kuusela, W. Alt, Continuum model of cell adhesion and migration. *J. Math. Biol.* **58**, 135 (2009)
88. C.I. Lacayo, Z. Pincus, M.M. Van Duijn, C.A. Wilson, D.A. Fletcher, F.B. Gertler, A. Mogilner, J.A. Theriot, Emergence of large-scale cell morphology and movement from local actin filament growth dynamics. *PLoS Biol.* **5**, 2035 (2007)
89. T. Lai, K.-H. Chiam, Mechanochemical model of cell migration on substrates of varying stiffness. *Phys. Rev. E* **84**, 061907 (2011)
90. L. Landau, E. Lifshitz, *Theory of Elasticity*. Course of Theoretical Physics, vol. 7 (Elsevier, Oxford, 1986)
91. J. Langer, Models of pattern formation in first-order phase transitions, in *Directions in Condensed Matter Physics*, ed. by G. Grinstein, G. Mazenko (World Scientific, Singapore, 1986), p. 165
92. J. Lee, K. Jacobson, The composition and dynamics of cell-substratum adhesions in locomoting fish keratocytes. *J. Cell Sci.* **110**, 2833 (1997)
93. P. Lee, C.W. Wolgemuth, Crawling cells can close wounds without purse strings or signaling. *PLoS Comput. Biol.* **7**(3), e1002007 (2011)
94. J. Lee, A. Ishihara, J.A. Theriot, K. Jacobson, Principles of locomotion for simple-shaped cells. *Nature* **362**, 167 (1993)
95. M. Lenz, T. Thoresen, M.L. Gardel, A.R. Dinner, Contractile units in disordered actomyosin bundles arise from F-actin buckling. *Phys. Rev. Lett.* **108**, 238107 (2012)
96. Y. Li, P. Bhimalapuram, A.R. Dinner, Model for how retrograde actin flow regulates adhesion traction stresses. *J. Phys. Condens. Matter* **22**, 194113 (2010)
97. A.D. Lieber, S. Yehudai-Resheff, E.L. Barnhart, J.A. Theriot, K. Keren, Membrane tension in rapidly moving cells is determined by cytoskeletal forces. *Curr. Biol.* **23**, 1409–1417 (2013)
98. O. Lieleg, M.M.A.E. Claessens, A.R. Bausch, Structure and dynamics of cross-linked actin networks. *Soft Matter* **6**, 218 (2010)

99. T.B. Liverpool, M.C. Marchetti, Bridging the microscopic and the hydrodynamic in active filament solutions. *Europhys. Lett.* **69**, 846 (2005)
100. C.M. Lo, H.B. Wang, M. Dembo, Y.L. Wang, Cell movement is guided by the rigidity of the substrate. *Biophys. J.* **79**, 144 (2000)
101. J. Löber, F. Ziebert, I.S. Aranson, Modeling crawling cell movement on soft engineered substrates. *Soft Matter* **10**(9), 1365–1373 (2014)
102. J. Löber, F. Ziebert, I.S. Aranson, Collisions of deformable cells lead to collective migration. *Sci. Rep.* **5**, 9172 (2015)
103. A.J. Loosley, J.X. Tang, Stick-slip motion and elastic coupling in crawling cells. *Phys. Rev. E* **86**(3), 031908 (2012)
104. M. Machacek, G. Danuser, Morphodynamic profiling of protrusion phenotypes. *Biophys. J.* **90**, 1439 (2006)
105. E. Maitrea, C. Misbah, P. Peyla, A. Raoult, Comparison between advected-field and level-set methods in the study of vesicle dynamics. *Physica D* **241**, 11461157 (2012)
106. W. Marth, A. Voigt, Signaling networks and cell motility: a computational approach using a phase field description. *J. Math. Biol.* **69**, 91–112 (2014)
107. E. Meyhöfer, J. Howard, The force generated by a single kinesin molecule against an elastic load. *Proc. Natl. Acad. Sci. U.S.A.* **92**, 574 (1995)
108. A. Mogilner, Mathematics of cell motility: have we got its number? *J. Math. Biol.* **58**, 105134 (2009)
109. A. Mogilner, K. Keren, The shape of motile cells. *Curr. Biol.* **19**, R762 (2009)
110. A. Mogilner, G. Oster, Cell motility driven by actin polymerization. *Biophys. J.* **71**, 3030–3045 (1996)
111. A. Mogilner, G. Oster, Force generation by actin polymerization II: the elastic ratchet and tethered filaments. *Biophys. J.* **84**, 1591–1605 (2003)
112. A. Mogilner, J. Allard, R. Wollman, Cell polarity: quantitative modeling as a tool in cell biology. *Science* **336**, 175 (2012)
113. S. Munevar, Y.L. Wang, M. Dembo, Traction force microscopy of migrating normal and H-ras transformed 3T3 fibroblasts. *Biophys. J.* **80**, 1744 (2001)
114. H. Nakazawa, K. Sekimoto, Polarity sorting in a bundle of actin filaments by two-headed myosins. *J. Phys. Soc. Jpn.* **65**, 2404 (1996)
115. M.P. Neilson, J.A. Mackenzie, S.D. Webb, R.H. Insall, Modeling cell movement and chemotaxis using pseudopod-based feedback. *SIAM J. Sci. Comput.* **33**, 1035 (2011)
116. S. Nourshargh, P. Hordijk, M. Sixt, Breaching multiple barriers: leukocyte motility through venular walls and the interstitium. *Nat. Rev. Mol. Cell Biol.* **11**, 366–378 (2010)
117. T. Ohta, T. Ohkuma, Deformable self-propelled particles. *Phys. Rev. Lett.* **102**(15), 154101 (2009)
118. S. Osher, R. Fedkiw, *Level Set Methods and Dynamic Implicit Surfaces* (Springer, New York, 2003)
119. S.P. Palecek, J.C. Loftus, M.H. Ginsberg, D.A. Lauffenburger, A.F. Horwitz, Integrin-ligand binding properties govern cell migration speed through cell-substratum adhesiveness. *Nature* **385**, 537 (1997)
120. S.H. Parekh, O. Chaudhuri, J.A. Theriot, D.A. Fletcher, Loading history determines the velocity of actin-network growth. *Nat. Cell Biol.* **7**, 1219 (2005)
121. R.J. Pelham, Y.-L. Wang, Cell locomotion and focal adhesions are regulated by substrate flexibility. *Proc. Natl. Acad. Sci. U.S.A.* **94**, 13661–13665 (1997)
122. B.N.J. Persson, *Sliding Friction* (Springer, Berlin, 2000)
123. F. Peruani, A. Deutsch, M. Bär, Nonequilibrium clustering of self-propelled rods. *Phys. Rev. E* **74**(3), 030904 (2006)
124. C.S. Peskin, G.M. Odell, G.F. Oster, Cellular motions and thermal fluctuations: the Brownian ratchet. *Biophys. J.* **65**, 316 (1993)
125. R. Peter, V. Schaller, F. Ziebert, W. Zimmermann, Pattern formation in active cytoskeletal networks. *New J. Phys.* **10**, 035002 (2008)

126. L. Petitjean, M. Reffay, E. Grasland-Mongrain, M. Poujade, B. Ladoux, A. Buguin, P. Silberzan, Velocity fields in a collectively migrating epithelium. *Biophys. J.* **98**, 1790–1800 (2010)
127. H. Pleiner, H.R. Brand, Spontaneous splay phases in polar nematic liquid crystals. *Europhys. Lett.* **9**, 243 (1989)
128. T.D. Pollard, J.A. Cooper, Actin, a central player in cell shape and movement. *Science* **326**, 1208 (2009)
129. M. Poujade, E. Grasland-Mongrain, A. Hertzog, J. Jouanneau, P. Chavrier, B. Ladoux, A. Buguin, P. Silberzan, Collective migration of an epithelial monolayer in response to a model wound. *Proc. Natl. Acad. Sci. U.S.A.* **104**, 15988–15993 (2007)
130. M. Prass, K. Jacobson, A. Mogilner, M. Radmacher, Direct measurement of the lamellipodial protrusive force in a migrating cell. *J. Cell Biol.* **174**, 767 (2006)
131. W.H. Press, S.A. Teukolsky, W.T. Vetterling, B.P. Flannery, *Numerical Recipes 3rd Edition: The Art of Scientific Computing* (Cambridge University Press, New York, 2007)
132. D. Raucher, M.P. Sheetz, Cell spreading and lamellipodial extension rate is regulated by membrane tension. *J. Cell Biol.* **148**, 127–136 (2000)
133. P. Recho, L. Truskinovsky, Asymmetry between pushing and pulling for crawling cells. *Phys. Rev. E* **87**(2), 022720 (2013)
134. P. Recho, T. Putelat, L. Truskinovsky, Contraction-driven cell motility. *Phys. Rev. Lett.* **111**, 108102 (2013)
135. J. Renkawitz, K. Schumann, M. Weber, T. Lämmermann, H. Pflicke, M. Piel, J. Polleux, J. Spatz, M. Sixt, Adaptive force transmission in amoeboid cell migration. *Nat. Cell Biol.* **11**, 1438 (2009)
136. C.G. Rolli, H. Nakayama, K. Yamaguchi, J.P. Spatz, R. Kemkemer, J. Nakanishi, Switchable adhesive substrates: revealing geometry dependence in collective cell behavior. *Biomaterials* **33**, 2409–2418 (2012)
137. B. Sabass, U.S. Schwarz, Modelling cytoskeletal flow over adhesion sites: competition between stochastic bond dynamics and intracellular relaxation. *J. Phys. Condens. Matt.* **22**, 194112 (2010)
138. A. Sacan, H. Ferhatosmanoglu, H. Coskun, CellTrack: an open-source software for cell tracking and motility analysis. *Bioinformatics* **24**, 1647 (2008)
139. E. Sackmann, R. Bruinsma, Cell adhesion as wetting transition? *Chem. Phys. Chem.* **3**, 262 (2002)
140. T. Sanchez, D.T.N. Chen, S.J. DeCamp, M. Heymann, Z. Dogic, Spontaneous motion in hierarchically assembled active matter. *Nature* **491**, 431 (2012)
141. C.H. Schreiber, M. Stewart, T. Duke, Simulation of cell motility that reproduces the force-velocity relationship. *Proc. Natl. Acad. Sci. U.S.A.* **107**, 9141 (2010)
142. U.S. Schwarz, M.L. Gardel, United we stand - integrating the actin cytoskeleton and cell-matrix adhesions in cellular mechanotransduction. *J. Cell Sci.* **125**, 3051 (2012)
143. U.S. Schwarz, S.A. Safran, Physics of adherent cells. *Rev. Mod. Phys.* **85**, 1327 (2013)
144. U.S. Schwarz, N.Q. Balaban, D. Riveline, A. Bershadsky, B. Geiger, S.A. Safran, Calculation of forces at focal adhesions from elastic substrate data: the effect of localized force and the need for regularization. *Biophys. J.* **83**, 1380 (2002)
145. D. Shao, W.J. Rappel, H. Levine, Computational model for cell morphodynamics. *Phys. Rev. Lett.* **105**, 108104 (2010)
146. D. Shao, H. Levine, W.-J. Rappel, Coupling actin flow, adhesion, and morphology in a computational cell motility model. *Proc. Natl. Acad. Sci. U.S.A.* **109**, 6851 (2012)
147. M.P. Sheetz, D. Felsenfeld, C.G. Galbraith, D. Choquet, Cell migration as a five-step cycle. *Biochem. Soc. Symp.* **65**, 233–243 (1999)
148. C. Shi, C.-H. Huang, P. Devreotes, P. Iglesias, Interaction of motility, directional sensing, and polarity modules recreates the behaviors of chemotaxing cells. *PLoS Cell Biol.* **9**, e1003122 (2013)
149. I. Singer-Loginova, H.M. Singer, The phase field technique for modeling multiphase materials. *Rep. Prog. Phys.* **71**, 106501 (2008)

150. A. Smith, U. Seifert, Effective adhesion strength of specifically bound vesicles. *Phys. Rev. E* **71**, 061902 (2005)
151. L.A. Smith, H. Aranda-Espinoza, J.B. Haun, M. Dembo, D.A. Hammer, Neutrophil traction stresses are concentrated in the uropod during migration. *Biophys. J.* **92**, L58 (2007)
152. J. Solon, I. Levental, K. Sengupta, P.C. Georges, P.A. Janmey, Fibroblast adaptation and stiffness matching to soft elastic substrates. *Biophys. J.* **93**, 4453 (2007)
153. A. Stéphanou, E. Mylona, M. Chaplain, P. Tracqui, A computational model of cell migration coupling the growth of focal adhesions with oscillatory cell protrusions. *J. Theor. Biol.* **253**, 701–716 (2008)
154. M. Sussman, P. Smereka, S. Osher, A level set approach for computing solutions to incompressible two-phase flow. *J. Comp. Phys.* **114**, 146 (1994)
155. T.M. Svitkina, A.B. Verkhovsky, K.M. McQuade, G.G. Borisy, Analysis of the actin-myosin II system in fish epidermal keratocytes: mechanism of cell body translocation. *J. Cell Biol.* **139**, 397 (1997)
156. B. Szabó, G.J. Szöllösi, B. Gönci, Z. Jurányi, D. Selmecki, T. Vicsek, Phase transition in the collective migration of tissue cells: experiment and model. *Phys. Rev. E* **74**(6), 061908 (2006)
157. M. Takeichi, Cadherins: a molecular family important in selective cell-cell adhesion. *Annu. Rev. Biochem.* **59**, 237 (1990)
158. J.L. Tan, J. Tien, D.M. Pirone, D.S. Gray, K. Bhadriraju, C.S. Chen, Cells lying on a bed of microneedles: an approach to isolate mechanical force. *Proc. Natl. Acad. Sci. U.S.A.* **100**, 1484 (2003)
159. M. Tarama, T. Ohta, Oscillatory motions of an active deformable particle. *Phys. Rev. E* **87**(6), 062912 (2013)
160. M. Thery, V. Racine, M. Piel, A. Pepin, A. Dimitrov, Y. Chen, J.B. Sibarita, M. Bornens, Anisotropy of cell adhesive microenvironment governs cell internal organization and orientation of polarity. *Proc. Natl. Acad. Sci. U.S.A.* **103**, 19771 (2006)
161. E. Tjhung, D. Marenduzzo, M.E. Cates, Spontaneous symmetry breaking in active droplets provides a generic route to motility. *Proc. Natl. Acad. Sci. U.S.A.* **109**(31), 12381–12386 (2012)
162. E. Tjhung, A. Tiribocchi, D. Marenduzzo, M.E. Cates, A minimal physical model captures the shapes of crawling cells. *Nat. Commun.* **6**, 5420 (2015)
163. L. Trichet, J. Le Digabel, R. Hawkins, S.R. Vedula, M. Gupta, C. Ribrault, P. Hersen, R. Voituriez, B. Ladoux, Evidence of a large-scale mechanosensing mechanism for cellular adaptation to substrate stiffness. *Proc. Natl. Acad. Sci. U.S.A.* **109**, 6933 (2012)
164. T.A. Ulrich, E.M. de Juan Pardo, S. Kumar, The mechanical rigidity of the extracellular matrix regulates the structure, motility, and proliferation of glioma cells. *Cancer Res.* **69**, 4167 (2009)
165. P. Vallotton, G. Danuser, S. Bohnet, J.-J. Meister, A.B. Verkhovsky, Tracking retrograde flow in keratocytes: news from the front. *Mol. Biol. Cell* **16**, 1223 (2005)
166. S.R.K. Vedula, M.C. Leong, T.L. Lai, P. Hersen, A.J. Kabla, C.T. Lim, B. Ladoux, Emerging modes of collective cell migration induced by geometrical constraints. *Proc. Natl. Acad. Sci. U.S.A.* **109**(32), 12974–12979 (2012)
167. A.B. Verkhovsky, T.M. Svitkina, G.G. Borisy, Self-polarization and directional motility of cytoplasm. *Curr. Biol.* **9**, 11–20 (1999)
168. D. Volfson, L.S. Tsimring, I.S. Aranson, Stick-slip dynamics of a granular layer under shear. *Phys. Rev. E* **69**(3), 031302 (2004)
169. J.H.-C. Wang, J.-S. Lin, Cell traction force and measurement methods. *Biomech. Model. Mechanobiol.* **6**, 361 (2007)
170. H.-B. Wang, M. Dembo, S.K. Hanks, Y.-L. Wang, Focal adhesion kinase is involved in mechanosensing during fibroblast migration. *Proc. Natl. Acad. Sci. U.S.A.* **98**, 11295–11300 (2001)
171. M.F. Ware, A. Wells, D.A. Lauffenburger, Epidermal growth factor alters fibroblast migration speed and directional persistence reciprocally and in a matrix-dependent manner. *J. Cell Sci.* **111**, 2423–2432 (1998)

172. J. Weichsel, U.S. Schwarz, Two competing orientation patterns explain experimentally observed anomalies in growing actin networks. *Proc. Natl. Acad. Sci. U.S.A.* **107**, 6304 (2010)
173. O.D. Weiner, W.A. Marganski, L.F. Wu, S.J. Altschuler, M.W. Kirschner, An actin-based wave generator organizes cell motility. *PLoS Biol.* **5**, e221 (2007)
174. R. Wittkowski, H. Löwen, H.R. Brand, Microscopic and macroscopic theories for the dynamics of polar liquid crystals. *Phys. Rev. E* **84**, 041708 (2011)
175. C.W. Wolgemuth, Lamellipodial contractions during crawling and spreading. *Biophys. J.* **89**, 1643 (2005)
176. C.W. Wolgemuth, M. Zajac, The moving boundary node method: a level set-based, finite volume algorithm with applications to cell motility. *J. Comp. Phys.* **229**, 7287 (2010)
177. C.W. Wolgemuth, J. Stajic, A. Mogilner, Redundant mechanisms for stable cell locomotion revealed by minimal models. *Biophys. J.* **101**, 545 (2011)
178. J. Xu, D. Wirtz, T. Pollard, Dynamic cross-linking by α -actinin determines the mechanical properties of actin filament networks. *J. Biol. Chem.* **273**, 9570 (1998)
179. H. Xu, R. Matkar, T. Kyu, Phase-field modeling on morphological landscape of isotactic polystyrene single crystals. *Phys. Rev. E* **72**, 011804 (2005)
180. P.T. Yam, C.A. Wilson, L. Ji, B. Hebert, E.L. Barnhart, N.A. Dye, P.W. Wiseman, G. Danuser, J.A. Theriot, Actin-myosin network reorganisation breaks symmetry at the cell rear to spontaneously initiate polarized cell motility. *J. Cell Biol.* **178**, 1207 (2007)
181. L. Yang, J.C. Effler, B.L. Kutscher, S.E. Sullivan, D.N. Robinson, P.A. Iglesias, Modeling cellular deformations using the level set formalism. *BMC Sys. Biol.* **2**, 68 (2008)
182. F. Ziebert, I.S. Aranson, Effects of adhesion dynamics and substrate compliance on the shape and motility of crawling cells. *PLoS ONE* **8**(5), e64511 (2013)
183. F. Ziebert, I.S. Aranson, Modular approach for modeling cell motility. *Eur. Phys. J. Spec. Top.* **223**, 1265–1277 (2014)
184. F. Ziebert, I.S. Aranson, L.S. Tsimring, Effects of cross-links on motor-mediated filament organization. *New J. Phys.* **9**, 421 (2007)
185. F. Ziebert, S. Swaminathan, I.S. Aranson, Model for self-polarization and motility of keratocyte fragments. *J. R. Soc. Interface* **9**, 1084 (2012)
186. J. Zimmermann, C. Brunner, M. Enculescu, M. Goegler, A. Ehrlicher, J. Käs, M. Falcke, Actin filament elasticity and retrograde flow shape the force-velocity relation of motile cells. *Biophys. J.* **102**, 287 (2012)

Chapter 2

Cell Crawling Driven by Spontaneous Actin Polymerization Waves

Karsten Kruse

2.1 Introduction

Cells have at their disposal a limited arsenal of machines to perform a large variety of tasks that allow them to proliferate and thus to sustain life. Contrary to a Swiss army knife that is a multifunctional tool with a particular instrument for each intended task, nature has followed a strategy that is more akin to Lego by using a limited number of building blocks in different combinations to generate a plethora of functions. This is true notably for cytoskeletal proteins that organize intracellular transport and drive vital processes like cell division and crawling. To assemble the various structures needed in these different contexts from a common pool of molecules, cells profit from the inherent ability of protein machines to self-organize. This mechanism for pattern formation has been promoted long ago in the context of morphogenesis [33, 67]. More recently, protein self-organization has been observed in reconstitution experiments, for example, for bacterial proteins involved in cell division [37] or for cytoskeletal proteins [2, 47, 50, 59]. These studies have revealed a number of patterns or motives that can be generated in this way. In particular, the possibility to form traveling waves has been demonstrated, which have also been observed *in vivo* [6, 24, 69, 72]. The relevance of these structures for physiological processes, though, is still largely unexplored. The probably best studied example in this context are the Min-protein oscillations in *E. coli*. Through a joined effort of *in vivo* studies, *in vitro* reconstitution experiments, and theoretical analysis

Electronic supplementary material The online version of this chapter (doi: [10.1007/978-3-319-24448-8_2](https://doi.org/10.1007/978-3-319-24448-8_2)) contains supplementary material, which is available to authorized users.

K. Kruse (✉)

Theoretical Physics, Saarland University, Postfach 151150, 66041 Saarbrücken, Germany
e-mail: k.kruse@physik.uni-saarland.de

there is now strong reason to believe that the Min oscillations observed in vivo are indeed due to self-organization [38]. For other systems this is much more difficult to achieve, because they are much more complicated as they involve a large number of different proteins.

In such a context, simplified theories can help to identify possible mechanisms of self-organization and to design experiments that can challenge these ideas and distinguish between different possibilities. In this chapter, we will focus on the analysis of spontaneously generated cytoskeletal waves in connection with cell migration. Here, we have notably in mind spontaneous migration that does not rely on an externally prescribed gradient. Experiments on fragments of neutrophils and fish keratocytes have shown that such motion can be generated by the actin cytoskeleton alone without a need for maintaining cell polarization by microtubules or genetic regulation [21, 32, 40].

However, due to the inherent complexity of actin-based cell crawling, which requires the generation of protrusions, the pulling of the cell body into the direction of motion, as well as momentum exchange with the substrate, which is in many cases done through the formation and solution of adhesion sites, this process has not yet been fully reconstituted in vitro. The sub-process that is probably best understood is that of forming protrusions by polymerization. The possibility to migrate by polymerization forces alone is dramatically illustrated by the motion of the pathogen *listeria monocytogenes* [27]. By now a fairly complete list of cytoskeletal proteins involved in this process is known [52], the proteins are characterized on a molecular scale, and a minimal set has been identified that can generate motility of inert beads in vitro [3, 10, 35]. Briefly, this mechanism relies on the generation of mechanical stress by polymerizing an actin gel on the surface of the bead, which at some point ruptures due to the mechanical stresses that build up and propels the bead similarly to a cherry pit squeezed between two fingers [22].

Due to the absence of a similar system to study other aspects of or even fully reconstitute cell crawling, for the time being, many of our ideas about it have to be tested by theory. Several approaches have been developed, in particular, for the dynamics at the leading edge, see, for example, the review by Ryan et al. [57]. They range from molecular dynamics simulations that attempt to capture the dynamics of individual proteins via continuum mean-field description to purely phenomenological macroscopic theories similar to traditional hydrodynamics. Before we survey in detail different physical frameworks for the study of cell motility driven by actin waves, we will first present experimental results on spontaneous actin waves. Finally, we will show various migration patterns that can be generated by these waves and conclude with a discussion of possible future directions.

2.2 Spontaneous Actin Waves

In recent years, spontaneous actin waves have been reported in different systems. Contraction–relaxation waves relying on the action of myosin motors were first observed in fibers of striated muscle [58]. These fibers consist of a periodic

arrangement of so-called sarcomeres that are the elementary contractile units of striated muscle. Sarcomeres contain bipolar myosin filaments interdigitating with actin filaments with their barbed ends pointing outwards. The structure is maintained by elastic structural elements. Upon activation of the motors, the unit contracts and requires an external force to stretch after contraction. Sarcomeres can oscillate spontaneously [48] and the coupling into a linear chain of the oscillating units then produces propagating contraction waves [29]. Similarly, contraction waves have been found in protoplasmic droplets of true slime mold *Physarum polycephalum* [64, 65] and in developing tissue [42, 63]. In the latter case, the elementary oscillating units are cells with an internal structure that are less organized than for sarcomeres. These oscillations may involve actin assembly dynamics. However, the importance of such waves for cell motility remains to be explored.

An early report of actin polymerization waves in single cells of the soil-living amoeba *Dictyostelium discoideum*, see Fig. 2.1, was published by Vicker [69]. These waves are connected to cellular shape changes, notably via the formation of lamellipodia and pseudopodia [69]. This finding suggested a tight link between actin waves and cell crawling [70]. This idea was later picked up in a work by Weiner et al. reporting on spontaneous actin waves in human neutrophils [72]. More detailed studies on the molecular mechanism underlying wave formation in *D. discoideum* followed [7, 8, 68]. Whereas these works emphasized the inherent dynamics of the actin cytoskeleton, other works focused on the coupling of the actin assembly dynamics to (spontaneous) signaling events involving Ras and PI3-kinase [30]. These works accumulated evidence that the actin cytoskeleton is an excitable medium in which waves are triggered by the signaling machinery. Studies on giant *D. discoideum* cells further supported this notion by reporting actin polymerization spiral waves and annihilation of colliding waves [23].

Actin polymerization waves have also been observed in other cell types, ranging from neutrophils mentioned above [72] to various cell lines, like porcine renal epithelial cells [45], murine melanoma and human leukemia cells [44], osteo-carcinoma cells [12], jurkat T cells [31], or mouse embryo fibroblasts [4]. The mechanism underlying actin assembly waves likely involves interactions with the plasma membrane. For example, the waves in human neutrophils are best observed with total internal reflection fluorescence (TIRF) microscopy, highlighting the importance of the membrane adjacent to the substrate for wave generation [72]. Also a detailed analysis of actin waves in *D. discoideum* showed that actin waves result from actin polymerization initiated at the plasma membrane [8]. The connection between actin polymerization and the plasma membrane may be also instrumental for the recently reported ability of actin waves to respond to topographical structures of the substrate [19].

Actin polymerization waves might also be linked to another wave-like behavior observed for adherent cells, namely circular dorsal ruffles [4, 49]. Early indications of these ruffles date back to the early 1980s [43], but their molecular origin is still poorly understood. It has been suggested that they require a coupling

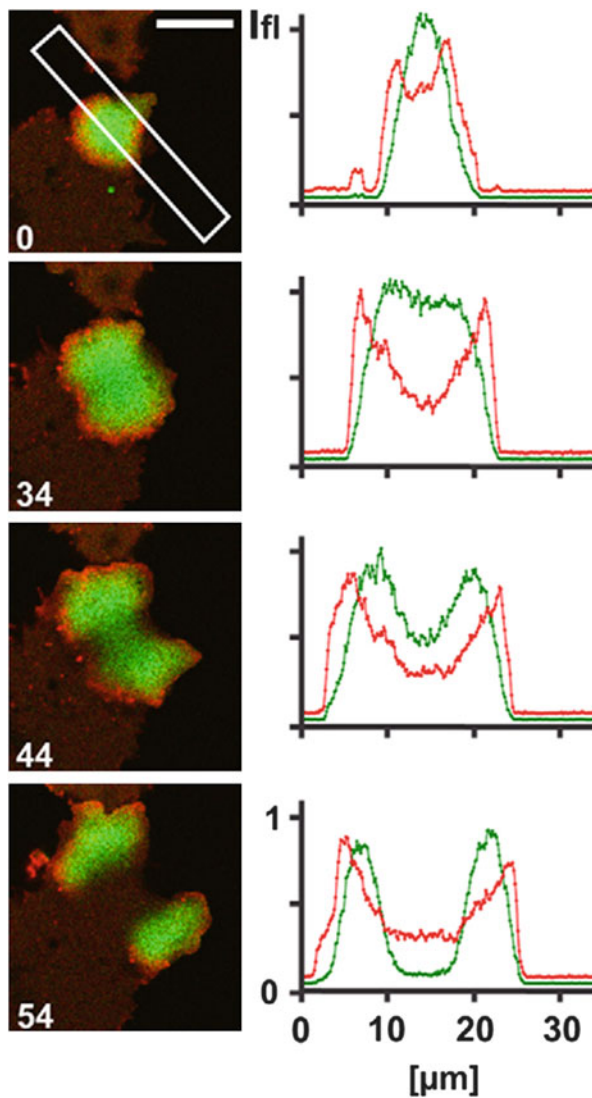


Fig. 2.1 Example of an expanding wave in *D. discoideum*. The cell was labeled for filamentous actin (red) and PIP3 (green). In the left panels subsequent snapshots are presented. In the corresponding right panels, scans of fluorescence intensities (I_{fi}) are displayed. Positions of the line scans are indicated in the first image. Taken from [23]

between membrane curvature and actin dynamics [28, 49, 62]. Various cell types spreading on planar substrates show contraction and lateral waves at their leading edge [9, 13, 26, 39], which may be due to similar mechanisms as circular dorsal ruffles.

In summary, spontaneous actin waves appear to be a widespread phenomenon in (adherent) eukaryotic cells. The molecular mechanisms leading to these waves as well as their possible functional roles remain to be understood. In the following, we will present some theoretical efforts that have been undertaken to explore possible mechanisms of wave formation and the effects of these waves on cellular shape changes.

2.3 Theoretical Descriptions of Cellular Actin Dynamics

As briefly reviewed in the previous section, different kinds of actin waves have been reported. Some involve the assembly of actin filaments, others are contraction waves. In this section, theoretical tools for describing actin dynamics will be presented. First, actin assembly will be discussed, then possible mechanisms underlying spontaneous actin polymerization waves.

2.3.1 *Actin Polymerization*

Before describing different approaches to collective actin dynamics, some words on the assembly of actin filaments are in order. Actin filaments are formed by non-covalent binding of actin monomers, also called globular actin or G-actin [1]. These monomers arrange into two protofilaments that form a double helix of about 8 nm in diameter. Actin filaments have two structurally distinct ends, respectively, denoted as barbed and pointed ends, that have their origin in the anisotropy of G-actin. This structural difference is accompanied by kinetic differences as the dynamics of G-actin exchange at the barbed end is faster than at the pointed end. This kinetics is further influenced by the nucleotide bound to an actin monomer. In general, the affinity of an actin monomer for binding to the filament is higher when it is bound to adenosine-tri-phosphate (ATP) than when it is bound to adenosine-di-phosphate (ADP) and inorganic phosphate (P_i) or to ADP alone. In this way a difference in the chemical potentials of ATP and its hydrolysis products ADP and P_i drives the assembly of actin filaments and keeps the system out of thermodynamic equilibrium.

The combination of kinetic polarity and coupling to ATP results in an actin assembly dynamics that is distinct from the assembly kinetics of commonly studied polymers. In particular, it can show treadmilling, where the filament grows at the barbed end and shrinks at the pointed end [71]. This phenomenon occurs when, on one hand, the attachment rate of G-actin bound to ATP is faster than its dissociation rate and also faster than the combined rates of ATP hydrolysis, release of P_i , and the dissociation of G-actin bound to ADP- P_i or ADP. Under these conditions, predominantly ATP-G-actin is added to barbed ends. ATP bound to an actin monomer in a filament hydrolyzes at a rate of 0.5 s^{-1} . Consequently, with increasing filament length, the probability increases to find at the pointed

end actin monomers that are bound to ADP- P_i or ADP. The corresponding rate of detachment from the filament is larger than the attachment rate of actin monomers to the pointed end. In this way, the filament will on average shrink at the pointed end. A detailed analysis of this mechanism has shown that treadmilling can in principle even generate a finite typical filament length, implying that growth at the barbed and disassembly at the pointed end occur, on average, at the same rate [20]. For rates measured in vitro, however, actin filaments will rather exhibit an exponential length distribution.

A simple way to describe the dynamics of the average filament length ℓ is the following. Let $v_p = ar_p$ denote the filament's growth velocity at the barbed end, where a is the length added to the filament by attachment of an actin monomer and r_p the corresponding rate. Let furthermore denote $v_d = ar_d(\ell)$ the shrinkage velocity at the pointed end, where $r_d(\ell)$ is the corresponding effective actin-monomer removal rate. The latter is an average of the ATP-, ADP- P_i -, and ADP-actin-monomer removal rates which effectively depends on the filament length, because essentially only ATP-actin monomers are added to the barbed end. Consequently,

$$\dot{\ell} = v_p - v_d(\ell). \quad (2.1)$$

For known $v_d(\ell)$, the average filament length can be calculated. More effort has to be invested if the whole length distribution should be computed.

Growth of a filament requires the presence of a nucleus that consists of three actin monomers. Only after its formation further assembly proceeds along the lines sketched above. Such nuclei rarely form spontaneously at physiological conditions. In cells the generation of new filaments is assisted by special cytoskeletal proteins [51]. For example, members of the formin family can assemble nuclei of actin filaments de novo. When activated these proteins typically reside at the plasma membrane. Another important factor for filament nucleation is the actin related protein (Arp) complex 2/3. It binds at the sides of existing filaments and can induce the branching of a new filament from the mother filament. The Arp2/3 complex is part of a larger complex, the Scar/WAVE complex, containing associated proteins that are necessary for activating the nucleator [66].¹ Contrary to formin, Arp 2/3 is associated with the filaments' pointed ends and protects them from shrinkage. Formins instead stay bound to the growing barbed ends and accelerate subunit addition. There are other examples of cytoskeletal proteins that can promote or inhibit the addition or removal of actin monomers at either filament end. Filaments can also be severed, but we refrain from a detailed discussion of these processes, because their role for the spontaneous emergence of actin waves is largely unknown.

¹The Wiskott-Aldrich syndrome protein (WASP) family is identified as the major regulators of the Arp2/3 complex. The WASP family consists of two principal classes of protein: WASP and SCAR/WAVE. WAVE was discovered by homology with WASP, but in mammalian cells WAVE is now more commonly used. SCAR is mostly used for the Dictyostelium protein and its mammalian homologues.

2.3.2 Mechanisms for Generating Spontaneous Actin Waves

After having presented basic features of actin assembly, we will now discuss several possible mechanisms underlying spontaneous cytoskeletal waves. One can broadly distinguish between waves that rely on transport or stresses generated by molecular motors and waves that emerge in the absence of motors. The corresponding mechanisms have been studied on different levels starting from rather molecular descriptions up to purely phenomenological theories.

2.3.2.1 Polymerization Waves in the Absence of Motors

We will start our discussion of possible mechanisms underlying spontaneous actin polymerization waves by exploring the consequences of actin treadmilling [14, 15]. This mechanism was introduced using a mean-field approach, where filaments are assumed to be rigid rods. The state of the system is given by the distribution c of filament barbed ends that depends on the position \mathbf{r} in space, the orientation of the filaments, which is given by a unit vector $\hat{\mathbf{u}}$ that points into the direction of the filament's barbed end, and the filament length ℓ , $c \equiv c(\mathbf{r}, \hat{\mathbf{u}}, \ell)$. In view of the discussion presented above, the length of a filament changes by net polymerization at the barbed and by net depolymerization at the pointed end. The respective growth and shrinkage velocities are v_p and v_d , where the depolymerization velocity in general depends on the filament length, $v_d \equiv v_d(\ell)$. Filaments nucleate only in the presence of nucleation promoting factors (NPFs) or “nucleators” for short. As a filament grows, the position of the barbed end will change. The dynamic equations for the density of barbed ends then reads [14]

$$\partial_t c = D \Delta c - \nabla \cdot v_p \hat{\mathbf{u}} c - \partial_\ell (v_p - v_d(\ell)) c. \quad (2.2)$$

The second term describes convection in real space due to filament growth, the last term convection in length space due to filament assembly and disassembly corresponding to Eq. (2.1). The diffusion term with the effective diffusion constant D has been introduced to account for fluctuations and to yield smooth densities. A corresponding term could be introduced also for the length dynamics, but it turns out that it does not have a qualitative effect on the system's behavior as long as it is not too big.

For simplicity, one may want to neglect the length-dependency of the depolymerization velocity v_d . There are two ways to generate in this case an exponential length distribution: in the case $v_p > v_d$, an effective degradation term $-k_{dc}$ prevents unlimited growth of the filaments. The degradation term resembles the effects of catastrophes observed for microtubules as well as very fast depolymerization that has been reported for actin under certain circumstances. Such a term is also generated if one includes a linear term in the length dependence of v_d . In the opposite case, $v_p < v_d$, a diffusion term $D_f \partial_\ell^2 c$ yields filaments of finite length. Below, we will focus on the case $v_p > v_d$ and use an effective degradation term $-k_{dc}$.

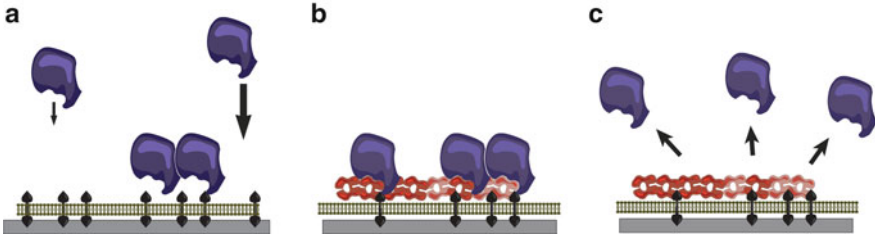


Fig. 2.2 Illustration of nucleator dynamics. (a) Nucleators (blue) exist in an active state on the membrane that is connected to the substrate (grey) by adhesion molecules (black). Inactive nucleators bind cooperatively to the membrane and thus become activated. (b) Active nucleators generate new actin filaments (red). (c) Actin filaments feed back on the nucleators and inactivate them

The nucleation of filaments is captured by the boundary condition on the current in length space at $\ell = 0$, $(v_p - v_d(\ell)) c|_{\ell=0} = \nu n_a$, where n_a is the density of active nucleators, see below, and ν the corresponding nucleation rate.

It remains to fix the dynamics of the nucleators, see Fig. 2.2. Their dynamics has been studied less than the dynamics of actin filaments. For simplicity, nucleators are assumed to exist in two different states, an active and an inactive one. In the present example, rather than the assembly dynamics of actin itself, it is the dynamics of nucleator activation and inactivation, which eventually generates the actin waves. To this end nucleators are assumed to be activated cooperatively. Although there does not seem to exist direct experimental evidence for such a process, one can easily imagine that the assembly of some parts of a nucleator complex promotes the assembly of further components of this complex and others. In addition to cooperative nucleator assembly there is a negative feedback by filaments that tend to inactivate nucleators. The dynamic equations read [15]

$$\partial_t n_a = D_a \Delta n_a + \omega_a (1 + \omega_0 n_a^2) n_i - \omega_i T n_a \quad (2.3)$$

$$\partial_t n_i = D_i \Delta n_i - \omega_a (1 + \omega_0 n_a^2) n_i + \omega_i T n_a. \quad (2.4)$$

Here, D_a and D_i are the diffusion constants of active and inactive nucleators, where $D_a \ll D_i$. The activation and inactivation rates are ω_a and ω_i , respectively, whereas ω_0 measures the cooperativity of nucleator activation. The total filament concentration at \mathbf{r} is given by $T(\mathbf{r}) = \int d\hat{\mathbf{u}} \int_0^\infty d\ell \int_0^\ell d\xi c(\mathbf{r} - \xi \hat{\mathbf{u}}, \hat{\mathbf{u}}, \ell)$ and figures in the rate of nucleator inactivation.

Numerical integration of the dynamic equations in one or two spatial dimensions shows that the system can spontaneously generate traveling waves. For a detailed analysis, dynamic equations (2.2)–(2.4) are not well suited. Furthermore, they account for some molecular details that, after all, might not be relevant for the macroscopic dynamics. One way to deal with both of these problems is to coarse-grain the system and to restrict attention to only the first modes in orientation space [16, 18]. Explicitly, one might focus attention on the total filament density

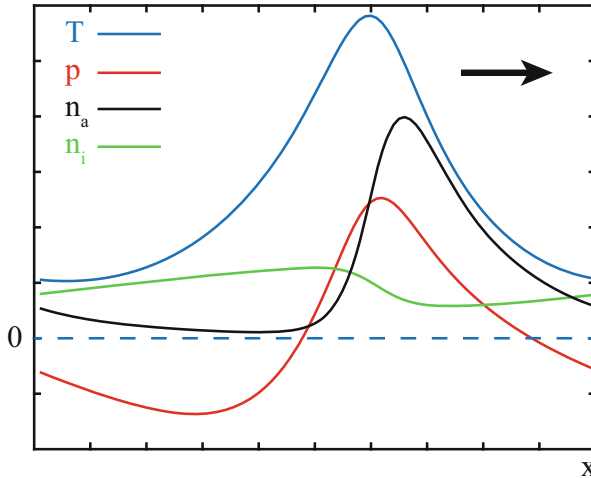


Fig. 2.3 Illustration of wave solution to Eqs. (2.3)–(2.6) propagating at constant speed. Shown are the actin density T (blue), the polarization field p (red), and the densities n_a of active (black) and n_i of inactive nucleators (green) in arbitrary units. The arrow indicates the direction of motion

T and the average filament orientation \mathbf{p} . Alternatively, purely phenomenological equations can be written for the cytoskeletal part of the system. Restricting attention to the dynamics fields T and \mathbf{p} and expanding the dynamics of the two fields up to linear order in terms of T , \mathbf{p} , and n_a and keeping only derivatives up to second order one obtains

$$\partial_t T = D \Delta T - k_d T - v_a \nabla \cdot \mathbf{p} + \nu n_a \quad (2.5)$$

$$\partial_t \mathbf{p} = D \Delta \mathbf{p} - k_d \mathbf{p} - v_a \nabla T. \quad (2.6)$$

The phenomenological constants in front of the various terms, D , v_a , k_d , and ν , have been given the values that result from coarse-graining equation (2.2).

This dynamic system spontaneously produces traveling waves similar to those of Eqs. (2.2)–(2.4). In Fig. 2.3, we present the profile of such a wave in one spatial dimension. Intuitively, the waves are maintained through the following process: filaments inactivate nucleators. These diffuse and are preferentially re-activated in a region around already activated nucleators. Nucleators that became activated ahead of the actin front have a longer live time than those activated behind the front. In this way the region of activated nucleators moves forward and consequently also the actin front. This mechanism suggests that the wave speed v_{wave} depends only weakly on the filament assembly velocity v_a , which is indeed the case. Rather it is set by a combination of the activation and inactivation rate, the amount of nucleators and their diffusion constant. Scaling suggests that $v_{\text{wave}} \sim D_i/\Omega_a$, where Ω_a is an effective activation rate that scales like $\omega_a(1 + \omega_0 N_a^2)$. Here, the amount of activated nucleators N_a grows with the total number of nucleators.

In two spatial dimensions the phase diagram is somewhat richer. In addition to traveling waves also spiral waves exist. Furthermore, spiral chaos can be observed.

Note, that for large values of k_d , the polarization field \mathbf{p} relaxes quickly. Since the diffusion constant D is expected to be small, the polarization field is essentially given by the gradient of the actin density, $\mathbf{p} \simeq v_a \nabla T / k_d$. This notably shows that maxima in the actin density should be associated with singularities of the polarization field, which is indeed displayed by the solutions to the dynamic equations.

It is instructive to analyze dynamic equations (2.3)–(2.6) in the homogeneous case, where all spatial derivatives vanish. In that case $\mathbf{p} \rightarrow 0$ and

$$\dot{n}_a = \omega_a (1 + \omega_0 n_a^2) (N - n_a) - \omega_i T n_a \quad (2.7)$$

$$\dot{T} = v n_a - k_d T, \quad (2.8)$$

where N denotes the total density of nucleators. These equations are very similar to that of the FitzHugh–Nagumo model, which is the paradigmatic example of an excitable system exhibiting traveling waves.

In [73], the authors took the similarity of the actin dynamics to an excitable medium as starting point and proposed a phenomenological approach by extending the FitzHugh–Nagumo model to space and by introducing an additional orientational field. In contrast to the above dynamics, the orientational field is not enslaved by the actin dynamics but has a proper internal dynamics. Explicitly, the model assumes the form

$$\partial_t T = \Delta T + v_a \nabla \cdot \mathbf{p} T - \omega T (T - T_1)(T - T_0) - k_d v + \sqrt{2T_T} \eta \quad (2.9)$$

$$\partial_t v = D_v \Delta v + \epsilon (T - v) \quad (2.10)$$

$$\partial_t \mathbf{p} = -\mathbf{h}_0 + T \mathbf{p} - p^2 \mathbf{p} + D \Delta \mathbf{p} - \alpha \nabla \times \nabla \times \mathbf{p} + \sqrt{2T_p} \xi. \quad (2.11)$$

The term proportional to α describes the effects of a finite bending energy of the actin filaments. The term proportional to k_d shows that T is not necessarily positive. Thus, one has to interpret T as the deviation from a reference state. The new field v describes the effects of some agent that degrades actin filaments. The quantities η and ξ both depend on space and time and represent Gaussian white noise with zero mean and unit variance. The amplitude of the noise terms is determined by the “effective temperatures” T_T and T_p that can differ.

In absence of noise, the homogeneous isotropic distribution is a stable stationary state of these dynamic equations. However, in some regions of parameter space, the system admits spatially localized heterogeneous solutions (“spots”). These spots can be unstable against perturbations of the polarization field. Under these conditions, the spots start to travel, may broaden with time, eventually leading to traveling waves. Traveling spots perform a persistent random walk due to the additive noise present in the dynamic equations.

Although the additive noise terms in the above equations are convenient for the analysis, a consistent treatment of fluctuations would lead to multiplicative noise.

For this reason stochastic simulations have been performed for spatially resolved actin assembly dynamics [11, 72]. The system introduced by Carlsson [11] provides a rather detailed description of the assembly dynamics of actin in three dimensions. It shows the emergence of spots that can spontaneously start to travel and transform into waves.

2.3.2.2 Cytoskeletal Waves in Presence of Motors

Molecular motors can generate stresses in the actin network and transport cargo along existing filaments. In both cases, the motors can lead to the emergence of cytoskeletal waves.

Motor-Induced Stresses

Waves resulting from the interplay of stress generating motors and a factor regulating motor-induced mechanical stresses are conveniently studied in a hydrodynamic approach for active gels [5, 55, 56]. This phenomenological approach is essentially built on conservation laws and the symmetries of the system [34] and has been applied to various cell biological problems [54]. In this approach, the stresses are coupled to motor dynamics by an “active” contribution to the stress that is proportional to the difference $\Delta\mu$ in the chemical potentials of ATP, ADP, and P_i , which drives the hydrolysis of ATP. On large time scales the gel behaves like a fluid and we will neglect elastic contributions in the following. For an isotropic fluid, this leads to an expression of the stress σ of the form [34]

$$\sigma = 2\eta\nabla\mathbf{v} + \zeta\Delta\mu, \quad (2.12)$$

where \mathbf{v} is the fluid velocity, η its shear viscosity, and ζ a phenomenological coupling constant between $\Delta\mu$ and the active stress. Its value is a priori unknown and has to be obtained from measurements or derived from molecular theories. Because the system operates at low Reynolds number, the dynamic equation for the fluid is then given by force balance

$$\gamma\mathbf{v} = \nabla \cdot \sigma. \quad (2.13)$$

Here, γ is an effective friction coefficient quantifying the dissipation as the actin network moves with respect to the surrounding fluid.

As such, this system does not generate waves. However, if the active part of the stress, $\zeta\Delta\mu$, itself depends on a regulator with density c , then oscillatory states and traveling waves can be generated [5, 55]. In a biological context, this regulator could, for example, be formed by the second messenger Ca^{2+} . The dynamics of the regulator is given by the continuity equation

$$\partial_t c = D \Delta c - \nabla \cdot \mathbf{v} c \quad (2.14)$$

and various couplings of the regulator to the active stress can be considered. Beyond the linear theory, the regulator might itself be subject to a more complicated dynamics involving different regulator states (active/inactive) that evolve according to non-linear reaction diffusion dynamics [56]. Let us note that the traveling contraction waves observed for muscle fibers can be described by very similar equations [29]. However, there, the role of the regulator is taken by an intrinsic activation/inactivation dynamics of the molecular motors.

In such systems, traveling and standing waves have been reported [5, 55, 56]. Interestingly, the traveling waves can be reflected at system boundaries [55]. In a two-dimensional circular domain the generated waves are reminiscent of patterns found in protoplasmic droplets of *P. polycephalum*. Whether these waves can be employed in the context of cell locomotion has not yet been studied.

Motor-Induced Transport

The effect of motor-induced transport of nucleators along filaments have been studied in a framework similar to Eqs. (2.2)–(2.4) [14]. Only active nucleators are considered and the corresponding continuity equation now reads

$$\partial_t n_a = D_m \Delta n_a - \nabla \cdot v_m \mathbf{p} n_a. \quad (2.15)$$

Here, v_m denotes the motor velocity. This equation is complemented by Eq. 2.2. This system can generate traveling waves for which the polarization field and the actin density resemble the profile shown in Fig. 2.3 [16].

The underlying mechanism is most easily understood in the case $D_m = 0$ and when all nucleators are localized at \mathbf{r}_m , which depends on time [16]. Then, $n_a = N\delta(\mathbf{r} - \mathbf{r}_m(t))$ and $\dot{\mathbf{r}}_m = v_m \mathbf{p}(\mathbf{r}_m)$. The nucleators act as a source of actin filaments and this source is transported along existing actin filaments. The newly generated filaments generate tracks for further polymerization. Contrary to the polymerization waves in absence of motors, the wave velocity depends on the polymerization velocity, whereas its dependence on the motor velocity is less pronounced, see Fig. 2.4.

Summarizing this section, we have seen that the actin cytoskeleton is prone to wave instabilities. The instabilities result from the interaction with factors regulating the rate of filament assembly or the activity of molecular motors. At the time of writing this chapter, there does not seem to be an *in vitro* experimental system that has been characterized sufficiently to allow for an identification of the relevant molecular mechanisms of spontaneous waves in disordered cytoskeletal networks.

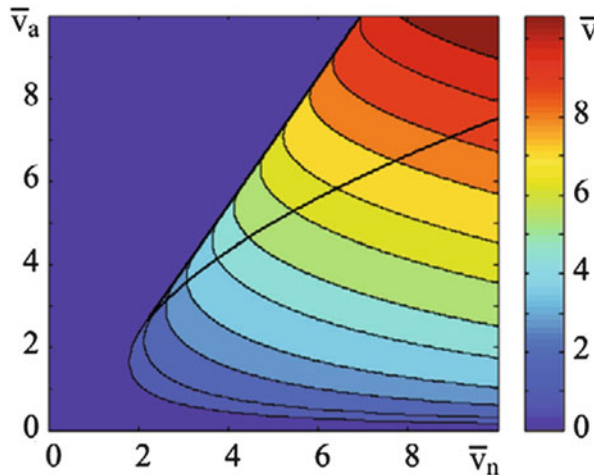


Fig. 2.4 Wave velocity vs nucleator velocity. Wave velocity v as a function of the nucleator velocity v_m and the assembly velocity v_a obtained for $D_m = 0$. The bars indicate that velocities have been de-dimensionalized by $(D/k_d)^{1/2}$. The black line delimits the region of coexistence of the stable homogeneous state and traveling waves. Taken from [16]

2.3.3 Coupling Actin Dynamics to the Membrane

In the context of cell migration, several approaches have been suggested to study the dynamics of the actin cytoskeleton confined by a lipid membrane. To this end, one first has to decide which aspects of the physical properties of the membrane should be accounted for. Notably, the plasma membrane is endowed with a surface tension. Also its bending rigidity can be important. In addition to the membrane properties, the interaction between the membrane and the cytoskeleton has to be specified. This interaction can be purely mechanical, but can also include regulatory elements. For example, the membrane can carry regulators of actin nucleation or growth.

Once these decisions are made, there are several techniques available to implement the physical properties of the membrane and the membrane–cytoskeleton interaction into a theory. As above, we will restrict our discussion to deterministic continuum approaches. On one hand, the membrane can be described as a sharp boundary. The coupling to the cytoskeleton is then captured by appropriate boundary conditions. Alternatively, one can associate with the boundary a potential describing the interactions between the cytoskeleton and the membrane. On the other hand, sharp boundaries can be circumvented by using phase fields or level set methods, for example, see Chaps. 1 and 3 of this book.

2.3.3.1 Sharp Boundary Methods

Let Γ denote the boundary of the cell and Ω the cell interior, such that $\partial\Omega = \Gamma$. In general, both quantities depend on time. One can introduce an energy \mathcal{F} associated with this boundary. Explicitly,

$$\mathcal{F} = \int_{\Gamma} d\mathbf{r} \kappa H^2 / 2 + \tau \Gamma + P\Omega, \quad (2.16)$$

where κ is the bending rigidity, H the mean curvature of Γ , τ the surface tension, P the difference between external and internal pressure, and Ω the volume enclosed by Γ .

For the kinetic approaches discussed above, where the filament length is kept as a dynamic quantity, it is rather cumbersome to account for the membrane–filament interactions through boundary conditions. Instead, an interaction potential has been introduced [17]. The corresponding contribution to the energy \mathcal{F} is

$$\int_{\Omega} d\mathbf{r} V(\mathbf{r}, \Gamma) c_{\text{tot}}^+(\mathbf{r}). \quad (2.17)$$

In this expression $c_{\text{tot}}^+(\mathbf{r}) = \int_0^\infty d\ell \int d\hat{\mathbf{u}} c(\mathbf{r}, \hat{\mathbf{u}}, \ell)$ is the total local density of the barbed ends at \mathbf{r} . It remains to fix the potential V . In the simplest case, V depends only on the (signed) distance d of a filament's barbed end to the boundary, $d(\mathbf{r}) = \theta(\mathbf{r}) \min_{\mathbf{r}' \in \Gamma} \|\mathbf{r} - \mathbf{r}'\|$, where $\theta(\mathbf{r})$ is -1 or $+1$, respectively, for \mathbf{r} inside or outside of the cell domain Ω . The functional form of the potential is largely unimportant as long as it is nearly constant within the cell domain and rises towards the boundary. In the limit, where the potential is zero for $d < 0$ and infinite for $d > 0$, one recovers a perfectly reflecting boundary. A similar approach has been used in a study of the shape and size of stereocilia and microvilli [53].

The dynamics of the boundary is assumed to be purely dissipative, such that

$$\partial_t \Gamma = -\zeta \frac{\delta \mathcal{F}}{\delta \Gamma}, \quad (2.18)$$

where $\delta/\delta\Gamma$ denotes the functional derivative with respect to variations of the boundary Γ and ζ is an effective mobility. The filaments are confined to the interior of Ω by the force density $\mathbf{f}_b = -\nabla_{\mathbf{r}} V(\mathbf{r}, \Gamma)$. The effects of this force density are incorporated by adding to the dynamic equations the term $\eta \nabla_{\mathbf{r}} \cdot \mathbf{f}_b c$, where η is an effective filament mobility. For simplicity it is assumed here to be isotropic and independent of the filament length. This way of describing the interactions between the membrane and the cytoskeleton assures that the system is globally force free.

From a computational point of view, sharp boundaries are rather difficult to handle. Whereas the filament density takes values on a discrete lattice, the mesh points of the boundary are not restricted to the lattice. One thus has to constantly track which lattice points are within the boundary and the distance between the lattice points and the boundary needs to be calculated. Phase-field methods avoid this difficulty.

2.3.3.2 Phase-Field Methods

The general idea behind using phase-field methods in connection with cell motility [46, 60, 74] is to introduce an auxiliary field ψ that indicates the cell interior and exterior, see also the contribution by Löber et al. to this volume, Chap. 1. It varies continuously between 0 and 1, where $\psi \rightarrow 1$ in the interior and $\psi \rightarrow 0$ in the exterior. Similar to the dynamics of Γ , Eq. (2.18), the dynamics of the phase field is determined by an intrinsic part and by the interaction with the cytoskeleton [74],

$$\partial_t \psi = D_\psi \Delta \psi + f(\psi, \delta) - \beta \mathbf{p} \cdot \nabla \psi. \quad (2.19)$$

The first two terms can be derived from an energy. The value of D_ψ determines the width of the interface between the cell interior and exterior. Physically, it captures the effects of the surface tension. The zeros of f determine the pure phases, $\psi = 0$ and $\psi = 1$. Often a cubic expression is used for f . Let us set

$$f(\psi, \delta) = \kappa \psi (1 - \psi)(\psi - \delta). \quad (2.20)$$

Then, the phase field relaxes into the state $\psi = 0$ for an initial value $\psi_0 < \delta$ and into the state $\psi = 1$ in the opposite case. The parameter κ determines the time scale on which the phase field reaches these values. The value of δ determines the boundary between the respective basins of attraction. For $\delta > 0.5$ the phase field will spread, whereas it will retract in the opposite case. Setting its value to (see Chap. 1)

$$\delta = \frac{1}{2} + \epsilon \left(\int d^2 \mathbf{r} \psi(\mathbf{r}) - V_0 \right), \quad (2.21)$$

allows to maintain a constant cell area V_0 [74]. The parameter $\epsilon > 0$ gives the stiffness of the constraint. In principle, its value can depend on the membrane surface tension and elasticity. However, different values of ϵ essentially amount to rescaling V_0 and D_ψ , such that the exact value of ϵ is not important. The above formulation neglects effects of the membrane bending stiffness, but the phase-field formalism can be extended to account for these effects.

The third term in the right-hand side of Eq. (2.19) couples the phase field to the polymerization dynamics of actin filaments. In this form filaments pointing with their barbed end towards the cell boundary push the boundary further outwards, whereas filaments pointing with their pointed end towards the cell boundary pull it inwards. The strength of the coupling between the filaments and the membrane is determined by the value of β .

To confine the dynamics of the cytoskeleton and the nucleators to the cell interior, all reaction terms in the dynamic equations are multiplied by ψ [18]. Also the currents should in principle be multiplied by ψ to prevent currents through the interface. However, this often reduces the stability of the numerical schemes that are used to solve the dynamic equations. It turns out that for non-conserved quantities this often is not an issue, because the loss is small and because there is no

dynamics outside the boundary. The fields can simply be degraded through a term $-k_{\text{deg}}(1 - \psi)c$, where c is any non-conserved field of interest. For conserved fields, this method is obviously inappropriate. In this case one either needs to develop numerically stable schemes to confine the currents to the cell interior. An alternative is to re-introduce the total amount of matter that has left the domain [18]. In this case, one has to check, that this does not affect the system's qualitative behavior. This is usually the case when the amount transported across the boundary in a single time step is small.

Force Balance

Since the phase-field formulation does not explicitly involve forces, it is helpful to briefly discuss force balance in this context [18]. The filaments are assumed to exchange momentum with the environment by being tightly connected to the substrate. Close to the sharp interface limit, that is for D_ψ small. Surface tension induces a force density $\mathbf{f}_{\text{ten}} = \gamma H \mathbf{n}$, where H is the membrane curvature and \mathbf{n} denotes the outward normal $\mathbf{n} = -\nabla\phi/|\nabla\phi|$ [60]. Actin polymerization forces are given by $\mathbf{f}_{\text{pol}} = \xi\beta\mathbf{n}\mathbf{n} \cdot \mathbf{p}$, where ξ is an effective friction coefficient. The movement of the membrane at velocity \mathbf{v} leads to dissipative forces, such that force balance at the boundary reads

$$\xi\mathbf{v} = \mathbf{f}_{\text{ten}} + \mathbf{f}_{\text{pol}}. \quad (2.22)$$

The sum over all external forces acting on the cytoskeleton must vanish. Under the assumptions made above, we only consider the traction and membrane forces on actin. Explicitly, we have

$$\mathbf{F}_{\text{tract}} + \oint d\ell \mathbf{f}_{\text{mem}} = 0, \quad (2.23)$$

where the integral is along the membrane and $\mathbf{f}_{\text{mem}} = -\mathbf{f}_{\text{pol}} = \mathbf{f}_{\text{ten}} - \xi\mathbf{v}$. Let us emphasize that the traction forces are confined to the position of the membrane. Indeed, the slime mold *D. discoideum* does not form focal adhesions and traction forces are essentially restricted to the outer boundaries [36].

2.4 Wave-Driven Migration

In this section, we will describe the behavior of waves confined to cellular domains. For the boundary, we will focus on the phase-field approach Eqs. (2.19)–(2.21). When appropriate, we will compare the results to that obtained for the sharp boundary model Eqs. (2.16)–(2.18).

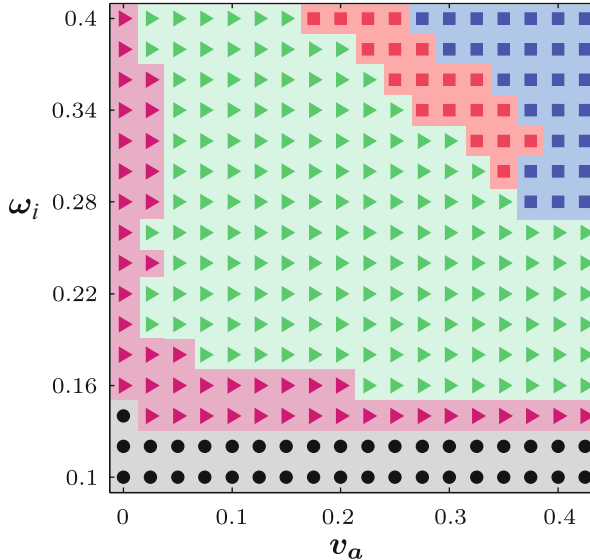


Fig. 2.5 Phase diagram. Phase diagram for the system defined by Eqs. (2.3)–(2.6) and (2.19)–(2.21) as a function of the dimensionless nucleator inactivation rate ω_i and the dimensionless actin polymerization velocity v_a . *Dots*: axially symmetric stationary states; *squares*: aperiodically appearing and vanishing blobs with (blue) and without (red) axial symmetry; *triangles*: stable (magenta) and unstable (green) spiral dynamics. Taken from [18]

2.4.1 Phase Diagram

Consider the system defined by Eqs. (2.3)–(2.6) and (2.19)–(2.21) in two dimensions, such that the dynamics is confined to the plane of the substrate. The reduction to two spatial dimensions is appropriate if the dynamics in the direction perpendicular to the substrate is irrelevant for the motion on the substrate. This is the case if the “cell” is flat as is the case for cell fragments [21, 32, 40].

The corresponding phase diagram as a function of the polymerization velocity v_a and the inactivation rate ω_i is presented in Fig. 2.5 [18]. The resulting patterns can be categorized into three broad classes: stationary patterns, spiral patterns, and axisymmetric patterns. Stationary patterns exist below a critical value of the inactivation rate ω_i that depends only weakly on the polymerization velocity v_a . They are circular symmetric with a radial polarization field, see Fig. 2.6a. The actin density decays from the center to the periphery.

The spiral patterns exist as long as ω_i is below a second critical value that decreases monotonically with increasing v_a . In these cases, the fields of the nucleators and the cytoskeleton self-organize either into stable or unstable spirals. For the stable spirals, the system’s center of mass does not move, but a perturbation propagates along the contour, see Fig. 2.6b. Such a state has also been reported in the sharp boundary case, where the perturbation was stronger than for the phase-field

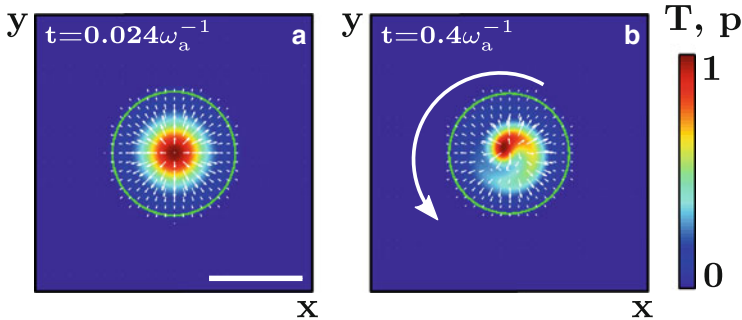


Fig. 2.6 States with no net center-of-mass motion. **(a)** Stationary state. **(b)** Stable rotating spiral. Actin density T is color coded, *arrows* indicate the polarization field \mathbf{p} . *Green line* indicates the cell boundary. Scale bar: 0.19λ . See also videos ch2_video1.mpg and ch2_video2.mpg. Modified from [18]

model [17]. These states are similar to protrusions that travel along the edge of spreading fibroblasts [9, 13, 39]. However, these waves are probably associated with the action of molecular motors. A mechanism for these waves involving an interplay between filament assembly and molecular motors waves was proposed in [25]. In that work, lateral waves are a consequence of the dynamics at the membrane, rather than a result of the bulk dynamics as in the present case. In addition, it has been proposed that membrane curvature might be involved in the wave-generating mechanism [49, 62].

For unstable spirals, actin forms blobs close to the cell's center and then spiral out to the periphery. At the periphery the spirals either dissolve and a new blob is subsequently generated in the cell center or they can get reflected. The migration patterns resulting from unstable spirals will be discussed below.

Beyond another critical value of ω_i that again decreases monotonically with increasing v_a , the cytoskeletal blobs are no longer reflected at the boundary, but always dissolve and then reform in the cell center. Again, two cases can be distinguished: blobs with and without reflectional symmetry. We will now discuss the associated migration patterns.

2.4.2 Persistent Migration Patterns

In the case, when the internal cytoskeletal dynamics is such that actin blobs are nucleated in the cell center and dissolve at the boundary without being reflected, the associated migration patterns are regular. In the simplest case, cells move along a straight line. However, since the actin blobs periodically appear and disappear, the cellular velocity also varies periodically, see Fig. 2.7. Migration with constant velocity \mathbf{v} has been obtained in the sharp boundary case [17]. In that case, all densities are of the form $c(\mathbf{r}, t) \equiv c(\mathbf{r} - \mathbf{v}t)$. Such a motion has been observed

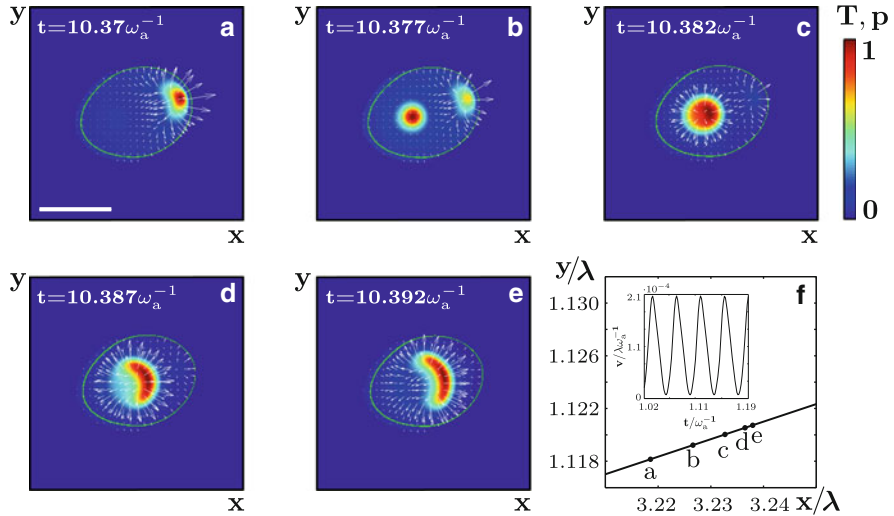


Fig. 2.7 Persistently moving (gliding) solution to Eqs. (2.3)–(2.6) and (2.19)–(2.21). (a)–(e) Subsequent snapshots of the actin density T and the polarization field \mathbf{p} . (f) Corresponding trajectory of the phase field's center of mass. Letters indicate its position at the times corresponding to panels (a)–(e). Inset: absolute value of the cell velocity as a function of time. Scale bar: 0.19λ . See also video ch2_video3.mpg. Taken from [18]

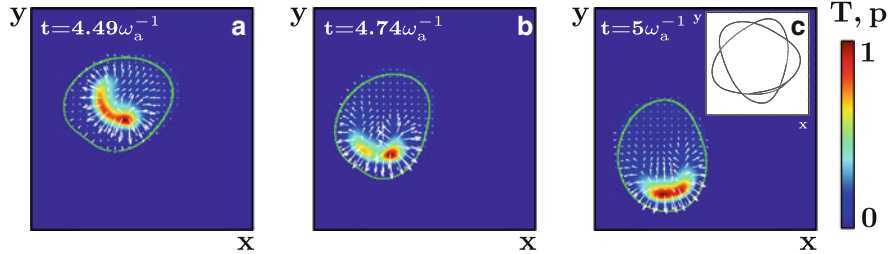


Fig. 2.8 Persistent motion generated by a blob lacking reflection symmetry. (a)–(c) Subsequent snapshot of the actin density T and the polarization field \mathbf{p} . Inset: center-of-mass trajectory. See video ch2_video4.mpg. Adapted from [18]

for fragments of fish keratocytes and of neutrophils [21, 32, 40]. Straight crawling but with periodic variations of the speed has been observed for the slime mold *D. discoideum* and in neutrophils [41, 61]. The detailed conditions for migration with constant or varying speed remain to be explored.

For blobs lacking a reflection symmetry, the center of mass is confined to a finite region on the substrate. The trajectory, it describes, is reminiscent of a Lissajous figure, see Fig. 2.8. The two inherent dominant frequencies of the trajectory result from the blob moving along the cell periphery and its roughly periodic breaking up and reformation.

2.4.3 Erratic Migration Patterns

Let us now turn to the migration pattern that is associated with unstable spirals. In the case a spiral becomes reflected from the cell boundary, it propagates to the opposite end of the cell. During reflection, it can change its handedness. In fact, the dynamics of the spirals appears to be intermittent: for some time intervals, the dynamics is regular with spirals being generated in the center and dissolving at the boundary, whereas during other intervals, spirals are frequently reflected. In the former case, the center of mass advances on arcs similar to the dynamics observed for the persistent migration pattern discussed above. Phases during which spirals become frequently reflected are associated with rather abrupt changes of the migration direction. Sometimes also the handedness of the trajectory before and after such a phase changes. In fact, a detailed analysis shows that the chiralities of subsequent arcs are uncorrelated. In combination, these two features can leads to apparently erratic migration patterns with the characteristic of a persistent random walk, see Fig. 2.9.

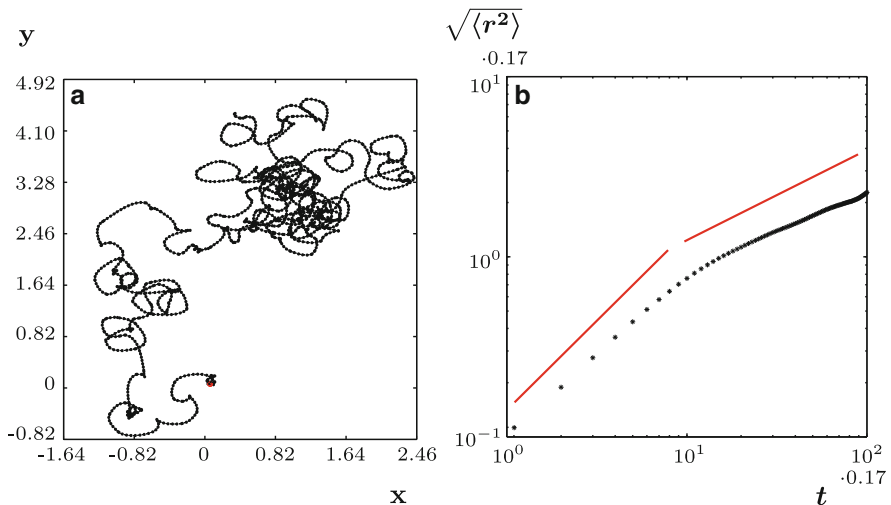


Fig. 2.9 Irregularly moving solution to Eqs. (2.3)–(2.6) and (2.19)–(2.21). **(a)** Trajectory of the center of mass of ψ . **(b)** Root mean squared displacement for the trajectory shown in **(a)**. Red lines indicate slopes 1 and 1/2. See video ch2_video5.mpg. Taken from [18]

2.5 Conclusions

The above discussion has shown that spontaneous actin waves are a common motif of cytoskeletal patterns and can be exploited by cells to drive migration. Various mechanisms underlying these waves have been studied from a theoretic point of view and probably others will be discovered in the future. A most pressing task is now to obtain further experimental data that allow to assess the relative importance of the various processes that have been considered in the theoretical works. The ultimate test for the proposed mechanisms is probably the reconstitution in vitro of traveling actin waves—a most daunting task.

From the theoretical side, further efforts are needed to study possible roles of contraction waves for cell migration. Also, the restriction to two spatial dimensions should be released. First studies in this direction have been performed [46]. These studies will be in particular important if one wants to study the importance of self-organized waves for migration in topographically structured environments and probably also for investigating cell ensembles. In a joined theoretical and experimental effort further measures have to be identified that will allow us to quantitatively compare data obtained from both approaches.

Out of the migration patterns presented above, the erratic migration patterns are probably the most intriguing ones. These results show that amoeboid motion can be the result of deterministic cytoskeletal processes. This motion has to be distinguished from the cases where the (sub)diffusive migration on large time scales results from extrinsic or molecular noise. Here, extrinsic noise refers to perturbations, for example, from interaction with other particles or fluctuating concentrations of chemical attractants or repellents. On the other hand, molecular noise results from the inherently stochastic dynamics of chemical reactions. Both sources of noise have in common that cells cannot control them. This is different for deterministic cytoskeletal processes, which can be regulated, for example, by changing the abundance of involved molecules or by modifying their properties through phosphorylation or other post-translational modifications.

Why would be the advantage for a cell to control its erratic migration? Whenever cells migrate in a gradient, be it chemical or physical, it is usually beneficial to move as accurately as possible up or down the gradient as it indicates an environment that promises to be richer in nutrients or threatens to be hazardous to them. In other cases, cells search for targets without external cues that could guide their migration. This strategy holds for some cells of the immune system that patrolling the body for pathogenic cells, for soil amoeba in nutrient depleted environments, or for metastatic cancer cells searching for new environments to settle. Depending on external conditions, different search strategies may differ in their efficiency. In constrained environments the persistence of random walks affects the mean search time. A detailed study of the dependence of the migration properties on parameters controlling cytoskeletal dynamics remains to be done. Also thorough experiments on the connection between search strategies and cytoskeletal dynamics are currently missing.

Looking even further into the future it will be interesting to see if and possibly how the cells use the multitude of patterns the cytoskeleton can spontaneously generate to respond to external stimuli and thus generate appropriate cell behavior. Any insight into such processes may be of relevance well beyond the fascinating process of cell migration.

2.6 Supplementary Movies

1. **Spiral I** (ch2_video1.mpg). The movie shows one-arm spiral solution, see Fig. 2.6.
2. **Spiral II** (ch2_video2.mpg). The movie shows well-developed spiral solution in larger cell, see Fig. 2.6.
3. **Gliding state** (ch2_video3.mpg). The movie shows acting dynamics and position of the center of mass in a persistently moving (gliding) cell, see Fig. 2.7.
4. **Persistent blob dynamics** (ch2_video4.mpg). The movie shows persistent dynamics of non-symmetric blob, see Fig. 2.8.
5. **Erratic motion** (ch2_video5.mpg). The movie shows erratic (run-and-tumble) states with spiral instability, see Fig. 2.9.

Acknowledgements I thank my past and current collaborators, notably, I.S. Aranson, K. Doubrovinski, A. Dreher, and C. Erlenkamper, for countless interesting discussions on actin waves and cell motility. The work was funded in part by SFB 1027 of Deutsche Forschungsgemeinschaft.

References

1. B. Alberts, A. Johnson, J. Lewis, M. Raff, K. Roberts, P. Walter, *Molecular Biology of The Cell*, 5th edn. (Garland Science, New York, 2008)
2. F. Backouche, L. Haviv, D. Groswasser, A. Bernheim-Groswasser, Active gels: dynamics of patterning and self-organization. *Phys. Biol.* **3**, 264–273 (2006)
3. A. Bernheim-Groswasser, S. Wiesner, R.M. Golsteyn, M.-F. Carlier, C. Sykes, The dynamics of actin-based motility depend on surface parameters. *Nature* **417**, 308–311 (2002)
4. E. Bernitt, C.G. Koh, N. Gov, H.-G. Döbereiner, Dynamics of actin waves on patterned substrates: a quantitative analysis of circular dorsal ruffles. *PLoS One* **10**, e0115857 (2015)
5. J.S. Bois, F. Julicher, S.W. Grill, Pattern formation in active fluids. *Phys. Rev. Lett.* **106**, 028103 (2011)
6. M. Bonny, E. Fischer-Friedrich, M. Loose, P. Schwille, K. Kruse, Membrane binding of MinE allows for a comprehensive description of min-protein pattern formation. *PLoS Comput. Biol.* **9**, e1003347 (2013)
7. T. Bretschneider, S. Diez, K. Anderson, J. Heuser, M. Clarke, A. Muller-Taubenberger, J. Kohler, G. Gerisch, Dynamic actin patterns and Arp2/3 assembly at the substrate-attached surface of motile cells. *Curr. Biol.* **14**, 1–10 (2004)

8. T. Bretschneider, K. Anderson, M. Ecke, A. Mueller-Taubenberger, B. Schroth-Diez, H.C. Ishikawa-Ankerhold, G. Gerisch, The three-dimensional dynamics of actin waves, a model of cytoskeletal self-organization. *Biophys. J.* **96**, 2888–2900 (2009)
9. D.T. Burnette, S. Manley, P. Sengupta, R. Sougrat, M.W. Davidson, B. Kachar, J. Lippincott-Schwartz, A role for actin arcs in the leading-edge advance of migrating cells. *Nat. Cell Biol.* **13**, 371–382 (2011)
10. L.A. Cameron, M.J. Footer, A. van Oudenaarden, J.A. Theriot, Motility of ActA protein-coated microspheres driven by actin polymerization. *Proc. Natl. Acad. Sci. U.S.A.* **96**, 4908–4913 (1999)
11. A.E. Carlsson, Dendritic actin filament nucleation causes traveling waves and patches. *Phys. Rev. Lett.* **104**, 228102 (2010)
12. L.B. Case, C. Waterman, Adhesive F-actin waves: a novel integrin-mediated adhesion complex coupled to ventral actin polymerization. *PLoS One* **6**, e26631 (2011)
13. H.-G. Doeberleiner, B.J. Dubin-Thaler, J.M. Hofman, H.S. Xenias, T.N. Sims, G. Giannone, M.L. Dustin, C.H. Wiggins, M.P. Sheetz, Lateral membrane waves constitute a universal dynamic pattern of motile cells. *Phys. Rev. Lett.* **97**, 038102 (2006)
14. K. Doubrovinski, K. Kruse, Self-organization of treadmilling filaments. *Phys. Rev. Lett.* **99**, 228104 (2007)
15. K. Doubrovinski, K. Kruse, Cytoskeletal waves in the absence of molecular motors. *Europhys. Lett.* **83**, 18003 (2008)
16. K. Doubrovinski, K. Kruse, Self-organization in systems of treadmilling filaments. *Eur. Phys. J. E* **31**, 95–104 (2010)
17. K. Doubrovinski, K. Kruse, Cell motility resulting from spontaneous polymerization waves. *Phys. Rev. Lett.* **107**, 258103 (2011)
18. A. Dreher, I.S. Aranson, K. Kruse, Spiral actin-polymerization waves can generate amoeboidal cell crawling. *New J. Phys.* **16**, 055007 (2014)
19. M.K. Driscoll, X. Sun, C. Guven, J.T. Fourkas, W. Losert, Cellular contact guidance through dynamic sensing of nanotopography. *ACS Nano* **8**, 3546–3555 (2014)
20. C. Erlenkämper, K. Kruse, Treadmilling and length distributions of active polar filaments. *J. Chem. Phys.* **139**, 164907 (2013)
21. U. Euteneuer, M. Schliwa, Persistent, directional motility of cells and cytoplasmic fragments in the absence of microtubules. *Nature* **310**, 58–61 (1984)
22. F. Gerbal, P. Chaikin, Y. Rabin, J. Prost, An elastic analysis of *Listeria monocytogenes* propulsion. *Biophys. J.* **79**, 2259–2275 (2000)
23. M. Gerhardt, M. Ecke, M. Walz, A. Stengl, C. Beta, G. Gerisch, Actin and PIP3 waves in giant cells reveal the inherent length scale of an excited state. *J. Cell Sci.* **127**, 4507–4517 (2014)
24. G. Gerisch, T. Bretschneider, A. Muller-Taubenberger, E. Simmeth, M. Ecke, S. Diez, K. Anderson, Mobile actin clusters and traveling waves in cells recovering from actin depolymerization. *Biophys. J.* **87**, 3493–3503 (2004)
25. A. Gholami, M. Enculescu, M. Falcke, Membrane waves driven by forces from actin filaments. *New J. Phys.* **14**, 115002 (2012)
26. G. Giannone, B.J. Dubin-Thaler, H.-G. Doeberleiner, N. Kieffer, A.R. Bresnick, M.P. Sheetz, Periodic lamellipodial contractions correlate with rearward actin waves. *Cell* **116**, 431–443 (2004)
27. E. Gouin, M.D. Welch, P. Cossart, Actin-based motility of intracellular pathogens. *Curr. Opin. Microbiol.* **8**, 35–45 (2005)
28. N.S. Gov, A. Gopinathan, Dynamics of membranes driven by actin polymerization. *Biophys. J.* **90**, 454–469 (2006)
29. S. Guenther, K. Kruse, Spontaneous waves in muscle fibres. *New J. Phys.* **9**, 417–417 (2007)
30. C.-H. Huang, M. Tang, C. Shi, P.A. Iglesias, P.N. Devreotes, An excitable signal integrator couples to an idling cytoskeletal oscillator to drive cell migration. *Nat. Cell Biol.* **15**, 1307–1318 (2013)
31. K.L. Hui, S.I. Kwak, A. Upadhyaya, Adhesion-dependent modulation of actin dynamics in Jurkat T cells. *Cytoskeleton (Hoboken)* **71**, 119–135 (2014)

32. H.U. Keller, M. Bessis, Migration and chemotaxis of anucleate cytoplasmic leukocyte fragments. *Nature* **258**, 723–724 (1975)
33. A.J. Koch, H. Meinhardt, Biological pattern-formation - from basic mechanisms to complex structures. *Rev. Mod. Phys.* **66**, 1481–1507 (1994)
34. K. Kruse, J.-F. Joanny, F. Julicher, J. Prost, K. Sekimoto, Aster, vortices, and rotating spirals in active gels of polar filaments. *Phys. Rev. Lett.* **92**, 078101 (2004)
35. T.P. Loisel, R. Boujemaa, D. Pantaloni, M.F. Carlier, Reconstitution of actin-based motility of *Listeria* and *Shigella* using pure proteins. *Nature* **401**, 613–616 (1999)
36. M.L. Lombardi, D.A. Knecht, M. Dembo, J. Lee, Traction force microscopy in *Dictyostelium* reveals distinct roles for myosin II motor and actin-crosslinking activity in polarized cell movement. *J. Cell Sci.* **120**, 1624–1634 (2007)
37. M. Loose, E. Fischer-Friedrich, J. Ries, K. Kruse, P. Schwille, Spatial regulators for bacterial cell division self-organize into surface waves in vitro. *Science* **320**, 789–792 (2008)
38. M. Loose, K. Kruse, P. Schwille, Protein self-organization: lessons from the min system. *Annu. Rev. Biophys.* **40**, 315–336 (2011)
39. M. Machacek, G. Danuser, Morphodynamic profiling of protrusion phenotypes. *Biophys. J.* **90**, 1439–1452 (2006)
40. S.E. Malawista, A. De Boisfleury Chevance, The cytokineplast - purified, stable, and functional motile machinery from human-blood polymorphonuclear leukocytes - possible formative role of heat-induced centrosomal dysfunction. *J. Cell Biol.* **95**, 960–973 (1982)
41. J.T. Mandeville, R.N. Ghosh, F.R. Maxfield, Intracellular calcium levels correlate with speed and persistent forward motion in migrating neutrophils. *Biophys. J.* **68**, 1207–1217 (1995)
42. A.C. Martin, M. Kaschube, E.F. Wieschaus, Pulsed contractions of an actin-myosin network drive apical constriction. *Nature* **457**, 495–499 (2009)
43. K. Mellstrom, A.S. Hoglund, M. Nister, C.H. Heldin, B. Westermark, U. Lindberg, The effect of platelet-derived growth-factor on morphology and motility of human glial-cells. *J. Muscle Res. Cell Motil.* **4**, 589–609 (1983)
44. A. Millius, S.N. Dandekar, A.R. Houk, O.D. Weiner, Neutrophils establish rapid and robust WAVE complex polarity in an actin-dependent fashion. *Curr. Biol.* **19**, 253–259 (2009)
45. K. Murthy, P. Wadsworth, Dual role for microtubules in regulating cortical contractility during cytokinesis. *J. Cell Sci.* **121**, 2350–2359 (2008)
46. S. Najem, M. Grant, Phase-field approach to chemotactic driving of neutrophil morphodynamics. *Phys. Rev. E* **88**, 034702 (2013)
47. F.J. Nedelec, T. Surrey, A.C. Maggs, S. Leibler, Self-organization of microtubules and motors. *Nature* **389**, 305–308 (1997)
48. N. Okamura, S. Ishiwata, Spontaneous oscillatory contraction of sarcomeres in skeletal myofibrils. *J. Muscle Res. Cell Motil.* **9**, 111–119 (1988)
49. B. Peleg, A. Disanza, G. Scita, N. Gov, Propagating cell-membrane waves driven by curved activators of actin polymerization. *PLoS One* **6**, e18635 (2011)
50. P.Y. Placais, M. Balland, T. Guerin, J.-F. Joanny, P. Martin, Spontaneous oscillations of a minimal actomyosin system under elastic loading. *Phys. Rev. Lett.* **103**, 158102 (2009)
51. T.D. Pollard, Regulation of actin filament assembly by Arp2/3 complex and formins. *Annu. Rev. Biophys. Biomol. Struct.* **36**, 451–477 (2007)
52. T.D. Pollard, G.G. Borisy, Cellular motility driven by assembly and disassembly of actin filaments. *Cell* **112**, 453–465 (2003)
53. J. Prost, C. Barbutta, J.-F. Joanny, Dynamical control of the shape and size of stereocilia and microvilli. *Biophys. J.* **93**, 1124–1133 (2007)
54. J. Prost, F. Jülicher, J.-F. Joanny, Active gel physics. *Nat. Phys.* **11**, 111–117 (2015)
55. M. Radzuweit, S. Alonso, H. Engel, M. Bär, Intracellular mechanochemical waves in an active poroelastic model. *Phys. Rev. Lett.* **110**, 138102 (2013)
56. M. Radzuweit, H. Engel, M. Bär, An active poroelastic model for mechanochemical patterns in protoplasmic droplets of *Physarum polycephalum*. *PLoS One* **9**, e99220 (2014)

57. G.L. Ryan, N. Watanabe, D. Vavylonis, A review of models of fluctuating protrusion and retraction patterns at the leading edge of motile cells. *Cytoskeleton (Hoboken)* **69**, 195–206 (2012)
58. D. Sasaki, H. Fujita, N. Fukuda, S. Kurihara, S. Ishiwata, Auto-oscillations of skinned myocardium correlating with heartbeat. *J. Muscle Res. Cell Motil.* **26**, 93–101 (2005)
59. V. Schaller, C. Weber, C. Semmrich, E. Frey, A.R. Bausch, Polar patterns of driven filaments. *Nature* **467**, 73–77 (2010)
60. D. Shao, W.-J. Rappel, H. Levine, Computational model for cell morphodynamics. *Phys. Rev. Lett.* **105**, 108104 (2010)
61. A.D. Shenderov, M.P. Sheetz, Inversely correlated cycles in speed and turning in an ameba: an oscillatory model of cell locomotion. *Biophys. J.* **72**, 2382–2389 (1997)
62. R. Shlomovitz, N.S. Gov, Membrane waves driven by actin and myosin. *Phys. Rev. Lett.* **98**, 168103 (2007)
63. J. Solon, A. Kaya-Copur, J. Colombelli, D. Brunner, Pulsed forces timed by a ratchet-like mechanism drive directed tissue movement during dorsal closure. *Cell* **137**, 1331–1342 (2009)
64. S. Takagi, T. Ueda, Emergence and transitions of dynamic patterns of thickness oscillation of the plasmodium of the true slime mold *Physarum polycephalum*. *Physica D* **237**, 420–427 (2008)
65. S. Takagi, T. Ueda, Annihilation and creation of rotating waves by a local light pulse in a protoplasmic droplet of the *Physarum plasmodium*. *Physica D* **239**, 873–878 (2010)
66. T. Takenawa, S. Suetsugu, The WASP-WAVE protein network: connecting the membrane to the cytoskeleton. *Nat. Rev. Mol. Cell Bio.* **8**, 37–48 (2007)
67. A.M. Turing, The chemical basis of morphogenesis. *Philos. Trans. R. Soc. B* **237**, 37–72 (1952)
68. D.M. Veltman, J.S. King, L.M. Machesky, R.H. Insall, SCAR knockouts in Dictyostelium: WASP assumes SCAR's position and upstream regulators in pseudopods. *J. Cell Biol.* **198**, 501–508 (2012)
69. M.G. Vicker, Reaction-diffusion waves of actin filament polymerization/depolymerization in Dictyostelium pseudopodium extension and cell locomotion. *Biophys. Chem.* **84**, 87–98 (2000)
70. M.G. Vicker, Eukaryotic cell locomotion depends on the propagation of self-organized reaction-diffusion waves and oscillations of actin filament assembly. *Exp. Cell Res.* **275**, 54–66 (2002)
71. A. Wegner, Head to tail polymerization of actin. *J. Mol. Biol.* **108**, 139–150 (1976)
72. O.D. Weiner, W.A. Marganski, L.F. Wu, S.J. Altschuler, M.W. Kirschner, An actin-based wave generator organizes cell motility. *PLoS Biol.* **5**, e221 (2007)
73. S. Whitelam, T. Bretschneider, N.J. Burroughs, Transformation from spots to waves in a model of actin pattern formation. *Phys. Rev. Lett.* **102**, 98103 (2009)
74. F. Ziebert, S. Swaminathan, I.S. Aranson, Model for self-polarization and motility of keratocyte fragments. *J. R. Soc. Interface* **9**, 1084–1092 (2012)

Chapter 3

A Modular View of the Signaling System Regulating Chemotaxis

Pablo A. Iglesias

3.1 Introduction

Directional migration is one of the nature’s most fundamental processes. Single-cell organisms, like bacteria or amoebae, rely on sensing and interpreting chemical cues to direct their movement in search of nutrients. This chemically guided movement, known as *chemotaxis*, is crucial during the development of the nervous system [63, 67] and is used by cells of the immune system to seek pathogens [10]. Inappropriate regulation of directed migration plays a role in excessive inflammation and inflammation-related diseases such as asthma [106], multiple sclerosis [12], and arthritis [46]. External cues also direct cancer cells to sites of metastasis [82].

The use of theoretical models to understand chemotaxis has a long history, both in the study of bacteria [9, 47], amoeba [58], and neutrophils [50]. In the case of bacterial chemotaxis, the development of detailed biochemical models has been aided by a thorough identification of the biochemical elements directing cell migration—*E. coli* chemotaxis is “arguably the best understood of all biological behaviors” [76]. However, despite a complete identification of the molecular players that enable this sensory system, numerous questions remain. For example, how do cells integrate various chemotactic cues? How do cells achieve their remarkable sensitivity? Theoretical models are at the forefront of research addressing these, and other important questions [91].

Electronic supplementary material The online version of this chapter (doi: 10.1007/978-3-319-24448-8_3) contains supplementary material, which is available to authorized users.

P.A. Iglesias (✉)

Department of Electrical and Computer Engineering, The Johns Hopkins University,
3400 N. Charles Street, Baltimore, MD 21218, USA
e-mail: pi@jhu.edu

The mechanism regulating the chemotactic behavior of larger, but slower, eukaryotic cells, is considerably less well understood. Part of this is the much greater complexity of these systems. For example, in one of the better-studied chemotactic model organisms, *Dictyostelium discoideum* amoeba, well over 100 genes are known to have a role in regulating some aspect of directional migration [92]. Dozens, if not hundreds, of other genes are also likely to be involved. Though the use of theoretical models can help, understanding a system of this complexity is impossible with some means of abstraction. In our research, we have advocated the development of *modular* models. In this context, a *module* is a model that describes only a small subset of the observable behavior, but whose parts may be interchangeable. This approach, common in engineering, has also been championed as a means of understanding biological systems [30].

The use of modular models to study chemotaxis of eukaryotic cells is particularly appropriate, as it is now generally accepted that the chemotactic response itself involves the integration of three separate but interrelated processes [37, 38, 81] (Fig. 3.1). The first, *directional sensing*, describes the cells' ability to recognize and amplify small differences in the spatial profile of an external signal so as to guide movement. The second, *polarization*, is the development of well-defined anterior

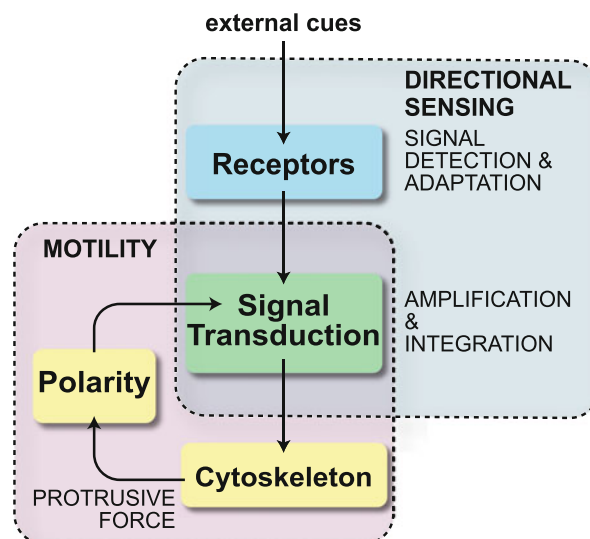


Fig. 3.1 Modular form of the chemotactic regulatory system. We view the chemotactic network of amoeboid cells as consisting of a number of interacting modules. Receptors, to which external ligands bind, are responsible for detection and adaptation. The system is subject to various external cues—the information from these sources is integrated and amplified by the signal transduction network. This module then signals to the cytoskeleton network, which provides the protrusive forces that propel the cell. It also sends a signal, through a feedback process, that is responsible for polarizing the cell. This polarization also has the effect of providing a memory that helps the cell to migrate persistently in the absence of external cues. These various modules can be grouped roughly into a directional sensing module, comprising of the receptors and signal transduction networks, and a motility module, which includes the signal transduction, cytoskeleton, and polarity modules

and posterior regions in a cell. Finally, the third is *motility*, which in the case of amoeboid cells refers to the periodic extension of cell protrusions at the front and retractions at the rear used to translocate the cell. Importantly, each of these processes can be observed independently. For example, cells can sense and interpret gradients of chemoattractant without movement. Conversely, cells can move in the absence of chemotactic gradients.

Of course, a complete treatment of any of these processes would be the subject of an entire chapter or even book. Here, we present some of the basic biological features of the underlying processes, then introduce models used to explain these individual processes, and then describe their interactions.

3.2 Motility

By definition, a chemotaxing cell must be able to move in its environment. The mechanisms used by cells to move are numerous. In our work on chemotaxis, we particularly focus on amoeboid cells such as *Dictyostelium* amoebae or neutrophils. These cells rely on actin polymerization to generate the necessary forces to move. The actin cytoskeleton is a highly complex system, and an area of considerable active research. As such, any realistic model (e.g., [23]) is going to be considerably more complicated than what is desirable or tractable for studying chemotaxis. For a useful introduction to the area, particularly focusing on mathematical models, we point the reader to recent reviews [64, 83]. Here, we focus on the connection between motility and chemotaxis, emphasizing the mechanism by which otherwise randomly migrating cells can be directed by external cues.

3.2.1 Random Motility

An important feature of virtually all chemotactic cells is that they remain motile even in the absence of directional cues. In amoeboid cells, this movement is achieved by the extension of *pseudopods*, actin-rich protrusions that are extended from the side of the cell. Because these extensions are relatively small a single one does not move the centroid of the cell in an appreciable way. For this to happen, several pseudopods must be extended in the same direction. This microscopic *persistence* in the location of pseudopods gives rise to a macroscopic persistence in the direction of motion. This was noted in fibroblasts [26] and *Dictyostelium* cells [80] in the 1970s. In the latter, the persistence time of motion has been measured to be in the order of 4–10 min [53, 80, 94].

More recently, aided by powerful automatic image analysis algorithms (reviewed in [109]), the nature of these pseudopods and the ensuing random migration has been characterized extensively [3, 14]. Pseudopod extensions appear to come in two forms. Most, approximately 85 % in wild-type *Dictyostelium* cells, split off from existing pseudopods, initially forming a “Y”-shape, before one of the two arms of the Y retracts leaving a single extension. Alternatively, de novo pseudopods

are formed at sites along the cell periphery where no activity has been observed recently. Importantly, though these two classes of pseudopodia lead to different cell morphologies, various aspects of their formation (e.g., growth rate, length distribution) do not seem to be significantly different [14]. Moreover, comparisons between the pseudopods of randomly migrating cells and cells responding to external stimuli do not differ appreciably, suggesting that there is some common mechanism for extending these protrusions.

3.2.2 Excitable Behavior

Twenty years ago, Vicker and colleagues reported the presence of oscillatory and traveling wave patterns in the shape of *Dictyostelium* cells [44]. Subsequent experiments demonstrated the existence of propagating waves of F-actin assembly [100, 101]. These findings seem not to have attracted much attention until, in 2007, Weiner et al. reported similar results in the basal membrane of migrating, neutrophil-like HL60 cells using total internal reflection fluorescence (TIRF) microscopy [108]. Since then, numerous cytoskeletal and signaling proteins have been shown to propagate in waves (reviewed in [36]). The existence of these waves has prompted a number of researchers to suggest the presence of an excitable network (EN) that controls the signaling network that regulates actin polymerization.

Excitable systems were first proposed by Hodgkin and Huxley to explain the all-or-nothing characteristic of action potentials in neurons [31]. An excitable system is a dynamical system with a single, stable equilibrium. As such, the response to small-scale perturbations simply dies out. However, sufficiently large perturbations elicit a large, characteristic response, before the system returns to its equilibrium. When the excitable elements are spatially distributed, as they are along an axon, the system is said to be an *excitable medium*. In this case, the triggered response gives rise to a propagated wave of activity that travels along the medium. Moreover, when two such waves collide, they annihilate each other, due to a refractory period that follows the activation of the triggered response and during which subsequent re-stimulation is impossible.

Consistent with the excitable membrane/cortex hypothesis, the observed actin waves annihilate each other upon a collision. Moreover, as the waves reach the cell perimeter, they appear to supply the force, through actin polymerization, used to propel the cell forward. These events likely correspond to the observed localization of these biosensors at the protruding edges of the cells seen in confocal or epifluorescence microscopy [79]. As such, wave propagation and extinction are related to extensions and retractions of pseudopods. Importantly, these waves do not depend on the presence of chemoattractant signaling [17], which is consistent with the notion that they have a role in directing randomly migrating cells.

It is important to note that, though the existence of traveling waves, and in particular, annihilating waves, is a signature of excitability, it is not conclusive proof of the presence of such a circuit [65]. However, subsequent experiments

have demonstrated that the network displays other characteristics of excitable systems [34, 71]. For example, the response to chemoattractant stimuli displays the classical all-or-nothing behavior of excitable systems. In particular, once a response is triggered, its magnitude and duration do not depend on the size of the stimulus. Second, the probability that the threshold for triggering a response is crossed does depend on the size of the stimulus. Thus, strong and weak stimuli lead to equally sized patches of activity around the cell, but the fraction of the cell that is covered by these patches is greater when the stimulus is stronger. Third, the triggering of the response in an EN is followed by a refractory period of approximately 45–60 s in which no further firings are possible despite the application of subsequent stimuli [34].

3.2.3 Models of Excitable Behavior

Based on the assumption that an EN is regulating actin polymerization, and hence cell migration, a number of models have been proposed to describe the presence of actin waves. Most of these are variations of activator-inhibitor systems [108, 109], though some include greater biological detail [19].

The activator, whose activity is denoted by X , is autocatalytic, implying a strong positive feedback loop. The inhibitor, whose activity is given by Y , is itself activated by X but provides negative feedback. The precise nature of the interactions between the two systems varies, but many of the proposed models rely on the classical FitzHugh–Nagumo (FHN) model [24, 68], in which the nullclines for the activator and inhibitor are cubic and linear functions, respectively. In our case [89, 110], we let

$$\frac{\partial X}{\partial t} = k_{xx} \frac{X^2}{k_M^2 + X^2} - k_{-x} X - k_{yx} Y + k_{ux} U + D_x \nabla^2 X \quad (3.1)$$

$$\frac{\partial Y}{\partial t} = k_{xy} X - k_{-y} Y + D_y \nabla^2 X. \quad (3.2)$$

Both components in this subsystem diffuse spatially, with diffusion coefficients D_x and D_y , respectively. The signal U is the input to the excitable system, which incorporates several components. For describing random activity, only two are needed:

$$U = U_{\text{basal}} + U_{\text{noise}}.$$

The first term, U_{basal} , is constant and represents a basal level of stimulation. The second, U_{noise} , is a white, stochastic process with zero mean and variance λ . It models the random fluctuations in the concentrations of the underlying regulators of the EN. The parameters used to describe this EN are given in Table 3.1, in the appendix.

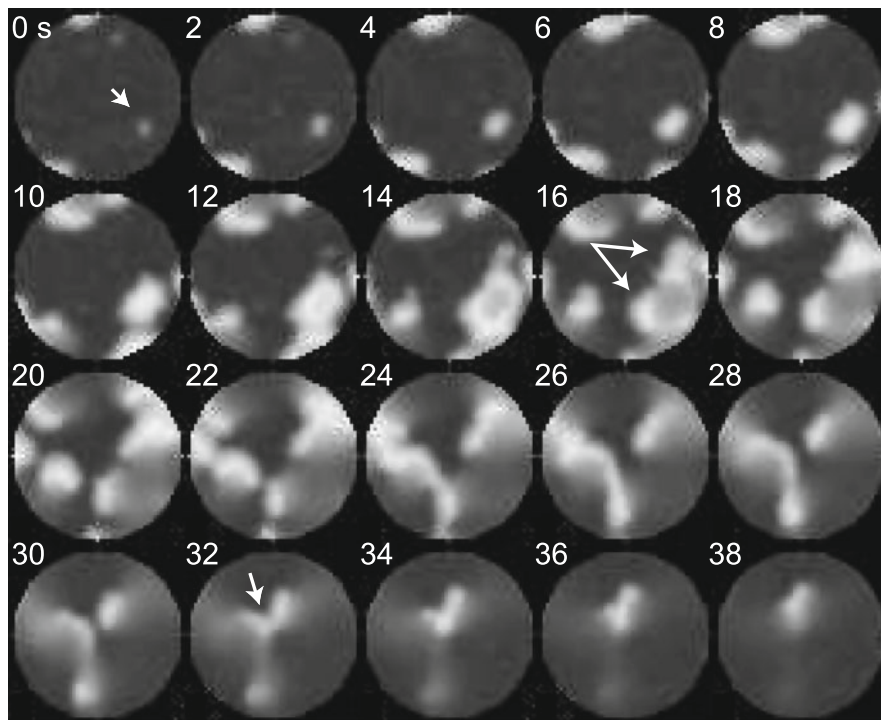


Fig. 3.2 Activity of the excitable network simulated in a two-dimensional surface. Shown are the levels of the inhibitor (Y). The waves can arise spontaneously, as shown in the frame at 0 s. After growing, they can split (see arrows at $t = 16$ s). Eventually, after a collision (arrows at $t = 32$ s) they annihilate each other. Pictures are snapshots from Supplemental Video #8 in [110]

When simulated in a two-dimensional environment, reminiscent of the basal surface of the cell imaged using TIRF, the system produces traveling waves that, when they collide, annihilate each other, consistent with experimental observations; see Fig. 3.2.

In practice, relating the activity of these waves to cell motion is difficult. Instead, most simulations that couple the activity of the EN to changes in cell morphology and movement rely on a two-dimensional depiction of the cell in which the activity of the EN is simulated in a periodic, one-dimensional surface that represents the boundary of the cell; see Fig. 3.3 (left). In this case, the spatial and temporal evolution of the EN's network activity is easily tracked using kymographs (kymograph, i.e. space-time diagram, is a graphical representation of spatial position over time in which a spatial axis represents time), similar to those generated experimentally [79]; see Fig. 3.3 (right).

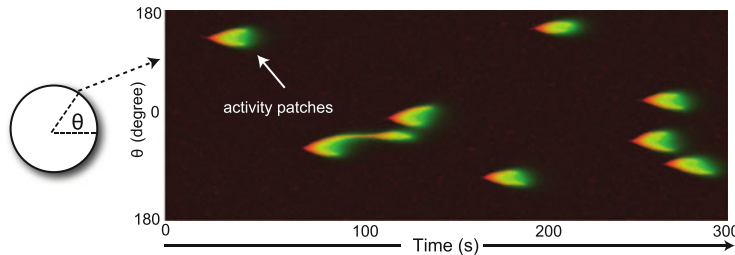


Fig. 3.3 Activity of the excitable network simulated in a periodic, one-dimensional surface. The surface represents the perimeter of the cell (*left*). The network behavior can best be visualized using a kymograph (*right*) that plots the activity at a given angle as a function of time. In this example, we plotted the levels of the activator (in *red*) and inhibitor (in *green*) for an unstimulated cell. Note how the *red* signal starts the firing. It is followed by a period where both signals coexist. The activity stops when there is only inhibition (*green*) present. Note also the propagation of the signal outward from its point of trigger—this is due to the diffusion-driven propagation of activation

3.2.4 Coupling EN Activity to Cellular Deformations

One of the motivations for using an EN is to represent the excitable nature of actin polymerization. Through this connection, we may assume that regions of high activity of the EN around the periphery of the cell coincide with regions of actin polymerization, which provide a protrusive force to the cell. Translating this force into cell movement requires a mechanical model of the cell, and a means for simulating cell shape changes. In our studies, we rely on *level set methods* (LSM) for simulating cell shape changes.

The LSM is a numerical technique for simulating evolving surfaces [74]. In the LSM, the cell perimeter (the surface in question) is defined implicitly using a potential function that evolves over time. This implicit representation of cell shape gives the LSM advantages in model simplicity and computational expense over other computational methods.¹ In particular, the cell is described as the zero-level set of a potential function $\varphi(\mathbf{z}, t)$, $\mathbf{z} \in \mathbb{R}^2$. We use a *signed distance function* as the potential function. This is the positive (resp. negative) distance to the boundary from a point outside (resp. inside) the cell. The evolution of the potential function is dictated by the Hamilton–Jacobi equation:

$$\frac{\partial \varphi(\mathbf{z}, t)}{\partial t} + v(\mathbf{z}, t)|\nabla \varphi(\mathbf{z}, t)| = 0, \quad (3.3)$$

where $v(\mathbf{z}, t)$ describes the local speed in normal direction of the potential function (Fig. 3.4b).

¹Discussion on similarities and differences between the LSM and the phase-field method can be found in Chap. 1. See [86, 87, 101, 118] for implementation of the phase-field method in the context of cell motility.

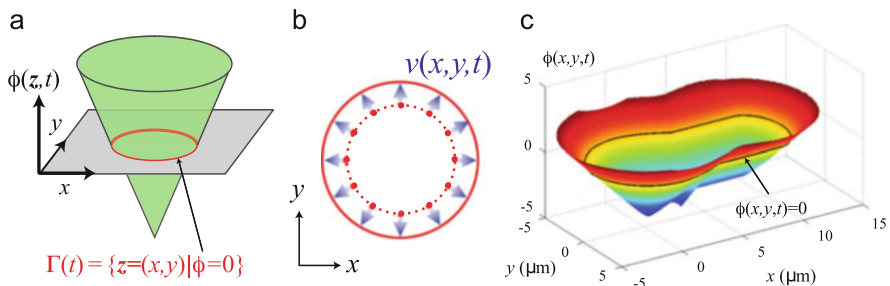


Fig. 3.4 The level set framework. (a) The implicit representation of cell boundary by connecting the points with zero level of potential function $\phi(\mathbf{z}, t)$. (b) The local velocity, $v(\mathbf{z}, t)$ is used to evolve the cell boundary. (c) The figure shows the potential function generated using the signed-distance function, of a cell being aspirated by a micropipette. Figure reprinted with permission from [114]. ©2008 Yang et al.

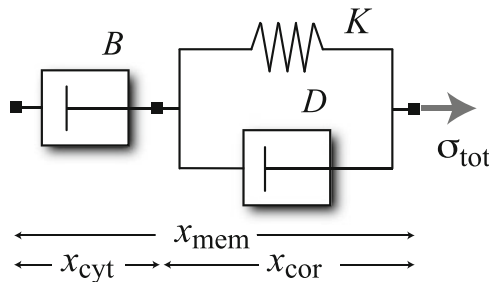


Fig. 3.5 Viscoelastic model of cell. Cell boundary/membrane displacements (x_{mem}) are generated by moving the potential function according to the total stress applied, σ_{total} (3.4). The spring-dashpot (K, D) elements represent the mostly elastic cortex, which moves a distance x_{cor} (3.5). The viscous component (B) represents the cytosol, which moves a distance x_{cyt}

3.2.5 Viscoelastic Cell Mechanical Model

To obtain the speed, $v(\mathbf{z}, t)$, we apply different stresses to the cell and use a viscoelastic mechanical model (Fig. 3.5) of the cell to determine the local velocity.

The mechanical description of the cell was previously identified based on micropipette aspiration experiments using *Dictyostelium* cells [114]. It incorporates several passive stresses, including the effect of cortical tension driving Laplace-like pressures on the cell, and volume conservation. It also includes active stresses allowing us to test the effectiveness of the EN in driving cellular motion. In our simulations, the activity of the EN was coupled to protrusive forces, so that higher activity at one location gave stronger protrusive stress.

Mathematically, the viscoelastic model is described by:

$$\dot{x}_{\text{mem}} = -(K/D)x_{\text{cor}} + (1/D + 1/B)\sigma_{\text{total}} \quad (3.4)$$

$$\dot{x}_{\text{cor}} = -(K/D)x_{\text{cor}} + (1/D)\sigma_{\text{total}}, \quad (3.5)$$

where σ_{total} is the total stress applied on the cell, x_{mem} and x_{cor} are the local displacements of the membrane and cortex, respectively, and K , D , and B are viscoelastic components of the cell describing the elasticity (K) and viscosity (D) of the membrane, and the viscosity (B) of the cytoplasm. The speed is given by:

$$v(\mathbf{z}, t) = \frac{dx_{\text{mem}}(t)}{dt}. \quad (3.6)$$

The parameters of viscoelastic model are shown in Table 3.3.

It remains to describe all the stresses acting on the cell. These fall under two classes: passive and active stresses. Specifically, we have:

Surface Tension (σ_{ten}) This arises from Laplace-like pressures at the interface between two surfaces [116]. It is given by:

$$\sigma_{\text{ten}} = \gamma k(x)\mathbf{n},$$

where γ is the local cortical tension, k is the local curvature, and \mathbf{n} is a normal unit vector.

Volume Conservation (σ_{vol}) This stress acts to ensure surface area conservation. It is implemented as a negative feedback based on deviations from the nominal area:

$$\sigma_{\text{vol}} = k_{\text{area}}(A(t) - A_0)\mathbf{n},$$

where A is the surface area enclosed by the cell boundary, either initially (A_0), or at time t ($A(t)$) (compare to Eq. (1.5) in Chap. 1).

Active Stresses (σ_{pro}) These are stresses generated by the activity of the EN. In our simulations, we made these proportional to the inhibitor (Y); using the activator (X) gives similar, but noisier, results. Specifically, we define:

$$\sigma_{\text{pro}} = \sigma_0 \gamma(\theta)\mathbf{n},$$

representing actin polymerization. The conversion factor between the level Y and the force is $\sigma_0 = 35 \text{ nN}/\mu\text{m}^2$. Based on the typical maximum activity level for Y seen in the simulations (approximately 0.05 A.U.), this resulted in protrusive forces in the range of 1–3 nN/ μm^2 , consistent with measured values of the maximum protrusive pressure due to actin polymerization (in the range of a few nN/ μm^2).

Using these contributions, we compute the total stress

$$\sigma_{\text{total}} = \sigma_{\text{pro}} + \sigma_{\text{ten}} + \sigma_{\text{vol}}$$

and use this to update the viscoelastic model parameters (x_{mem} and x_{cor}) in (3.4) and (3.5).

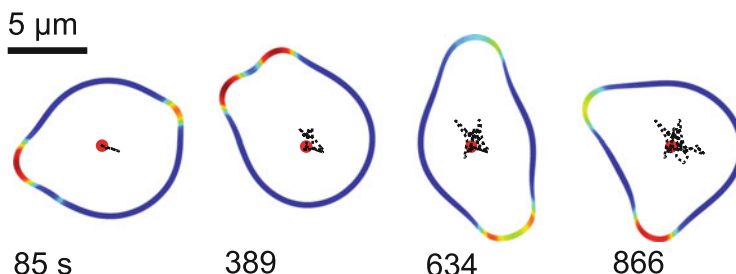


Fig. 3.6 Changes in cellular morphology due to random EN firings in an unstimulated cell. Note how the regions of high activity (marked as *red spots* along the boundary) drive cellular protrusions. The *dotted line* in the center marks the drifting of the cell centroid, which drifts minimally from the starting point, marked by the *red circle*. Figure from [89], ©Shi et al. Used by permission under the Creative Commons Attribution License

3.2.6 Simulations of Random Motility

Based on the models described above, we simulated the activity of an unstimulated cell; see Fig. 3.6. As previously seen in the kymographs (Fig. 3.3), spontaneous firings of the EN occur around the perimeter of the cell. Owing to the coupling between activity of the EN and protrusive force, the cell extends a projection at points along the cell where a random firing has taken place. These protrusions last only as long as the EN remains active. Thereafter, the protrusive force disappears, and is overwhelmed by cortical tension and rounding forces. This causes the cell to recover its mostly round shape until a new firing repeats the process. Overall, the cell centroid does not drift from the starting point appreciably. This lack of overall cell displacement can be attributed to an absence of directional persistence in the location of the EN firings. Before addressing the lack of persistence in the model, we next consider how this motility module can be coupled to the cell's ability to detect chemoattractant signals.

3.3 Directional Sensing and Adaptation

Chemotactic amoebae and neutrophils both sense external chemoattractant signals using G-protein coupled receptors [92]. In contrast to the bacterial sensing mechanism, which relies on a temporal comparison of receptor occupancy to elucidate the nature of the gradient (klinokinesis), these larger and slower cells are able to sense static spatial gradients. This is best illustrated in cells that are unable to move because of the addition of inhibitors of actin polymerization such as Latrunculin [75]. Owing to their inability to polymerize actin, Latrunculin-treated cells round up. However, when exposed to a chemoattractant gradient, intracellular markers polarize to one side of the cell, and remain there until the gradient is

removed. Most of the known markers are found preferentially at the side of the cell with highest receptor occupancy (e.g., PH-domains [75], PI3K, etc.) but there are examples of proteins that find their way to the back, including the phosphatase PTEN [40]. These localizations are also seen in randomly migrating cells and, remarkably, in dividing cells, where the cleavage furrow and poles serve as the “back” of “fronts” of the two daughter cells [41]. Interestingly, the degree of polarization of these markers exceeds that of the external gradient in Latrunculin-treated and untreated cells, though the degree of spatial localization is higher for the latter [42]. This suggests the presence of both actin-independent and actin-dependent mechanisms for amplifying the external signal.

When the stimulus is spatially uniform, the cellular response is initially global—front markers translocate to membrane replacing back markers that become cytosolic. However, this translocation is only transient. Within 25–30 s, the various markers return to their prestimulus levels [22], though recent experiments have suggested that at certain chemoattractant doses, this *adaptation* is only partial [95, 117].

3.3.1 Local Excitation, Global Inhibition

The varying nature of the response leads to an interesting question. Why is the response to spatially graded response persistent, but only transient when the whole cell experiences a global stimulus? The transient aspect of the response is reminiscent of the adaptation seen in the bacterial chemotactic response.

Over the years, several models have been proposed to account for adaptive responses. The first, due to Koshland [47], posited that complementary *excitation* and *inhibition* processes, both mediated by receptor occupancy, control a *response regulator* that signals to downstream events. The relative rates at which the excitation and inhibition processes are regulated by receptor occupancy control the transient signal. If the inhibitory process is slower, then an increase in receptor occupancy causes the excitation to rise quickly, leading to a concomitant increase in the level of the response regulator. However, as the slower inhibition catches up, the response regulator peaks and eventually drops to prestimulus levels. The form of this model is now commonly called an *incoherent feedforward loop*, particularly in gene networks where it is a commonly found motif [88].

A second class of models, based on negative feedback regulation, was proposed by Barkai and Leibler [8]. Their primary goal was to show that the adaptation process could be made *robust*—that is, insensitive to particular parameter changes, a property of the bacterial chemotactic network that was shown to hold experimentally [1]. Subsequent analysis has suggested that these two classes of models are the only two that can achieve signal detection and adaptation [57]. Moreover, they both achieve robust adaptation because of the presence of *integral control* action—a common design motif of engineering control systems [4, 49, 90, 115].

Though both classes of models explain the transient response of the signaling system, neither explains the ability to detect gradients persistently. However, with slight modification, both can also be made to explain the latter. In particular, in the Koshland model, if the excitation process is assumed to be spatially localized to the site of receptor occupancy, but the inhibition is global, then the response regulator responds only transiently to the spatially uniform changes in the level of the stimulus, but persistently at the side facing the highest receptor occupancy when exposed to an external gradient. This *local-excitation, global-inhibition* (LEGI) model is now a hallmark of many models of gradient sensing in chemotactic cells [7, 52, 69, 72, 95, 103, 117].

The model can be described by the following partial differential equations:

$$\frac{\partial E}{\partial t} = k_e S - k_{-e} E \quad (3.7)$$

$$\frac{\partial I}{\partial t} = k_i S - k_{-i} I + D_i \nabla^2 I \quad (3.8)$$

$$\frac{\partial R}{\partial t} = k_r E - k_{-r} IR. \quad (3.9)$$

Here, the variables S , E , I , and R represent the levels of the external signal, excitation, inhibition, and response regulator, respectively. In this description, we have assumed that only the inhibitor can diffuse. In practice, the other elements could also be diffusive, provided that their dispersion (λ ; the square root of the ratio between diffusion and inactivation rate) is smaller than that of the inhibitor; i.e.:

$$\lambda_e = \sqrt{\frac{D_e}{k_{-e}}} < \lambda_i = \sqrt{\frac{D_i}{k_{-i}}}.$$

Note that other implementations of the LEGI mechanism are possible, though the general form is the same [113]. Parameter values for the LEGI module are given in Table 3.2. Simulations showing the response of the LEGI mechanism to spatially uniform changes in the stimulus level are shown in Fig. 3.7. The response of the mechanism to the introduction of a spatially graded stimulus is shown in Fig. 3.8.

3.3.2 Experimental Support for the LEGI Mechanism

The LEGI model has been questioned because of the lack of biochemical entities behind it. In the model, the occupied receptor, or closely related species like G-proteins, fit the requirements of the excitation process. In particular, receptor occupancy and G-protein dissociation are local indicators of the external chemoattractant concentration. Moreover, they are localized and persistent signals, thus fitting the requirements of the excitation. Thus, this aspect of the model is not controversial. However, the precise identity of the inhibitor remains elusive.

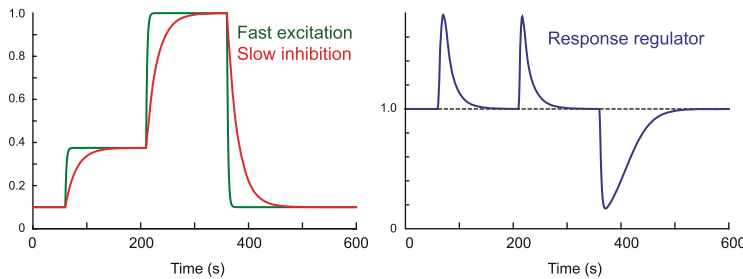


Fig. 3.7 Response of LEGI mechanism to spatially uniform changes in stimulus. The *left panel* shows the response of the excitation and inhibition processes to changes in the external stimulus, from $S = 0.1$ at $t = 0$ s, to $S = 0.375$ at $t = 60$ s, to $S = 1$ at $t = 210$ s, and back to $S = 0.1$ at $t = 360$ s. Notice how both the excitation and inhibition processes track the stimulus, but the response of excitation is faster than that of the inhibition. These signals lead to an adaptive response in the response regulator. When there is an increase in the stimulus, the response regulator increases transiently. In response to a removal of the stimulus, the response regulator dips below the basal level

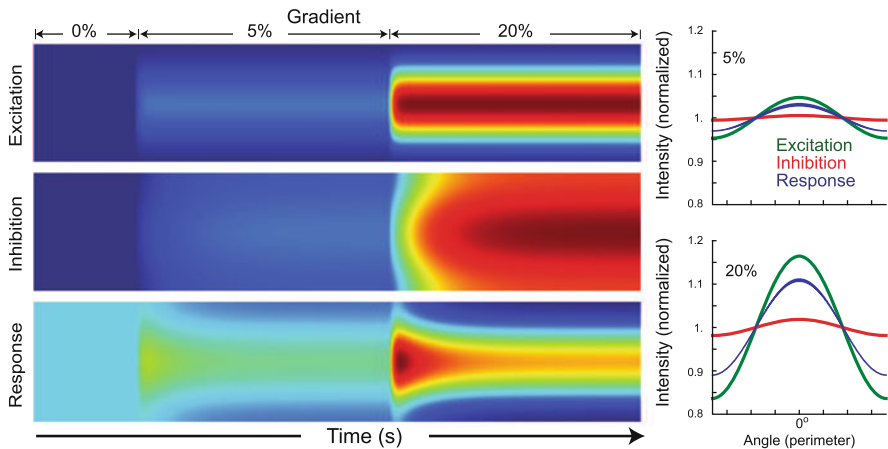


Fig. 3.8 Response of LEGI mechanism to spatially graded stimulus. The *left three panels* show kymographs of the excitation and inhibition processes and the response regulator to graded stimuli, defined by $1 + \delta + \delta \cos(\theta)$ where the $\delta = \{0, 0.05, 0.20\}$ specify the gradients. This simulation assumes that $D_I = 10 \mu\text{m}/\text{s}^2$, $D_E = D_R = 0.2 \mu\text{m}/\text{s}^2$. Note how the inhibition is mostly diffuse, but the excitation retains most of the spatial information. The response regulator maintains the localization. Note, however, that the spatial gradient in the response is smaller than that of the excitation (which is a close to that of the stimulus). This is best seen in the graphs in the *right panels*, which show the steady-state distribution of the three signals for 5 and 20 % gradients, normalized by their mean value. Finally, note that even though the stimulus intensity at the back never decreases, the response at the back gets progressively more negative, indicative of a suppression of activity at the back

Nevertheless, there are a number of experiments that suggest that *Dictyostelium* cells do employ some variant of the LEGI. For example, one prediction of the LEGI mechanism is that the response of the cell depends on the *relative* steepness of the gradient (see below). Moreover, an increase in the overall level of receptor occupancy is expected to lead to a weaker, rather than stronger response. These properties, which require a spatially diffuse inhibitor, have both been observed experimentally [42].

A second requirement of the LEGI model is that the inhibitor be generated locally by receptor occupancy, and there is experimental evidence for this [112].

A third prediction of the LEGI mechanism is that after the cell has adapted, removal of the stimulus should result in a drop in activity. This property requires the presence of a persistent inhibition that is slower than excitation. Recently, this was observed experimentally—following removal of the stimulus, localized patches of Ras activity decreased in intensity before eventually recovering [96].

Fourth, we note that the negative feedback adaptation mechanism can also be made to detect spatial signals using a LEGI-like mechanism [39], so the presence of an inhibitor is itself not proof of the form of (3.8)–(3.9). However, when the transient response of the one “front” marker was compared against the two classes of markers, Takeda et al. found that it was the IFF loop that best fit the data [95].

Finally, we stress that the precise nature of the inhibition need not be biochemical. For example, there is evidence that the cortex/membrane elasticity provides inhibitory signals that prevent the cell from polarizing effectively [33, 43].

3.4 Coupling Directional Sensing to Motility

From its earliest implementations as a means of explaining the gradient sensing capabilities of *Dictyostelium* cells [51], it quickly became apparent that the LEGI mechanism suffers from one major problem: a lack of amplification. On its own, the spatial distribution of the response regulator [R in (3.9)] in the LEGI model is shallower than that of S ; see Fig. 3.8.

To illustrate why this is true we can solve for the steady-state distribution of R . Assume a one-dimensional, periodic domain, and that the stimulus is given by

$$S(\theta) = s_0 + s_1 \cos \theta, \quad \theta \in [-\pi, \pi)$$

with $0 < s_1 < s_0$ and define the relative gradient as the concentration at its peak compared to its midpoint: $S(0)/S(\pi/2) = 1 + s_1/s_0$. At steady-state, the excitation, inhibition processes, and the response regulator have distributions [49]:

$$\begin{aligned} E(\theta) &= \frac{k_e}{k_{-e}} (s_0 + s_1 \cos \theta) \\ I(\theta) &= \frac{k_i}{k_{-i}} s_0 + \frac{k_i}{k_{-i} + D_i} s_1 \cos \theta, \end{aligned}$$

$$\text{and } R(\theta) = \frac{k_r E(\theta)}{k_{-r} I(\theta)} = \frac{k_r k_e k_{-i}}{k_{-r} k_{-e} k_i} \frac{1 + (s_1/s_0) \cos \theta}{1 + \frac{k_{-i}}{k_{-i} + D_i} (s_1/s_0) \cos \theta}$$

and the relative gradient in the response is

$$\frac{R(0)}{R(\pi/2)} = \frac{1 + (s_1/s_0)}{1 + \frac{k_{-i}}{k_{-i} + D_i} (s_1/s_0)} \leq 1 + s_1/s_0.$$

Equality is only achieved if $D_i = \infty$. This represents a truly global inhibitor whose concentration is uniform throughout the environment. Note that in this case the response regulator has distribution

$$R(\theta) = 1 + (s_1/s_0) \cos \theta$$

showing that the spatial distribution represents the relative gradient: s_1/s_0 .

Several modifications to the basic LEGI mechanism have been proposed to counteract this lack of amplification, from the use of positive feedback [51], to the presence of downstream switch-like circuits [51, 52, 103].

In this latter category, we proposed that the LEGI mechanism feed into the EN discussed in Sect. 3.2.3, creating a *LEGI-biased excitable network* (LEGI-BEN) [110]. This model is expected to combine desirable features of both modules. First, the LEGI mechanism provides the adaptation property and the ability to detect spatial gradients. In the latter case, the EN greatly amplifies the shallow gradient in the response regulator to generate an amplified, downstream signal.

To couple the LEGI and BEN modules, we add a contribution to the EN input that is proportional to the LEGI response regulator:

$$U = U_{\text{basal}} + U_{\text{noise}} + U_{\text{LEGI}}, \quad (3.10)$$

where $U_{\text{LEGI}} = \lambda R$ and λ is a scaling parameter.

3.4.1 Response of LEGI-BEN to Spatially Uniform Stimulation

To test the LEGI-BEN architecture, we carried out several simulations. First, we simulated the response of the system to spatially uniform stimuli. As shown in the kymograph of this simulation in Fig. 3.9, the cell responds to the stimulus with a global rise in the activities of the activator X , followed by that of Y . The reason for this firing is that, as the LEGI mechanism responds to the rise in stimulus, the response regulator changes the equilibrium of the EN. The EN finds itself far away from the equilibrium, so it commences a trajectory around the phase plane—a process that takes approximately 30 s. As the system returns to its prestimulus level, portions of the cell undergo a second round of firings. These *second peaks*, which

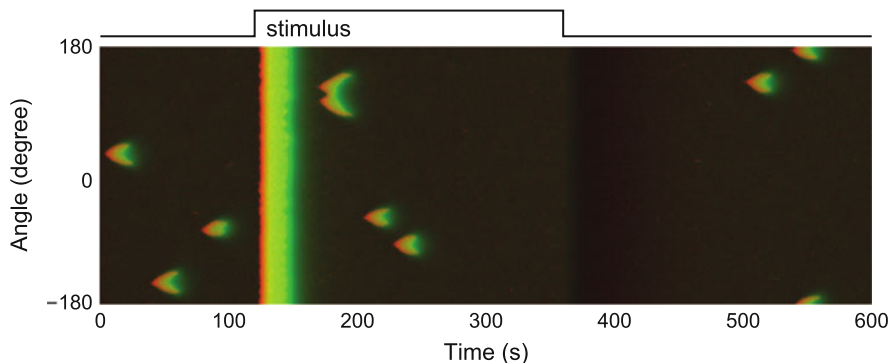


Fig. 3.9 Simulation with addition of uniform stimulus. Kymograph showing the activity of the excitation (in red) and inhibition (in green) for cell that is initially unstimulated. After 120 s the stimulus is applied and is then removed at 360 s

are seen experimentally [20, 79], occur because of the difference in the time scales between the LEGI and EN modules. The EN system has a characteristic time of approximately 30 s, which is the time that it takes for the system to reset following a firing. The LEGI mechanism, on the other hand, takes approximately 2 min to adapt completely. Thus, after 30 s, when the EN is back at its resting point, the LEGI is only partially adapted. This has the effect of reducing the threshold for firing of the EN. It is not completely eliminated, which explains why the activity is only “patchy.” A possible third round of firings is possible, but only for small portions of the cell.

There are several points to note regarding this response. First, wherever there is a firing, be it a random stochastic firing of the unstimulated system, or first or second peak responses, the intensity is approximately the same. Thus, the nature of the firing does not depend on its origin. This is in agreement with experimental characterizations of the response of cells [34, 69].

Second, once there is a firing of the EN, that particular portion of the cell experiences a refractory period during which no further firings are possible. To see this, we simulated the response of the cell to two brief stimulus pulses of duration 2 s (Fig. 3.10a). Note how the cell is unable to respond to the second stimulation. However, as we space the two pulses further apart, the cell is able to respond to the second stimulus. This refractory period is a hallmark of excitable systems and has been observed experimentally, having a recovery with half-time of approximately 8 s [34].

These simulations were repeated but allowing the LEGI mechanism to adapt fully to the first stimulus which, in this case, was 60 s long; see Fig. 3.10b. The same pattern is observed. If the delay between the end of the removal of the first stimulus and the application of the second stimulus is short, then the second stimulus does not elicit a response. However, the length of the delay required to have a response to the second stimulus is longer—a 40 s delay, which was sufficient when the first stimulus was short, does not elicit a secondary response. In this case, 60 s or more are needed.

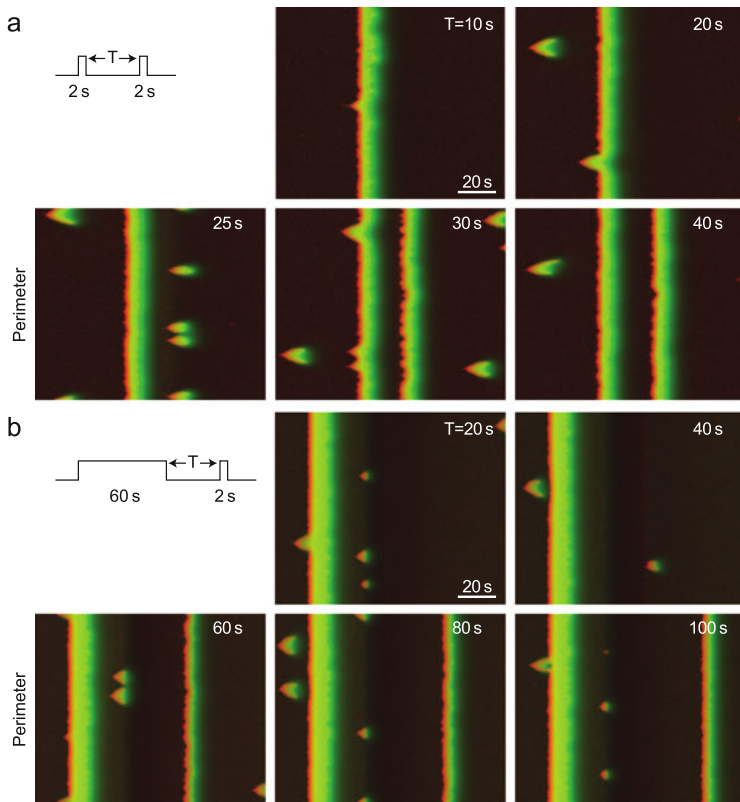


Fig. 3.10 Simulation of refractory period. (a) Response of the LEGI-BEN to consecutive 2-s pulses, spaced T seconds apart. When presented 10 or 20 s after the first, the second pulse does not elicit a second response. At 25 s spacing, a patchy response starts appearing due to the second pulse. After 30 or 40 s, the response to the second stimulus matches that of the first. These simulations also show several randomly generated patches. (b) The experiment was repeated using a longer (60 s) initial stimulus

3.4.2 Response of LEGI-BEN to Spatially Graded Stimulation

We can also test the capabilities of the LEGI-BEN to sense and amplify the external gradients. To this end, we simulated the cellular response to the imposition of a gradient (see Fig. 3.11). Note that imposition of the stimulus first causes a global response as the cell experiences a rise in chemoattractant everywhere. However, following that initial response, there is a subsequent nearly periodic response that is localized to the region of the cell where the stimulus levels are above the mean—this is roughly half the cell. This becomes more focused over time covering a smaller

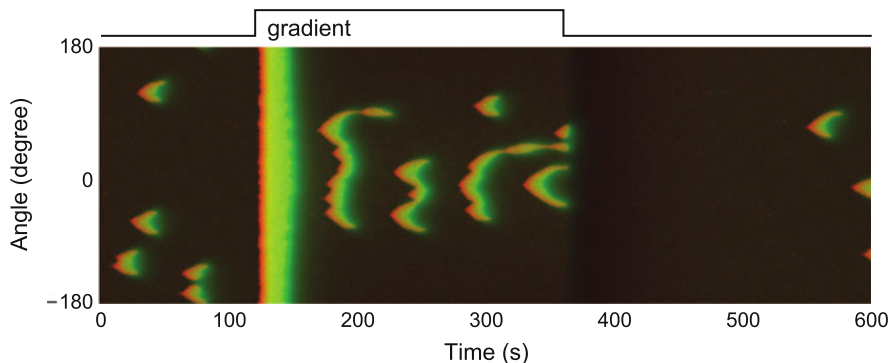


Fig. 3.11 Simulation of LEGI-BEN under spatially graded stimulus. Kymograph showing the the activity of the excitation (in red) and inhibition (in green) for cell that is initially unstimulated. At 120 s, a graded stimulus is applied with a difference of $\pm 5\%$ between front (center of the kymograph) and back (edges). This gradient was then removed at 360 s and the cell allowed to return to basal level

fraction of the cell. This is a persistent response that only disappears after removal of the stimulus, after which the cell goes quiet before eventually returning to basal levels of activity.

Several things are worth noting from the kymograph. First, the localization of activities is highly graded. In contrast to the LEGI response, in which the spatial distribution of the response is smaller than (or at best, equal to) the gradient of the external stimulus, the response of LEGI-BEN shows nearly complete abrogation at the side with lower concentration. This threshold in the response was seen and characterized experimentally [42]. Second, within the region demonstrating a response, there is a large degree of randomness. Firings can occur in different places and tend to migrate around the cell region. These “dancing crescents” have also been detected experimentally [34, 85, 104].

3.4.3 Morphological Changes Induced by LEGI-BEN

We next used the LEGI-BEN system to simulate cell migration using the LSM. These simulations demonstrated features consistent with experimental observations (Fig. 3.12). First, cells elongated in response to the external gradient and moved towards the source of the stimulus (Fig. 3.12a). Second, the precise movement of the cell exhibits the pseudopod split observed experimentally (Fig. 3.12b). The wave properties of the EN cause activity to propagate along the cell membrane. This propagation leads to morphological changes in which the protrusion alternates directions. Third, when a migrating cell is given a uniform stimulus, the initial increase in activity causes a global outward protrusion that is then followed by

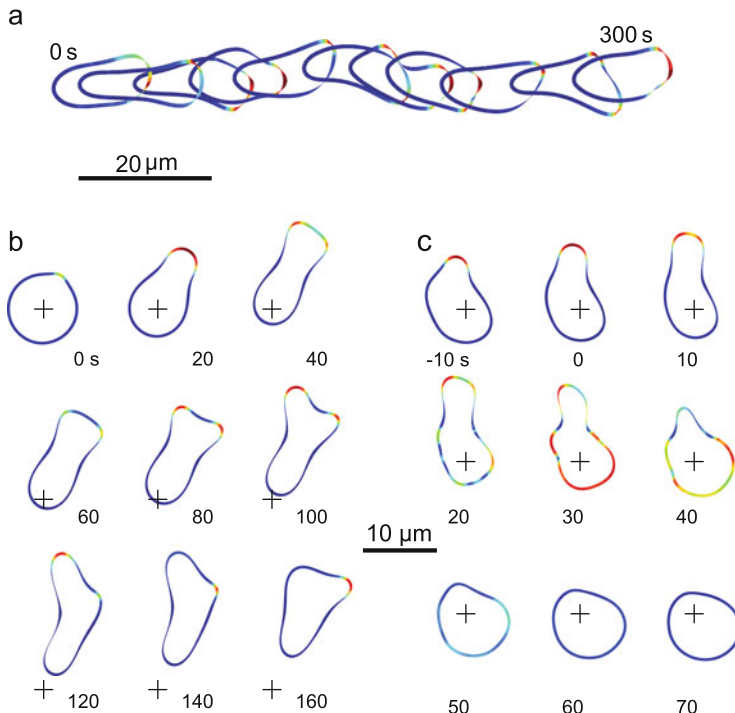


Fig. 3.12 Cellular migration achieved using the LEGI-BEN mechanism. (a) Shapes of the cell simulated by the LSM in which the protrusive stress, σ_{pro} , is obtained by solving the LEGI-BEN reaction diffusion equations. Initially, the cell started as a *circle*, 10 μm in diameter. The snapshots shown are 30 s apart and represent 300 s of movement. The gradient steepness is 19 %, to the right. (b) Pseudopod splitting in a simulation of a migrating cell using the LEGI-BEN mechanism. Note how the initial pseudopod splits in two between 20 and 40 s. Initially, the left branch is stronger (100 s) but once it stalls, the right branch becomes stronger (160 s). (c) Initial response to a uniform stimulus, followed by cell rounding, or “cringe.” Thereafter, the cell resumes its movement (not shown). Panels (b) and (c) are from [89], ©Shi et al. Used by permission under the Creative Commons Attribution License

a quiescent period in which there is no activity. Morphologically, this behavior manifests itself in the cell’s rounding up (Fig. 3.12c). This behavior is seen experimentally, where it is referred to as a “cringe” [25].

3.5 Polarization and Directional Persistence

When the cell is stimulated by a gradient, the LEGI mechanism biases the activity of the EN so that all, or nearly all, of the firings occur in the region of the cell experiencing greatest chemoattractant concentration. This causes the cell to elongate and subsequently move in the direction of the gradient, as seen in the simulations

(Fig. 3.12a). Though in the absence of a gradient the EN is triggered frequently leading to protrusions, the cell does not move away appreciably from its starting point (Fig. 3.6). This can be attributed to a lack of persistence in the directionality of the protrusions and the fact that a single protrusion is not sufficient to move the cell centroid.

To overcome these limitations in the LEGI-BEN mechanism, we developed a *Polarity* (POL) module [89]. The rationale for this system is the notion that after an EN firing, the probability that a subsequent firing occurs at the same point along the membrane should be higher, at least temporarily. To accomplish this, we proposed a positive feedback loop from the protrusive stress to the EN:

$$\frac{\partial Z}{\partial t} = -k_{-Z}Z + k_Z\sigma_{\text{pro}}$$

with Z feeding into the EN input. The effect of this equation is that, following a protrusion, the variable Z increases initially, but then begins to disappear with a half-life given by $t_{1/2} = \ln(2)/k_{-Z}$ unless it is renewed by further firings. Thus, at least for the duration of an elevated Z signal, the cell remembers the location of the firing. As such, the value of k_{-Z} is related to the persistence time of the cell's random migration. However, the precise correspondence is not straightforward because P increases with each subsequent firing.

Simulations based on this mechanism (not shown) did display an increase in persistence. An initial random firing at a given particular location led to subsequent persistent firings at that same spot along the cell. However, additional random firings occurred at other points along the membrane also led to persistent firings. Over time, the cell became hyperactive.

To overcome this hyperactivity, we proposed that POL should increase the probability of subsequent firings at locations where a firing did take place, but at the same time *lower* the probability that firings occurred elsewhere. The functional form of the resultant POL module is quite similar to LEGI. There is a local excitation (Z , as above) and a global inhibition (W) that regulate the degree of polarity (P) in complementary ways. Both processes take the protrusive stress as their input:

$$\frac{\partial Z}{\partial t} = -k_{-Z}Z + k_Z\sigma_{\text{pro}} + D_Z\nabla^2 Z \quad (3.11)$$

$$\frac{\partial W}{\partial t} = -k_{-W}W + k_W\sigma_{\text{pro}} + D_W\nabla^2 W \quad (3.12)$$

$$\frac{\partial P}{\partial t} = -k_{-P}P + k_P(Z - W). \quad (3.13)$$

For simplicity, we let D_W be sufficiently high that W is spatially independent:

$$\frac{dW}{dt} = -k_{-W}W + \frac{k_W}{2\pi} \int_{-\pi}^{\pi} \sigma_{\text{pro}}(\theta) d\theta$$

and we let $k_P = k_{-P}$ be sufficiently fast so that $P = Z - W$. Note how the polarization module is activated by signal σ_{pro} , which represents actin polymerization and is proportional to Y . Lastly, we modify (3.10) for the input to the EN so as to include a contribution from P :

$$U = U_{\text{basal}} + U_{\text{noise}} + U_{\text{LEGI}} + U_{\text{Pol}}, \quad (3.14)$$

where $U_{\text{Pol}} = \varphi P$. The parameter φ scales the relative contribution of the polarity cue with respect to that of the LEGI mechanism.

3.5.1 Simulations of LEGI-BEN-POL

To test the model with the POL module, we carried out a number of simulations. First, we considered its effect on randomly migrating cells. As seen in Fig. 3.13, cells with POL successfully migrate for their initial position, though the direction is random. Moreover, we see that the degree of migration can be modulated by the strength of POL's contribution to the EN. For example, cells without POL, or with reduced strength (low value of φ) do not venture as far from the initial position as

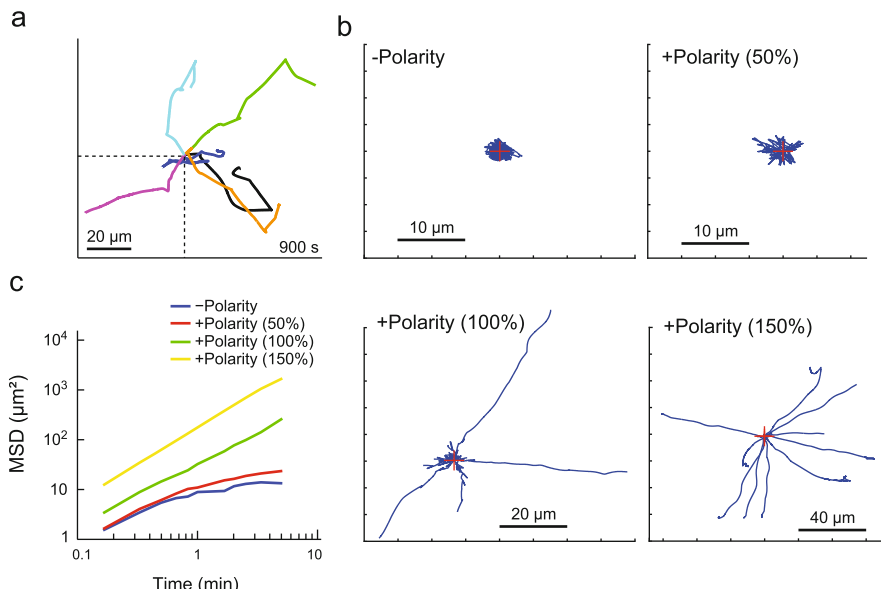


Fig. 3.13 Random migration of LEGI-BEN-POL system. (a) Individual trajectories of unstimulated cells. (b) Mean-square displacement over time of cells with varying level of strength in the POL module. (c) Individual trajectories of cells from panel (b). Figure from [89], ©Shi et al. Used by permission under the Creative Commons Attribution License

cells that have normal or increased values of φ . This average dispersion of cells is captured by plotting the mean-square displacement of cells over time (Fig. 3.13b) or by looking at individual cells' trajectories (Fig. 3.13c). Interestingly, the latter shows that for the intermediate values of φ , the degree to which cells move diffuse into the environment can be quite variable. While some cells stay close to the initial position, similar to cells with low values of φ , others migrate far away from the initial position with little turning, similar to cells with high values of φ .

We next considered the effect of the polarity module on chemotaxing cells. When exposed to chemoattractant gradients, the simulations showed preferential activity of the EN in the direction of the gradient (Fig. 3.14a). This is seen in cells with or without the polarity module. In both cases, the spatial localization of the response was greater with increasing steepness of the chemoattractant gradient. Simulations of these cells showed that they translocate further towards the chemoattractant source as the gradient steepness increases (Fig. 3.14a right panels). In all three gradients tested, cells with the polarity module show a greater degree of localization of the response in the direction of the external gradient than cells without the polarity module. This is also evident by computing the chemotactic index of these cells (Fig. 3.14b). Interestingly, at very high gradients, the advantage of the polarity module is minimal. However, at intermediate and low concentration levels, the chemotactic index was much greater with the polarity module than without it.

Experimentally, polarized cells have been shown to turn gradually in response to changes in the chemoattractant gradient. To test whether this effect was seen in our cells, we recreated this experiment. Whereas chemotaxing cells lacking the polarity module make an immediate change in their direction following the change in the gradient direction, cells with the polarity module make gradual “U-turns” ; see Fig. 3.15. Cells without or with the polarity module were introduced to a gradient (pointing to the right) and allowed to start chemotaxing for 500 s(a) or 450 s (b). At this point, the gradient direction was reversed so that it now pointed to the left. The cell without the polarity module immediately stopped moving. Any subsequent movement was in the new direction. In contrast, the cell with the polarity module makes a considerably more gradual turn, taking approximately 3–4 min before it is realigned to the new gradient location.

3.5.2 *Modeling In Silico Mutants*

One of the potential benefits of a computational model is that it allows biologists to consider the effect of various interactions on various aspects of the chemotactic response. For example, how does the strength of a feedback loop affect the chemotactic index? How is morphology affected? The ensuing in silico mutants can then be compared to genetically modified cells so as to categorize the specific contribution that the gene's product has on the signaling system.

As an illustration of this, we considered the effect of varying the strengths of the two feedback loops in the polarity module; Fig. 3.16. We reduced the strength

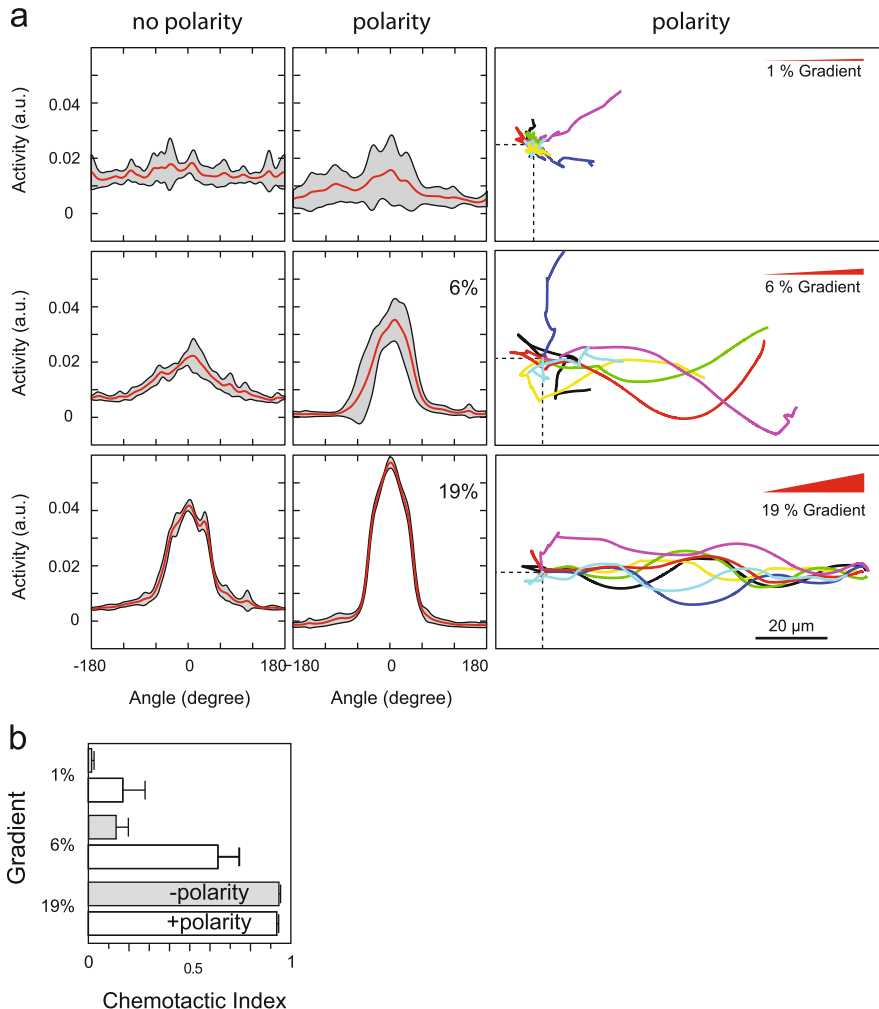


Fig. 3.14 Chemotaxis of LEGI-BEN-POL system. **(a)** The panels on the *left* show the spatial distribution of the activity of the EN (Y) of simulated cells without or with the polarity module for varying chemoattractant gradient steepness (1, 6, and 19 %). The *solid line* shows the mean and the *shaded region* marks one standard deviation away from the mean. The plots on the *right* show the response of cells to gradients of the varying steepness. All trajectories are for 900 s of simulated time. **(b)** The chemotactic index of cells without or with the polarity module was computed for varying gradient steepness. Data represent the mean and error bars of the standard deviation. Figure adapted from [89], ©Shi et al. Used by permission under the Creative Commons Attribution License

of the negative feedback loop. In simulations, these cells migrated with nearly indistinguishable chemotactic index when compared to wild-type cell simulations. However, the activity of the EN increased greatly and the cells became hyperactive.

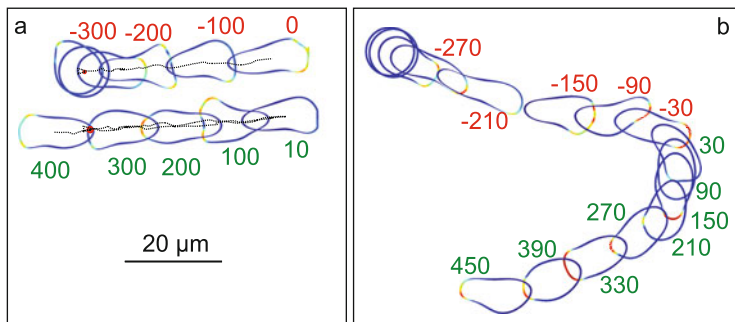


Fig. 3.15 Response of cells to changes in the gradient. Cells without (a) or with (b) the polarity module chemotaxing to a gradient (pointing to the right). The gradient was then changed (marked 0 s) so that it now pointed to the left. In the figure, the outlines of the cell without the polarity module have been moved down after the gradient change. Otherwise, these cells would completely overlap the outlines before the gradient change. This can be seen in the dotted lines that mark the trajectory of the cell, and in the red circles that mark the starting point. For the cell with the polarity module, no such change is needed. Figure adapted from [89], ©Shi et al. Used by permission under the Creative Commons Attribution License

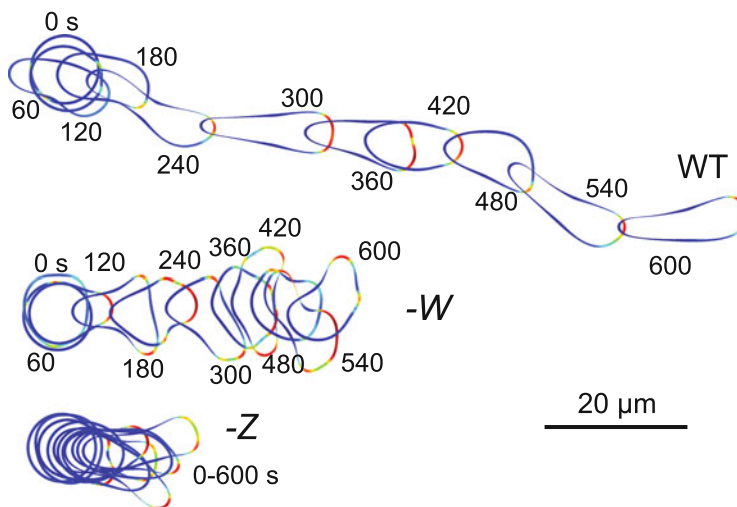


Fig. 3.16 Chemotactic ability of in silico mutants. Simulation of cells chemotaxing to a gradient (pointing to the right). The “Z” and “W” mutants have their contribution to polarity reduced by 50 % each. Figure adapted from [89], ©Shi et al. Used by permission under the Creative Commons Attribution License

Importantly, rather than increasing chemotactic migration, these cells had motility defects; they generated multiple simultaneous protrusions which, in many cases, did not point directly towards the source. Moreover, they resultant morphology had a broad area facing the gradient. The results of these simulations were reminiscent of those of *pten*-cells [40] or cells with constitutively active RasC [18]. These cells also

show elevated levels of PH-domain and actin polymerization along the leading edge. However, these elevated levels result in *less* polarized cells, and thus directional migration is reduced—as seen in our simulations.

We also simulated chemotaxis of cells where the strength of the positive feedback loop was reduced by 50 %. Once again, the alignment of these cells with the external gradient was as good as WT cells. However, the EN’s level of activity was lower and so the cells moved only slowly in the direction of the gradient. The cells in these simulations resemble cells lacking PI3K [32] which chemotax, but not as efficiently as wild-type cells.

3.6 The Cytoskeletal Oscillatory Network

As seen above, simulations of an integrated system combining LEGI, EN, and POL modules recreated most of the observed behaviors of chemotactic cells [89]. However, it combines into a single module all the excitable behavior of the signaling and cytoskeletal molecules. Recently, experiments have revealed differences between the behavior of these two classes of molecules [34].

TIRF microscopy revealed that elements of the cytoskeletal network, including HSPC300 (a component of the SCAR/Wave complex), LimE Δ coil (a sensor of actin polymerization [16]), dynacortin (an actin-crosslinking protein [43]), and coronin (a regulator of actin disassembly) undergo rapid oscillations. These patterns appear exclusively at convex regions around the perimeter of the basal surface of the cell, and have a period of approximately 10 s [34]. While they appear to push out the surface of the cell, consistent with actin polymerization protrusive forces, these extensions are small and do not propel the centroid of the cell in any meaningful way. Moreover, these oscillations are out of phase.

In contrast, signaling molecules such as the Ras-binding domain (RBD) and PH-domain-containing proteins are considerably broader, last longer but do not appear to oscillate. These observations led us to postulate that cytoskeletal and signaling molecules are part of two separate but coupled systems with distinct dynamical behaviors. The former consists of a fast, *cytoskeletal oscillatory network* (CON); the latter forming a slower, *signal transduction excitable network* (STEN), see also discussion on the cytoskeletal waves in Chap. 2.

In the STEN-CON coupled model, CON proteins are continuously active, but these oscillatory perturbations are not sufficiently strong to cause cell migration. The STEN module integrates signals from various sources (e.g., LEGI and POL modules as well as stochastic perturbations). Being an EN, super-threshold perturbations to the STEN elicit high activity that synchronizes and amplifies CON oscillations allowing actin polymerization to move forward.

3.6.1 Mathematical Description of STEN-CON

Because the STEN network exhibits the same pattern of activity previously considered by the EN network, we used the same set of equations and parameters to describe STEN:

$$\begin{aligned}\frac{\partial X_{\text{ST}}}{\partial t} &= k_{xx\text{ST}} \frac{X_{\text{ST}}^2}{k_{M_{x\text{ST}}}^2 + X_{\text{ST}}^2} - k_{-x\text{ST}} X_{\text{ST}} - k_{yx\text{ST}} Y_{\text{ST}} + k_{ux\text{ST}} U_{\text{ST}} + D_{x\text{ST}} \nabla^2 X_{\text{ST}} \\ \frac{\partial Y_{\text{ST}}}{\partial t} &= k_{xy\text{ST}} X_{\text{ST}} - k_{-y\text{ST}} Y_{\text{ST}} + D_{y\text{ST}} \nabla^2 Y_{\text{ST}}.\end{aligned}$$

In contrast, because CON components exhibit oscillatory behavior, we conjectured that this behavior could be due to limit-cycle oscillations of the underlying EN. Many excitable systems, including the FHN network, display Hopf bifurcations in response to changes in network parameters [35, 48]. These bifurcations occur as the single stable equilibrium loses stability leading to oscillatory behavior. We had previously shown that the network of (3.1) and (3.2) also displays similar Hopf bifurcations [109]. Thus, we considered the following model for the CON:

$$\begin{aligned}\frac{\partial X_{\text{CN}}}{\partial t} &= k_{xx\text{CN}} \frac{X_{\text{CN}}^2}{k_{M_{x\text{CN}}}^2 + X_{\text{CN}}^2} - k_{-x\text{CN}} X_{\text{CN}} - k_{yx\text{CN}} Y_{\text{CN}} + k_{ux\text{CN}} U_{\text{CN}} + D_{x\text{CN}} \nabla^2 X_{\text{CN}} \\ \frac{\partial Y_{\text{CN}}}{\partial t} &= k_{xy\text{CN}} X_{\text{CN}} - k_{-y\text{CN}} Y_{\text{CN}} + D_{y\text{CN}} \nabla^2 Y_{\text{CN}}.\end{aligned}$$

Note that it has the same format as the EN above. The only difference is in the nature of the equilibrium as determined by the different parameter values.

Our attempts to recreate the oscillatory behavior of CON proteins with this network with oscillatory parameters were unsuccessful. As expected, the system oscillated, but the oscillations tended to synchronize in the cell (not shown). In contrast, we found that we could obtain oscillatory behavior from the simulations if we assumed a different point along the bifurcation diagram. Both the FHN and the EN in (3.1) and (3.2) can also exhibit bistability, in which two stable equilibria coexist; see Fig. 3.17. If these equilibria occur near the bifurcation points, both can exhibit excitable-like behavior, in which super-threshold perturbations cause the system to move from one equilibrium to the other (i.e., low-to-high or high-to-low). These changes, of course, are stochastic in nature, and hence are not guaranteed. However, in the presence of sufficiently high level of noise relative to the size of the threshold, they occur with sufficiently high frequency as to be nearly indistinguishable from noise [45, 102, 107]. We found that these stochastic oscillations could recreate the behavior of the system accurately; see Fig. 3.17.

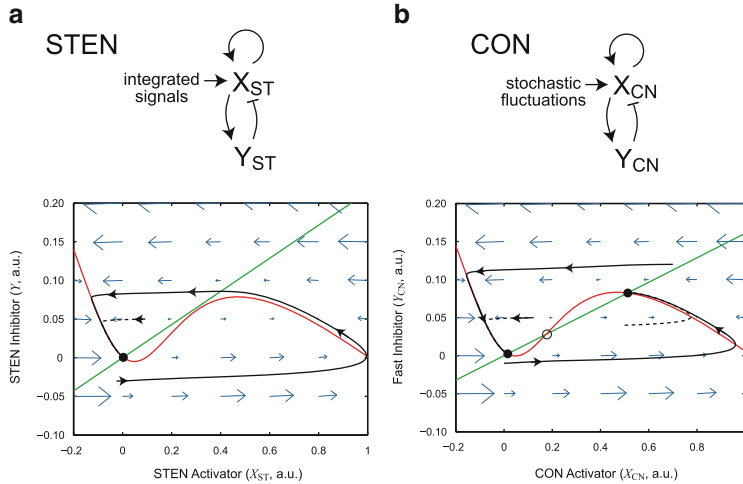


Fig. 3.17 Phase-plane description of STEN and CON modules. The STEN and CON modules are described by activator-inhibitor systems. On the right, we show the two nullclines for the systems: the activator, X nullclines in red; the inhibitor, Y nullclines in green. In STEN, the two nullclines meet at only one stable equilibrium (marked by small black circle). Small deviations from this equilibrium can lead to large excursions (see black line) before the system returns to its unique steady-state. In the CON, the nullclines intersect at three different points: two stable (black circles) and one unstable (white circle). The two stable equilibria correspond to points of low and high activity. In both cases, deviations from these points will cause the system to switch to the other equilibria. In the presence of sufficient noise, these changes will occur with high regulatory, giving rise to stochastic oscillations. Figure adapted from Ref [34], ©Huang et al. Used by permission

3.6.2 STEN-CON Coupling

We have not yet specified the inputs to both modules. For the STEN, we assume that

$$U_{ST} = U_{\text{basal-ST}} + U_{\text{noise}} + U_{\text{LEGI}} + U_{\text{Pol}} + f(X_{CN}). \quad (3.15)$$

Except for the last term, all other contributions to the input are as in the LEGI-BEN-POL network described in (3.10) above. The function $f(X_{CN})$ in (3.15) is used to trigger STEN based on the activity of CON. To this end, we first integrate nearby CON activity:

$$\tilde{X}_{CN}(\theta_0) = \int_{\theta_0 - \Delta\theta}^{\theta_0 + \Delta\theta} X_{CN}(\theta) d\theta$$

using $\Delta\theta = 15^\circ$ to specify the integration width. This weighted activity is then compared to a threshold:

$$h(X_{CN}(\theta)) = \begin{cases} 0, & \text{if } \tilde{X}_{CN}(\theta) < \tilde{X}_{CN-\text{th}} \\ 1, & \text{otherwise.} \end{cases}$$

Finally, the coupling term $f(X_{\text{CN}})$ is obtained by multiplying this function by a stochastic component:

$$f(X_{\text{CN}}(\theta)) = h(X_{\text{CN}}(\theta))\tilde{N}_{\text{CN}}. \quad (3.16)$$

Here $\tilde{U}_{\text{noise-CN}}$ is a white noise process with unit variance and a mean of 0.05.

For CON, we assumed that

$$U_{\text{CN}} = U_{\text{basal-CN}} + U_{\text{noise-CN}} + g(X_{\text{ST}}). \quad (3.17)$$

The first two terms are basal and stochastic contributions. The function of $g(X_{\text{ST}})$ is simply a binary function based on whether the activity of the STEN is above or below a threshold:

$$g(X_{\text{ST}}(\theta)) = \begin{cases} g_B, & \text{if } X_{\text{ST}}(\theta) < X_{\text{ST-th}} \\ g_S, & \text{otherwise.} \end{cases}$$

Parameter values for this network are all found in Table 3.4.

3.6.3 Simulations of Coupled STEN-CON Systems

We carried out simulations of the STEN-CON system for unstimulated cells; in these simulations, we do not incorporate a contribution from the POL module ($U_{\text{Pol}} = 0$). In kymographs, STEN activity displays random patches reminiscent of those seen in the EN; see Fig. 3.17a. In contrast, the activity of the CON displays numerous small-scale oscillations around the perimeter. These oscillations can be present even a times and places along the cell perimeter where the STEN is quiescent. However, whenever and wherever the STEN fires, the level of activity of CON also increases—the regions where the CON was oscillating become broader.

When we used the CON activity to drive cellular protrusions using the LSM, we found that the oscillatory regions give rise to small-scale undulations of the perimeter, as seen experimentally. However, the agglomeration of CON activity that follows the triggering of STEN leads to a large-scale protrusions that allow the cell to move; see Figs. 3.17b, 3.18.

Fig. 3.18 Simulation of STEN-CON coupling model. (a) Kymographs describing the activities of the STEN and CON systems around the perimeter of the circle. (b) Intensity plots of the slow and fast systems corresponding to rectangles 1 and 2 in panel (a). (c) The activity of the CON was used to drive protrusions in the LSM framework. Shown are three snapshots of the activity (using Y as a marker) around the perimeter for STEN (green), CON (red), and merged. Note that at 90 s, the only activity seen is in the CON, where small-scale oscillations are present. At 120 s, the STEN begins to fire (marked by the *white arrow*). Thereafter, both STEN and CON show elevated levels. The cell also has a large protrusion there, marked by the *dotted square*. These simulations do not assume constant volume, as they attempt to recreate the basal surface of the cell observed using TIRF microscopy. Reprinted from [34], with permission

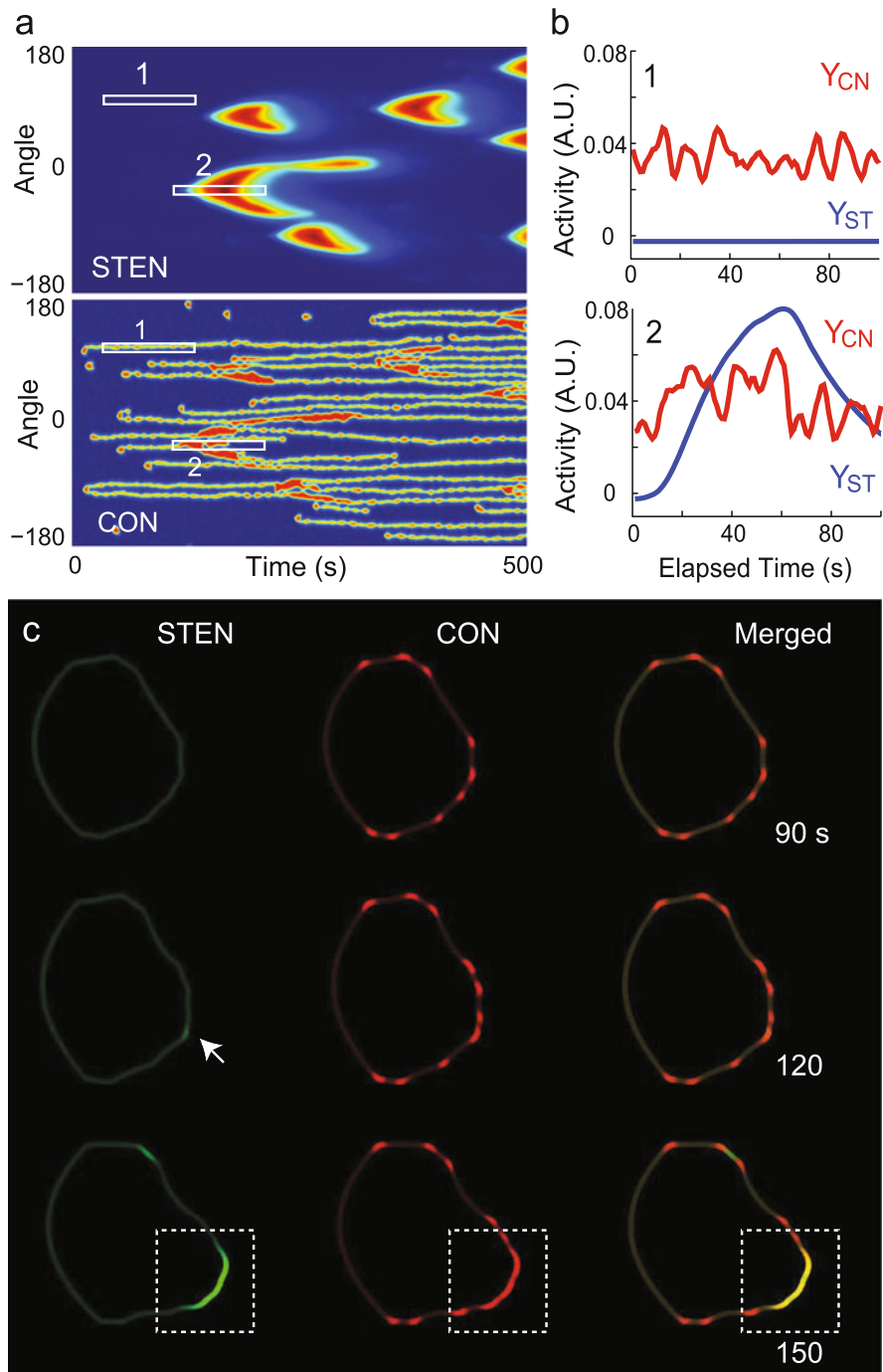


Fig. 3.18 (continued)

3.7 Discussion and Conclusions

Depending on the experimental conditions, chemotactic cells display a wide array of behaviors, summarized in Table 3.1. The model presented here recreates these behaviors. The modular nature of the module suggests a number of questions.

Do cells really use a modular network or could the elements be integrated? It is difficult to state with certainty whether cells use a modular network. Clearly, the *behavior* of cells follows the delineation that we propose here. For example, *Dictyostelium* cells undergo a transformation from an unpolarized to a polarized state, so polarity is something that is intrinsically different from migration or gradient sensing. It is possible that the loops that we introduce as part of the POL module could be included into the EN as additional excitation and inhibition signals. Similarly, in our model, we set the LEGI module as something separate from the EN, in which the LEGIs excitation and inhibition signals dictate the level

Table 3.1 Behaviors simulated; adapted from [89]

| Behavior | | |
|-----------------------------------|-----------------------------------|---|
| <i>Unstimulated cells</i> | | |
| 1. | Persistent motion | [11, 13, 14, 54, 94, 98] |
| 2. | Pseudopod splitting | [3, 13, 111] |
| 3. | Random activity patches | [61, 75, 78] |
| 4. | Excitable behavior | [5, 6, 15, 28, 29, 59, 97, 100, 108, 110] |
| 5. | Oscillatory cytoskeletal activity | [34] |
| <i>Spatially uniform stimulus</i> | | |
| 6. | Freeze, cringe, spread | [25] |
| 7. | Transient signaling events | [20, 78, 79, 95] |
| 8. | Long-term adaptation | [21, 60, 75, 99, 105, 119] |
| <i>Spatially graded stimulus</i> | | |
| 9. | Directional response/migration | Many |
| 10. | Biased location of patches | [84, 96] |
| 11. | Amplified response | [42, 73] |
| 12. | Response to simultaneous cues | [42] |
| 13. | Sensitivity adjustment | [21, 42, 99, 119] |
| 14. | Adjustment of polarity | [93] |
| 15. | Turning to changing gradient | [3, 27, 93] |

References refer to published experimental observations of these behaviors

of response regulator output outside the EN. These two complementary signals could, in theory, enter the EN at different points or even be part of the EN itself. One model that integrates several of these signals is that due to Meinhardt [62] which can also recreate many of the behaviors of chemotaxing cells [55, 70]. This model has two negative feedback loops into the EN (roughly equivalent to introducing W into EN) and a single positive feedback loop (equivalent to incorporating Z into the autocatalytic loop in X). Moreover, it does not have perfect adaptation; rather, the external chemoattractant signal S feeds directly into the EN. Recent experiments, however, reveal that the form of the Meinhardt model, whereby adaptation is achieved as a feedback process, does not recreate the double stimulation experiments of Fig. 3.10 [96].

Does the need to introduce additional components to account for new experimental evidence not point to a weakness of the model? As we characterize the *behavior* of chemotaxing cells in greater detail, it is not surprising that we will come across behaviors that cannot be represented by the existing model. It is important to note that the complexity of the model, even if one includes all its modules, is orders of magnitude simpler than that of the real network. For example, it is known that at least four independent pathways regulate chemotaxis. In the model presented here there is a single direct pathway from the chemoattractant signal to the protrusive forces.

Since the elements of each module are phenomenological, what use is such a model to an experimentalist? We do not presume to speak for experimental biologists, but it is clear that a system as complicated as that regulating chemotaxis in amoebae requires some level of abstraction if one is to understand the underlying network. A model at the level of detail presented here provides a framework for this understanding. While it is true that we choose not to label the models components with biochemical entities, we do so because we believe that the current level of understanding of the system does not allow it. Nevertheless, a conceptual model such as this one can still make experimentally testable predictions.

Acknowledgements Much of the research described here is the work of two very talented graduate students: Yuan Xiong, currently at Novartis, and Changji Shi, who works at Oracle. We also benefited greatly from discussions with Dr. Chuan-Hsiang (Bear) Huang. The movie 8 was created by Flori Yellin, working on an summer REU in my lab. Finally, I wish to acknowledge Peter N. Devreotes, with whom I have had a long-standing collaboration. None of this work would have been possible without him. Over the years, the work described in this chapter was funded in part by the NIH through grants to PAI and PND.

Appendix

Below we briefly discuss the choice of parameters for the various modules.

Numerical Parameters of LEGI-BEN-POL

Because the model is an abstraction of the underlying network, the parameters do not have physical meaning. In our simulations, they were obtained empirically by specifying certain desirable behavior matching observed phenomena (frequency of firings, size of firings, etc.) and fitting them using a least-squares optimization [110]. The nominal parameter values are given in Table 3.2.

Sensitivity analysis of the network shows that, in most cases, the model is quite insensitive to parameter changes [89]. In fact, several simulations have been done using parameters different from the nominal ones. For example, it is possible to vary the LEGI parameters almost arbitrarily without affecting the module’s ability to recreate perfect adaptation [51]. Where the model is most sensitive is in the “distance” between the LEGI basal level and the EN threshold. For the system to generate sufficient amplification, these two values must be close—but not so close as to have the unstimulated cell constantly crossing the threshold. The relative distance between these two points is affected by a number of parameters, including the strengths of the two loops in the EN. Note that this is a general weakness of any model that relies on threshold. An important area of research would be how to study how cells can operate near these bifurcation points [66].

Table 3.2 Parameters of
LEGI, EN, and POL modules

| LEGI module | | | |
|-------------|--------------------------------|--------------------|--------------------------------|
| k_e | 0.5 s^{-1} | k_{-e} | 0.5 s^{-1} |
| k_i | 0.1 s^{-1} | k_{-i} | 0.1 s^{-1} |
| k_r | 0.06 s^{-1} | k_{-r} | 0.1 s^{-1} |
| D_I | $1 \mu\text{m}^2/\text{s}$ | | |
| EN module | | | |
| k_{xx} | 2.5 s^{-1} | k_{xy} | 0.019 s^{-1} |
| k_{-x} | 2.3 s^{-1} | k_{-y} | 0.088 s^{-1} |
| k_M | 0.32 | U_{basal} | -0.063 |
| k_{yx} | 8.6 s^{-1} | k_{ux} | 0.8 s^{-1} |
| D_X | $0.016 \mu\text{m}^2/\text{s}$ | D_Y | $0.038 \mu\text{m}^2/\text{s}$ |
| λ | 2 | φ | 2 |
| POL module | | | |
| k_Z | 0.023 s^{-1} | k_{-Z} | 0.015 s^{-1} |
| k_W | 0.035 s^{-1} | k_{-W} | 0.012 s^{-1} |
| D_Z | $0.04 \mu\text{m}^2/\text{s}$ | | |

Table 3.3 Mechanical parameters used to simulate cell movement

| Parameter | Value | Units |
|-------------------|-------|---------------------------------|
| K | 0.098 | $\text{nN } \mu\text{m}^{-3}$ |
| D | 0.064 | $\text{nN } \mu\text{m}^{-3}$ |
| B | 6.09 | $\text{nN s } \mu\text{m}^{-3}$ |
| γ | 1.00 | $\text{nN } \mu\text{m}$ |
| σ_0 | 35 | $\text{nN s } \mu\text{m}^{-3}$ |
| k_{area} | 1 | $\text{nN } \mu\text{m}^{-2}$ |

Mechanical Parameters Used to Simulate Cell Movement

The viscoelastic model used here to describe cellular deformations is also a simplification of the underlying mechanical system. These parameters were obtained by fitting experimental measurements of aspirated wild-type *Dictyostelium* cells using a micropipette [77, 114]. They are given in Table 3.3. Similar measurements for a number of genetically modified *Dictyostelium* strains are given by Luo et al. in [56].

Numerical Parameters of the STEN-CON Coupled Network

Finally, we present the model parameters for the STEN-CON coupled network (Table 3.4). The STEN is meant to recreate the parameters of the EN above. The CON altered parameters so that the system exhibits bistability. Note that in the LSM simulations, volume conservation is not included, since these simulations were meant to recreate the shapes and patterns of activity seen in TIRM images. Since these capture only the basal membrane of the cell, the surface area in contact with the slide is not conserved.

Supplementary Movies

1. Activity of the excitable network simulated in a two-dimensional surface; see Fig. 3.2. The movie is recreated from [110].
2. Changes in cellular morphology due to random EN firings in an unstimulated cell; see Fig. 3.6. Movie from [89], ©Shi et al. Used by permission under the Creative Commons Attribution License.
3. Response of a cell lacking the polarity module to a spatial gradient; see Fig. 3.12a.
4. Random migration of five cells with the LEGI-BEN-POL set of modules, but no external gradient. Compare with the trajectories traced in Fig. 3.13a. Movie from [89], ©Shi et al. Used by permission under the Creative Commons Attribution License.

Table 3.4 STEN-CON model parameters

| STEN | | | |
|-----------------------|---------------------------------|--------------------|---------------------------------|
| $k_{xx\text{ST}}$ | 0.7 s^{-1} | $k_{xy\text{ST}}$ | 0.0051 s^{-1} |
| $k_{-x\text{ST}}$ | 0.63 s^{-1} | $k_{-x\text{ST}}$ | 0.024 s^{-1} |
| $k_{yx\text{ST}}$ | 2.35 s^{-1} | $k_{yx\text{ST}}$ | 1 s^{-1} |
| $D_{x\text{ST}}$ | $0.0059 \mu\text{m}^2/\text{s}$ | $D_{y\text{ST}}$ | $0.0151 \mu\text{m}^2/\text{s}$ |
| $k_{M\text{ST}}$ | 0.32 | | |
| $U_{\text{basal-ST}}$ | -0.0138 | U_{noise} | 0 |
| CON | | | |
| $k_{xx\text{CN}}$ | 0.19 s^{-1} | $k_{xy\text{CN}}$ | 0.0011 s^{-1} |
| $k_{-x\text{CN}}$ | 0.18 s^{-1} | $k_{-x\text{CN}}$ | 0.0067 s^{-1} |
| $k_{yx\text{CN}}$ | 0.65 s^{-1} | $k_{yx\text{CN}}$ | 1 s^{-1} |
| $D_{x\text{CN}}$ | $0.091 \mu\text{m}^2/\text{s}$ | $D_{y\text{CN}}$ | $0.0236 \mu\text{m}^2/\text{s}$ |
| $k_{M\text{CN}}$ | 0.32 | | |
| $U_{\text{basal-CN}}$ | 0.1 | U_{noise} | 0 |
| STEN-CON coupling | | | |
| $X_{\text{CN-th}}$ | 7 A.U. | $X_{\text{ST-th}}$ | 0 A.U. |
| g_B | 1.25 A.U. | g_{sig} | 1.3 A.U. |

5. Change in the directional movement of an unpolarized cell in changing gradients. The initial 19 % gradient, which pointed to the top was switched to point towards the bottom at 500 s. This simulation corresponds to Fig. 3.15a, though it was rotated to fit the figure better. Movie from [89], ©Shi et al. Used by permission under the Creative Commons Attribution License.
6. Change in the directional movement of an unpolarized cell in changing gradients. An initial 6 % gradient pointing to the right was applied at 300 s. It was subsequently switched to point towards the top at 900 s. Movie from [89], ©Shi et al. Used by permission under the Creative Commons Attribution License.
7. Change in the directional movement of polarized cell in changing gradients. An initial 6 % gradient pointing to the right was applied at 300 s. It was subsequently switched to point towards the top at 900 s. Movie from [89], ©Shi et al. Used by permission under the Creative Commons Attribution License.
8. Movement of a LEGI-BEN-POL cell in a bifurcating channel. The cell is responding to a point source gradient located at the top “+” sign. The channel was made to resemble experiments using neutrophils [2, Fig. 2].

References

1. U. Alon, M.G. Surette, N. Barkai, S. Leibler, Robustness in bacterial chemotaxis. *Nature* **397**(6715), 168–171 (1999)
2. V. Ambravaneswaran, I.Y. Wong, A.J. Aranyosi, M. Toner, D. Irimia, Directional decisions during neutrophil chemotaxis inside bifurcating channels. *Integr. Biol. (Camb.)* **2**(11–12), 639–647 (2010)

3. N. Andrew, R.H. Insall, Chemotaxis in shallow gradients is mediated independently of PtdIns 3-kinase by biased choices between random protrusions. *Nat. Cell Biol.* **9**(2), 193–200 (2007)
4. B.W. Andrews, P.A. Iglesias, E.D. Sontag, Signal detection and approximate adaptation implies an approximate internal model, in *2006 45th IEEE Conference on Decision and Control*, pp. 2364–2369 (IEEE, 2006)
5. Y. Arai, T. Shibata, S. Matsuoka, M.J. Sato, T. Yanagida, M. Ueda, Self-organization of the phosphatidylinositol lipids signaling system for random cell migration. *Proc. Natl. Acad. Sci. U.S.A.* **107**(27), 12399–12404 (2010)
6. Y. Asano, A. Nagasaki, T.Q.P. Uyeda, Correlated waves of actin filaments and PIP3 in *Dictyostelium* cells. *Cell Motil. Cytoskeleton* **65**(12), 923–34 (2008)
7. Y. Bao, Y. Chen, C. Ledderose, L. Li, W.G. Junger, Pannexin 1 channels link chemoattractant receptor signaling to local excitation and global inhibition responses at the front and back of polarized neutrophils. *J. Biol. Chem.* **288**(31), 22650–22657 (2013)
8. N. Barkai, S. Leibler, Robustness in simple biochemical networks. *Nature* **387**(6636), 913–917 (1997)
9. H.C. Berg, E.M. Purcell, Physics of chemoreception. *Biophys. J.* **20**(2), 193–219 (1977)
10. D.A. Bloes, D. Kretschmer, A. Peschel, Enemy attraction: bacterial agonists for leukocyte chemotaxis receptors. *Nat. Rev. Microbiol.* **13**(2), 95–104 (2015)
11. H. Bödeker, C. Beta, T. Frank, E. Bodenschatz, Quantitative analysis of random amoeboid motion. *Europhys. Lett.* **90**(2), 28005 (2010)
12. S. Bose, J. Cho, Role of chemokine CCL2 and its receptor CCR2 in neurodegenerative diseases. *Arch. Pharm. Res.* **36**(9), 1039–1050 (2013)
13. L. Bosgraaf, P.J.M. Van Haastert, Navigation of chemotactic cells by parallel signaling to pseudopod persistence and orientation. *PLoS One* **4**(8), e6842 (2009)
14. L. Bosgraaf, P.J.M. Van Haastert, The ordered extension of pseudopodia by amoeboid cells in the absence of external cues. *PLoS One* **4**(4), e5253 (2009)
15. T. Bretschneider, J. Jonkman, J. Köhler, O. Medalia, K. Barisic, I. Weber, E.H.K. Stelzer, W. Baumeister, G. Gerisch, Dynamic organization of the actin system in the motile cells of *Dictyostelium*. *J. Muscle Res. Cell. Motil.* **23**(7–8), 639–649 (2002)
16. T. Bretschneider, S. Diez, K. Anderson, J. Heuser, M. Clarke, A. Müller-Taubenberger, J. Köhler, G. Gerisch, Dynamic actin patterns and Arp2/3 assembly at the substrate-attached surface of motile cells. *Curr. Biol.* **14**(1), 1–10 (2004)
17. T. Bretschneider, K. Anderson, M. Ecke, A. Müller-Taubenberger, B. Schroth-Diez, H.C. Ishikawa-Ankerhold, G. Gerisch, The three-dimensional dynamics of actin waves, a model of cytoskeletal self-organization. *Biophys. J.* **96**(7), 2888–2900 (2009)
18. H. Cai, S. Das, Y. Kamimura, Y. Long, C.A. Parent, P.N. Devreotes, Ras-mediated activation of the TORC2-PKB pathway is critical for chemotaxis. *J. Cell. Biol.* **190**(2), 233–45 (2010)
19. A.E. Carlsson, Dendritic actin filament nucleation causes traveling waves and patches. *Phys. Rev. Lett.* **104**(22), 228102 (2010)
20. L. Chen, C. Janetopoulos, Y.E. Huang, M. Iijima, J. Borleis, P.N. Devreotes, Two phases of actin polymerization display different dependencies on PI(3,4,5)P3 accumulation and have unique roles during chemotaxis. *Mol. Biol. Cell* **14**(12), 5028–5037 (2003)
21. P.N. Devreotes, T.L. Steck, Cyclic 3',5' AMP relay in *Dictyostelium discoideum*. II. Requirements for the initiation and termination of the response. *J. Cell Biol.* **80**(2), 300–309 (1979)
22. M.C. Dinauer, T.L. Steck, P.N. Devreotes, Cyclic 3',5'-AMP relay in *Dictyostelium discoideum*. V. Adaptation of the cAMP signaling response during cAMP stimulation. *J. Cell Biol.* **86**(2), 554–561 (1980)
23. J.A. Ditlev, N.M. Vacanti, I.L. Novak, L.M. Loew, An open model of actin dendritic nucleation. *Biophys. J.* **96**(9), 3529–3542 (2009)
24. R. Fitzhugh, Impulses and physiological states in theoretical models of nerve membrane. *Biophys. J.* **1**(6), 445–466 (1961)
25. R.P. Futrelle, *Dictyostelium* chemotactic response to spatial and temporal gradients. Theories of the limits of chemotactic sensitivity and of pseudochemotaxis. *J. Cell. Biochem.* **18**(2), 197–212 (1982)

26. M.H. Gail, C.W. Boone, The locomotion of mouse fibroblasts in tissue culture. *Biophys. J.* **10**(10), 980–993 (1970)
27. G. Gerisch, H. Fromm, A. Huesgen, U. Wick, Control of cell-contact sites by cyclic AMP pulses in differentiating *Dictyostelium* cells. *Nature* **255**(5509), 547–549 (1975)
28. G. Gerisch, T. Bretschneider, A. Müller-Taubenberger, E. Simmeth, M. Ecke, S. Diez, K. Anderson, Mobile actin clusters and traveling waves in cells recovering from actin depolymerization. *Biophys. J.* **87**(5), 3493–3503 (2004)
29. G. Gerisch, B. Schroth-Diez, A. Müller-Taubenberger, M. Ecke, PIP3 waves and PTEN dynamics in the emergence of cell polarity. *Biophys. J.* **103**(6), 1170–1178 (2012)
30. L.H. Hartwell, J.J. Hopfield, S. Leibler, A.W. Murray, From molecular to modular cell biology. *Nature* **402**(6761 Suppl), C47–C52 (1999)
31. A.L. Hodgkin, A.F. Huxley, A quantitative description of membrane current and its application to conduction and excitation in nerve. *J. Physiol.* **117**(4), 500–544 (1952)
32. O. Hoeller, R.R. Kay, Chemotaxis in the absence of PIP3 gradients. *Curr. Biol.* **17**(9), 813–817 (2007)
33. A.R. Houk, A. Jilkine, C.O. Mejean, R. Boltyanskiy, E.R. Dufresne, S.B. Angenent, S.J. Altschuler, L.F. Wu, O.D. Weiner, Membrane tension maintains cell polarity by confining signals to the leading edge during neutrophil migration. *Cell* **148**(1–2), 175–188 (2012)
34. C.-H. Huang, M. Tang, C. Shi, P.A. Iglesias, P.N. Devreotes, An excitable signal integrator couples to an idling cytoskeletal oscillator to drive cell migration. *Nat. Cell Biol.* **15**(11), 1307–1316 (2013)
35. P. Iglesias, Excitable systems in cell motility, in *2013 IEEE 52nd Annual Conference on Decision and Control (CDC)*, pp. 757–762, Florence (2013)
36. P.A. Iglesias, P.N. Devreotes, Navigating through models of chemotaxis. *Curr. Opin. Cell Biol.* **20**(1), 35–40 (2008)
37. P.A. Iglesias, P.N. Devreotes, Biased excitable networks: how cells direct motion in response to gradients. *Curr. Opin. Cell Biol.* **24**(2), 245–253 (2012)
38. P.A. Iglesias, A. Levchenko, Modeling the cell’s guidance system. *Sci. STKE* **2002**(148), re12 (2002)
39. P.A. Iglesias, C. Shi, Comparison of adaptation motifs: temporal, stochastic and spatial responses. *IET Syst. Biol.* **8**(6), 268–281 (2014)
40. M. Iijima, Y.E. Huang, P. Devreotes, Temporal and spatial regulation of chemotaxis. *Dev. Cell* **3**(4), 469–478 (2002)
41. C. Janetopoulos, P. Devreotes, Phosphoinositide signaling plays a key role in cytokinesis. *J. Cell Biol.* **174**(4), 485–490 (2006)
42. C. Janetopoulos, L. Ma, P.N. Devreotes, P.A. Iglesias, Chemoattractant induced phosphatidylinositol 3,4,5-trisphosphate accumulation is spatially amplified and adapts, independent of the actin cytoskeleton. *Proc. Natl. Acad. Sci. U.S.A.* **101**(24), 8951–8956 (2004)
43. C. Kabacoff, Y. Xiong, R. Musib, E.M. Reichl, J. Kim, P.A. Iglesias, D.N. Robinson, Dynacortin facilitates polarization of chemotaxing cells. *BMC Biol.* **5**, 53 (2007)
44. T. Killich, P.J. Plath, X. Wei, H. Bultmann, L. Rensing, M.G. Vicker, The locomotion, shape and pseudopodial dynamics of unstimulated *Dictyostelium* cells are not random. *J. Cell Sci.* **106**(Pt 4), 1005–1013 (1993)
45. J. Kim, P. Heslop-Harrison, I. Postlethwaite, D.G. Bates, Stochastic noise and synchronisation during *Dictyostelium* aggregation make cAMP oscillations robust. *PLoS Comput. Biol.* **3**(11), e218 (2007)
46. S.-J. Kim, Z. Chen, N.D. Chamberlain, A.B. Essani, M.V. Volin, M.A. Amin, S. Volkov, E.M. Gravallese, S. Arami, W. Swedler, N.E. Lane, A. Mehta, N. Sweiss, S. Shahrara, Ligation of TLR5 promotes myeloid cell infiltration and differentiation into mature osteoclasts in rheumatoid arthritis and experimental arthritis. *J. Immunol.* **193**(8), 3902–3913 (2014)
47. D.E. Koshland Jr., A response regulator model in a simple sensory system. *Science* **196**(4294), 1055–1063 (1977)
48. T. Kostova, R. Ravindran, M. Schonbek, FitzHugh-Nagumo revisited: types of bifurcations, periodical forcing and stability regions by a Lyapunov functional. *Int. J. Bifurcation Chaos* **14**(03), 913–925 (2004)

49. J. Krishnan, P.A. Iglesias, Analysis of the signal transduction properties of a module of spatial sensing in eukaryotic chemotaxis. *Bull. Math. Biol.* **65**(1), 95–128 (2003)
50. D.A. Lauffenburger, Influence of external concentration fluctuations on leukocyte chemotactic orientation. *Cell Biophys.* **4**(2–3), 177–209 (1982)
51. A. Levchenko, P.A. Iglesias, Models of eukaryotic gradient sensing: application to chemotaxis of amoebae and neutrophils. *Biophys. J.* **82**(1/Pt 1), 50–63 (2002)
52. H. Levine, D.A. Kessler, W.-J. Rappel, Directional sensing in eukaryotic chemotaxis: a balanced inactivation model. *Proc. Natl. Acad. Sci. U.S.A.* **103**(26), 9761–9766 (2006)
53. L. Li, S.F. Nørrelykke, E.C. Cox, Persistent cell motion in the absence of external signals: a search strategy for eukaryotic cells. *PLoS One* **3**(5), e2093 (2008)
54. L. Li, E.C. Cox, H. Flyvbjerg, Dicty dynamics': *Dictyostelium* motility as persistent random motion. *Phys. Biol.* **8**(4), 046006 (2011)
55. R. Lockley, G. Ladds, T. Bretschneider, Image based validation of dynamical models for cell reorientation. *Cytometry A*, 471–480 (2015)
56. W. Luo, C.-h. Yu, Z.Z. Lieu, J. Allard, A. Mogilner, M.P. Sheetz, A.D. Bershadsky, Analysis of the local organization and dynamics of cellular actin networks. *J. Cell Biol.* **202**(7), 1057–1073 (2013)
57. W. Ma, A. Trusina, H. El-Samad, W.A. Lim, C. Tang, Defining network topologies that can achieve biochemical adaptation. *Cell* **138**(4), 760–773 (2009)
58. S.A. MacKay, Computer simulation of aggregation in *Dictyostelium discoideum*. *J. Cell Sci.* **33**, 1–16 (1978)
59. Y.T. Maeda, J. Inose, M.Y. Matsuo, S. Iwaya, M. Sano, Ordered patterns of cell shape and orientational correlation during spontaneous cell migration. *PLoS One* **3**(11), e3734 (2008)
60. R. Meili, C. Ellsworth, S. Lee, T.B. Reddy, H. Ma, R.A. Firtel, Chemoattractant mediated transient activation and membrane localization of Akt/PKB is required for efficient chemotaxis to cAMP in *Dictyostelium*. *EMBO J.* **18**(8), 2092–2105 (1999)
61. R. Meili, C. Ellsworth, R.A. Firtel, A novel Akt/PKB-related kinase is essential for morphogenesis in *Dictyostelium*. *Curr. Biol.* **10**(12), 708–717 (2000)
62. H. Meinhardt, Orientation of chemotactic cells and growth cones: models and mechanisms. *J. Cell Sci.* **112**(Pt 17), 2867–2874 (1999)
63. G.-L. Ming, S.T. Wong, J. Henley, X.-B. Yuan, H.-J. Song, N.C. Spitzer, M.-M. Poo, Adaptation in the chemotactic guidance of nerve growth cones. *Nature* **417**(6887), 411–418 (2002)
64. A. Mogilner, On the edge: modeling protrusion. *Curr. Opin. Cell Biol.* **18**(1), 32–39 (2006)
65. A. Mogilner, J. Allard, R. Wollman, Cell polarity: quantitative modeling as a tool in cell biology. *Science* **336**(6078), 175–179 (2012)
66. L. Moreau, E. Sontag, Balancing at the border of instability. *Phys. Rev. E Stat. Nonlin. Soft Matter Phys.* **68**(2/Pt 1), 020901 (2003)
67. D. Mortimer, T. Fothergill, Z. Pujic, L.J. Richards, G.J. Goodhill, Growth cone chemotaxis. *Trends Neurosci.* **31**(2), 90–98 (2008)
68. J. Nagumo, S. Arimoto, S. Yoshizawa, An active pulse transmission line simulating nerve axon. *Proc. IRE* **50**(10), 2061–2070 (1962)
69. A. Nakajima, S. Ishihara, D. Imoto, S. Sawai, Rectified directional sensing in long-range cell migration. *Nat. Commun.* **5**, 5367 (2014)
70. M.P. Neilson, D.M. Veltman, P.J.M. van Haastert, S.D. Webb, J.A. Mackenzie, R.H. Insall, Chemotaxis: a feedback-based computational model robustly predicts multiple aspects of real cell behaviour. *PLoS Biol.* **9**(5), e1000618 (2011)
71. M. Nishikawa, M. Hörning, M. Ueda, T. Shibata, Excitable signal transduction induces both spontaneous and directional cell asymmetries in the phosphatidylinositol lipid signaling system for eukaryotic chemotaxis. *Biophys. J.* **106**(3), 723–734 (2014)

72. P.R. O'Neill, W.K.A. Karunarathne, V. Kalyanaraman, J.R. Silvius, N. Gautam, G-protein signaling leverages subunit-dependent membrane affinity to differentially control $\beta\gamma$ translocation to intracellular membranes. *Proc. Natl. Acad. Sci. U.S.A.* **109**(51), E3568–E3577 (2012)
73. M.D. Onsum, K. Wong, P. Herzmark, H.R. Bourne, A.P. Arkin, Morphology matters in immune cell chemotaxis: membrane asymmetry affects amplification. *Phys. Biol.* **3**(3), 190–199
74. S. Osher, R.P. Fedkiw, *Level Set Methods and Dynamic Implicit Surfaces*. Applied Mathematical Sciences, vol. 153 (Springer, New York, 2003)
75. C.A. Parent, B.J. Blacklock, W.M. Froehlich, D.B. Murphy, P.N. Devreotes, G protein signaling events are activated at the leading edge of chemotactic cells. *Cell* **95**(1), 81–91 (1998)
76. J.S. Parkinson, Bacterial chemotaxis: a new player in response regulator dephosphorylation. *J. Bacteriol.* **185**(5), 1492–1494 (2003)
77. C.C. Poirier, W.P. Ng, D.N. Robinson, P.A. Iglesias, Deconvolution of the cellular force-generating subsystems that govern cytokinesis furrow ingression. *PLoS Comput. Biol.* **8**(4), e1002467 (2012)
78. M. Postma, J. Roelofs, J. Goedhart, T.W.J. Gadella, A.J.W.G. Visser, P.J.M. Van Haastert, Uniform cAMP stimulation of *Dictyostelium* cells induces localized patches of signal transduction and pseudopodia. *Mol. Biol. Cell* **14**(12), 5019–5027 (2003)
79. M. Postma, J. Roelofs, J. Goedhart, H.M. Loovers, A.J.W.G. Visser, P.J.M. Van Haastert, Sensitization of *Dictyostelium* chemotaxis by phosphoinositide-3-kinase-mediated self-organizing signalling patches. *J. Cell Sci.* **117**(Pt 14), 2925–2935 (2004)
80. M.J. Potel, S.A. Mackay, Preaggregative cell motion in *Dictyostelium*. *J. Cell Sci.* **36**, 281–309 (1979)
81. W.-J. Rappel, W.F. Loomis, Eukaryotic chemotaxis. *Wiley Interdiscip. Rev. Syst. Biol. Med.* **1**(1), 141–149 (2009)
82. E.T. Roussos, J.S. Condeelis, A. Patsialou, Chemotaxis in cancer. *Nat. Rev. Cancer* **11**(8), 573–587 (2011)
83. G.L. Ryan, N. Watanabe, D. Vavylonis, A review of models of fluctuating protrusion and retraction patterns at the leading edge of motile cells. *Cytoskeleton (Hoboken)* **69**(4), 195–206 (2012)
84. A. Samadani, J. Mettetal, A. van Oudenaarden, Cellular asymmetry and individuality in directional sensing. *Proc. Natl. Acad. Sci. U.S.A.* **103**(31), 11549–11554 (2006)
85. H. Senoo, M. Iijima, Rho GTPase: a molecular compass for directional cell migration. *Commun. Integr. Biol.* **6**(6), e27681 (2013)
86. D. Shao, W.-J. Rappel, H. Levine, Computational model for cell morphodynamics. *Phys. Rev. Lett.* **105**(10), 108104 (2010)
87. D. Shao, H. Levine, W.-J. Rappel, Coupling actin flow, adhesion, and morphology in a computational cell motility model. *Proc. Natl. Acad. Sci. U.S.A.* **109**, 6851 (2012)
88. S.S. Shen-Orr, R. Milo, S. Mangan, U. Alon, Network motifs in the transcriptional regulation network of *Escherichia coli*. *Nat. Genet.* **31**(1), 64–68 (2002)
89. C. Shi, C.-H. Huang, P.N. Devreotes, P.A. Iglesias, Interaction of motility, directional sensing, and polarity modules recreates the behaviors of chemotaxing cells. *PLoS Comput. Biol.* **9**(7), e1003122 (2013)
90. E.D. Sontag, Adaptation and regulation with signal detection implies internal model. *Syst. Control Lett.* **50**(2), 119–126 (2003)
91. V. Sourjik, N. S. Wingreen, Responding to chemical gradients: bacterial chemotaxis. *Curr. Opin. Cell Biol.* **24**(2), 262–268 (2012)
92. K.F. Swaney, C.-H. Huang, P.N. Devreotes, Eukaryotic chemotaxis: a network of signaling pathways controls motility, directional sensing, and polarity. *Annu. Rev. Biophys.* **39**, 265–289 (2010)
93. J.A. Swanson, D.L. Taylor, Local and spatially coordinated movements in *Dictyostelium discoideum* amoebae during chemotaxis. *Cell* **28**(2), 225–232 (1982)

94. H. Takagi, M.J. Sato, T. Yanagida, M. Ueda, Functional analysis of spontaneous cell movement under different physiological conditions. *PLoS One* **3**(7), e2648 (2008)
95. K. Takeda, D. Shao, M. Adler, P.G. Charest, W.F. Loomis, H. Levine, A. Groisman, W.-J. Rappel, R.A. Firtel, Incoherent feedforward control governs adaptation of activated Ras in a eukaryotic chemotaxis pathway. *Sci. Signal.* **5**(205), ra2 (2012)
96. M. Tang, M. Wang, C. Shi, P.A. Iglesias, P.N. Devreotes, C.-H. Huang, Evolutionarily conserved coupling of adaptive and excitable networks mediates eukaryotic chemotaxis. *Nat. Commun.* **5**, 5175 (2014)
97. D. Taniguchi, S. Ishihara, T. Oonuki, M. Honda-Kitahara, K. Kaneko, S. Sawai, Phase geometries of two-dimensional excitable waves govern selforganized morphodynamics of amoeboid cells. *Proc. Natl. Acad. Sci. U.S.A.* **110**(13), 5016–5021 (2013)
98. R.T. Tranquillo, D.A. Lauffenburger, S.H. Zigmond, A stochastic model for leukocyte random motility and chemotaxis based on receptor binding fluctuations. *J. Cell Biol.* **106**(2), 303–309 (1988)
99. P.J. Van Haastert, Sensory adaptation of *Dictyostelium discoideum* cells to chemotactic signals. *J. Cell Biol.* **96**(6), 1559–1565 (1983)
100. M.G. Vicker, Reaction-diffusion waves of actin filament polymerization/depolymerization in *Dictyostelium* pseudopodium extension and cell locomotion. *Biophys. Chem.* **84**(2), 87–98 (2000)
101. M.G. Vicker, F-actin assembly in *Dictyostelium* cell locomotion and shape oscillations propagates as a self-organized reaction-diffusion wave. *FEBS Lett.* **510**(1–2), 5–9 (2002)
102. J.M. Vilar, R. V. Solé, J.M. Rubí, Noise and periodic modulations in neural excitable media. *Phys. Rev. E Stat. Phys. Plasmas Fluids Relat. Interdiscip. Topics* **59**(5/Pt B), 5920–5927 (1999)
103. C.J. Wang, A. Bergmann, B. Lin, K. Kim, A. Levchenko, Diverse sensitivity thresholds in dynamic signaling responses by social amoebae. *Sci. Signal.* **5**(213), ra17 (2012)
104. Y. Wang, H. Senoo, H. Sesaki, M. Iijima, Rho GTPases orient directional sensing in chemotaxis. *Proc. Natl. Acad. Sci. U.S.A.* **110**(49), E4723–E4732 (2013)
105. M.-J. Wang, Y. Artemenko, W.-J. Cai, P.A. Iglesias, P.N. Devreotes, The directional response of chemotactic cells depends on a balance between cytoskeletal architecture and the external gradient. *Cell Rep.* **9**(3), 1110–1121 (2014)
106. M. Wegmann, Targeting eosinophil biology in asthma therapy. *Am. J. Respir. Cell Mol. Biol.* **45**(4), 667–674 (2011)
107. L.S. Weinberger, J.C. Burnett, J.E. Toettcher, A.P. Arkin, D.V. Schaffer, Stochastic gene expression in a lentiviral positive-feedback loop: HIV-1 Tat fluctuations drive phenotypic diversity. *Cell* **122**(2), 169–182 (2005)
108. O.D. Weiner, W.A. Marganski, L.F. Wu, S.J. Altschuler, M.W. Kirschner, An actin-based wave generator organizes cell motility. *PLoS Biol.* **5**(9), e221 (2007)
109. Y. Xiong, P.A. Iglesias, Tools for analyzing cell shape changes during chemotaxis. *Integr. Biol. (Camb.)* **2**(11–12), 561–567 (2010)
110. Y. Xiong, C.-H. Huang, P.A. Iglesias, P.N. Devreotes, Cells navigate with a local-excitation, global-inhibition-biased excitable network. *Proc. Natl. Acad. Sci. U.S.A.* **107**(40), 17079–17086 (2010)
111. Y. Xiong, C. Kabacoff, J. Franca-Koh, P.N. Devreotes, D.N. Robinson, P.A. Iglesias, Automated characterization of cell shape changes during amoeboid motility by skeletonization. *BMC Syst. Biol.* **4**, 33 (2010)
112. X. Xu, M. Meier-Schellersheim, J. Yan, T. Jin, Locally controlled inhibitory mechanisms are involved in eukaryotic GPCR-mediated chemosensing. *J. Cell Biol.* **178**(1), 141–153 (2007)
113. L. Yang, P.A. Iglesias, Positive feedback may cause the biphasic response observed in the chemoattractant-induced response of *Dictyostelium* cells. *Syst. Control Lett.* **55**(4), 329–337 (2006)
114. L. Yang, J.C. Effler, B.L. Kutscher, S.E. Sullivan, D.N. Robinson, P.A. Iglesias, Modeling cellular deformations using the level set formalism. *BMC Syst. Biol.* **2**, 68 (2008)

115. T.M. Yi, Y. Huang, M.I. Simon, J. Doyle, Robust perfect adaptation in bacterial chemotaxis through integral feedback control. *Proc. Natl. Acad. Sci. U.S.A.* **97**(9), 4649–4653 (2000)
116. W. Zhang, D.N. Robinson, Balance of actively generated contractile and resistive forces controls cytokinesis dynamics. *Proc. Natl. Acad. Sci. U.S.A.* **102**(20), 7186–7191 (2005)
117. J. Zhang, W.-H. Guo, Y.-L. Wang, Microtubules stabilize cell polarity by localizing rear signals. *Proc. Natl. Acad. Sci. U.S.A.* **111**(46), 16383–16388 (2014)
118. F. Ziebert, S. Swaminathan, I.S. Aranson, Model for self-polarization and motility of keratocyte fragments. *J. R. Soc. Interface* **9**, 1084 (2012)
119. S.H. Zigmond, S.J. Sullivan, Sensory adaptation of leukocytes to chemotactic peptides. *J. Cell Biol.* **82**(2), 517–527 (1979)

Chapter 4

Cell Locomotion in One Dimension

Pierre Recho and Lev Truskinovsky

4.1 Introduction

The ability of cells to self-propel is essential for most biological processes: in the early life of an embryo, stem cells move to form tissues and organs, during the immune response, leukocytes migrate through capillaries to attack infections and collective motion of epithelial cells is necessary for wound healing. While the molecular and biochemical basis of cell motility is basically known, the underlying mechanical theory of active continuum media is still under development [3, 23, 34, 39, 55, 71, 102, 118, 125, 168].

At a rather schematic level, sufficient for our purposes, a cell can be viewed as an elastic ‘bag’ whose interior is separated from the exterior by a bi-layer lipid membrane. The membrane is attached from inside to a cortex—an active muscle-type layer maintaining the cell’s shape. The interior is filled with a passive medium, the cytosol, where all essential cell organelles are immersed. The active machinery inside the cytosol, ensuring self-propulsion, resides in the cytoskeleton: a perpetually renewed network of actin filaments that is cross-linked by myosin motors while being transiently attached to the cell exterior through adhesion proteins. The main active processes in the cytoskeleton are: the non-equilibrium polymerization of actin fibers, the relative sliding of actin fibers induced by myosin motors and the active bonding of trans-membrane proteins to viscous or elastic substrate [5, 23, 66, 102, 105].

P. Recho (✉)

Mathematical Institute, University of Oxford, Woodstock Road, Oxford OX26GG, UK
e-mail: recho@maths.ox.ac.uk

L. Truskinovsky

LMS, CNRS-UMR 7649, École Polytechnique, Route de Saclay, 91128 Palaiseau, France
e-mail: trusk@lms.polytechnique.fr

The elementary mechanisms responsible for the steady crawling of keratocytes, flattened cells with fibroblastic functions that will be our main object of study, have been identified [2, 15, 16, 44, 65, 102, 127, 146, 160]. Like most other eukaryotic cells, they self-propel by advancing the front and retracting the rear. The advance starts with protrusion through active polymerization in the frontal area of the cell (the lamellipodium) with a simultaneous formation of adhesion clusters at the advancing edge. After the adhesion of the protruding part of the cell is secured, the cytoskeleton contracts due to activity of myosin motors. The contraction leads to detachment at the rear and disassembly of the actin network through de-polymerization.

It is usually assumed that active polymerization ensuring protrusion can be described as the work of spatially distributed ‘pushers’, generating positive force couples, while active contraction can be viewed as an outcome of the mechanical action of distributed ‘pullers’, responsible for negative force couples. One of our main goals will be to show that the relative roles of pushers and pullers in cellular motility may be interchangeable and tightly linked to the task to be performed, see also [33, 95, 124, 132, 144]. The active side of the reversible adhesion of adhesive patches (focal adhesions) is understood insufficiently and we treat them as passive viscous binders whose spatial distribution may be regulated actively [52].

The three main components of the motility mechanism (polymerization, contraction and adhesion) depend upon continuous supply of energy provided by the ATP hydrolysis. They also require intricate regulation by complex signaling pathways involving chemical and mechanical feedback loops and the implied synchronization allows the cell to move with a relatively stable shape and velocity [13, 152]. While the general crawling mechanisms described above can support non-stationary translocation of the cell body [6, 12, 93], in this chapter we focus exclusively on the study of steady motility modes and will deal, outside transients, with cell fragments advancing at a constant velocity.

A variety of multi-scale simulation approaches targeting various cell motility mechanisms can be found in the literature, see the reviews in [14, 34, 102, 120, 152, 163]. Among them, prominent role is occupied by continuum mechanical models, although the underlying rheological assumptions may be rather diverse. Thus, in some models, the cytoskeleton is viewed as a highly viscous active *fluid* moving through a cytoplasm by generating internal contractile stresses [7, 63, 77, 109]. In other models, the cytoskeleton is represented as an active gel whose polar nature is modeled in the framework of the theory of *liquid crystals* [28, 71, 73, 75, 82, 118]. The active gel theory approach has been quite successful in reproducing various sub cellular structures observed *in vivo* [46, 47, 49, 134] and we basically follow it in this chapter albeit without an explicit reference to local orientational order. At sufficiently fast time scales, the cytoskeleton can be also modeled as an active *solid* with highly nonlinear scale-free rheology [24, 116]. The range of rheological models compatible with mechanical behavior of cytoskeleton reflects the incredible adaptability of this active medium and mirrors the variety of different motility modes in disparate types of cells.

In addition to bulk rheology, various surface elements of the motility machinery have been subjected to focused studies. It was shown that in some cases the plasmic membrane with its attached cortex can be viewed as a passive elastic surface and modeled by phase field methods allowing one to pass smoothly through topological transitions [55, 153, 163]. In other cases, the membrane may also play an active role, for instance, an asymmetric distribution of channels on the surface of the membrane can be responsible for a particular mechanism of cell motility relying on variation of osmotic pressure [147]. Another type of activity is associated with muscle-type contractions in the cortex that play an important role in blebbing [139, 151] and mitosis [133, 156]. An important role of active feedback between the shape of a crawling cell and the diffusion of pushers along the plasma membrane, was emphasized in [3]. While most models assume that the cell membrane interacts with the exterior of the cell through passive viscous forces, active dynamics of adhesion complexes has recently become an area of intense research driven in part by the finding of a complex dependence of the crawling velocity on the adhesive properties of the environment [43, 44, 52, 88, 89, 107, 129, 138, 168].

The account of these and other relevant factors, including realistic geometry, G-actin transport, Rac/Rho-regulation, etc., has led to the development of rather comprehensive models of cell motility that are adequate not only qualitatively but also quantitatively and can already serve as powerful predictive tools, see for instance [14, 48, 55, 91, 131, 141, 153, 166] and other chapters of this book. However, a physical understanding of the separate roles played in various macroscopic manifestations by individual active components of the self-propulsion machinery and the appreciation of the associated competition and cooperation between different ‘players’ is usually obscured by geometrical and bio-chemical complexity of such models and remain hidden behind opaque computational schemes [48, 63, 141, 152, 163, 165, 166, 169].

To bring some transparency into the interplay between contraction, protrusion and adhesion and to develop the associated intuition, we overview in this chapter a set of deliberately simplified models of lamellipodial cell motility allowing one to achieve analytical results without sacrificing the main effect which each model is intended to illustrate. All these models involve one-dimensional projection of the complex intra-cellular dynamics on the direction of locomotion.

More specifically, we assume that the motor part of a crawling eukaryotic cell can be viewed as a one-dimensional continuum layer. The two free boundaries representing the front and the rear of the moving fragment are the places where the external fluxes can operate and the external loads can be applied. In particular, we suppose that actin treadmilling can take place only on these boundaries and that it can be modeled as an influx of mass at the front boundary and its disappearance at the rear boundary. The actomyosin cytoskeleton is modeled as an active gel and active contraction is represented by a spatially inhomogeneous pre-stress [83]. Adhesion is treated as spatially inhomogeneous viscous friction [48, 61, 75, 86, 131, 141].

In pursuit of analytic transparency, we decouple the momentum balance equation from the mass transport equation by assuming infinite compressibility of the

cross-linked actin network [75, 131]. The density of motors is either assumed to be constant or modeled by an advection-diffusion equation where the advection is due to the flow of actin. To ensure that the crawling cell maintains its size, we introduce a phenomenological cortex/osmolarity mediated quasi-elastic interaction between the front and the back of the self-propelling fragment [11, 12, 49, 93]; a comparison of such mean field elasticity with more conventional bulk elasticity models can be found in [122]. Similar coupling between the front and the rear of the fragment may have an active origin as well resulting from different rates of polymerization and de-polymerization at the extremities of the lamellipodium [50].

Different effects are emphasized in the three sections of this review and the corresponding minimal systems of equations, capable of capturing the desired effects, are adjusted accordingly. In all three sections our goal is to provide evidence that individual active mechanisms can either act separately or have to be coordinated in order to ensure the required performance.

In the first section we focus on active contraction while maximally simplifying adhesion and fully neglecting active protrusion. We build upon the observation that motility initiation in keratocytes may be triggered by raising the contractility of myosin [40, 92, 114, 159, 161, 167]. It is also known that cells may self-propel by contraction only [76]. By limiting our attention to ‘pullers’, we confront the existing theories of polarization and motility that place the main emphasis on ‘pushers’ and link motility initiation with active treadmilling and protrusion. Mathematically, our one-dimensional model reduces to a dynamical system of a Keller–Segel-type, however, in contrast to its chemotactic analog, the nonlocality in this system which we call *autotaxis* is due to mechanical rather than chemical feedback. If compared with previous studies of Keller–Segel-type problems, our setting is complicated by the presence of free boundaries equipped with Stefan type boundary conditions. The model provides compelling evidence that both, the initiation of motility, associated with polarization, and its arrest, associated with re-symmetrization, may be fully controlled by the average contractility of motor proteins.

While contraction is crucial for pulling the organelles, protrusion is known to be the main mechanism of pushing [74]. In the second section we shift our focus to protrusion while maximally simplifying the description of contraction. More specifically, we assume that motor concentration is time independent and spatially homogeneous and keep adhesion passive. Our main result is that the roles of protrusion and contraction as the dominant mechanism of self-propulsion may be interchangeable depending on the character of the mechanical task performed by the cell. We identify a macroscopic signature of the dominance of each of the two mechanisms by demonstrating that the force-velocity relation associated with pushing is necessarily concave while pulling-dominated force-velocity relation may be convex-concave with an interval of negative mobility.

Finally, in the third section we mainly focus on active adhesion allowing it to optimally accommodate the dominating driving mode. We take an inverse engineering approach and use as optimality criterion the maximization of the overall velocity. For the given strength of protrusion, we prescribe the average level of contractile activity, and then search for the optimal internal distribution of contractile and

adhesive units. Our analysis of the ensuing variational problem demonstrates that radically different distributions of focal adhesions are most favorable depending on the domineering active mechanism of self-propulsion. Thus, for contraction-dominated motility, focal adhesions have to cooperate with pullers which end up localizing at the trailing edge of the cell while for protrusion-dominated motility they must conspire with pushers which concentrate at the leading edge of the cell. Both types of crawling mechanisms have been observed experimentally.

4.2 Contraction

As we have already mentioned, the problem of finding the mechanism of motility initiation is most commonly addressed in the framework emphasizing active polymerization [17, 32, 41, 64, 103, 135]. With such emphasis on ‘pushers’, spontaneous polarization was studied by Callan-Jones et al. [30], John et al. [74], Hawkins et al. [60], Hawkins and Voituriez [58], Doubrovinski and Kruse [48], and Blanch-Mercader and Casademunt [20]. In [10, 169] and [168], polarization was interpreted as a result of an inhomogeneity of adhesive interactions. Yet another group of authors successfully argued that cell polarity may be induced by a Turing-type instability [8, 70, 104, 157]. Such a diversity of modeling approaches is, of course, a manifestation of the fact that very different mechanisms of motility initiation are engaged in cells of different types.

The experimental evidence that contraction may be the leading factor behind the polarization of keratocytes has been broadly discussed in the literature. It was realized that active contraction creates an asymmetry-amplifying positive feedback because it causes actin flow which in turn carries the regulators of contraction [4, 14, 81, 124, 133]. In constrained conditions such autotaxis generates peaks in the concentration of stress activators (myosin motors) [22, 67] and this patterning mechanism was used, for instance, to model polarization induced by angular cortex flow [59, 61]. Closely related heuristic models of the Keller–Segel type [112] employing essentially the same physical mechanism of instability (autotaxis) and also describing symmetry breaking and localization were independently proposed in [31, 80]. In all these models, however, the effect of contraction (pullers) was obscured by the account of other mechanisms, in particular, polymerization induced protrusion (pushers), and the focus was on generation of internal flow and the resulting pattern formation, rather than on the problem of ensuring steady translocation of a cell.

More recent models of contraction-induced polarization relying on splay instability in an active gel were proposed in [55, 152, 153]. In these model, however, ‘pushers’ were not the only players, in particular, polarization was induced by a local phase transition from non-polar to polar gel. In a closely related paper [29], the motility initiation was attributed to a contraction-induced instability in a poro-elastic active gel permeated by a solvent. Here again the non-contractile active mechanism was involved as well and therefore the domineering role of contraction could not be made explicit.

A question intimately related to the problem of motility initiation is how the resulting steady translocation of a cell can be halted. Several computational models provided an indication that the two phenomena are related and that motility initiation and motility arrest may emerge from a re-entrant behavior of the same branch of motile regimes [55, 80, 124, 153]. However, it is still not clear whether motility initiation and motility arrest can be both fully contraction-driven. To address this issue we present in this section an analytically tractable one-dimensional model which answers the question positively and shows that the increase of contractility may cause not only polarization but also re-symmetrization.

Following previous work, we exploit the Keller–Segel (autotaxis) mechanism, but now in a free boundary setting. In contrast to most previous studies, our contraction driven translocation of a cell is caused exclusively by the internal flow generated by molecular motors (pullers) and no other active agents are involved, see also [124, 125]. While most of the elements of the proposed model have been anticipated by the comprehensive computational approaches, e.g. [131], it was previously not apparent that the initiation of motility, the steady translocation, the re-symmetrization and the arrest of motility can be all captured already in such a minimal model.

On the mathematical side, we show that the increase of contractility beyond a well defined threshold leads to a bifurcation from a static symmetric solution of the governing system of equations (of Keller–Segel type) describing non-motile cell to an asymmetric traveling wave (TW) solution describing steadily moving cell. While several TW regimes are available at the same value of parameters, we show that stable TW solutions localize motors at the trailing edge of the cell in agreement with observations [40, 92, 114, 159, 161, 167]. Moreover, we show that if adhesion with the extra-cellular substrate is sufficiently low, the increase of motor-induced contraction may induce transition from the steady state TW solution back to a static solution. This re-symmetrization transition, leading to the motility arrest, can be directly associated with the behavior of keratocytes prior to cell division [84, 85, 145] and our model shows that such a re-entrant behavior can be ensured exclusively by ‘pullers’ without any engagement of either active protrusion or liquid crystal elasticity.

4.2.1 A Toy Model

Our point of departure is a conceptual model elucidating the mechanism of contraction-driven crawling and emphasizing the role of symmetry breaking in achieving the state of steady self propulsion.

Recall that in crawling cells, the ‘motor part’ containing contracting cytoskeleton (lamellipodium), is a thin active layer located close to the leading edge of the cell, see Fig. 4.1. We assume that all mechanical action originates in lamellipodium and that from the mechanical viewpoint the rest of the cell, including the nucleus, can be interpreted as cargo. The main task will be to develop a model of freely moving

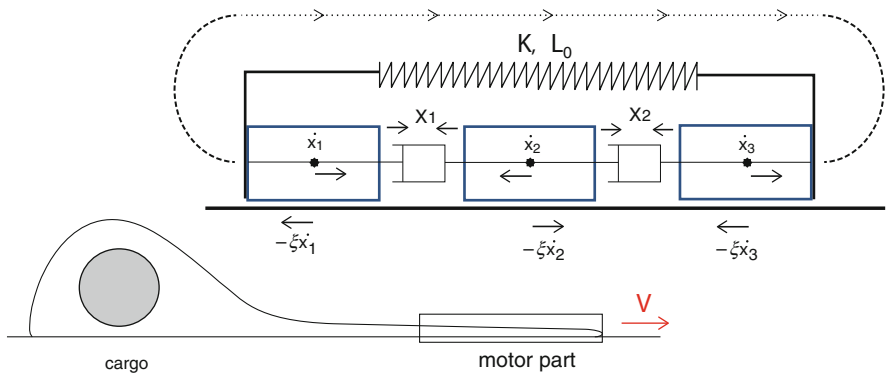


Fig. 4.1 Conceptual discrete model of the motility mechanism in a crawling keratocyte cell

lamellipodium which we schematize as a segment of active gel in viscous contact with a rigid background. The actin network inside the gel is contracted by myosin motors which leads to an internal flow opposed by the viscous interaction with the background. The unidirectional flow is a result of the asymmetry of contraction that ultimately propels the cell.

The simplest model elucidating this mechanism involves three rigid blocks of size l_b placed in a frictional contact with a rigid support, characterized by the viscous friction coefficient ξ . The neighboring blocks are connected by *active pullers* (force dipoles) exerting contractile forces. The long range signaling ensuring the control of cell volume is modeled by a linear spring with stiffness k connecting the first and the last block. To regularize the problem we place in parallel with contractile elements additional *dashpots* characterized by the viscosity coefficient η .

In the absence of inertia, we can write the force balance equations for our system in the form

$$\begin{aligned} -l_b \xi \dot{x}_1 + k \frac{x_3 - x_1 - L_0}{L_0} + \chi_1 - \eta \frac{\dot{x}_1 - \dot{x}_2}{l_b} &= 0 \\ -l_b \xi \dot{x}_2 - \chi_1 + \chi_2 - \eta \frac{\dot{x}_2 - \dot{x}_1}{l_b} - \eta \frac{\dot{x}_2 - \dot{x}_3}{l_b} &= 0 \\ -l_b \xi \dot{x}_3 - k \frac{x_3 - x_1 - L_0}{L_0} - \chi_2 - \eta \frac{\dot{x}_3 - \dot{x}_2}{l_b} &= 0, \end{aligned} \quad (4.1)$$

where $x_1(t), x_2(t), x_3(t)$ are the current positions of the blocks and L_0 is the reference length of a linear spring. This spring describes the membrane-cortex ‘bag’ around the lamellipodium allowing the inhomogeneous contraction to be transformed into a protruding force. We assume that polarization has already taken place and therefore the contractile force dipoles $\chi_1 \geq 0$ and $\chi_2 \geq 0$ acting between the two pairs of blocks are not the same $\chi_1 \neq \chi_2$. The polarization itself requires additional constructs and will be addressed later.

The system (4.1) can be rewritten as three decoupled equations for the length of our active segment $L(t) = x_3(t) - x_1(t)$, its geometric center $G(t) = (x_3(t) + x_1(t))/2$ and the position of a central block $x_2(t)$ representing the internal flow:

$$\begin{aligned} -l_b \xi (1 + l_0^2/l_b^2) \dot{L} &= \chi_1 + \chi_2 + 2k(L/L_0 - 1) \\ 2l_b \xi (1 + 3l_0^2/l_b^2) \dot{G} &= \chi_1 - \chi_2 \\ -l_b \xi (1 + 3l_0^2/l_b^2) \dot{x}_2 &= \chi_1 - \chi_2. \end{aligned} \quad (4.2)$$

Here $l_0 = \sqrt{\eta/\xi}$ is the hydrodynamic length scale which will ultimately play the role of a regularizing parameter. The first equation shows that the length is converging to a steady state value:

$$L = L_0(1 - (\chi_1 + \chi_2)/(2k)).$$

Notice that in order to avoid the collapse of the layer due to contraction, it is necessary to ensure that the spring has sufficiently large stiffness $k > (\chi_1 + \chi_2)/2$. We also observe that independently of the value of the evolving length $L(t)$, the velocity of the geometrical center of our train of blocks V is always the same

$$V = \dot{G} = \frac{\chi_1 - \chi_2}{2l_b \xi (1 + 3l_0^2/l_b^2)}. \quad (4.3)$$

One can see that this mechanical system can move as a whole only if $\chi_1 \neq \chi_2$. This emphasizes the crucial role played in cell motility by the inhomogeneity of contraction. The origin of the implied gradients and the mechanism allowing the cell to maintain the inhomogeneity, will be addressed already in the continuum setting.

We observe that the middle block moves in the direction opposite to the motion of the center of the system with a constant velocity $\dot{x}_2 = -2V$. Therefore, it takes a finite time $\sim L/(3V)$ for the central block to collide with the block at the rear and additional assumptions are needed to extend the dynamics beyond the collision point.

To model circulation (turnover) of the cytoskeleton in a one-dimensional setting, we assume that while the flow is continuous along the contact surface, the cytoskeleton disintegrates into small pieces (actin monomers) at the trailing edge and reintegrates at the leading edge. This assumption allows us to close the treadmilling cycle, even though the details of the discontinuous part of the cycle, involving both reaction and an almost frictionless transport of monomers, will not be resolved by the model. The reverse flow will be replaced by instantaneous jumps maintaining the overall mass balance. We also neglect the active propulsion on the frontal boundary due to growth of the network.

More specifically, we assume that as a result of each collision a block at the rear is instantaneously removed from the chain and at the same time an identical block is added at the front. In other words, each (equilibrium) de-polymerization event at the rear is matched by an (equilibrium) polymerization event at the front. Essentially, we suppose that at the time scale of frictional (continuous) dynamics the reverse transport of monomers takes place instantaneously: we implicitly assume the existence of a stationary gradient of chemical potential of actin monomers and of a large pool of monomers ready to be added to the network at the front as soon as one of them is released at the rear.

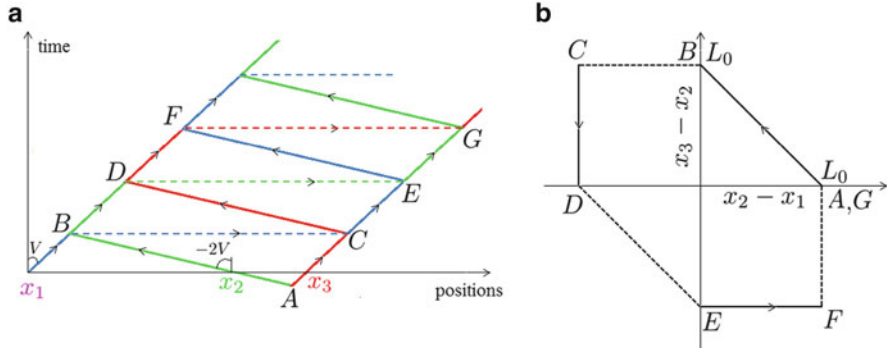


Fig. 4.2 (a) Schematic representation of the motion of individual particles (blocks) forming the motor part of a crawler in a steady state regime (three particle case). Trajectories in space time coordinates of the particles x_1 (magenta, $OBCEF$), x_2 (green, $ABDEG$) and x_3 (red, $ACDFG$); dashed lines show the jump parts of the crawling cycle. Continuous flows have to overcome friction while the jumps are assumed to be friction free. (b) A closed loop constituting one full stroke in the parameter space ($x_2 - x_1$, $x_3 - x_2$). The time of one full stroke (A to G) is $T_s = L/V$ and the distance traveled by the crawler per stroke is $VT_s = L$

The structure of the resulting stroke in the t, x plane and in the $x_2 - x_1, x_3 - x_2$ plane is shown in Fig. 4.2. One can see that each block maintains its identity through the whole cycle and that its trajectory involves a succession of continuous segments described by (4.1) that are interrupted by instantaneous frictionless jumps from the rear to the front. Notice that in this interpretation the blocks can change order and the condition $x_1 < x_2 < x_3$ is not always satisfied. For instance, when the blocks x_1 and x_2 collide at point B , the block x_1 disappears at the back (point B) and reappears at the front (point C) ahead of the block x_3 . This jump mimics the frictionless part of the treadmilling cycle. It is clear that already in 2D formulation such jumps are not necessary because the reverse flow of actin can be modeled directly (see examples in the other chapters of this volume).

Consider now the case of N coupled blocks. Then, the force balance for the central blocks $j \in [2, N - 1]$ reads

$$-l_b \xi \dot{x}_j - \chi_{j-1} + \chi_j - \eta \frac{\dot{x}_j - \dot{x}_{j-1}}{l_b} - \eta \frac{\dot{x}_j - \dot{x}_{j+1}}{l_b} = 0.$$

This system of equations can be written in the matrix form,

$$\mathbf{T}\dot{\mathbf{x}} = \mathbf{b}, \quad (4.4)$$

where we denoted by $\dot{\mathbf{x}}$ the unknown vector $\dot{x}_1, \dots, \dot{x}_N$. The tri-diagonal matrix

$$\mathbf{T} = \begin{bmatrix} -(2 + \frac{l_b^2}{l_0^2}) & 1 & 0 & 0 & 0 \\ 1 & -(2 + \frac{l_b^2}{l_0^2}) & 1 & 0 & 0 \\ 0 & \ddots & \ddots & \ddots & 0 \\ 0 & 0 & 1 & -(2 + \frac{l_b^2}{l_0^2}) & 1 \\ 0 & 0 & 0 & 1 & -(2 + \frac{l_b^2}{l_0^2}) \end{bmatrix}$$

describes the viscous coupling and frictional interaction with the background while the vector

$$\mathbf{b} = \frac{l_b}{\xi l_0^2} \begin{bmatrix} -\chi_1 + \sigma_0 - \frac{\xi l_0^2}{l_b} \dot{x}_1 \\ \chi_1 - \chi_2 \\ \vdots \\ \chi_{N-2} - \chi_{N-1} \\ \chi_{N-1} - \sigma_0 - \frac{\xi l_0^2}{l_b} \dot{x}_N \end{bmatrix}$$

with $\sigma_0 = -k(x_N - x_1 - L_0)/L_0$ carries the information about the active forcing, the mean field type elasticity and the boundary layer effects. To find the solution $\dot{\mathbf{x}}$, we need to invert the matrix \mathbf{T} and then solve a system of two coupled linear equations $\dot{x}_1 = (\mathbf{R} \mathbf{b})_1$ and $\dot{x}_N = (\mathbf{R} \mathbf{b})_N$ where $\mathbf{R} = \mathbf{T}^{-1}$. The components of the matrix \mathbf{R} can be found explicitly [98]

$$R_{i,j} = \frac{\cosh((N+1-j-i)\lambda) - \cosh((N+1-|j-i|)\lambda)}{2 \sinh(\lambda) \sinh((N+1)\lambda)},$$

where $\lambda = \text{arccosh}(1 + l_b^2/2l_0^2)$. Knowing the ‘velocity field’, we can now compute the steady state value of the length

$$L = L_0 \left(1 - \frac{\sum_{j=1}^{N-1} \cosh(\lambda(j-N/2)) \chi_j}{\sum_{j=1}^{N-1} \cosh(\lambda(j-N/2)) k} \right).$$

From this formula we see again that a finite stiffness is necessary to prevent the collapse of the system under the action of contractile stresses: assuming for instance that $\chi_i = \bar{\chi}$ we obtain the low bound for the admissible elasticity modulus $k > \bar{\chi}$.

The steady velocity $V = (\dot{x}_N + \dot{x}_1)/2$ of the geometrical center of the system can be also computed explicitly

$$V = -\frac{l_b \sum_{j=1}^{N-1} \sinh(\lambda(j - N/2)) \chi_j}{2\eta \sinh(\lambda N/2)}.$$

For N even, by denoting $M = N/2$, we can rewrite this expression in the form

$$V = -\frac{l_b \sum_{j=1}^{M-1} \sinh(j\lambda)(\chi_{M+j} - \chi_{M-j})}{2\eta \sinh(\lambda M)}$$

from where it is clear that (as in the case of three blocks) the symmetry of the vector χ with respect to the center must be broken for the system to be able to self-propel. An interesting mathematical problem associated with the absence of commutation between the zero viscosity limit and the continuum limit is discussed in [126].

4.2.2 Continuum Thermodynamics

Quite expectantly, our toy model of contraction-dominate crawling, has left us with many unanswered questions. For instance, it is not clear what is the microscopic nature of the active contraction forces χ_1 and χ_2 introduced ad hoc in the discrete model and how does the system creates and maintains the asymmetry $\chi_1 \neq \chi_2$. To answer these and other related questions we need to formulate a consistent thermo-mechanical continuum model that can be viewed as a limit of our discrete model but which goes much beyond it in detailing the physical mechanisms of both symmetry breaking and symmetry recovery.

To our advantage, such theory already exists [75, 82, 96] and the goal of this section will be to adapt it to our needs. It is known as the active gel theory and its main idea is the local orientation-induced tensorial coupling of chemistry and mechanics. Even though in a one dimensional setting the orientational order is trivial, this general framework will allow us to point out directly where the ‘activity’ assumption is embedded into the general continuum mechanical formulation. In contrast to previous expositions of the active gel theory where the main emphasis was on force balance, here we emphasize the energetic side of the chemo-mechanical coupling, see also [125].

Denote by $l_-(t)$ and $l_+(t)$ the moving rear and front boundaries of a one-dimensional segment occupied by a continuum body. We suppose that the system is driven externally, by applied forces, and internally, by chemical reactions. To describe the resulting motion we follow the standard approach of continuum mechanics [42]. First we introduce mass density $\rho(x, t)$ and velocity $v(x, t)$ satisfying the mass balance equation

$$\partial_t \rho + \partial_x(\rho v) = 0, \quad (4.5)$$

which was automatic in the discrete model. Since in this section the main focus is on contraction, we assume that there is no external mass flux (no growth)

$$\dot{m} = \rho_+ [\dot{l}_+(t) - v(l_+(t), t)] = \rho_- [\dot{l}_-(t) - v(l_-(t), t)] = 0,$$

or

$$\dot{l}_\pm(t) = v(l_\pm(t), t).$$

We modify this assumption in Sects. 4.3 and 4.4 to account for active polymerization.

To write the momentum balance equation we introduce the stress $\sigma(x, t)$ and assume that the body is loaded by bulk forces $g(x, t)$ (friction forces in the discrete model). Then assuming that the inertial effects can be neglected we can write for the bulk points

$$\partial_x \sigma = g \quad (4.6)$$

which is the analog of (4.1) in the discrete setting. We also assume that dead tractions σ_0^\pm are applied at the moving boundaries l_\pm , so that $\sigma(l_\pm) = \sigma_0^\pm$. Notice that the ‘volume preserving’ global spring which was an essential feature of the discrete model can be also absorbed into σ_0^\pm as will be made clear when we discuss physiologically meaningful boundary conditions in the next section.

Suppose that our continuum body is a mixture of active and passive components and that the mass fraction of the active component (a factor distinguishing between χ_1 and χ_2 in the discrete model) satisfies the balance equation

$$\rho \dot{\phi} = \partial_x J, \quad (4.7)$$

where J is the flux of the active component. The ‘activity’ of the active component has been so far fully implicit and the term itself will be justified only at the end of this section.

Next, we assume that there is a chemical reaction, responsible for contraction and implicit in the discrete setting, which proceeds with the rate v per unit mass, so that

$$\rho(\partial_t \zeta + v \partial_x \zeta) = v, \quad (4.8)$$

where ζ is the reaction progress variable. For analytical simplicity we also postulate that our ‘active’ material is infinitely compressible (recall that connectors between the blocks in the discrete model did not contain regular elastic springs) and that the dynamics is isothermal. Then the free energy density can be written as $f = f(\phi, \zeta)$.

Four the four unknown functions $\phi(x, t)$, $\zeta(x, t)$, $\rho(x, t)$ and $v(x, t)$ we now have four equations (4.5)–(4.8), however, even if the functional dependence of the free energy density on its arguments is known, they still contain unidentified entities

σ , v and J . To introduce constitutive relations linking these entities with our main unknown functions, we start with the expression for the global dissipation in the system $W - \dot{F} = R \geq 0$, where $F = \int_{l_-}^{l_+} \rho f dx$ is the total free energy of the system. If we introduce notation $[Q]_-^+ = Q^+ - Q^-$, we can write the power of external forces W in the form

$$W = - \int_{l_-}^{l_+} g v dx + [\sigma_0 l]_-^+ = \int_{l_-}^{l_+} (-g v + \partial_x(\sigma v)) dx = \int_{l_-}^{l_+} \sigma \partial_x v dx.$$

Using mass balance equation we can also write

$$\dot{F} = \int_{l_-}^{l_+} (\partial_t \rho f + \rho \partial_t f) dx + [\rho f l]_-^+ = \int_{l_-}^{l_+} \rho (\partial_t f + v \partial_x f) dx + \dot{m} [f]_-^+.$$

Since in this section we neglect active treadmilling $\dot{m} = 0$ and we obtain

$$\dot{F} = \int_{l_-}^{l_+} \rho \dot{f} dx = \int_{l_-}^{l_+} \rho (-A \dot{\zeta} + \mu \dot{\phi}) dx,$$

where $A(\phi, \zeta) = -\partial_\xi f$ is the affinity of the reaction and $\mu(\phi, \zeta) = \partial_\phi f$ is the chemical potential of the active component of the mixture. Assuming that there is no external flux of the active component through the boundaries, we finally write the expression for dissipation R in the form

$$R = \int_{l_-}^{l_+} (\sigma \partial_x v + v A + J \partial_x \mu) dx. \quad (4.9)$$

The three terms under the integral in (4.9) can be interpreted as products of the thermodynamic fluxes $\sigma, \rho \dot{\zeta}, J$ and the conjugate thermodynamic forces $\partial_x v, A, \partial_x \mu$. In the absence of microscopic models, we make a simplifying assumption that fluxes and forces are related linearly but since the system is at a finite distance from equilibrium, we allow the coefficients in these relations may be state (ϕ, ζ, ρ, v) dependent.

To further simplify the model we assume that diffusion is decoupled from the other two non-equilibrium mechanisms and write

$$J = l_{33} \partial_x \mu. \quad (4.10)$$

If we now define the mass density of the active component as $c = \phi \rho$ (we use different types of letters, c and ρ , for physically similar quantities to stress their different roles in the theory), we obtain the advection diffusion equation

$$\partial_t c + \partial_x(c v) = \partial_x(l_{33} \partial_x \mu),$$

where $l_{33} \geq 0$ is a mobility per unit volume.

We further suppose that reaction and deformation are coupled (chemo-mechanical effect, introduced for passive systems in [51]) so that

$$\begin{aligned}\sigma &= l_{11}\partial_x v + l_{12}A \\ v &= -l_{12}\partial_x v + l_{22}A.\end{aligned}\quad (4.11)$$

Here $l_{11} = \eta \geq 0$ is the standard Newtonian viscosity and l_{22} is a linearized reaction rate. The simplest way to express the fact that the active component plays a role of a catalyst for the reaction is to assume that $l_{22} = bc$ where b is a constant. Similarly, we assume that the reaction-deformation coupling is amplified in the presence of the active component and write $l_{12} = ac$, where a is another constant.

The first consequence of (4.11) is the constitutive relation

$$\sigma = \eta\partial_x v + aAc,\quad (4.12)$$

where the second term in the right hand side represents the ‘active’ stress emerging from mechano-chemical coupling. We assume that $a > 0$ which ensures that the reaction induced stresses are contractile whenever $A > 0$. Notice that (4.12) is the continuum analog of the corresponding relation in the discrete model where we implicitly used the notation $\chi = aAc$ and assumed that the right hand side depends on location of the corresponding bond but not on time.

The second consequence of (4.11) is the mechanical feedback to kinetics

$$\partial_t \zeta + v\partial_x \zeta = \phi(bA - a\partial_x v).\quad (4.13)$$

In the cell motility context, Eq. (4.13) describes spatial and temporal inhomogeneity of ATP hydrolysis supporting self-propulsion; observe that the reaction stops completely in the absence of ‘active’ component ($\phi = 0$).

To close the system we need to specify the expression for the free energy $f(\phi, \zeta)$. First of all we assume that the mixture is dilute and write

$$f = f_0(\zeta) + k_B T \phi \log \phi,$$

where k_B is the Boltzmann constant. Therefore $\mu = \mu_0 + k_B T \log \phi$ and $\partial_x \mu = k_B T (\partial_x c/c - \partial_x \rho/\rho)$. To recover a standard diffusion equation we need to make an additional assumption that the variation of the total density is small compared to the variation of the density of motors $\partial_x c/c \gg \partial_x \rho/\rho$. Then we can write $D = \varsigma k_B T$, where $\varsigma = l_{33}/c$ is the mobility per motor. To remain in the framework of Onsager theory of diffusion we need to assume that $c \sim \bar{c}$ and $l_{33} = l_{33}(\bar{c})$; this approximation clearly fails near the singularities of c where the model needs to be appropriately modified. Under these assumption we obtain that the density of the active component $c(x, t)$ satisfies the standard advection diffusion equation

$$\partial_t c + \partial_x(cv) - D\partial_{xx}c = 0.\quad (4.14)$$

To view this model from a slightly broader angle, consider a simple mixture model with two species representing attached and detached motors. The attached motors are advected with the velocity of actin filaments and can detach. The detached motors are freely diffusing, and can also attach. Suppose also that the attachment-detachment process can be described by a first order kinetic equation. Then the system of equations governing the evolution of the densities of attached c and detached c_d motors can be written as:

$$\begin{aligned}\partial_t c + \partial_x(cv) &= k_{\text{on}}c_d - k_{\text{off}}c \\ \partial_t c_d - \tilde{D}\partial_{xx}c_d &= k_{\text{off}}c - k_{\text{on}}c_d,\end{aligned}$$

where k_{on} and k_{off} are the chemical rates of attachment and detachment and \tilde{D} is the diffusion coefficient of detached motors in the cytosol. Now suppose that the attachment-detachment process is chemically equilibrated and hence $c/c_d = K$, where $K = k_{\text{on}}/k_{\text{off}}$ is the reaction constant. Then for the attached motors performing contraction we obtain

$$((K+1)/K)\partial_t c + \partial_x(cv) - (\tilde{D}/K)\partial_{xx}c = 0.$$

Equation (4.14) is obtained in the limit $K \rightarrow \infty$ (fast attachment) and $\tilde{D}/K \rightarrow D$ (fast diffusion).

We now turn our attention to the dependence of the free energy on the reaction progress variable ζ . A standard assumption for a closed system would be that $f_0(\zeta)$ behaves quadratically around a minimum $\zeta = \zeta_0$ where $A = 0$. In this case ζ_0 represents equilibrium reaction progress. Instead, to emphasize the open nature of the system, we assume that

$$f_0(\zeta) = -A_0\zeta, \quad (4.15)$$

where $A_0 > 0$ is a prescribed constant measure of non-equilibrium. The seemingly innocent assumption (4.15) constitutes the main aspect of ‘activity’ in the model of active gel because all other constitutive elements of the model are conventional and passive [125].

The fact that the ‘distance’ from the equilibrium is independent of the reaction progress implies that there exists an exterior out of equilibrium chemostat. The ‘bottomless’ decrease of the free energy reflects the capability of the chemostat to continuously rebuild the non-equilibrium state. The energetic cost of such rebuilding must be compensated externally and the corresponding power delivered by the chemostat can be written as

$$\begin{aligned}-\dot{F} &= \int_{l_-}^{l_+} (\rho\dot{\zeta}A_0 + J\partial_x\mu)dx \\ &= \int_{l_-}^{l_+} [gv + \eta(\partial_x v)^2 + bA_0^2\rho + D(k_B T/\bar{c})(\partial_x c)^2] dx \geq 0.\end{aligned} \quad (4.16)$$

This expression is quite natural: the first term in the right hand side describe the work against the applied force, while the other three terms characterize dissipation due to viscosity, reaction and diffusion. Equation (4.16) allows one to assess the efficiency of the underling active mechanism, see [125] for more detail.

The transparency of this model which becomes apparent in the next sections is due to the splitting of the main problem into several nested sub-problems. The main sub-problem is mechanical, providing a closed system of equation for v , σ and ρ . It includes the momentum balance equation (4.6), the constitutive equation (4.12) and the advection-diffusion equation (4.14) that are coupled through the velocity field. The second sub-problem concerns the transport of mass and the corresponding balance equation (4.5) can be solved once the velocity field v is known. The solution of this sub-problem provides ρ . The transport problem decouples from the mechanical problem because of the assumption of infinite compressibility indicating that the thermodynamical stress is equal to zero and the density variations do not affect the momentum balance. The last sub-problem concerns the reaction progress Eq. (4.13) that requires for its solution the knowledge of the velocity field v , the mass density ρ and the active component density c and which provides us with the field ζ . The kinetic equation decouples from the force balance and the mass transport problems because of the assumption that the free energy f does not depend on ρ and depends on ϕ and ζ only additively. Both of these assumptions are made to ensure analytic simplicity and can be easily dropped in numerical experiments.

4.2.3 Specialization of the Model

We now accommodate our general theory for the modeling of the lamellipodium viewed as a one dimensional continuum layer in frictional contact with a rigid background. Assuming that in (4.6) the friction is viscous $g(x, t) = \xi v(x, t)$ we write the force balance in the form

$$\partial_x \sigma = \xi v. \quad (4.17)$$

Equation (4.17) is the continuous analog of the system (4.4) in the discrete problem and similar to the discrete model, we denoted by ξ the coefficient of viscous friction [48, 61, 75, 86, 131, 141]. A microscopic justification of the idea that the time-averaged shear stress generated by constantly engaging and disengaging focal adhesions is proportional to the velocity of the retrograde flow can be found in [149]. There is evidence (both experimental [22, 53, 54, 102, 136] and theoretical [44, 99]) that this assumption describes the behavior of focal adhesions accurately only when the retrograde flow is sufficiently slow. The behavior of adhesion strength in the broader range of velocities is biphasic and since we neglect this effect, we potentially misrepresent sufficiently fast dynamics.

Following (4.12), see also [22, 67, 75, 83], we describe the constitutive behavior of the gel in the form

$$\sigma = \eta \partial_x v + \chi c, \quad (4.18)$$

where η is the bulk viscosity and $\chi = aA_0 > 0$ is a constant representing contractile pre-stress per unit motor mass. The constitutive relation (4.18) generalizes the parallel bundling of dashpots and contractile units in the discrete model. The important new element is that now the strength of the contractile elements is an unknown function which may vary in both space and time (in the discrete model the dependence of c on x was fixed). We assume that the function $c(x, t)$ satisfies the convection-diffusion equation (4.14). Behind this assumption is the idea that myosin motors, actively cross-linking the actin network, are advected by the network flow and can also diffuse due to thermal fluctuations [13, 22, 61, 131, 166].

To account for cortex/membrane elasticity and other means of volume control in a moving cell we further assume that, as in the discrete model, the boundaries of our moving active segment are linked through a linear spring [12, 49, 93, 124]. This assumption affects the values of the stress on the free boundaries $l_-(t)$ and $l_+(t)$:

$$\sigma_0^\pm = -k(L(t) - L_0)/L_0,$$

where $L(t) = l_+(t) - l_-(t)$ is the length of the moving segment, k is the effective elastic stiffness and L_0 is the reference length of the spring.

As in the general theory we assume that our self-propelling segment is isolated in the sense that $\dot{m} = 0$ and therefore the free boundaries move with the internal flow $\dot{l}_\pm = v(l_\pm)$. We imply here that the addition and deletion of F-actin particles inserted at the front and taken away at the rear does not contribute to fronts propulsion. We also impose a zero flux condition for the active component $\partial_x c(l_\pm(t), t) = 0$ ensuring that the average concentration of motors

$$c_0 = \frac{1}{L_0} \int_{l_-(t)}^{l_+(t)} c(x, t) dx \quad (4.19)$$

is preserved. To complete the setting of the ensuing (statically determinate) mechanical problem we impose the initial conditions $l_\pm(0) = l_\pm^0$ and $c(x, 0) = c^0(x)$.

If we now normalize length by L_0 , time by L_0^2/D , stress by k , concentration by c_0 and density by M/L_0 , we can rewrite the main system of equations (4.17), (4.18), (4.14) in dimensionless form (without changing the notations)

$$\begin{aligned} -\mathcal{L}\partial_{xx}\sigma + \sigma &= \mathcal{P}c, \\ \partial_t c + \mathcal{K}\partial_x(c\partial_x\sigma) &= \partial_{xx}c. \end{aligned} \quad (4.20)$$

Here we introduced three main dimensionless constants of the problem: $\mathcal{L} = \eta/(\xi L_0^2)$ —the scale of viscous interaction; $\mathcal{K} = k/(\xi D)$ —the non-dimensional measure of diffusion and finally $\mathcal{P} = c_0\chi/k$ —the scale of contractility. In (4.20) one immediately sees the structure of the Keller–Segel system from the theory of chemotaxis, e.g. [112]. The role of the distributed chemical attractant is played by the stress field σ whose gradient is the driving force affecting the ‘colony’ of myosin motors. Therefore in this model [124, 125] the spontaneous localization, which is a typical feature of chemotaxis, is driven by mechanical rather than chemical gradients.

We refer to the mechanism of generating and sustaining mechanical inhomogeneities described by system (4.20) as autotaxis [123]. In physical terms it can be characterized as follows. Suppose that the motor proteins (our active component) with sufficient contractility induce internal stress which can overcome the hydrodynamic resistance and induce flow. The flow produces a drift of motors in the direction of the regions where they concentrate and such autocatalytic amplification is the mechanism of the positive feedback in our model. The ensuing runaway is countered by diffusion of active component which penalizes creation of concentration gradients and thus plays the role of a negative feedback. When a critical contractility of active component is reached, the homogeneous distribution of motors becomes unstable. The contraction asymmetry then induces a flow of actin filaments towards the trailing edge thus producing frictional forces which propel the cell forward. The eventual build up of a balance between drift and diffusion leads to the formation of a pattern. As we show below, among various admissible patterns, whose number increases with contractility, the stable ones localize motors at the trailing edge as observed in experiments.

The main mathematical difference between ours and the standard chemotaxis problem is that we have free boundaries. Using dimensionless variables we can rewrite the boundary conditions in the form

$$\dot{l}_{\pm}(t) = \mathcal{K} \partial_x \sigma(l_{\pm}(t), t), \quad (4.21)$$

$$\sigma(l_{\pm}(t), t) = -(L(t) - 1), \quad (4.22)$$

$$\partial_x c(l_{\pm}(t), t) = 0 \quad (4.23)$$

while the integral constraint (4.19) reduces to $\int_{l_-}^{l_+} c(x, t) dx = 1$.

4.2.4 Non-Local Reformulation

Since the first of the equations (4.20) is linear, it can be solved explicitly for σ

$$\sigma(x, t) = -\frac{(L - 1) \cosh[(G - x)/\sqrt{\mathcal{Z}}]}{\cosh[L/(2\sqrt{\mathcal{Z}})]} + \frac{\mathcal{P}}{\sqrt{\mathcal{Z}}} \int_{l_-}^{l_+} \Psi(x, y) c(y) dy, \quad (4.24)$$

where

$$\Psi(x, y) = \frac{\sinh[(l_+ - x)/\sqrt{\mathcal{Z}}] \sinh[(y - l_-)/\sqrt{\mathcal{Z}}]}{\sinh(L/\sqrt{\mathcal{Z}})} - H(y - x) \sinh[(y - x)/\sqrt{\mathcal{Z}}].$$

We introduced the notations: $H(x)$ —the Heaviside function and $G(t) = [l_-(t) + l_+(t)]/2$ is the position of the geometric center of the moving fragment. By eliminating σ from (4.20)₂ we obtain a single non-local partial differential equation with quadratic nonlinearity for $c(x, t)$

$$\begin{aligned} & \partial_t c(x, t) - \mathcal{K}(L-1) \partial_x [\theta(x)c(x, t)] \\ & + \frac{\mathcal{K}\mathcal{P}}{\sqrt{\mathcal{Z}}} \partial_x \left(\int_{l_-}^{l_+} \varphi(x, y)c(y, t)dy \right) = \partial_{xx}c(x, t), \end{aligned} \quad (4.25)$$

where the auxiliary velocity field

$$\theta(x) = \frac{\sinh[(x-G)/\sqrt{\mathcal{Z}}]}{\cosh[L/(2\sqrt{\mathcal{Z}})]}$$

describes advective flow induced by the elastic coupling between the rear and the front of the active segment. The feedback behind contraction-driven motility is contained in the kernel

$$\varphi(x, y) = -\frac{\cosh[(l_+ - x)/\sqrt{\mathcal{Z}}] \sinh[(y - l_-)/\sqrt{\mathcal{Z}}]}{\sinh(L/\sqrt{\mathcal{Z}})} + H(y-x) \cosh[(y-x)/\sqrt{\mathcal{Z}}],$$

which is due to viscosity-induced interactions in the system and the effect of the boundaries. Notice that this kernel has the action/reaction symmetry $\varphi(x, y) = -\varphi(l_+ + l_- - x, l_+ + l_- - y)$ which is a fundamental constraint imposed by the balance of momentum [79, 80, 154]. An interesting zero viscosity limit of the obtained system of equations leading to singular solutions is discussed in [126].

Using the boundary conditions (4.21) we find from (4.24) an explicit formula for the (time dependent) velocity of the center of our active segment

$$\dot{G} = \frac{\mathcal{K}\mathcal{P}}{2\mathcal{Z}} \int_{l_-}^{l_+} \frac{\sinh\left(\frac{G-x}{\sqrt{\mathcal{Z}}}\right)}{\sinh\left(\frac{L}{2\sqrt{\mathcal{Z}}}\right)} c(x, t) dx, \quad (4.26)$$

from which we infer that the maximal velocity of the self propelling segment is equal to $\mathcal{K}\mathcal{P}/(2\mathcal{Z})$. Similarly we obtain an equation for the evolving length of the segment

$$\dot{L} = -2 \frac{\mathcal{K}}{\sqrt{\mathcal{Z}}} (L-1) \tanh\left(\frac{L}{2\sqrt{\mathcal{Z}}}\right) - \frac{\mathcal{K}\mathcal{P}}{\mathcal{Z}} \int_{l_-}^{l_+} \frac{\cosh\left(\frac{G-x}{\sqrt{\mathcal{Z}}}\right)}{\cosh\left(\frac{L}{2\sqrt{\mathcal{Z}}}\right)} c(x, t) dx. \quad (4.27)$$

Notice that in (4.26) only the odd component of the function $c(x, t)$ [with respect to the moving center $G(t)$] contributes to the integral while in (4.27) only the even component matters. In particular, if the concentration of motors is an even function of x then $\dot{G} = 0$ and the segment does not move as a whole. This statement is a direct analog of Purcell's theorem [119] for a crawling body.

Given our interest in the steady modes of cell motility, which are typical for keratocytes [13], we need to study the traveling wave (TW) solutions of the main system (4.20). To find such solutions we assume that the front and the rear of the segment travel with the same speed $\dot{l}_\pm(t) \equiv V$, ensuring the constancy of the length $L(t) \equiv L$, and that both the stress and the myosin concentration depend exclusively

on the appropriately chosen co-moving coordinate $u = (x - x_0 - Vt)/L_0 \in [-1/2, 1/2]$. Using this ansatz we find that Eq. (4.20)₂ can be solved explicitly

$$c(u) = \frac{\exp[s(u) - VLu]}{L \int_{-1/2}^{1/2} \exp[s(u) - VLu] du}. \quad (4.28)$$

Here for convenience we introduced a new stress variable $s(u) = \mathcal{K}[\sigma(u) + (L-1)]$ which represents the inhomogeneous contribution to internal stress field due to active pre-stress. The system (4.20) reduces to the single nonlocal equation

$$-\frac{\mathcal{L}}{L^2} s''(u) + s(u) - \mathcal{K}(L-1) = \mathcal{K}\mathcal{P} \frac{\exp[s(u) - LVu]}{L \int_{-1/2}^{1/2} \exp[s(u) - VLu] du}, \quad (4.29)$$

supplemented by the boundary conditions

$$s(\pm 1/2) = 0 \quad \text{and} \quad s'(\pm 1/2) = LV. \quad (4.30)$$

The two ‘additional’ boundary conditions in (4.30) allow one to determine parameters V and L along with the function $s(u)$. After the problem (4.29), (4.30) is solved, the motor concentration profile can be found explicitly by using Eq. (4.28).

4.2.5 Static Solutions

Initiation of motility is associated with a symmetry breaking instability of a static (non-motile) solution. To identify non-motile configurations we need to find solutions of (4.29) with $V = 0$. Notice that these solutions may still describe the states with nontrivial active internal rearrangements of both actin and myosin [22].

If $V = 0$, Eq. (4.29) simplifies considerably

$$-\frac{\mathcal{L}}{L^2} s'' + s - \mathcal{K}(L-1) = \mathcal{K}\mathcal{P} \frac{\exp(s)}{L \int_{-1/2}^{1/2} \exp(s(u)) du}. \quad (4.31)$$

The nonlocal Eq. (4.31) was studied extensively in many domains of science from chemotaxis [140] to turbulence [27] and gauge theory [148]. In our case, this equation where parameter L remains unknown, has to be solved with three boundary conditions $s'(-1/2) = s(\pm 1/2) = 0$ because the forth boundary condition $s'(1) = 0$ is satisfied automatically.

We begin with the study of the regular solutions of (4.31). Instead of \mathcal{K} and \mathcal{P} , it will be convenient to use another set of parameters $A := \mathcal{K}(L-1) \leq 0$ and $B := \mathcal{K}\mathcal{P}/(L \int_{-1/2}^{1/2} \exp(s(u)) du) \geq 0$. In terms of parameters (A, B) the problem (4.31) reads

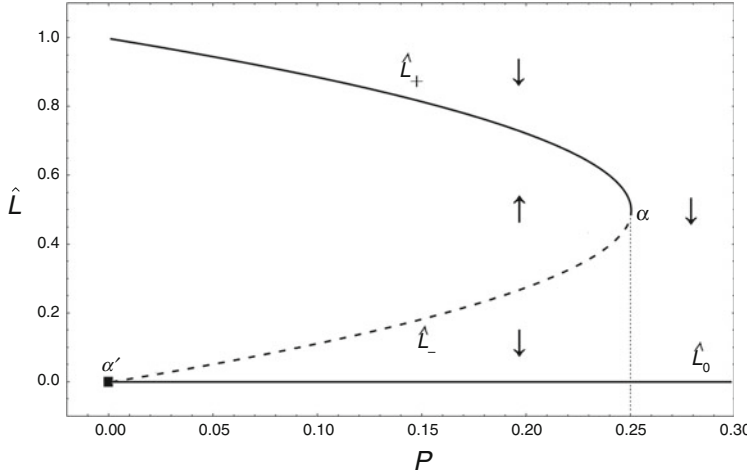


Fig. 4.3 Three families of trivial static solutions \hat{L}_+ , \hat{L}_- and \hat{L}_0 parameterized by \mathcal{P} . Solid lines show stable branches while dotted lines correspond to unstable branches. Arrows depict the basin of attraction of each branch

$$-\frac{\mathcal{Z}}{L^2} s'' + s - A = B \exp(s) \quad \text{with} \quad s'(-1/2) = s(\pm 1/2) = 0. \quad (4.32)$$

A trivial homogeneous solution of this problem $s(u) = 0$ exists when $A + B = 0$ which is equivalent in the $(\mathcal{P}, \mathcal{K})$ parametrization to $L = \hat{L}_{\pm}$ with,

$$\hat{L}_{\pm} = (1 \pm \sqrt{1 - 4\mathcal{P}})/2. \quad (4.33)$$

The sub-branches with longer and shorter lengths $\hat{L}_+(\mathcal{P})$ and $\hat{L}_-(\mathcal{P})$, respectively, that meet at point α where $\hat{L}_-(\mathcal{P}) = \hat{L}_+(\mathcal{P})$ are illustrated in Fig. 4.3.

To obtain nontrivial static solutions we multiply (4.32) by s' , integrate and use the boundary conditions to obtain the ‘energy integral’ $s'^2 = W(s)$, where

$$W(s) = \frac{L^2}{\mathcal{Z}} (s^2 - 2As - 2B[\exp(s) - 1]).$$

The general solution of this equation can be expressed as a quadrature,

$$u = \pm \int^{s(u)} W^{-1/2}(r) dr.$$

A detailed analysis of these solutions can be found in [126].

In addition to regular solutions described above Eq.(4.31) has measure-valued solutions corresponding to collapsed cells with length $\hat{L}_0 = 0$. First of all, as we see in Fig. 4.3, $\hat{L}_-(\mathcal{P}) \rightarrow 0$ when $\mathcal{P} \rightarrow 0$ (point α') and therefore the limiting

distribution of motors is concentrated on an infinitely small domain. To characterize the asymptotic structure of such singular solutions we suppose that $L \gg 1$ and that the maximum of s is of order L . Then, by ignoring higher order terms, we deduce from (4.31) a simplified boundary value problem

$$-s'' \approx \mathcal{K}\mathcal{P}L / (\mathcal{Z} \int_{-1/2}^{1/2} [1 + s(u)] du) \quad \text{with} \quad s'(-1/2) = s(\pm 1/2) = 0. \quad (4.34)$$

Then $s(u) \approx \mathcal{K}\mathcal{P}L(1/2 + u)(1/2 - u)/(2\mathcal{Z})$ and the remaining boundary condition $s'(-1/2) = 0$ is automatically satisfied in the limit $L \rightarrow 0$. We can then conclude that the singular solutions are of the form $s(x) = \lim_{L \rightarrow 0} Lf(x/L)$, where $f(u) = \mathcal{K}\mathcal{P}(1/2 + u)(1/2 - u)/(2\mathcal{Z})$. Singular solutions of this type can be useful in the description of cell splitting in a cortical geometry [156]; they are also known in other fields where stationary states are described by Eq. (4.31) [27, 36, 56, 108]. The presence of such solutions is a sign that in a properly augmented theory, accounting for the vanishing length, one can expect localization with active contraction balanced by a regularization mechanism, say active treadmilling [124]. Our numerical solutions of a non-steady problem, which are naturally regularized because of the finite mesh size, show that the almost singular solutions of the type described above serve as attractors for initial data with $L < \hat{L}_-$ when $\mathcal{P} < 1/4$. Moreover, numerical experiments suggest that they are the only attractors for $\mathcal{P} > 1/4$. This means that even in the presence of a cortex-type spring, an active segment fragment necessarily collapses after the contractility parameter reaches the threshold $\mathcal{P}_{\max} = 1/4$.

4.2.6 Linear Stability

We first show that motile branches with $V \neq 0$ can bifurcate only from trivial static solutions with $s(u) = 0$, $V = 0$ and $L = \hat{L}_\pm$. If $V \neq 0$ we can multiply (4.29) by $s' - VL$, to find that

$$\exp(LV/2) - \exp(-LV/2) = LV \int_{-1/2}^{1/2} \exp[s(u) - VLu] du. \quad (4.35)$$

From (4.35), in the limit $V \rightarrow 0$ we obtain that $\int_{-1/2}^{1/2} \exp(s(u)) du = 1$. Since static solutions $s(u)$ must be necessarily sign definite [126] the limiting static solution can be only trivial $s(u) = 0$. As we have seen in Fig. 4.3, there are two non-singular families of trivial solutions: one with longer (\hat{L}_+ family) and the other with shorter (\hat{L}_- family) lengths.

To find the bifurcation points along the trivial branch [$s = 0, V = 0, L = \hat{L}_\pm(\mathcal{P})$], we introduce infinitesimal perturbations $\delta s(u)$, δV , δL and linearize (4.29) together with boundary conditions (4.30). We obtain the boundary value problem

$$\delta s'' - \omega^2 \delta s = \frac{\mathcal{Z}\omega^2 - \hat{L}^2}{\hat{L}^2(\hat{L}-1)} \left(\mathcal{Z} \frac{2\hat{L}-1}{\hat{L}} \omega^2 \delta L + \hat{L}^3(\hat{L}-1) u \delta V \right), \quad (4.36)$$

$$\delta s(\pm 1/2) = 0, \quad \delta s'(\pm 1/2) = \hat{L} \delta V, \quad (4.37)$$

where we introduced the notation $\omega^2 = (\hat{L}^2 - \mathcal{K} \mathcal{P} \hat{L})/\mathcal{Z}$. Since $\omega = 0$ at the trivial branch $\delta s = \delta V = \delta L = 0$, we can assume that $\omega \neq 0$. The general solution of the problem (4.36), (4.37) can be written explicitly

$$\begin{aligned} \delta s(u) = & C_1 \sinh(-\omega u) + C_2 \cosh(-\omega u) \\ & - \frac{\mathcal{Z}\omega^2 - \hat{L}^2}{\omega^2 \hat{L}^2(\hat{L}-1)} \left(\mathcal{Z} \frac{2\hat{L}-1}{\hat{L}} \omega^2 \delta L + \hat{L}^3(\hat{L}-1) u \delta V \right). \end{aligned}$$

Using boundary conditions (4.37) we obtain a transcendental equation for ω

$$2\hat{L}[\cosh(\omega) - 1] - \mathcal{K} \mathcal{P} \omega \sinh(\omega) = 0. \quad (4.38)$$

The detailed analysis of this equation is presented in [126]. Here we only show the locus of bifurcation points in the $(\mathcal{K}, \mathcal{P})$ plane (Fig. 4.4). For motile solutions we use notations D_i and for nontrivial static solutions—notations S_i where $i = 1, 2, \dots$. In Fig. 4.4 the lines marked by $+$ and $-$ correspond to bifurcations originating on the trivial sub-branches \hat{L}_+ and \hat{L}_- , respectively.

If parameter \mathcal{P} is held constant while \mathcal{K} is changing each family D_i and S_i is represented by two points. For solutions bifurcating from the trivial branch \hat{L}_+ , we have bifurcations at $\mathcal{K}_+ = (\hat{L}_+^2 - \mathcal{Z}\omega^2)/(\mathcal{P}\hat{L}_+)$, which gives points $D_1^+, S_1^+, D_2^+, S_2^+, \dots$ and for the branch \hat{L}_- , bifurcations take place at $\mathcal{K}_- = (\hat{L}_-^2 - \mathcal{Z}\omega^2)/(\mathcal{P}\hat{L}_-)$ which gives points $D_1^-, S_1^-, D_2^-, S_2^-, \dots$. Notice that the total number of bifurcation points increases to infinity as $\mathcal{K} \rightarrow \infty$.

Now consider the case when $\mathcal{K} = \text{const}$ and \mathcal{P} is varied. A line $\mathcal{K} = \text{const}$ in the $(\mathcal{K}, \mathcal{P})$ plane cuts again each curve D_i and S_i in two points which we denote D_1^*, S_1^*, \dots (solutions with longer lengths) and $D_1^{**}, S_1^{**}, \dots$ (solutions with shorter lengths), see Figs. 4.3 and 4.4. In most cases one of these two points is a bifurcation originating from the \hat{L}_- trivial solution while the other is from the \hat{L}_+ trivial solution. However, as we show in the inset in Fig. 4.4 the two points may also bifurcate from the same branch \hat{L}_+ . Such bifurcations are of particular interest because they describe both motility initiation and motility arrest.

After bifurcation points are known one can use the Lyapunov–Schmidt reduction technique to identify the nature of the corresponding bifurcations [9, 78, 106]. The analysis presented in [126] shows that the bifurcations from the trivial to the nontrivial static branch are always transcritical. The bifurcations to motile branches can be either subcritical or supercritical. In particular, at a given \mathcal{K} the bifurcation from a static homogeneous solution with longer length is always supercritical while the bifurcation from a static homogeneous solution with smaller length can be either subcritical or supercritical depending on the value of \mathcal{K} , see [126].

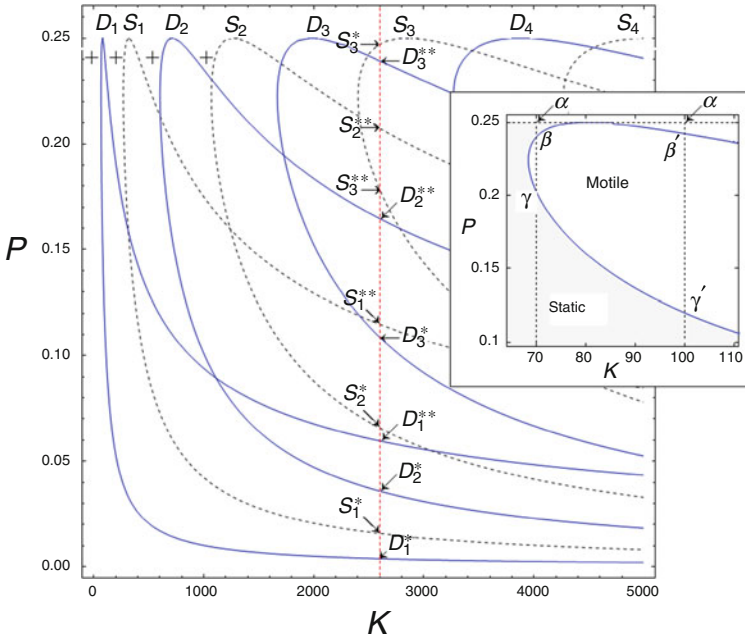


Fig. 4.4 Locus of the bifurcation points in the $(\mathcal{K}, \mathcal{P})$ plane for $\mathcal{L} = 1$. Inset shows a zoom on the D_1 branch around the turning point at $\mathcal{P} = 1/4$ where \hat{L}_- and \hat{L}_+ branches meet. The detailed bifurcation diagrams for $\mathcal{P} = 0.245$ and $\mathcal{K} = 70$ and 100 are shown in Figs. 4.5 and 4.6 from where the meaning of labels β , γ , β' , γ' becomes clear. The bifurcation points related to the cut $\mathcal{K} = 2600$ (red dashed line) in the (\mathcal{P}, L) space are shown in Fig. 4.3

4.2.7 Motile Solutions

To illustrate different types of nontrivial solutions of bifurcations we used the nonlinear continuation methods to solve the boundary value problem (4.29)–(4.30) numerically for successive values of parameters \mathcal{K} and \mathcal{P} (tracking algorithm, see [45]). In Fig. 4.5a we show the continuation in \mathcal{K} for both static and motile configurations at fixed \mathcal{P} ; the corresponding profiles of motor concentration, stress and velocity are shown in Fig. 4.5b. One can see that each pitchfork (for motile branches) and each transcritical (for static branches) bifurcation points gives rise to two nontrivial solutions. For instance, along the static branch \hat{L}_+ , the bifurcation point D_1^+ is associated with two motile supercritical branches whereas the point S_1^+ is associated with two transcritical static branches. Each pair of motile solutions is symmetric with two opposite polarizations corresponding to two different signs of the velocity. Along the first motile branch originating at D_1^+ , the myosin motors concentrate at the trailing edge. For the second motile branch originating at D_2^+ , there is an additional peak in the concentration profile, see Fig. 4.5b. In contrast, the static bifurcation point S_1^+ gives rise to two symmetric configurations with different

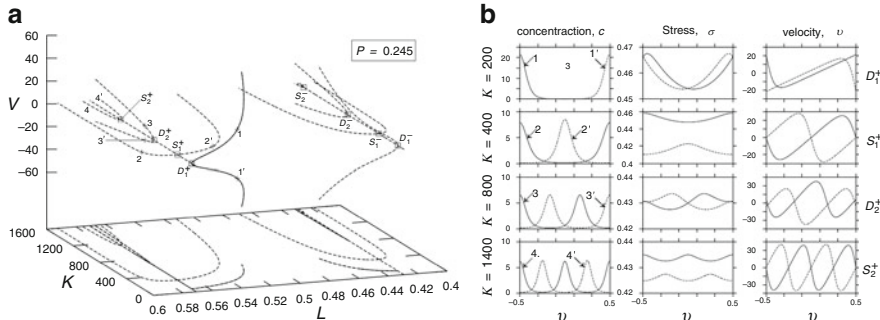


Fig. 4.5 (a) Bifurcation diagram with \mathcal{K} as a parameter showing nontrivial solutions branching from families of homogeneous static solutions \hat{L}_+ and \hat{L}_- . The value $P = 0.245$ and $\mathcal{Z} = 1$ are fixed. Solid lines show stable motile branches while all the dotted lines correspond to unstable solutions. The internal configurations corresponding to branches indicated by numbers (1, 1', 2, 2', etc) are shown in (b). The projection of the bifurcation diagram on the (\mathcal{K}, L) plane is also shown below. (b) Internal profiles associated with successive bifurcated solutions shown in (a) for $P = 0.245$ and $\mathcal{Z} = 1$. Our notation (1,3) correspond to asymmetric motile branches while (2,4) describe symmetric static branches

lengths and with myosin motors concentrated either in the middle of the cell or near the boundaries, see Fig. 4.5b. As one would expect, the higher order static and motile bifurcation points produce solutions with more complex internal patterns. For the branches bifurcating from the trivial configurations belonging to \hat{L}_- family, the picture is similar, see Fig. 4.5a.

In Fig. 4.6, we show in more detail the nontrivial solutions originating from the motile bifurcation points D_1 at two values of parameter \mathcal{K} which correspond to two sections $\alpha\beta$ and $\alpha\beta'$ shown in Fig. 4.4 (insert). Notice that a single solution connects the bifurcation points D_1^* (supercritical) and D_1^{**} (sub- or super-critical) which may belong either to one family \hat{L}_+ ($\alpha\beta$ where D_1^* is the same as D_1^+ and D_1^{**} is the same as D_1^+) or to two different families \hat{L}_+ and \hat{L}_- ($\alpha\beta'$ where D_1^* is the same as D_1^+ and D_1^{**} is the same as D_1^-). In the former case, the nontrivial motile branch has a turning point at a finite value of $P < 1/4$ giving rise to a re-entrant behavior. Similar behavior was also observed in some other models of cell motility, e.g. [55, 80, 153].

As illustrated in Fig. 4.6 and shown more clearly in a phase diagram in Fig. 4.7a, in the re-entrant regime (sufficiently low \mathcal{K}), the increase of the average concentration of myosin (increase of P at fixed \mathcal{K}) first polarizes the cell and initiates motility, but then, if the contractility is increased further, the cell may becomes symmetric again by re-stabilizing in another static homogeneous configuration (see Fig. 4.6, $\mathcal{K} = 70$). We reiterate that re-symmetrization and arrest prior to division (known also as ‘mitotic cell rounding’) is a common feature of almost all animal cells [84, 85, 145]. In this respect, it is interesting that if contractility (P) is increased further, the cell collapses to a point because our effective ‘size preserving spring’ cannot support the contraction any more. Following [156], we can associate

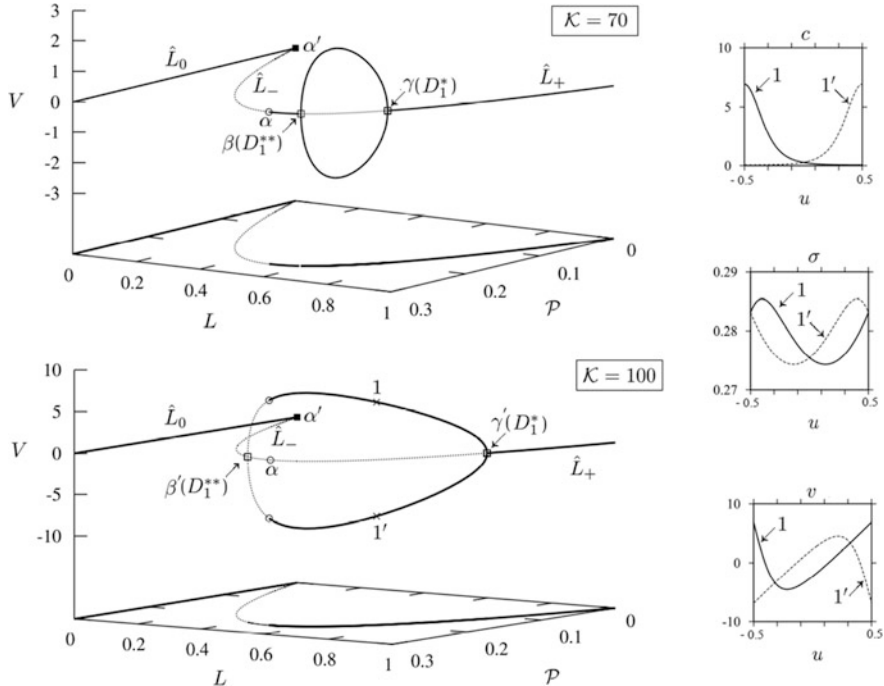


Fig. 4.6 Bifurcation diagrams along parameter \mathcal{P} showing motile branches connecting points D_1^* and D_1^{**} . Corresponding bifurcation points are shown in *insert* in Fig. 4.4. Solid lines show stable motile branches while all the dotted lines correspond to unstable solutions. The projection of the bifurcation diagram on the (\mathcal{P}, L) plane is also shown. Parameter \mathcal{K} is fixed in each graph to $\mathcal{K} = 70$ and $\mathcal{K} = 100$. Internal profiles on the two symmetric motile branches are also shown for $\mathcal{K} = 100$. Parameter $\mathcal{Z} = 1$

such collapse with cell division. We can then argue that our deliberately minimal model succeeds in reproducing a rather general pattern of cell behavior by showing that symmetrization (stabilization) in space immediately precedes the division.

While the physical meaning of the non-dimensional parameter \mathcal{P} in this discussion is rather clear (contractility measure), the significance of varying \mathcal{K} at fixed \mathcal{Z} is less obvious because both of these parameters depend on frictional strength of the background. Adhesivity of the cell to the substrate is known to be a crucial parameter for motility initiation and arrest for various cell types [10, 91]. To explicitly expose the role of friction, it is instructive to interpret parameter $1/\mathcal{K}$ as a measure of adhesivity while keeping the ratio \mathcal{Z}/\mathcal{K} , which does not have any relation to friction, at a constant level.

The phase diagram in the $(\mathcal{P}, 1/\mathcal{K})$ plane at fixed \mathcal{Z}/\mathcal{K} is shown in Fig. 4.7b. In this diagram a horizontal path extending from left to right describes a succession of states with fixed adhesivity and increasing contractility. One can see that at high adhesivity motility ceases to exist, moreover as contractility increases static solutions eventually collapse. If the adhesivity is below a certain threshold, the

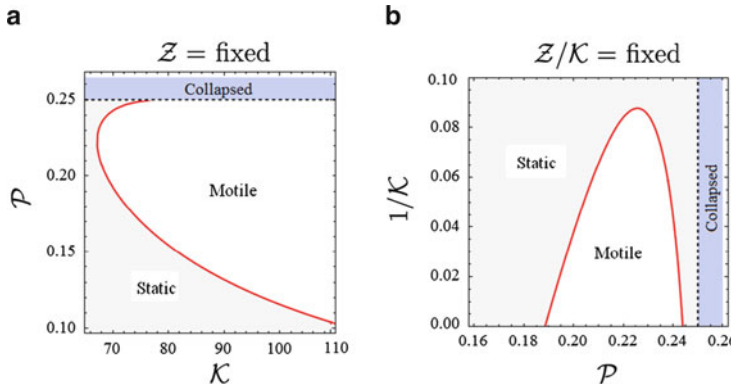


Fig. 4.7 (a) Phase diagram of the system (4.20) in the parameter plane $(\mathcal{K}, \mathcal{P})$ at fixed $\mathcal{Z} = 1$. (b) Phase diagram of the same system (4.20) in the parameter plane $(\mathcal{P}, 1/\mathcal{K})$ at fixed $\mathcal{Z}/\mathcal{K} = 0.015$. The solid (red) line indicates the motility bifurcation point (D_1^+ similar to Fig. 4.4), while the black dashed lines indicate the collapse threshold ($\mathcal{P}_{\max} = 1/4$)

contractility increase first causes polarization of a static configuration and motility initiation; further increase of contractility causes re-symmetrization, arrest and eventually collapse. An interesting regime corresponds to the very tip of the motile domain shown in Fig. 4.7b. Near this ‘critical’ point the motility can be sustained in a narrow ‘homeostatic window’ of parameters and can be easily arrested by either increase or decrease of contractility.

Very recently new experimental results elucidating motility initiation in fish keratocytes have appeared [14]. According to these experiments, at a fixed contractility level (fixed \mathcal{P} in our model), the increase of surface adhesivity (increase of $1/\mathcal{K}$ in our model) promotes static configurations while lowering adhesivity initiates motility. As it follows from Fig. 4.7b, these observations are in agreement with our predictions. Our model also explains another observation made in [14] that at a fixed adhesivity, a blebbistatin (a contractility inhibitor) treatment promotes arrest of the cells while a calyculin A treatment (a contractility stimulator) initiates motility. The question whether a more substantial increase of contractility in experiment can lead to re-symmetrization and arrest remains open. It is promising in this respect that some cells are known to undergo static to motile transformation in response to a *decrease* in the level of contractility [68, 90]. The minimal model presented in [14] is exactly a 2D version of the one formulated in [122] and further developed in the present paper. While active protrusion and nonlinear regulation of adhesion were also accounted for in [14] to get a realistic cell shape, it is rather remarkable that the fundamental pattern of motility initiation (including its dependence on contractility and adhesivity) can be already captured within our much more transparent setting, see Fig. 4.7b and [126].

Among various branches of the TW solutions studied above only stable ones have physical sense. The stability was studied numerically in [123] and here we briefly summarize the results of the solution of the corresponding perturbed initial value problems.

The numerical experiments suggest that the trivial branch \hat{L}_- is unstable together with all nontrivial non-singular static solutions. The singular static solutions from the \hat{L}_0 family appear to be locally stable. Instead, the dynamic solutions are all unstable except for the branches bifurcating from the points D_1^+ on the trivial branch \hat{L}_+ . The trivial branch \hat{L}_+ branch is locally stable until the first (motile) bifurcation D_1^+ . Both symmetric subbranches of D_1^+ (subfamilies 1 and 1' in Fig. 4.5a, b are stable and this justifies the above speculations about motility initiation and motility arrest. Moreover, we found that some unstable multi-peaked static and dynamic solutions are long living. This behavior, which was also observed in [22, 67, 80] in the problem with fixed boundaries, is reminiscent of the spinodal decomposition in a 1D Cahn–Hilliard model where the coarsening process gets critically slowed down near multiple saddle points [35].

4.2.8 Passive Actin Treadmilling

We recall that our assumption that the bulk stiffness of the cytoskeleton is equal to zero (infinite compressibility assumption [75, 131]) allowed us to uncouple the force balance problem from the mass transport problem. As we have seen in the previous section, by solving our Keller–Segel system we can obtain the velocity field and the concentration of motors. To recover the mass distribution of the cytoskeleton we need to solve a decoupled mass balance equation (4.5) with a kinematically prescribed velocity field and initial condition $\rho(x, 0) = \rho_0(x)$. Knowing $v(x, t)$ also means that we know trajectories of the free boundaries $l_-(t)$ and $l_+(t)$ and since both edges move with the particles the total mass $M = \int_{l_-(t)}^{l_+(t)} \rho(x, t) dx$ is conserved.

In dimensionless variables the mass balance equation (4.5) can be written as

$$\partial_t \rho + \mathcal{K} \partial_x (\rho \partial_x \sigma) = 0 \quad (4.39)$$

and the total mass constraint takes the form $\int_{l_-(t)}^{l_+(t)} \rho(x, t) dx = 1$. Supposing that the velocity field $v(x, t) = \mathcal{K} \partial_x \sigma(x, t)$ is known, we solve (4.39) by the method of characteristics. Denote the trajectories of the mass particles by $x = x(\zeta, t)$, where $l_-(0) \leq \zeta \leq l_+(0)$ is the Lagrangian coordinate at $t = 0$, the characteristic curves can be found from the equations

$$\frac{dx(\zeta, s)}{ds} = v(x(\zeta, s), s). \quad (4.40)$$

Along these curves we must have

$$\frac{d\rho(x(\zeta, s), s)}{ds} = -\rho(x(\zeta, s), s) \partial_x v(x(\zeta, s), s).$$

Integration of this equation gives an explicit formula for the mass density

$$\rho(x(\zeta, t), t) = \rho_0(\zeta) \exp \left\{ - \int_0^t \partial_x v(x(\zeta, s), s) ds \right\}. \quad (4.41)$$

For TW solutions of (4.20), the velocity field in (4.40) depends on the normalized co-moving variable u and the normalized Lagrangian variable $\hat{\zeta} = \zeta/L(0) - 1/2$, both in the interval $[-1/2, 1/2]$. Then $v = v(u)$ and Eq. (4.40) reduces to

$$\frac{du(\hat{\zeta}, s)}{ds} = \frac{v(u(\hat{\zeta}, s)) - V}{L}. \quad (4.42)$$

For instance, close to the bifurcation points, for the motile branches D_m^\pm we need to solve the characteristic equation

$$\frac{du(\hat{\zeta}, s)}{ds} = \varsigma \left\{ - \frac{L^2}{\omega_c^3 \cos(\omega_c/2)} \left[\omega_c \cos(\omega_c u(\hat{\zeta}, s)) - 2 \sin(\omega_c/2) \right] - 1 \right\}, \quad (4.43)$$

where ω_c is the corresponding solution of Eq. (4.38). In Fig. 4.8, we show the sample solutions of (4.43) corresponding to homogeneous initial conditions $u(\hat{\zeta}, 0) = \hat{\zeta}$ and positive ς .

According to (4.42) the points of the body where $v = V$ are singular because the relative flow there is stagnated. If at such point the slope of the function $v(u)$ is negative we obtain a sink of particle trajectories $u = \gamma_+$ (i.e. an attractor for particles as $t \rightarrow \infty$) whereas if the slope of the function $v(u)$ is positive, the singular point $u = \gamma_-$ corresponds to a source of particle trajectories (an attractor as $t \rightarrow -\infty$). Then all mass points (corresponding to different values of $\hat{\zeta}$) come from

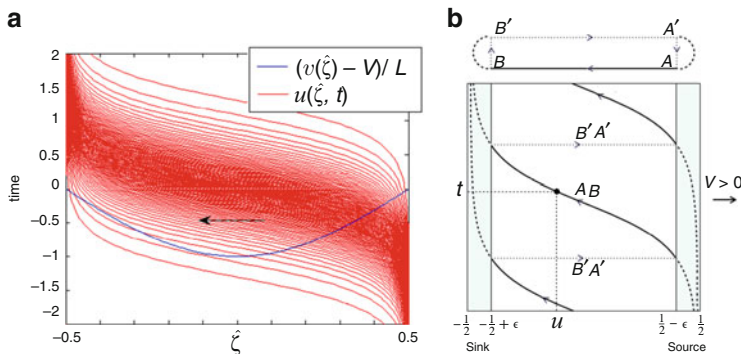


Fig. 4.8 (a) Trajectories of particles from a source to a sink for the first motile bifurcation point associated with positive velocity for initially homogeneously distributed set of particles. (b) Trajectory of an individual actin particle undergoing passive treadmilling for a typical solution on the D_1 motile branch with $V > 0$. Shaded regions are excluded domains of singular behavior

the sources where the characteristic curves accumulate at large negative times and disappear in the sinks where the characteristic curves accumulate at large positive time. An important feature of the flows described by (4.42) is that it takes an infinite time for a mass particle to reach a sink or to leave a source because $(v(u) - V)^{-1}$ is not integrable in the neighborhood of γ_- and γ_+ . As a result the total mass flux is equal to zero

$$\dot{m} = \left(\int_{\gamma_-}^{\gamma_+} \frac{du}{v(u) - V} \right)^{-1} = 0.$$

To illustrate this point we recall that for the TW solutions the general formula (4.41) describing the mass distribution simplifies

$$L\rho(u(\hat{\zeta}, t), t)\{v(u(\hat{\zeta}, t)) - V\} = \dot{m}. \quad (4.44)$$

The fact that $\dot{m} = 0$ implies that mass density ρ infinitely localizes in the singular points (sources and sinks) while vanishing elsewhere.

To close the cycle of passive treadmilling we need to regularize the problem near the singular points by cutting out small regularization domains of size ϵ around the sources and sinks and appropriately reconnecting the incoming and the outgoing flows of matter. In this way we obtain an effective ‘polymerization zone’ around each source $\Gamma_- = \{u \in [-1/2, 1/2] / |u - \gamma_-| < \epsilon\}$ and an effective ‘depolymerization zone’ around each sink $\Gamma_+ = \{u \in [-1/2, 1/2] / |u - \gamma_+| < \epsilon\}$. We assume that in the domain Γ_- the network is constantly assembled from the abundant monomers while in the domain Γ_+ it is constantly disassembled so that the pool of monomers is replenished. The ensuing closure of the treadmilling cycle is instantaneous (jump process) allowing the monomers to avoid the frictional contact with the environment. In other words, we assume that the jump part of the treadmilling cycle is a passive equilibrium process driven exclusively by myosin contraction.

In the regularized problem the mass flux

$$\dot{m} = \left(\int_{\partial\Gamma_-}^{\partial\Gamma_+} \frac{du}{v(u) - V} \right)^{-1}$$

becomes finite and the corresponding density profiles, that are now defined only outside sources and sinks, can be found using formula (4.44) with $\dot{m} \neq 0$. As in our discrete model, here we also represent the ‘returning’ flow by discontinuities so that a particle reaching the boundary of the sink region following a smooth trajectory (path AB in Fig. 4.8) instantly reappears on the boundary of the source region (path $B'A'$ on Fig. 4.8b).

4.2.9 Nonlinear Active Stress

The fact that the bifurcation leading to polarization and motility initiation is always a supercritical pitchfork indicates that in the present form the model does not allow for metastability and coexistence of motile and non-motile configurations [55, 153, 168]. However, to capture this effect we need to modify our model only slightly. The main idea is to consider a more realistic nonlinear dependence of the active stress on motor concentration.

To this end we rewrite the main system of equations in the form

$$\begin{aligned} -\mathcal{Z}\partial_{xx}\sigma + \sigma &= \mathcal{P}\Phi(rc)/r, \\ \partial_t c + \mathcal{K}\partial_x(c\partial_x\sigma) &= \partial_{xx}c, \end{aligned} \quad (4.45)$$

where, following [22], we set $r = c_0/c^*$ and assume that the function $\Phi(x)$ is linear at small values of x but then saturates after around $x = 1$. In computations we use a particular form of nonlinearity $\Phi(x) = x/(1+x)$.

For simplicity we first analyze the ‘rigid’ limit where $k \rightarrow \infty$ and $L \rightarrow L_0$ while the stress on the boundaries $-k(L/L_0 - 1)$ remains finite. Notice that in this limit, which also means that $\mathcal{P} \rightarrow 0$ and $\mathcal{K} \rightarrow \infty$, we have to re-scale the stress by $c_0\chi$ instead of k . If with some abuse of notations, we denote $\sigma := \sigma/\mathcal{P}$, the new dimensionless parameter replacing \mathcal{K} and \mathcal{P} will be $\lambda = c_0\chi/(\xi D) = \mathcal{K}\mathcal{P}$, see also [22, 59, 61, 67]). The mechanical boundary conditions can be written in the form $\sigma(l_{\pm}(t), t) = \sigma_0$ and $\dot{l}_{\pm} = \lambda\partial_x\sigma(l_{\pm}(t), t)$, where $\sigma_0 = -\lim_{\mathcal{P} \rightarrow 0} \lim_{L \rightarrow 1} (L-1)/\mathcal{P}$.

For TW solutions we can write the analogue of (4.29)

$$-\mathcal{Z}s'' + s + s_0 = \frac{\lambda}{r}\Phi\left(r \frac{\exp(s - Vu)}{\int_0^1 \exp(s - Vu)du}\right), \quad (4.46)$$

where $s = \lambda(\sigma - \sigma_0)$ and $s_0 = \lambda\sigma_0$. The boundary conditions take the form $s(0) = s(1) = 0$ and $s'(0) = s'(1) = V$. The difference with our static solutions, described in Sect. 4.2.5, is that now we have to find the stress at the boundary s_0 instead of the length L .

The analytical study of the motility initiation bifurcation in this case is presented in [126]. The numerical results are illustrated in Fig. 4.9. As we see, when the nondimensional parameter r is small, which means that we are in the linear regime, the bifurcation from static to motile regime is a supercritical pitchfork. However, at larger values of r the nature of the bifurcation changes from supercritical to subcritical. This opens an interval of metastability where both the homogeneous static state and the inhomogeneous motile state are locally stable.

In Fig. 4.10 we illustrate the effect of choosing a threshold-type dependence of contractile stress on the concentration of motors. Here we dropped the assumption that the length of the moving segment is fixed. A comparison of Fig. 4.10 with Fig. 4.7b shows that the saturation of contractile stress introduces a finite zone

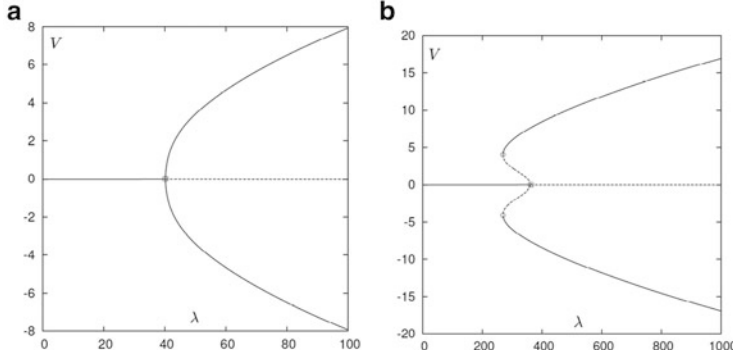


Fig. 4.9 Bifurcation diagrams in the nonlinear model with fixed length (infinite stiffness) (4.46) showing the possibility of a switch from supercritical to subcritical bifurcation. Parameters: $\Ζ = 1$. (a) $r = 1$. (b) $r = 5$

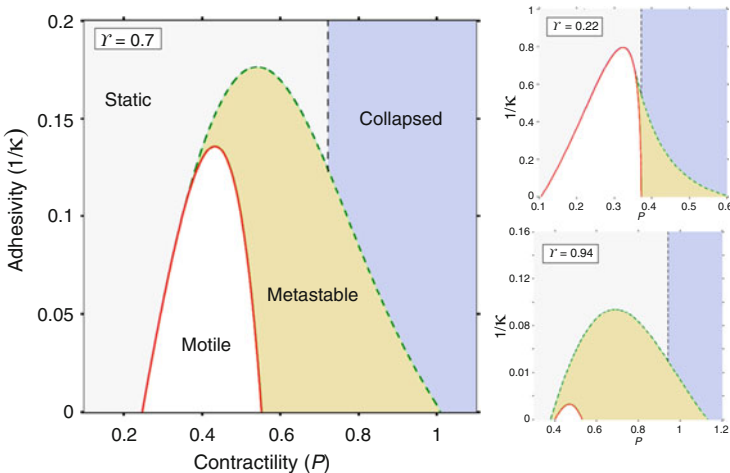


Fig. 4.10 Left: phase diagram in the parameter plane $(\mathcal{P}, 1/\kappa)$ for the system (4.45) (with no length constraint). The parameter $\Ζ/\kappa \approx 6 \times 10^{-3}$ is fixed at its experimental value. The *solid* (red) line indicates the motile bifurcation threshold for the branch D_1^+ (similar to Fig. 4.7b), while the *dashed line* bounding the metastability domain indicates the location of the turning points on the motile branch in the appropriate analog of Fig. 4.9b. The *dashed line* separating static and collapsed configurations indicates the location of the turning point α in Fig. 4.3. Right: effects of a high (top) and low (bottom) concentration saturation thresholds

of metastability where finite perturbations are required to switch between static to a motile regimes. This prediction was recently confirmed *in vivo* by Barnhart et al. [14] and the metastability domain as in Fig. 4.10 was mapped experimentally. We also observe that for sufficiently large values of the saturation threshold r ,

our model predicts metastability and hysteresis during both, motility initiation and motility arrest. On the arrest side [84], this prediction can be linked to the hysteresis associated with cell division [156].

4.2.10 Discussion

In this section we were mostly concerned with the discussion of the autotaxis mechanism of cell motility. The main idea is that pullers can propel the passive medium by inflicting contraction because they are themselves advected by this medium which creates an autocatalytic effect [97]. The inevitable build up of mechanical gradients in these conditions is limited by diffusion which resists the runaway and provides the negative feedback. After the symmetry of the static configuration is broken in the conditions where matter can circulate, the resultant contraction-driven flow ensures the perpetual renewal of the network and then frictional interaction with the environment allows for the steady translocation of the cell body.

A prototypical model presented in this section provides an alternative qualitative explanation of the experiments of Verkhovsky et al. [159], Yam et al. [167] that have been previously interpreted in terms of active polymerization inducing the growth of actin network [20]. Most strikingly, the predictions of this model are also in quantitative agreement with experimental data presented in [159], see [126] for a detailed comparison. This is rather remarkable in view of a schematic nature of this model and the absence of fitting parameters. The model also captures a durotactic effect since the directional motion cannot be initiated if friction with the substrate is larger than a threshold value. Below this threshold, motile regimes exist in a finite range of contractility. This means that if the cell is already in motion, it can recover the symmetric (static) configuration either by lowering or by increasing the amount of operating motors. The possibility of cell arrest under the increased contractility should be investigated in focused experiments.

We have also shown that when the contractility depends on the motor concentration nonlinearly, the system exhibits a metastability range where both static and motile regimes are stable and can coexist. In the corresponding interval of parameters a mechanical perturbation may be used to switch back and forth between static and dynamic regimes. This prediction of the model is particularly important in the context of collective cell motility (in tissues) where contact interactions are able to either initiate or terminate the motion [1, 62, 155, 158].

4.3 Protrusion

In this section we introduce a new active mechanism, polymerization-induced protrusion, and search for conditions when it can overshadow active contraction and become the main driver of self-propulsion. To maintain analytic transparency

we simplify the description of contraction by disabling the autotaxis mechanism and assuming that the distribution of motors is uniform in space and constant in time.

The crucial observation, justifying the introduction of a protrusion-centered motility mechanism, is that eukaryotic cells do not only self-propel and carry cargoes by pulling, but can also exert forces on obstacles performing mechanical pushing. However, it is quite clear that pushing cannot be accomplished efficiently by contraction only. In other words, pullers must pull while pushing should be delegated to pushers.

In this section we show that protrusion dominated motility, performed largely by pushers, may have a very particular macroscopic signature: the concavity of the force velocity relation. We also show that pulling can be also driven exclusively by protrusion but only for small values of the pulling force: it must be necessarily replaced by contraction-centered mechanism when the pulling force is sufficiently large. The substitution of one mechanism by another with increasing load is manifested by a more complex convex-concave structure of the force velocity relation. Most interesting, our model suggests that competition between protrusion and contraction can produce negative mobility in a biologically relevant range.

Viewed more broadly, the results of this section illustrate the possibility of active readjustment of the force generating mechanism in response to changes in the dipole structure of external forces showing that if necessary ‘pushers’ can replace ‘pullers’ and visa versa.

4.3.1 The Model

To model a loaded self-propelling active fragment we maintain the force balance equation (4.17) but modify the mechanical boundary conditions and write

$$\sigma(l_{\pm}(t), t) = q_{\pm}.$$

In our notations $q_+ < 0$ corresponds to pushing (at the front) and $q_- > 0$ to pulling (at the rear). In this description the mean-field elasticity has been omitted given that active protrusion provides an independent mechanism of maintaining a particular ‘cell volume’ (see more about this below). It will also be convenient to define the resultant force

$$Q = q_- - q_+ \geq 0$$

which we assume to be positive and acting against the polarization direction induced by protrusion. We also introduce the force asymmetry factor

$$\epsilon = \frac{q_- + q_+}{Q},$$

which characterizes the first moment of the external force distribution. We notice that $-1 \leq \epsilon \leq 1$ with $\epsilon > 0$ corresponding to pulling and $\epsilon < 0$ —to pushing.

The protrusive ‘force’ in our model will be introduced implicitly through the new kinematic constraints on the unknown functions $l_+(t)$ and $l_-(t)$ [75, 83, 86, 122, 131]

$$\dot{l}_\pm = v(l_\pm(t), t) + v_\pm. \quad (4.47)$$

Here $v_+ > 0$ and $v_- > 0$ are the polymerization and the depolymerization velocities, respectively. While there is considerable experimental evidence that active polymerization is indeed localized at the leading edge of a crawling cell, the de-polymerization may be spread along the length of the lamellipodium [75, 131]. However, in the interest of analytic transparency, such spreading will be ignored in this study (see the analysis of this assumption in [122]).

Observe that our assumption (4.47) implies that there is a nonzero (negative) mass flux going through the system

$$\dot{m} = -\rho(l_\pm(t), t)v_\pm.$$

To account for this flux we need to slightly modify the theoretical framework introduced in the first section, in particular, (4.9) has to be modified since there is now an incoming and outgoing fluxes of free energy associated with production polymerized monomers at the front and dissociating the filaments into free monomers at the rear. By following the same steps as in the first section we obtain

$$R = \int_{l_-}^{l_+} (\sigma \partial_x v + v A + J \partial_x \mu) dx - \dot{m} \Delta \mu, \quad (4.48)$$

where $\Delta \mu = [f + p/\rho]_-^+$ is the driving force of active treadmilling. Since for our infinitely compressible gel the thermodynamic pressure $p = 0$ we obtain $\Delta \mu = f(l_+(t)) - f(l_-(t))$. A knowledge of polymerization/depolymerization reaction kinetics can provide us with the kinetic relation whose simplest form would be $\dot{m} = \psi(\Delta \mu)$ and then we also need to specify the externally (for our model) imposed driving force $\Delta \mu$. However, to maintain the decoupling between the force balance problem and the mass transport problem, secured by our infinite compressibility assumption, we define protrusion by prescribing two other pieces of information: the kinematic variables v_\pm .

In fact, it will prove natural to work with a slightly different set of parameters. Thus, parameter

$$V_m = \frac{v_- + v_+}{2} \geq 0$$

prescribes polarity of the cell and provides the scale of the maximal velocity. The remaining kinematic parameter

$$\Delta V = v_+ - v_-,$$

introduces the asymmetry between polymerization and de-polymerization and, as we show below, quantifies the degree of engagement of the contractile mechanism.

The other constitutive hypotheses will be as in the previous section except that we assume for simplicity that in the transport of motors diffusion dominates drift and $c(x, t) \equiv c_0$. Then the contraction-generated pre-stress is also constant $\chi_0 = aA_0c_0 > 0$, which is a rather usual assumption in the models of active gels [75, 83]. Notice that in the previous section we used the notation χ for contractile pre-stress per unit motor mass which is now irrelevant since c does not depend on either space or time.

If we now normalize length by $\sqrt{\eta/\xi}$, time by η/χ_0 and stress by χ_0 , we obtain a free boundary problem which depends on four dimensionless parameters.

$$\begin{aligned} -\partial_{xx}\sigma + \sigma &= 1 \\ \sigma(l_{\pm}(t), t) &= q_{\pm} \\ \dot{l}_{\pm} &= v_{\pm} + \partial_x\sigma(l_{\pm}(t), t). \end{aligned} \quad (4.49)$$

The linear force balance equation with mechanical boundary conditions can be integrated (see [75, 83] for the case without cargo) and we obtain

$$v(x, t) = \frac{A_- \cosh(l_-(t) - x) + A_+ \cosh(l_+(t) - x)}{\sinh(l_+(t) - l_-(t))}, \quad (4.50)$$

where

$$A_{\pm} = \pm(1 - Q(\epsilon \pm 1)/2). \quad (4.51)$$

Knowledge of the velocity field and the use of kinematic boundary conditions allows one to obtain a closed dynamical problem for the total length $L(t)$

$$\dot{L} = \Delta V + (\epsilon Q - 2) \tanh\left(\frac{L}{2}\right). \quad (4.52)$$

After this equation is solved the position of the geometrical center of the cell $G(t)$ can be found by direct integration from

$$\dot{G} = V_m - \frac{Q}{2 \tanh(L/2)}. \quad (4.53)$$

To specify solutions of (4.52) and (4.53) we need to supply the initial conditions $L(0)$ and $G(0)$ that also fix the initial velocity profile through (4.50).

We are interested in traveling wave (TW) solutions of (4.52) describing steadily translocating active fragments. The corresponding critical points of (4.52) exist if and only if

$$0 < \Delta V < 2 - \epsilon Q. \quad (4.54)$$

When these conditions are satisfied the length stabilizes as $t \rightarrow \infty$ at the value

$$L = 2 \tanh^{-1} \left(\frac{\Delta V}{2 - \epsilon Q} \right) > 0.$$

4.3.2 Force Velocity Relation

Notice that at $t \rightarrow \infty$ the function \dot{G} converges to a constant V given by the force-velocity relation

$$V = V_m - \frac{Q}{\Delta V} + \frac{\epsilon Q^2}{2 \Delta V}. \quad (4.55)$$

In our notations the fragment moves to the right against the load if $V > 0$ and is dragged backwards by the load if $V < 0$. The maximum velocity $V^* = V_m$ is achieved when there is no load $Q = 0$ and the corresponding reference length will be denoted by $L^* = L(Q = 0)$. Since the TW regimes are stable only if $2 - \epsilon Q > 0$, pushing ($\epsilon < 0$) contributes to stability while pulling ($\epsilon > 0$) plays a destabilizing role.

At $\Delta V = 0$ the loaded fragment shrinks to a point while at $\Delta V = 2 - \epsilon Q$ its length diverges. For singular solutions with $L = \infty$ which are only relevant in the case of pulling, the force velocity relation can be extended beyond the singularity formation threshold as

$$V = V_m - Q/2. \quad (4.56)$$

The full force-velocity relation in the (V, Q) plane including both regular and singular solutions is illustrated in Fig. 4.11a, b. One can see that it is markedly different for $\epsilon > 0$ (pulling) and $\epsilon < 0$ (pushing). The main feature distinguishing pushing from pulling is the curvature of the force velocity relation which in the regular regimes (4.55) is given by $\partial^2 V / \partial Q^2 = \epsilon / \Delta V$, and in the singular (pulling) regimes by $\partial^2 V / \partial Q^2 = 0$. One can also see that the curvature is always negative in pushing regimes with $\epsilon < 0$ which means that the corresponding force velocity relation is concave. Under pulling loads with $\epsilon > 0$ the force velocity curve is convex for regular regimes and is linear for singular regimes.

In the pushing regimes the force velocity curve is characterized by the stall force $Q^* = (1 - \sqrt{1 - 2\epsilon \Delta V V_m})/\epsilon$ and the maximum velocity $V^* = V_m$, see Fig. 4.11b. The concavity of the force velocity relation in this case agrees with experiments [26, 115, 135, 170]. In the case of pulling, the force-velocity relation is convex for $Q < Q_c = (2 - \Delta V)/\epsilon$, where $L < \infty$ and is linear for $Q > Q_c$, where $L = \infty$, see Fig. 4.11a. In the convex range the function $V(Q)$ is non-monotone when $\Delta V < 1$ and one can distinguish two regimes: the branch $Q < Q_n = 1/\epsilon$ where the mobility is positive, $V(Q) \sim V_m - Q/\Delta V$, and, as we show below,

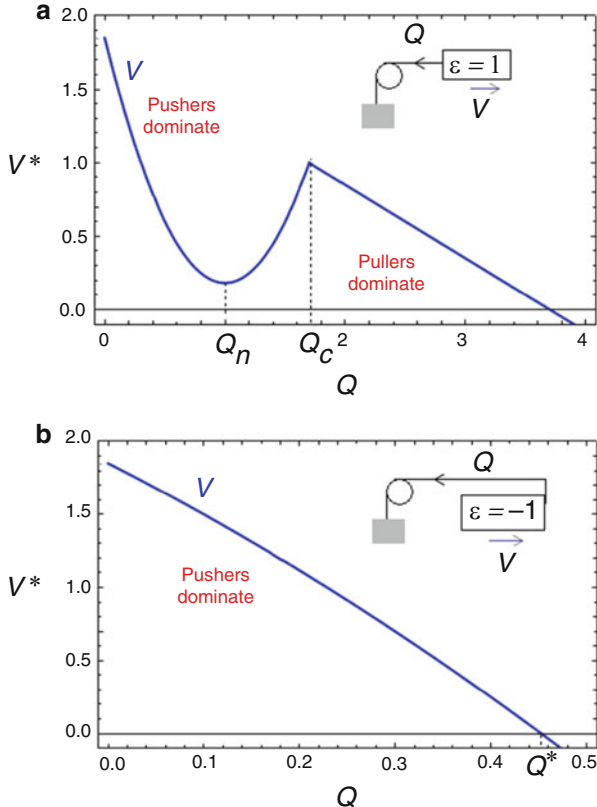


Fig. 4.11 The typical force-velocity relations in pure pulling (a) and pushing (b) regimes

protrusion dominates, and the branch $Q_c > Q > Q_n$ where the mobility is negative, $V(Q) \sim \epsilon Q^2 / (2\Delta V)$ and the dominant active mechanism is contraction. Along the negative mobility branch the cell elongates to support larger loads till the length diverges at a critical value $Q = Q_c$. Beyond this value, we obtain configurations with infinitely separated boundary layers and mobility becomes again positive. The associated density profiles are discussed in [122].

The observed differences in the structure of force velocity relations in the regimes of pushing and pulling can be interpreted in terms of the competition between pushers and pullers. We begin with an observation [33, 83] that the analysis of the global force balance, $L \int_{-1/2}^{1/2} v(u) du = -Q$, does not allow one to distinguish between pushing and pulling. To identify the role of different active agents we need to consider the balance of couples where an important role is played by the sign of the dipole component of the applied load.

By multiplying the force balance equation (4.49) in the TW regime by u and integrating over the body of the cell we obtain

$$\frac{\epsilon}{2}Q - L \int_{-1/2}^{1/2} uv(u)du = \int_{-1/2}^{1/2} \sigma(u)du. \quad (4.57)$$

The first term in the left hand side $T_e = \frac{\epsilon}{2}Q$ is the moment of external forces. Since we assumed that $Q > 0$, pulling is associated with a positive applied dipole while pushing—with a negative applied dipole. The second term on the left hand side $T_f = -L \int_{-1/2}^{1/2} uv(u)du$ represents frictional dipole which may have different signs. The integral on the right hand side defines the active dipole which can be also rewritten as $T_a = \int_{-1/2}^{1/2} (1 + L^{-1} \partial_u v)du$. This term can be further decomposed into the sum $T_c + T_p$ where contraction component is $T_c = 1 > 0$ and protrusion component is $T_p = -\Delta V/L < 0$. The opposite signs of these two terms suggest that the underlying active mechanisms are inherently different: the protrusion term represents distributed pushers while the contraction term represents distributed pullers [132, 144].

Due to the presence of a contraction (positive) force dipoles the rear boundary of the cell is pulled forward while the front boundary is pulled backward. As a compensation, contraction produces internal retrograde flow at the rear and pro-grade flow at the front. In contrast, protrusion (negative) force dipole pushes the rear of the cell backward while the front of the cell is pushed forward. This is compensated internally by retrograde flow at the front and pro-grade at the rear. These flows must be superimposed with the mean flow $\bar{v} = -Q/L$ which is associated solely with the total applied force and is therefore always retrograde.

It is now natural to identify the point Q_n in Fig. 4.11a with a crossover from pushers dominated to pullers dominated regimes. This interpretation is supported by comparing the magnitudes of the two competing active couples. The observed crossover correlates with the transition from positive to negative mobility which also takes place at Q_n . Negative mobility has been discussed previously in the context of individual [38, 57, 94, 130] and interacting [25, 110] Brownian motors. The regimes where velocity of the crawling cell increases with an opposing pulling force at the rear have been envisioned in [72] where negative mobility was attributed to the coupling between the velocity of retraction and the applied force $v_-(Q)$ [113]. In our model such coupling is absent which shows that negative motility may also have a different origin. The parameter estimates showing that negative motility is realistic in physiological conditions can be found in [122].

4.3.3 Elastic Regularization

The obtained force-velocity relations are not fully satisfactory because some of the solutions have diverging length. A natural way to regularize such singular solutions

is to introduce an intermediate-time stiffness of the cell. Such stiffness, which we have already encountered in the previous section, can in some regimes prevent cells from contraction-induced collapse, it sets the rest length and it may also keep this length from diverging in the case of super critical pulling. Time dependent visco-elastic properties of the cytoskeleton [21, 37, 101] are usually incorporated either in the framework of a short time (Maxwell) elastic model [28, 73, 75, 121, 131] or a long time (Kelvin–Voigt) elastic model [10, 86, 111].

The simplest purely elastic regularization, already considered in the previous section, is through mean field coupling between the leading and trailing edges of a cell [12, 49, 117, 142]. If this coupling is linear elastic, the applied loads become

$$q_{\pm} \rightarrow q_{\pm} + k \frac{L - L_0}{L_0},$$

where $k > 0$ is a dimensionless stiffness and L_0 is a prescribed dimensionless reference length (for the comparison with models of bulk linear elasticity, see [122]). The meaning of parameter L_0 is clear from the fact that for $k > 1$ and $V_m = \Delta V = 0$ there exists a nontrivial static solution with $L = L_0(1 - 1/k)$ (preferred length).

In dynamics the steady state (TW) solution is now stable for all $\Delta V > 0$ and to find $L(Q)$ one needs to solve

$$\Delta V = \left(2 - \epsilon Q + 2k \frac{L - L_0}{L_0} \right) \tanh \left(\frac{L}{2} \right).$$

Then, the force velocity relation can be found from the relation

$$V(Q) = V_m - \frac{Q}{2 \tanh \left(\frac{L(Q)}{2} \right)}.$$

The k dependence of the force velocity relation is illustrated in Fig. 4.12. We observe that independently of the value of k all force-velocity curves cross at $Q = 0$ where $V = V^*$. The second common intersection point is at

$$Q_I = \frac{1}{\epsilon} \left(2 - \frac{\Delta V}{\tanh \left(\frac{L_0}{2} \right)} \right).$$

As we see, at $k \rightarrow 0$ the mean field force-velocity curves approach their minimal model counterparts including both the regular regimes with finite cell lengths and the singular regimes with infinite cell lengths. However, despite similarity in shape between the force velocity curves in the minimal model and in the regularized model with $k \sim 0$, the length of the cell in the regularized model is always *finite* so that infinite stretching, undermining the minimal model, does not take place.

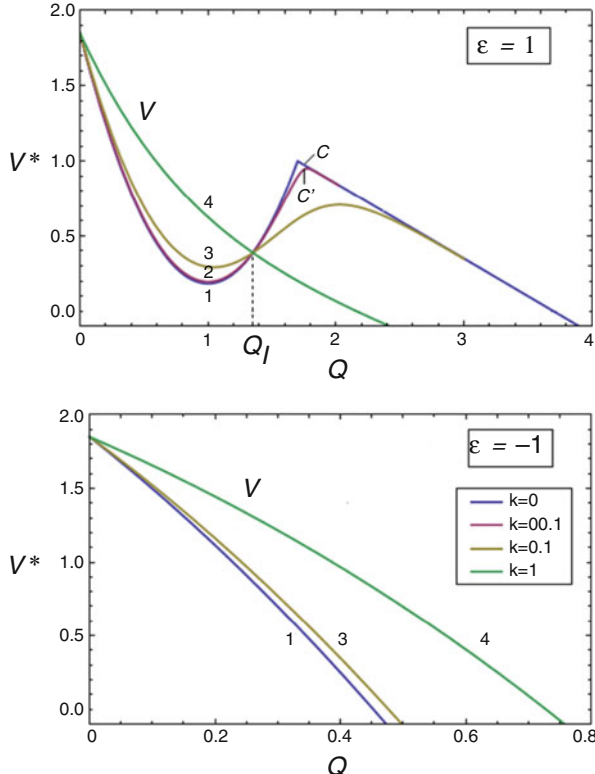


Fig. 4.12 Force velocity relations in pure pushing and pulling modes with different $k_{1,2,3,4} = \{0, 0.01, 0.1, 1\}$ and $L_0 = 1$. Driving parameters are $v_- = 1.7$ and $v_+ = 2$. The minimal model is recovered at $k = 0$

The phenomenon of negative mobility for the pulled cells survives in the mean field model and disappears only at a critical value of the stiffness $k = k^*(\Delta V)$, see Fig. 4.13. The qualitative difference in convexity between pulling and pushing persists beyond $k^*(\Delta V)$, see for instance regime with $k = 1$ in Fig. 4.12. However, at $k \gg k^*(\Delta V)$ the force-velocity relations associated with pushing and pulling regimes become similar.

To check robustness of these predictions we studied in [122] three different extensions of this model allowing for inhomogeneous friction, bulk depolymerization and density dependent contractile pre-stress. Our analysis shows that for all these augmented models our main conclusion about the difference in convexity properties between the force velocity curves in pushing and pulling regimes remain valid.

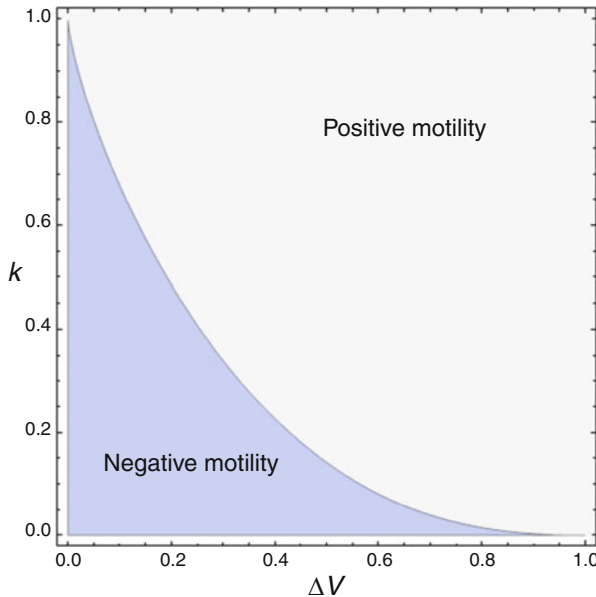


Fig. 4.13 Domain of negative motility in the parameter space $(k, \Delta V)$. The boundary between regimes with positive and negative motility is given by the function $k = k^*(\Delta V)$

4.3.4 Alternative Driving Modes

So far we have been using an assumption that protrusion is driven by the kinematic fluxes characterized by parameters v_+ , v_- or V_m , ΔV . According to this assumption, illustrated in Fig. 4.14, we impose separately the velocities of polymerizing (arriving) and de-polymerizing (departing) mass points, see also [75, 83, 86, 102, 131]. The fact that nothing has been said about the densities of the arriving or departing material allows one to decouple the mechanical problem from the mass transportation problem. The resulting analytic transparency, however, comes at a cost.

First, it is clear that active treadmilling in our model is characterized by only one parameter, the mass flux \dot{m} , so by fixing two parameters V_m and ΔV we are implicitly constraining both treadmilling and contraction. This is also clear from the fact that parameter $\Delta V = v_+ - v_-$ serves as a measure of (dimensionless) energy consumption in the contraction mechanism $P_c = - \int_{l_-}^{l_+} \partial_x v > 0$. Indeed, for the TW regimes the integral terms can be computed explicitly giving $P_c = \Delta V$.

Second, by prescribing the kinematic fluxes v_+ and v_- we have no direct control of the treadmilling mass flux. As a result we encounter singular regimes with $\dot{m} = 0$ which leads to either infinite mass localization inside the cell [122]. Third, by focusing on kinematic fluxes we do not put any restrictions on the energy consumption required to sustain different active mechanisms which appears to be a natural biological constraint.

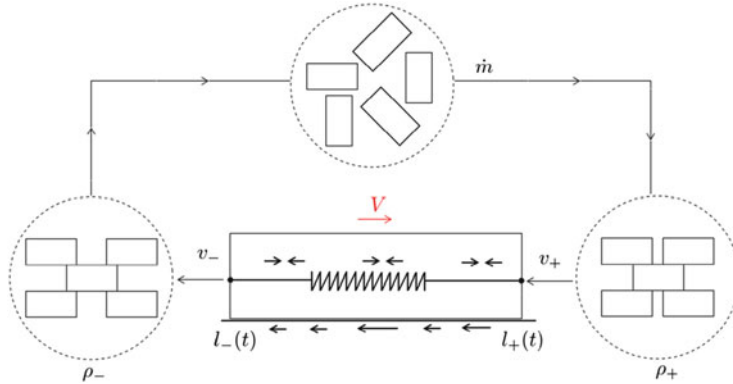


Fig. 4.14 Schematic structure of the treadmilling cycle showing different densities of arriving (polymerizing) and departing (depolymerizing) material

Notice also that the problem setting where driving is performed through parameters v_+ and v_- contains an implicit assumption that the material arrives with a particular density (particular structural organization). Another implicit assumption is that the departing material has a density which depends on the activity of the contractile machinery. While these assumptions are plausible, they may not be the most natural ones from the biological point of view.

In view of these limitations of the model with kinematic driving, it is instructive to consider an alternative modality of driving by imposing constraints on energetic parameters. The main difficulty in dealing with non kinematic driving schemes is that they couple the mechanical and the mass transport problems already in the minimal setting.

Assume, for instance, that the cell controls the treadmilling rate, characterized by the total mass flux $\dot{m} < 0$, and the energetics of the contraction process, characterized by the consumed power $P_c = \Delta V$. The advantage of this new parametrization is that protrusion and contraction can now be controlled independently.

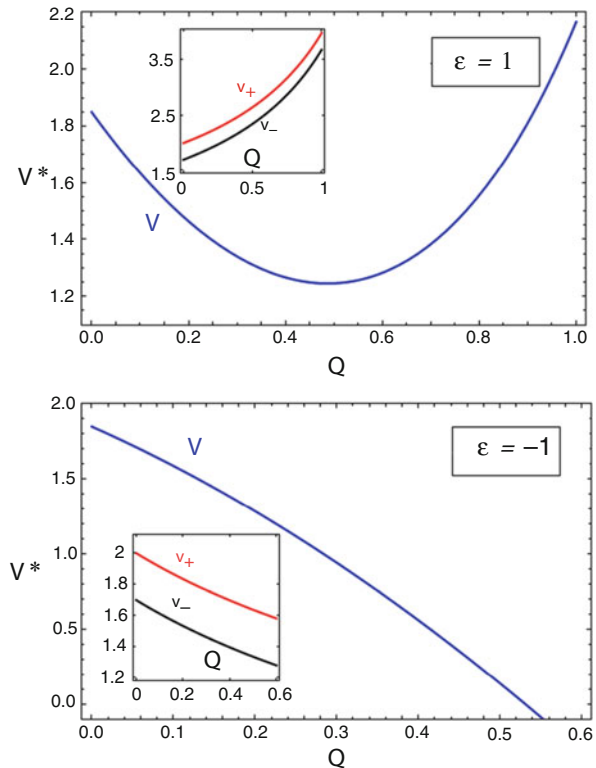
If we choose the pair (\dot{m}, P_c) as the parameters instead of $(V_m, \Delta V)$, we again obtain stable TV solutions given that $P_c < 2 - Q\epsilon$ and $\dot{m} < 0$. The proposed driving mode is in fact equivalent to the kinematic driving mode in the TW regimes because the Jacobian of the transformation $(v_-, v_+) \rightarrow (P_c((v_-, v_+)), \dot{m}(v_-, v_+))$

$$\det \begin{pmatrix} \frac{\partial P_c}{\partial v_-} & \frac{\partial \dot{m}}{\partial v_-} \\ \frac{\partial P_c}{\partial v_+} & \frac{\partial \dot{m}}{\partial v_+} \end{pmatrix} = \frac{\int_{-1/2}^{1/2} \frac{du}{(v(u)-V)^2}}{L(\int_{-1/2}^{1/2} \frac{du}{v(u)-V})^2} \geq \frac{1}{L}$$

is strictly positive for $0 < L < \infty$.

In Fig. 4.15 we show the force velocity relations in the minimal model with prescribed (\dot{m}, P_c) . One can see that the qualitative difference between pushing and pulling endures in this new setting, moreover, we again observe regimes with

Fig. 4.15 Force velocity relations in pure pushing and pulling TW regimes when driving is performed by imposing $\dot{m} = -6.1$ and $P_c = 0.3$. Insets show the ensuing dependencies of v_+ and v_- on Q



negative mobility. It is interesting that by fixing parameters P_c and \dot{m} we induce a dependence of the polymerization and depolymerization rates (v_- , v_+) on Q (see the inserts in Fig. 4.15) which agrees qualitatively with the trends suggested in [83] based on the polymerization ratchet model. We also note that at sufficiently strong pulling loads $Q > Q_c = (2 - P_c)/\epsilon$, the cell length L diverges which suggests that also in the case of non-kinematic driving the minimal model should still be elastically regularized.

Ultimately, the choice of the driving mode requires microscopic modeling and the answer may depend on the type of the cell, the environment and the regime of loading.

4.3.5 Discussion

In this section we studied an interplay between contraction and protrusion required to sustain and carry various cargoes. By using an analytically transparent framework we demonstrated that contraction and protrusion mechanisms can interchange their roles as one varies the dipole component of the external load.

Our model predicts a possibility of a sharp transition between protrusion dominated motility and contraction dominated motility in response to an increase of the pulling force. This transition has a macroscopic signature and can be in principle identified experimentally with a negative mobility range on a force-velocity curve. Vis-à-vis the general behavior of active media, we have shown that an interplay between ‘pushers’ and ‘pullers’ can lead to observable effects in the presence of applied loads. The importance of the idea that different active mechanisms can swap roles depending on the task goes far beyond the subject of cell motility.

While our minimal model still under-represents some physical effects (e.g. autotaxis of myosin motors, active adhesion, complex membrane dynamics, etc. [48, 63, 141, 163, 165, 166, 169]) it allows one to go beyond force velocity relations and study the efficiency of cargo-pulling machinery. Thus, in [122] we have shown that a competition between protrusion and contraction can result in a bi-modal structure of the load-efficiency relation.

Perhaps our most intriguing finding is that the fine structure of the force-velocity relation may depend on the modality of external driving and we argued that kinematic driving may not be the only physically and biologically natural choice. In particular, we suggested that instead of the rates of polymerization and depolymerization, the cell may be controlling the energy supplies required for the functioning of contraction and protrusion mechanisms. We have shown, however, that while the detailed shape of the force velocity relation depends on the choice of the driving mode, its loading-sensitive convexity-concavity structure is a robust feature of the model.

4.4 Adhesion

In this section we turn our attention to adhesion. We remain in the general framework developed in the previous sections, see also [2, 44, 65, 83, 102, 124, 127, 146, 160], and study the active re-organization of adhesive complexes inside a self-propelling layer ensuring an optimal cost-performance trade-off for steady self propulsion. We assume that (in the range of interest) the energetic cost of self-propulsion is velocity independent (cf. [125]) and adopt, as an optimality criterion, the maximization of the overall velocity. We are interested in steady translocation and assume that the internal distributions of mechanical parameters are compatible with the traveling wave ansatz. This simplifying assumption allows us to replace the optimization of the crawling stroke in space and time by a purely spatial optimization of the internal distribution of active elements in the co-moving coordinate system. In a similar but simpler setting the dependence of cell velocity on the distribution of adhesion properties was first studied by Carlsson [33].

Our main result is that depending on the outcome of the competition between contraction and protrusion mechanisms, the ‘optimal’ adhesion would cooperate either with one or the other.

4.4.1 The Model

Since our knowledge of the mechanism controlling the transport and the intensity of active agents performing adhesion is rather limited, we adopt in this section a semi-kinematic approach and treat the corresponding distribution as a functional control parameter constrained by the fundamental mechanical balances. We then pose a variational problem of finding the optimal temporal and spatial distributions of this control parameter inside a crawling continuum body. In view of some successful attempts to justify such reverse engineering approach [125], we anticipate that our optimal solutions will be eventually backed by an appropriate constitutive theory describing active adhesive clusters.

The object of our study is again a one-dimensional segment of viscous active gel representing the cell lamellipodium on a frictional substrate. The force balance will be still written in the form (4.17) but we now assume that the frictional coefficient, mimicking the distribution of focal adhesions, is space and time dependent $\xi(x, t) \geq 0$. We also now assume that the active pre-stress $\chi_0(x, t) \geq 0$ is a function of space and time, however, instead of writing an equation for $c(x, t)$ we view the function $\chi_0(x, t)$, entering the constitutive law $\sigma = \eta\partial_x v + \chi_0$, as an independent functional degree of freedom.

We further assume that some internal mechanism (stiffness of the cell cortex [12, 21, 49, 93, 117, 142], osmotic pressure actively controlled by the channels and pumps on the cell membrane [69, 147], etc.) maintains a given size $L(t) = L_0$ of the cell (the ‘rigid’ model briefly discussed in Sect. 4.2.9). To model active protrusion we again impose the two kinematic Stefan type boundary conditions (4.47).

The two functions $\chi_0(x, t)$ and $\xi(x, t)$ will be interpreted as infinite dimensional controls parameters and found through an optimization procedure. Even in the absence of a detailed microscopic model governing the rearrangement of these agents we still need to subject them to integral constraints prescribing the average number of adhesion complexes [13]

$$\frac{1}{L} \int_{l_-(t)}^{l_+(t)} \xi(x, t) dx = \xi^*, \quad (4.58)$$

where $\xi^* > 0$ is a given constant and

$$\frac{1}{L} \int_{l_-(t)}^{l_+(t)} \chi_0(x, t) dx = \chi^*, \quad (4.59)$$

where $\chi^* > 0$ is another given constant representing the average number of contractile motors [150]. It is clear from (4.58), (4.59) that since we prescribe the density of active agents, the performance of the self-propulsion machinery will be proportional to the length of the active segment, so the appropriate velocity functional must be also normalized by the total length.

To simplify the analysis we assume that the motion of the active segment is steady [75, 131] with unknown velocity $V = \dot{l}_- = \dot{l}_+$ and that the unknown functions σ, v and the unknown controls ξ, χ depend exclusively on the co-moving coordinate u . Then in dimensionless variables $\sigma := \sigma/\chi^*$, $x := x/\sqrt{\eta/\xi^*}$, $t := t/(\eta/\chi^*)$, $\xi := \xi/\xi^*$ and $\chi := \chi/\chi^*$ we obtain the force balance equation

$$-\frac{1}{L^2} \partial_u \left(\frac{\partial_u \sigma(u)}{g_1(u)} \right) + \sigma(u) = g_2(u). \quad (4.60)$$

The re-scaled control functions

$$g_1(u) = \xi(Lu) \geq 0, g_2(u) = \chi_0(Lu) \geq 0$$

must satisfy the constraints

$$\int_{-1/2}^{1/2} g_1(u) du = \int_{-1/2}^{1/2} g_2(u) du = 1. \quad (4.61)$$

The boundary conditions take the form

$$\begin{cases} \sigma(-1/2) = \sigma(1/2) \\ \frac{1}{L^2} \left(\frac{\partial_u \sigma(1/2)}{g_1(1/2)} - \frac{\partial_u \sigma(-1/2)}{g_1(-1/2)} \right) = -\overline{\Delta V}, \end{cases} \quad (4.62)$$

where

$$\overline{\Delta V} := \frac{\Delta V}{L}.$$

The dimensionless velocity of the segment per length $\overline{V} = V/L$ can be found from the formula

$$\overline{V} = \overline{V_m} + \frac{1}{2L^2} \left(\frac{\partial_u \sigma(1/2)}{g_1(1/2)} + \frac{\partial_u \sigma(-1/2)}{g_1(-1/2)} \right), \quad (4.63)$$

where

$$\overline{V_m} := \frac{V_m}{L}.$$

If we now assume that the two parameters $(\overline{V_m}, \overline{\Delta V})$, characterizing actin treadmilling, are fixed we can pose the optimization problem of finding the controls $g_1(u), g_2(u)$ ensuring the maximization of the normalized velocity \overline{V} . This problem is nontrivial because the functional $\overline{V}\{g_1, g_2\}$ is prescribed implicitly through the unknown solution of the boundary value problem (4.60), (4.62). To our advantage this linear elliptic problem is classical, e.g. [100].

We observe that parameter $\overline{V_m}$ enters the expression for the velocity (4.63) in an additive way and does not affect the solution of the optimization problem. The reason is that $\overline{V_m}$ characterizes a propulsion mode associated with simple accretion of the material at the front and its simultaneous removal at the rear; when $\overline{V_m} \neq 0$ an a priori polarity is imposed and the problem of motility initiation disappears. In view of the complete independence of this mode of self-propulsion from our controls, we assume without loss of generality that $\overline{V_m} = 0$.

In contrast to $\overline{V_m}$, the second parameter $\overline{\Delta V}$, also characterizing the protrusion strength, does not induce polarity. As we have seen in the previous section, this parameter represents the mechanical action of pushers. Indeed, consider again the global balance of couples in the co-moving coordinate system [see also (4.57)]

$$L \int_{-1/2}^{1/2} g_1(u)v(u)udu - \sigma_0 = -\overline{\Delta V} + \int_{-1/2}^{1/2} g_2(u)du. \quad (4.64)$$

Here the first term in the left hand side $-T_f = L \int_{-1/2}^{1/2} g_1(u)v(u)udu$ characterizes the total moment due to external (frictional) forces [137] and the second term $T_r = \sigma_0$ corresponds to passive reaction forces resulting from the prescription of the length of the segment. The first term in the right hand side $-T_p = T = \overline{\Delta V}$ is due to active protrusion, while the second term $T_a = \int_{-1/2}^{1/2} g_2(u)du = 1$ is due to active contraction. Our assumption that $\overline{\Delta V} > 0$ means that the protrusion couple has a negative sign showing that the corresponding force dipoles act on the surrounding medium by pushing outward and creating negative stress. Instead, the contraction couple has a positive sign because the contractile forces pull inward and the induced stresses are positive. We can therefore (tentatively) argue that motility is protrusion-dominated when $T > 1$ and it is contraction-dominated when $0 < T < 1$. This assertion will be supported in what follows by rigorous analysis.

4.4.2 Contraction Driven Motility

The simplest analytically transparent case is when protrusion is disabled $\overline{\Delta V} = 0$ and motility is fully contraction-driven.

Suppose first that $g_1 \equiv 1$ which means that the adhesion complexes are distributed uniformly. Then the velocity can be expressed as a quadrature

$$\overline{V} = -\frac{1}{2 \sinh(\frac{L}{2})} \int_{-1/2}^{1/2} \sinh(Lu)g_2(u)du \quad (4.65)$$

here again we see that if the function $g_2(u)$ is even, then $\overline{V} = 0$ (analog of Purcell's theorem [87, 119]). If the distribution $g_2(u)$ is non-symmetric and, for instance, more motors are placed at the rear of the segment, the velocity will become positive.

Using the fact $g_2(u) \geq 0$ we can also conclude from (4.65) that $\bar{V} \leq 1/2$. This upper bound is reached when all the motors are fully localized at the rear and $g_2(u) = \delta(u + 1/2)$.

Now, consider the general case when the focal adhesions are distributed inhomogeneously: $g_1(u) \neq \text{const}$. Since (4.60) is a Sturm–Liouville problem, its solution can be written as

$$\sigma(u) = \sigma_0 - \int_{-1/2}^{1/2} G(u, s) [g_2(s) - \sigma_0] ds, \quad (4.66)$$

where the Green's function $G(u, s)$ can be represented by two auxiliary functions $h(u)$ and $f(u)$

$$G(u, s) = \frac{1}{C} [h(u)f(s)\mathbf{1}_{[s < u]} + h(s)f(u)\mathbf{1}_{[u < s]}], \quad (4.67)$$

solving the following standard boundary value problems [100]:

$$\begin{cases} (\frac{1}{g_1}h')' = L^2 h \\ h(-1/2) = 1, h(1/2) = 1 \end{cases}, \quad \begin{cases} (\frac{1}{g_1}f')' = L^2 f \\ f(-1/2) = 1, f(1/2) = -1 \end{cases}. \quad (4.68)$$

In (4.67), $C = (hf' - fh')/g_1$ is a constant involving the Wronskian of the two auxiliary functions $h(u)$ and $f(u)$ and $\mathbf{1}$ is the indicator function. We can now write

$$\bar{V} = \frac{1}{2} \int_{-1/2}^{1/2} f(u)(g_2(u) - \hat{g}_2) du, \quad (4.69)$$

where we introduced a new measure of inhomogeneity of contraction:

$$\hat{g}_2 = \frac{\int_{-1/2}^{1/2} h(u)g_2(u) du}{\int_{-1/2}^{1/2} h(u) du}.$$

If both functions $g_{1,2}(u)$ are even, then $f(u)$ is odd and, since the integral of a product of an odd and an even functions is equal to zero, we obtain that $\bar{V} = 0$. The same result follows if we assume that contraction is homogeneous $g_2(u) = \hat{g}_2 = 1$ while the adhesion distribution $g_1(u)$ is arbitrary. Therefore, to ensure motility at $\Delta\bar{V} = 0$, contraction must be inhomogeneous while adhesion may still be uniform (provided contraction is not even).

To find the optimal distributions $g_1(u)$, $g_2(u)$ we proceed in two steps. We first show that $\bar{V} \leq 1$ and then find a configuration of controls allowing the cell to reach this bound.

Notice that we can rewrite (4.69) in the form

$$\bar{V} = \frac{1}{2} \left(\int_{S_+} f(u)(g_2(u) - \hat{g}_2) du + \int_{S_-} f(u)(g_2(u) - \hat{g}_2) du \right),$$

where we defined the domains $S_- = \{u/g_2(u) \leq \hat{g}_2\}$ and $S_+ = \{u/g_2(u) > \hat{g}_2\}$. Applying the maximum principle to (4.68) we obtain that $1 \geq h(u) \geq 0$ and $h(u) \geq f(u) \geq -h(u)$. Using the bounds on f , we can write

$$\bar{V} \leq \frac{1}{2} \left(\int_{S_+} h(u)g_2(u) du + \hat{g}_2 \int_{S_-} h(u) du \right).$$

Since the integrands are positive and $h(u) \leq 1$ it finally follows that

$$\bar{V} \leq \int_{-1/2}^{1/2} h(u)g_2(u) du \leq \int_{-1/2}^{1/2} g_2(u) du = 1. \quad (4.70)$$

Observe that in the case of a homogeneous adhesion, the velocity could reach only one half of this maximal value.

We now show that the maximal value of velocity $\bar{V} = 1$ can be reached if both controls $g_1(u)$ and $g_2(u)$ are fully localized. Take $\theta > 0$ and consider a regularized distribution

$$g_1(u; \theta) = \frac{1}{\pi} \frac{\theta}{\theta^2 + (u - u_1)^2}.$$

For this choice of $g_1(u)$ the auxiliary functions $h(u)$ and $f(u)$ can be written explicitly in term of Legendre polynomials. In the limit $\theta \rightarrow 0$ we obtain $\lim_{\theta \rightarrow 0} g_1(u; \theta) = \delta(u - u_1)$. Then

$$h(u) = 1 \text{ and } f(u) = \begin{cases} 1 & \text{if } u \leq u_1 \\ -1 & \text{if } u > u_1. \end{cases}$$

By using these explicit expressions we can rewrite (4.69) in the form

$$\bar{V} = \frac{1}{2} \left[\int_{-1/2}^{u_1} g_2(u) du - \int_{u_1}^{1/2} g_2(u) du - 2u_1 \right]. \quad (4.71)$$

If we now suppose that $g_2(u) = \delta(u - u_2)$ the expression for velocity reduces to

$$\bar{V} = \frac{1}{2} \begin{cases} 1 - 2u_1 & \text{if } u_2 < u_1 \\ -2u_1 & \text{if } u_2 = u_1 \\ -1 - 2u_1 & \text{if } u_2 > u_1 \end{cases}.$$

It is now clear that the velocity reaches its maximal value as $u_1 \rightarrow -1/2$ while $u_2 < u_1$. We can then formally write $u_2 = u_1 = -1/2$ and claim that controls $g_2(u) = g_1(u) = \delta(u + 1/2)$ saturate the bound $\bar{V} = 1$. Notice, however, that if we assume directly $u_1 = u_2 \rightarrow -1/2$ in (4.71), we obtain $\bar{V} = 1/2$. This is in agreement with the physical intuition that the anchorage point must be located to the right of the pulling force dipole: in this case the pulling forces advance the rear edge of the segment with minimal slipping. Mathematically, we encounter here the case of non-commutation of the limiting procedures $u_2 \rightarrow -1/2$, $u_1 \rightarrow -1/2$ and we obtain $\bar{V} = 1$ only if the limits are taken in the above order.

To summarize, the optimization of the distribution of focal adhesions allows the contraction-driven segment to reach the value of velocity which is twice as large as when the adhesion is uniform. This means that in order to improve performance, the adhesion must conspire with the contraction machinery making sure that both the motors and the adhesive centers are localized at the trailing edge. Interestingly, exactly this type of correlation between the stresses created by contraction and the distribution of focal adhesions was observed in experiments and numerical simulations [18, 52, 143, 161, 162, 164]. The localization of adhesion complexes close to cell edges, where contraction is the strongest, has been also reported outside the motility context [19, 43, 107].

4.4.3 The General Case

We now turn to the general case where both contraction and protrusion are active. In particular, the protrusive power will be characterized by the parameter $\Delta\bar{V} = T > 0$ which was assumed to be equal to zero in the previous section. In this more general setting we can write

$$\bar{V} = \frac{1}{2} \left[\frac{\int_{-1/2}^{1/2} f(u) du}{\int_{-1/2}^{1/2} h(u) du} T + \int_{-1/2}^{1/2} f(u)(g_2(u) - \hat{g}_2) du \right]. \quad (4.72)$$

As we see, the first term in the right hand side is associated with protrusion-based (filament driven) motility while the second term is the contribution due to contraction-based (motor driven) motility [128]. We notice that if $g_1(u)$ is even, then $f(u)$ is odd and $h(u)$ is even, leading to

$$\frac{\int_{-1/2}^{1/2} f(u) du}{\int_{-1/2}^{1/2} h(u) du} = 0.$$

If $g_2(u)$ is also even, then

$$\int_{-1/2}^{1/2} f(u)(g_2(u) - \hat{g}_2) du = 0.$$

In this case the velocity of the segment is fully controlled by the accretion mechanism characterized by the parameter \bar{V}_m .

Consider first the case of protrusion-driven motility by assuming that contraction is homogeneous $g_2(u) \equiv 1$ and therefore does not contribute to the overall velocity. By using again the maximum principle we obtain inequalities

$$-1 \leq \frac{\int_{-1/2}^{1/2} f(u) du}{\int_{-1/2}^{1/2} h(u) du} \leq 1,$$

leading to the upper bound

$$\bar{V} \leq \frac{T}{2}. \quad (4.73)$$

The maximum of the protrusive contribution to velocity is reached when, $g_1(u) = \delta(u - \frac{1}{2})$, because in this case $h = 1$ and $f = 1$ almost everywhere. Observe, that the optimal solution in the case of protrusion-driven motility is in some sense *opposite* to the solution $g_1(u) = \delta(u + 1/2)$ obtained in the case of the contraction-driven motility.

Based on (4.70) and (4.73) we can now argue that in the case when both treadmilling and contraction are present, an upper bound for velocity is

$$\bar{V} \leq \frac{T}{2} + 1.$$

However, in view of the incompatibility of the corresponding optimal controls, this bound cannot be reached. The optimal strategy for focal adhesions would then require a compromise between the necessity to localize adhesion at the trailing edge in order to assist the contraction mechanism and the competing need to localize adhesion at the leading edge in order to improve the protrusion power of the cell.

To obtain a lower bound for \bar{V} we now consider a particular test function representing a weighted sum of our competing optimal controls, $g_1(u) = q\delta(u + 1/2) + (1-q)\delta(u - 1/2)$. We also chose $g_2(u) = \delta(u - u_0)$, where $q \in [0, 1]$ and $u_0 \in [-1/2, 1/2]$ are two parameters to be optimized. Then, by solving (4.68) we obtain,

$$f(u) = \begin{cases} 1 & \text{if } u = -1/2 \\ \frac{1-2q}{1+q(1-q)L^2} & \text{if } u \in]-1/2, 1/2[\\ -1 & \text{if } u = 1/2 \end{cases}$$

and,

$$h(u) = \begin{cases} 1 & \text{if } u = -1/2 \\ \frac{1}{1+q(1-q)L^2} & \text{if } u \in]-1/2, 1/2[\\ 1 & \text{if } u = 1/2, \end{cases}$$

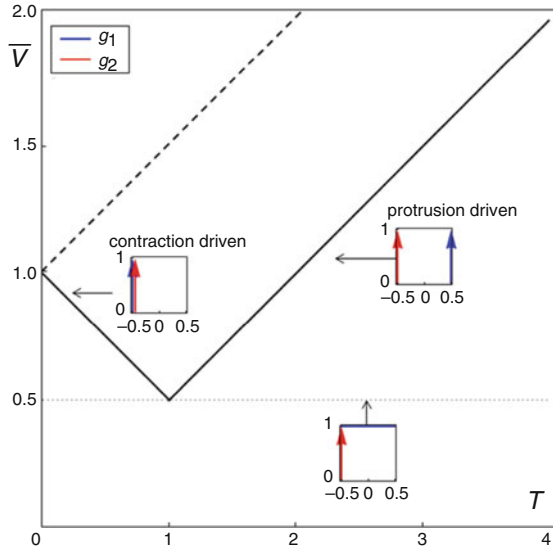


Fig. 4.16 Solid lines: lower bound on the optimal velocity of self-propulsion \bar{V} as a function of the measure of the (relative) protrusive strength T . The optimal strategy depends on whether contraction ($T < 1$) or protrusion ($T > 1$) dominates. The dashed line represents the upper bound obtained by formally summing the incompatible upper bounds for the protrusion and contraction based strategies. The dotted line represents a sub-optimal strategy obtained under the assumption that adhesion is homogeneous. Insets illustrate the associated configurations of controls $g_1(u)$ and $g_2(u)$

which leads to the expression for the velocity

$$\bar{V} = \frac{T}{2}(1 - 2q) + \frac{1}{2}(f(u_0) - (1 - 2q)h(u_0)).$$

The optimization with respect to u_0 gives $u_0 = -1/2$ and

$$\bar{V} = \frac{T}{2} - q(T - 1).$$

Finally, optimizing in q we obtain that if $T < 1$, we must have $q = 0$ and if $T > 1$, we must have $q = 1$. This result, illustrated in Fig. 4.16, suggests that there is a switch at $T = 1$ between the contraction-centered optimization strategy ($q = 0$) and the protrusion-centered optimization strategy ($q = 1$). Notice that the switch takes place exactly when the negative protrusion generated couple T becomes equal to the positive contractile couple equal to 1. At a ‘critical’ state $T = 1$, the two active mechanisms neutralize each other and active dipoles become invisible behind the passive terms in Eq. (4.64): in this case the optimal position of active agents becomes indeterminate.

To show that the low bound obtained above is rather close to being optimal we solved in [123] the optimization problem numerically. Our numerical results are in full agreement with the analytic bounds. In [123] we also used a perturbation analysis to provide additional evidence that our lower bounds are close to being optimal.

Based on all these studies we conjecture that the function $\bar{V}(T)$, representing the optimal velocity, is piece-wise linear with a kink at $T = 1$. The presence of a threshold indicates a switch from contraction-dominated motility pattern to protrusion-dominated motility pattern. As the relative power of protrusion, epitomized by T , increases beyond this threshold, the focal adhesions, maintaining the optimality of the self-propulsion velocity, must migrate from the trailing to the leading edge of the active segment. The dynamic migration of adhesion proteins to the edges has been observed in experiments [107]. In real cells, however, both edges are usually populated by adhesion complexes and we can speculate that in this way cells can adjust more smoothly to transitions from one driving mode to another.

4.4.4 Discussion

In this section we studied optimal strategies allowing cells to move faster by actively coordinating spatial distributions of contractile and adhesive agents. Our study reveals that if adhesion complexes can detect the dominating mechanism of self-propulsion, they can self-organize to ensure the best performance.

We made specific predictions regarding the advantageous correlations between the distributions of adhesive and force producing agents and showed that the dependence of the maximal velocity of self-propulsion on the relative strength of contraction and protrusion may be non-monotone. In particular, our model predicts that a limited activation of protrusion will necessarily lower the maximal velocity achieved in a purely contractile mode of self-propulsion. However, as the protrusion strength increases, protrusion can overtake contraction and the velocity of self-propulsion will increase beyond the level achieved in the contraction-dominated case.

In the first section we saw that contraction-driven motility mechanism may be sufficient to ensure cell polarization, motility initiation, motility arrest and the symmetrization of a cell before mitosis [124, 126]. However, from the analysis presented in the present section it becomes evident that, if the speed of self-propulsion is an issue, cells should mostly rely on protrusion. More specifically, to maximize its velocity performance after motility initiation a cell must switch from contraction-dominated to protrusion-dominated motility mechanism by increasing the protrusive power and appropriately rearranging the distribution of adhesive complexes, see [122] for comparison with experiment. We have seen in the previous section that similar transitions between contraction and protrusion mechanisms can be used by a cell to accommodate different types of cargo.

A schematic nature of the proposed one-dimensional model conceals considerable complexity of the actual cell motility phenomenon which involves intricate bio-chemical feedback loops, geometrically complex mechanical flows and highly nontrivial rheological behavior. In particular, the singular nature of the obtained optimal distributions can be at least partially linked to the fact that polymerization and depolymerization processes are localized at the edges. The situation is complicated further by the fact that the dominant trade-off condition, controlling the self-organization of active agents, is still unknown notwithstanding some recent results in this direction [125]. However, even in the absence of the definitive optimization criterion and with minimal assumptions about the inner working of the motility machinery, our study reveals that depending on the task and the available resources a cell may have to modify its mode of operation rather drastically to ensure the best performance.

4.5 Conclusions

In this chapter we used one-dimensional representations of cellular crawling to illustrate various interactions between the sub-mechanisms of the motility machinery. First, we used a one-dimensional model to expose a crucial role played in cell motility by the nonlocal feedback between contraction and advection and showed that both, motility initiation (implying polarization) and motility arrest (associated with re-symmetrization) may be exclusively contraction-driven. We then demonstrated that a one-dimensional approach presents a unique analytic perspective on the load-induced switching between contraction and protrusion as the dominating motility mechanisms and allows one to trace how different tasks can be accomplished by the structural shifts in motility machinery. Finally, we used a one-dimensional model to provide evidence that radically different spatial distributions of adhesive complexes may be optimal depending on the domineering mechanism of self-propulsion.

While our basic models were rooted in the same theory of active gels we treated contraction-induced active stresses differently in different sections of this chapter. In the first section, focused on contraction proper, we introduced a rather detailed physical model accounting of both force generation and transport of force producing elements. In the second section, where protrusion was the main player, we made a simplifying assumption that the motors are uniformly distributed in the lamellipodium. In the third section aiming at active redistribution of adhesive complexes we did not specify the transport mechanism for contractile elements allowing them to redistribute optimally to ensure that the velocity of directional motility takes the largest value. Some of these assumptions are obviously extreme and have been made with a single purpose of highlighting a particular sub-mechanism of cell motility which would be otherwise obscured by various other contributing factors. However, the unavoidable oversimplifications associated with these assumptions, allowed us to reveal several robust effects:

1. The role played in cell motility by the nonlocal feedback between the mechanics and the transport of active agents.
2. The competition between the dominating driving modes and the possibility of abrupt switches between them depending on the task.
3. A feasibility that the physical mechanism of self-propulsion allows the system to ensure certain optimality of the response.

Despite the overall appeal of the proposed one-dimensional models, they leaves several crucial questions unanswered. Thus, our focus on a normal velocity of self-propulsion obscured the detailed description of the reverse flow of actin monomers which we have replaced with an opaque jump process. Similarly, our desire to maximally limit the number of allowed activity mechanisms, forced us to assume that polymerization of actin monomers and their transport are fast, equilibrium processes. The assumption of infinite compressibility of the cytoskeleton, which is behind the decoupling of the mass transport from the momentum balance, is equally questionable in the light of recent advances in the understanding of cytoskeletal constitutive response [24, 116]. Finally, our schematic depiction of focal adhesions as passive frictional pads needs to be corrected by the account of the ATP driven integrin activity and the mechanical feedback from the binders to the cytoskeleton [138]. These and other simplifications would have to be reconsidered in a richer setting with realistic flow geometry which will also open a way towards more adequate description of the membrane and to account for the polar nature of the gel [55, 96, 152].

Ultimately, the answer to the question whether the proposed simplified description is sufficient to provide the fundamental explanation of the motility initiation and arrest, of the cargo-induced switch between contraction and protrusion and of the adjustment of adhesive mechanism to changes in domineering self-propulsion mode, will depend on the extent to which the inclusion of the factors mentioned above affects our main conclusions. A more thorough analysis will also open the way towards much deeper understanding of each of these effects, in particular, it should be able to explain the remarkable efficiency of the autotaxis mechanism of self-propulsion delivering almost optimal performance at a minimal metabolic cost [125].

Acknowledgements Considerable part of this research was conducted in collaboration with J-F. Joanny and T. Putelat. We thank F. Alouges, D. Ambrosi, O. du Roure, J. Etienne, G. Geymonnat, A. Grosberg, K. Kruse, and C. Verdier for helpful discussions.

References

1. M. Abercrombie, Contact inhibition: the phenomenon and its biological implications. *Natl. Cancer Inst. Monogr.* **26**, 249 (1967)
2. M. Abercrombie, Croonian lecture, 1978 - crawling movement of metazoan cells (English). *Proc. R. Soc. Lond. Ser B Biol. Sci.* **207**(1167), 129–147 (1980)

3. Y. Adler, S. Givli, Closing the loop: lamellipodia dynamics from the perspective of front propagation. *Phys. Rev. E* **88**(4), 042708 (2013)
4. A. Ahmadi, M.C. Marchetti, T.B. Liverpool, Hydrodynamics of isotropic and liquid crystalline active polymer solutions. *Phys. Rev. E* **74**(6), 061913 (2006)
5. B. Alberts, A. Johnson, J. Lewis, M. Raff, K. Roberts, P. Walter, *Molecular Biology of the Cell*, 4th edn. (Garland Science Taylor & Francis Group, New York, 2002)
6. J. Allard, A. Mogilner, Traveling waves in actin dynamics and cell motility. *Curr. Opin. Cell Biol.* **25**(1), 107–115 (2013)
7. W. Alt, M. Dembo, Cytoplasm dynamics and cell motion: two-phase flow models. *Math. Biosci.* **156**(12), 207–228 (1999)
8. S.J. Altschuler, S.B. Angenent, Y. Wang, L.F. Wu, On the spontaneous emergence of cell polarity. *Nature* **454**(7206), 886–889 (2008)
9. J.C. Amazigo, B. Budiansky, G.F. Carrier, Asymptotic analyses of the buckling of imperfect columns on nonlinear elastic foundations. *Int. J. Solids Struct.* **6**(10), 1341–1356 (1970)
10. S. Banerjee, M.C. Marchetti, Substrate rigidity deforms and polarizes active gels. *Europhys. Lett.* **96**(2), 28003 (2011)
11. S. Banerjee, M.C. Marchetti, Contractile stresses in cohesive cell layers on finite-thickness substrates. *Phys. Rev. Lett.* **109**(10), 108101 (2012)
12. E.L. Barnhart, G.M. Allen, F. Julicher, J.A. Theriot, Bipedal locomotion in crawling cells. *Biophys. J.* **98**(6), 933–942 (2010)
13. E.L. Barnhart, K.-C. Lee, K. Keren, A. Mogilner, J.A. Theriot, An adhesion-dependent switch between mechanisms that determine motile cell shape. *PLoS Biol.* **9**(5), e1001059 (2011)
14. E. Barnhart, K.-C. Lee, G.M. Allen, J.A. Theriot, A. Mogilner, Balance between cell-substrate adhesion and myosin contraction determines the frequency of motility initiation in fish keratocytes. *PNAS* **112**(16), 5045–5050 (2015) published ahead of print April 6, 2015
15. P. Bell, Cell behavior - a tribute to Abercrombie, in ed. by R. Michael - Bellairs, A. Curtis, G. Dunn (English). *Am Scientist* **72**(1), 88–89 (1984)
16. R. Bellairs, Michael Abercrombie (1912–1979) (English). *Int. J. Dev. Biol.* **44**(1), 23–28 (2000)
17. A. Bernheim-Groswasser, J. Prost, C. Sykes, Mechanism of actin-based motility: a dynamic state diagram (English). *Biophys. J.* **89**(2), 1411–1419 (2005)
18. A. Bershadsky, M. Kozlov, B. Geiger, Adhesion-mediated mechanosensitivity: a time to experiment, and a time to theorize. *Curr. Opin. Cell Biol.* **18**(5), 472–481 (2006)
19. A. Besser, U.S. Schwarz, Coupling biochemistry and mechanics in cell adhesion: a model for inhomogeneous stress fiber contraction. *New J. Phys.* **9**(11), 425 (2007)
20. C. Blanch-Mercader, J. Casademunt, Spontaneous motility of actin lamellar fragments. *Phys. Rev. Lett.* **110**(7), 078102 (2013)
21. D. Boal, *Mechanics of the Cell* (Cambridge University Press, Cambridge, 2002)
22. J.S. Bois, F. Jülicher, S.W. Grill, Pattern formation in active fluids. *Phys. Rev. Lett.* **106**(2), 028103 (2011)
23. D. Bray, *Cell Movements: From Molecules to Motility*, 2nd edn. (Garland Science, New York, 2000)
24. C.P. Broedersz, F.C. MacKintosh, Modeling semiflexible polymer networks. *Rev. Mod. Phys.* **86**(3), 995–1036 (2014)
25. J. Brugués, J. Casademunt, Self-organization and cooperativity of weakly coupled molecular motors under unequal loading. *Phys. Rev. Lett.* **102**(11), 118104 (2009)
26. C. Brunner, A. Ehrlicher, B. Kohlstrunk, D. Knebel, J. Ks, M. Goegler, Cell migration through small gaps. *Eur. Biophys. J.* **35**(8), 713–719 (2006). doi:10.1007/s00249-006-0079-1
27. E. Caglioti, P.L. Lions, C. Marchioro, M. Pulvirenti, A special class of stationary flows for two-dimensional Euler equations: a statistical mechanics description. *Commun. Math. Phys.* **143**, 501–525 (1992)
28. A.C. Callan-Jones, F. Julicher, Hydrodynamics of active permeating gels. *New J. Phys.* **13**(9), 093027 (2011). <http://stacks.iop.org/1367-2630/13/i=9/a=093027>

29. A. Callan-Jones, R. Voituriez, Active gel model of amoeboid cell motility. *New J. Phys.* **15**(2), 025022 (2013)
30. A.C. Callan-Jones, J.-F. Joanny, J. Prost, Viscous-fingering-like instability of cell fragments. *Phys. Rev. Lett.* **100**(25), 258106 (2008)
31. V. Calvez, N. Meunier, R. Voituriez, A one-dimensional Keller-Segel equation with a drift issued from the boundary. *C. R. Math.* **348**(1112), 629–634 (2010)
32. O. Campas, L. Mahadevan, J.-F. Joanny, Actin network growth under load (English). *Biophys. J.* **102**(5), 1049–1058 (2012)
33. A.E. Carlsson, Mechanisms of cell propulsion by active stresses. *New J. Phys.* **13**(7), 073009 (2011)
34. A.E. Carlsson, D. Sept, Mathematical modeling of cell migration (English), in *Biophysical Tools for Biologists: Vol 1 In Vitro Techniques*. Methods in Cell Biology, vol. 84 (Elsevier Academic Press Inc, San Diego, 2008), pp. 911+
35. J. Carr, R.L. Pego, Metastable patterns in solutions of $ut = e^2 u_{xx} - f(u)$. *Commun. Pure Appl. Math.* **42**(5), 523–576 (1989)
36. C. Chen, C. Lin, On the symmetry of blowup solutions to a mean field equation. *Ann. Inst. Henri Poincaré (C) Non Linear Anal.* **18**(3), 271–296 (2001) [Elsevier]
37. D.T.N. Chen, Q. Wen, P.A. Janmey, J.C. Crocker, A.G. Yodh, Rheology of soft materials, in *Annual Review of Condensed Matter Physics*, ed. by J.S. Langer, vol. 1 (2010), pp. 301–322. <http://www.annualreviews.org/doi/abs/10.1146/annurev-connmatphys-070909-104120>
38. B. Cleuren, C. Van den Broeck, Brownian motion with absolute negative mobility (English). *Phys. Rev. E* **67**(5), Part 2 (2003)
39. B.N. Cox, D.W. Smith, On strain and stress in living cells. *J. Mech. Phys. Solids* **71**, 239–252 (2014)
40. G. Csucs, K. Quirin, G. Danuser, Locomotion of fish epidermal keratocytes on spatially selective adhesion patterns. *Cell Motil. Cytoskeleton* **64**(11), 856–867 (2007)
41. A.T. Dawes, G.B. Ermentrout, E.N. Cytrynbaum, L. Edelstein-Keshet, Actin filament branching and protrusion velocity in a simple 1D model of a motile cell. *J. Theor. Biol.* **242**(2), 265–279 (2006)
42. S.R. De Groot, P. Mazur, *Non-Equilibrium Thermodynamics* (Courier Dover Publications, New York, 2013)
43. V.S. Deshpande, M. Mrksich, R.M. McMeeking, A.G. Evans, A bio-mechanical model for coupling cell contractility with focal adhesion formation (English). *J. Mech. Phys. Solids* **56**(4), 1484–1510 (2008)
44. P. DiMilla, K. Barbee, D. Lauffenburger, Mathematical-model for the effects of adhesion and mechanics on cell-migration speed (English). *Biophys. J.* **60**(1), 15–37 (1991)
45. E. Doedel, A. Champneys, F. Dercole, T. Fairgrieve, Y.A. Kuznetsov, B. Oldeman, R. Paffenroth, B Sandstede, X. Wang, C. Zhang, AUTO-07p, in *Continuation and Bifurcation Software for Ordinary Differential Equations* (2007). Available at <http://cmvl.cs.concordia.ca/auto>
46. K. Doubrovinski, K. Kruse, Self-organization of treadmilling filaments. *Phys. Rev. Lett.* **99**(22), 228104 (2007)
47. K. Doubrovinski, K. Kruse, Self-organization in systems of treadmilling filaments (English). *Eur. Phys. J. E* **31**(1), 95–104 (2010)
48. K. Doubrovinski, K. Kruse, Cell motility resulting from spontaneous polymerization waves. *Phys. Rev. Lett.* **107**(25), 258103 (2011)
49. X. Du, K. Doubrovinski, M. Osterfield, Self-organized cell motility from motor-filament interactions. *Biophys. J.* **102**(8), 1738–1745 (2012)
50. J. Étienne, D. Mitrossilis, J. Fouchard, N. Bufl, P. Durand-Smet, A. Asnacios, Collective dynamics of actomyosin cortex endow cells with intrinsic mechanosensing properties. arXiv preprint. arXiv:1407.2765, accepted in PNAS (2014)
51. B. Finlayson, L. Scriven, Convective instability by active stress. *Proc. R. Soc. Lond. A. Math. Phys. Sci.* **310**(1501), 183–219 (1969)

52. H. Gao, J. Qian, B. Chen, Probing mechanical principles of focal contacts in cell-matrix adhesion with a coupled stochastic-elastic modelling framework. *J. R. Soc. Interface* **8**(62), 1217–1232 (2011)
53. M.L. Gardel, B. Sabass, L. Ji, G. Danuser, U.S. Schwarz, C.M. Waterman, Traction stress in focal adhesions correlates biphasically with actin retrograde flow speed. *J. Cell Biol.* **183**(6), 999–1005 (2008)
54. M.L. Gardel, I.C. Schneider, Y. Aratyn-Schaus, C.M. Waterman, Mechanical integration of actin and adhesion dynamics in cell migration, in *Annual Review of Cell and Developmental Biology*, ed. by R. Schekman, L. Goldstein, R. Lehmann, vol. 26. (2010), pp. 315–333. <http://www.annualreviews.org/doi/abs/10.1146/annurev.cellbio.011209.122036>
55. L. Giomi, A. DeSimone, Spontaneous division and motility in active nematic droplets. *Phys. Rev. Lett.* **112**(14), 147802 (2014)
56. F. Gladiali, M. Grossi, H. Ohtsuka, T. Suzuki, Morse indices of multiple blow-up solutions to the two-dimensional Gel'fand problem. *arXiv preprint arXiv:1210.1373* (2012)
57. P. Haenggi, F. Marchesoni, S. Savel'ev, G. Schmid, Asymmetry in shape causing absolute negative mobility (English). *Phys. Rev. E* **82**(4), Part 1 (2010)
58. R.J. Hawkins, R. Voituriez, Mechanisms of cell motion in confined geometries. *Math. Model. Nat. Phenom.* **5**(1), 84–105 (2010)
59. R.J. Hawkins, O. Bénichou, M. Piel, R. Voituriez, Rebuilding cytoskeleton roads: Active-transport-induced polarization of cells. *Phys. Rev. E Stat. Nonlinear Soft Matter Phys.* **80**(4), 040903+ (2009)
60. R.J. Hawkins, M. Piel, G. Faure-Andre, A.M. Lennon-Dumenil, J.F. Joanny, J. Prost, R. Voituriez, Pushing off the walls: a mechanism of cell motility in confinement (English). *Phys. Rev. Lett.* **102**(5), 058103 (2009)
61. R.J. Hawkins, R. Poincloux, O. Benichou, M. Piel, P. Chavrier, R. Voituriez, Spontaneous contractility-mediated cortical flow generates cell migration in three-dimensional environments. *Biophys. J.* **101**(5), 1041–1045 (2011)
62. C.A. Heckman, Contact inhibition revisited. *J. Cellular Physiol.* **220**(3), 574–575 (2009)
63. M. Herant, M. Dembo, Form and function in cell motility: from fibroblasts to keratocytes. *Biophys. J.* **98**(8), 1408–1417 (2010)
64. N. Hodge, P. Papadopoulos, Continuum modeling and numerical simulation of cell motility. *J. Math. Biol.* **64**(7), 1253–1279 (2012)
65. B.D. Hoffman, J.C. Crocker, Cell mechanics: dissecting the physical responses of cells to force. *Annu. Rev. Biomed. Eng.* **11**, 259–288 (2009)
66. J. Howard, *Mechanics of Motor Proteins and the Cytoskeleton* (Sinauer Associates, Sunderland, 2001)
67. J. Howard, S.W. Grill, J.S. Bois, Turing's next steps: the mechanochemical basis of morphogenesis. *Nat. Rev. Mol. Cell Biol.* **12**(6), 392–398 (2011)
68. E.-M. Hur, I.H. Yang, D.-H. Kim, J. Byun, W.-L. Xu, P.R. Nicovich, R. Cheong, A. Levchenko, N. Thakor, F.-Q. Zhou, et al., Engineering neuronal growth cones to promote axon regeneration over inhibitory molecules. *Proc. Natl. Acad. Sci.* **108**(12), 5057–5062 (2011)
69. H. Jiang, S.X. Sun, Cellular pressure and volume regulation and implications for cell mechanics. *Biophys. J.* **105**(3), 609–619 (2013)
70. A. Jilkine, L. Edelstein-Keshet, A comparison of mathematical models for polarization of single eukaryotic cells in response to guided cues. *PLoS Comput. Biol.* **7**(4), e1001121 (2011)
71. J.-F. Joanny, J. Prost, Constructing tools for the description of cell dynamics, in *Biological Physics: Poincaré Seminar 2009*, ed. by B. Duplantier, V. Rivasseau. Progress in Mathematical Physics, vol. 60. 12th Poincaré Seminar on Biological Physics, Inst Henri Poincaré, Paris, Jan 31, 2009. Commissariat Energie Atomique, Div Sci Matiere; Daniel Iagolnitzer Fdn; Ecole Polytechnique (2011), pp. 1–32
72. J. Joanny, F. Julicher, J. Prost, Motion of an adhesive gel in a swelling gradient: a mechanism for cell locomotion (English). *Phys. Rev. Lett.* **90**(16), 168102 (2003)
73. J.F. Joanny, F. Julicher, K. Kruse, J. Prost, Hydrodynamic theory for multi-component active polar gels (English). *New J. Phys.* **9**(11), 422 (2007)

74. K. John, P. Peyla, K. Kassner, J. Prost, C. Misbah, Nonlinear study of symmetry breaking in actin gels: implications for cellular motility. *Phys. Rev. Lett.* **100**(6), 068101 (2008)
75. F. Julicher, K. Kruse, J. Prost, J.-F. Joanny, Active behavior of the cytoskeleton (English). *Phys. Rep. Rev. Section Phys. Lett.* **449**(1–3), 3–28 (2007)
76. H. Keller, A.D. Zadeh, P. Eggle, Localised depletion of polymerised actin at the front of Walker carcinosarcoma cells increases the speed of locomotion. *Cell Motil. Cytoskeleton* **53**(3), 189–202 (2002)
77. L. Kimpton, J. Whiteley, S. Waters, J. Oliver, On a poroviscoelastic model for cell crawling. *J. Math. Biol.* **70**(1), 133–171 (2015)
78. W. Koiter, *Current Trends in the Theory of Buckling* (Springer, Berlin, 1976)
79. K. Kruse, F. Julicher, Actively contracting bundles of polar filaments. *Phys. Rev. Lett.* **85**(8), 1778–1781 (2000)
80. K. Kruse, F. Jülicher, Self-organization and mechanical properties of active filament bundles. *Phys. Rev. E* **67**(5), 051913 (2003)
81. K. Kruse, A. Zumdieck, F. Jülicher, Continuum theory of contractile fibres. *Europhys. Lett.* **64**(5), 716 (2003)
82. K. Kruse, J. Joanny, F. Julicher, J. Prost, K. Sekimoto, Generic theory of active polar gels: a paradigm for cytoskeletal dynamics (English). *Eur. Phys. J. E* **16**(1), 5–16 (2005)
83. K. Kruse, J.F. Joanny, F. Julicher, J. Prost, Contractility and retrograde flow in lamellipodium motion (English). *Phys. Biol.* **3**(2), 130–137 (2006)
84. O.M. Lancaster, B. Baum, Shaping up to divide: coordinating actin and microtubule cytoskeletal remodelling during mitosis. *Semin. Cell Dev. Biol.* **34**(0), 109–115 (2014)
85. O.M. Lancaster, M.L. Berre, A. Dimitrakopoulos, D. Bonazzi, E. Zlotek- Zlotkiewicz, R. Picone, T. Duke, M. Piel, B. Baum, Mitotic rounding alters cell geometry to ensure efficient bipolar spindle formation. *Dev. Cell* **25**(3), 270–283 (2013)
86. K. Larripa, A. Mogilner, Transport of a 1D viscoelastic actin-myosin strip of gel as a model of a crawling cell (English). *Physica A-Stat. Mech. Appl.* **372**(1) (2006). Workshop on Common Trends in Traffic Systems, Kanpur, Feb 08–10, 2006, pp. 113–123
87. E. Lauga, T.R. Powers, The hydrodynamics of swimming microorganisms (English). *Rep. Progr. Phys.* **72**(9), 096601 (2009)
88. Y. Lin, A model of cell motility leading to biphasic dependence of transport speed on adhesive strength. *J. Mech. Phys. Solids* **58**(4), 502–514 (2010)
89. Y. Lin, M. Inamdar, L. Freund, The competition between Brownian motion and adhesion in soft materials. *J. Mech. Phys. Solids* **56**(1), 241–250 (2008)
90. Z. Liu, L. A. van Grunsven, E. Van Rossem, B. Schroyen, J.-P. Timmermans, A. Geerts, H. Reynaert, Blebbistatin inhibits contraction and accelerates migration in mouse hepatic stellate cells. *Br. J. Pharmacol.* **159**(2), 304–315 (2010)
91. J. Löber, F. Ziebert, I.S. Aranson, Modeling crawling cell movement on soft engineered substrates. *Soft Matter* **10**(9), 1365–1373 (2014)
92. M.L. Lombardi, D.A. Knecht, M. Dembo, J. Lee, Traction force microscopy in Dictyostelium reveals distinct roles for myosin II motor and actin-crosslinking activity in polarized cell movement. *J. Cell Sci.* **120**(Pt 9), 1624–1634 (2007)
93. A.J. Loosley, J.X. Tang, Stick-slip motion and elastic coupling in crawling cells. *Phys. Rev. E* **86**(3), Part 1 (2012)
94. L. Machura, M. Kostur, P. Talkner, J. Luczka, P. Haenggi, Absolute negative mobility induced by thermal equilibrium fluctuations (English). *Phys. Rev. Lett.* **98**(4), 040601 (2007)
95. M.C. Marchetti, J.-F. Joanny, S. Ramaswamy, T.B. Liverpool, J. Prost, M. Rao, R. Aditi Simha, Soft active matter. (2012). ArXiv e-prints. arXiv:1207.2929 [cond-mat.soft]
96. M. Marchetti, J. Joanny, S. Ramaswamy, T. Liverpool, J. Prost, M. Rao, R.A. Simha, Hydrodynamics of soft active matter. *Rev. Mod. Phys.* **85**(3), 1143 (2013)
97. M. Mayer, M. Depken, J.S. Bois, F. Julicher, S.W. Grill, Anisotropies in cortical tension reveal the physical basis of polarizing cortical flows. *Nature* **467**(7315), 617–U150 (2010)
98. G. Meurant, A review on the inverse of symmetrical tridiagonal and block tridiagonal matrices (English). *SIAM J. Matrix Anal. Appl.* **13**(3), 707–728 (1992)

99. Q. Mi, D. Swigon, B. Riviere, S. Cetin, Y. Vodovotz, D.J. Hackam, One-dimensional elastic continuum model of enterocyte layer migration (English). *Biophys. J.* **93**(11), 3745–3752 (2007)
100. S. Mikhlin, *Linear Integral Equations* (Hindustan Publishing Corp., DELHI (India) 1960)
101. M.R.K. Mofrad, Rheology of the cytoskeleton. *Ann. Rev. Fluid Mech.* **41**, 433–453 (2009)
102. A. Mogilner, Mathematics of cell motility: have we got its number? (English). *J. Math. Biol.* **58**(1–2) (2009). International Conference on Industrial and Applied Mathematics (Zurich, 2007), pp. 105–134
103. A. Mogilner, L. Edelstein-Keshet, Regulation of actin dynamics in rapidly moving cells: a quantitative analysis (English). *Biophys. J.* **83**(3), 1237–1258 (2002)
104. Y. Mori, A. Jilkine, L. Edelstein-Keshet, Wave-pinning and cell polarity from a bistable reaction-diffusion system. *Biophys. J.* **94**(9), 3684–3697 (2008)
105. C. Nelson, Paluch, Ewa K, Nelson, Celeste M, Biais, Nicolas, Fabry, Ben, Moeller, Jens, Pruitt, Beth L, Wollnik, Carina, Kudryasheva, Galina and Rehfeldt, Florian, Federle, Walter, Mechanotransduction: use the force (s). *BMC Biol.*, BioMed Central Ltd **13**(1), 47 (2015). <http://www.biomedcentral.com/1741-7007/13/47>
106. L. Nirenberg, *Topics in Nonlinear Functional Analysis*, vol. 6 (American Mathematical Society, Providence, RI, 1974)
107. I.L. Novak, B.M. Slepchenko, A. Mogilner, L.M. Loew, Cooperativity between cell contractility and adhesion. *Phys. Rev. Lett.* **93**(26), 268109 (2004)
108. H. Ohtsuka, A concentration phenomenon around a shrinking hole for solutions of mean field equations. *Osaka J. Math.* **39**, 395–407 (2002)
109. J. Oliver, J. King, K. McKinlay, P. Brown, D. Grant, C. Scotchford, J. Wood, Thin-film theories for two-phase reactive flow models of active cell motion. *Math. Med. Biol.* **22**(1), 53–98 (2005)
110. J.G. Orlandi, C. Blanch-Mercader, J. Brugués, J. Casademunt, Cooperativity of self-organized Brownian motors pulling on soft cargoes. *Phys. Rev. E* **82**(6), 061903 (2010)
111. A. Pathak, V.S. Deshpande, R.M. McMeeking, A.G. Evans, The simulation of stress fibre and focal adhesion development in cells on patterned substrates (English). *J. R. Soc. Interface* **5**(22), 507–524 (2008)
112. B. Perthame, *Growth, Reaction, Movement and Diffusion from Biology*. Lecture Notes, University Paris **6** (2012)
113. C. Peskin, G. Odell, G. Oster, Cellular motions and thermal fluctuations - the Brownian ratchet (English). *Biophys. J.* **65**(1), 316–324 (1993)
114. R. Poincloux, O. Collin, F. Lizárraga, M. Romao, M. Debray, M. Piel, P. Chavrier, Contractility of the cell rear drives invasion of breast tumor cells in 3D Matrigel. *Proc. Natl. Acad. Sci. U.S.A.* **108**(5), 1943–1948 (2011)
115. M. Prass, K. Jacobson, A. Mogilner, M. Radmacher, Direct measurement of the lamellipodial protrusive force in a migrating cell. *J. Cell Biol.* **174**, 767–772 (2006)
116. R.H. Pritchard, Y.Y. Shery Huang, E.M. Terentjev, Mechanics of biological networks: from the cell cytoskeleton to connective tissue. *Soft Matter* **10**(12), 1864–1884 (2014)
117. J. Prost, C. Barbutta, J.-F. Joanny, Dynamical control of the shape and size of Stereocilia and Microvilli. *Biophys. J.* **93**(4), 1124–1133 (2007)
118. J. Prost, F. Jülicher, J. Joanny, Active gel physics. *Nat. Phys.* **11**(2), 111–117 (2015)
119. E.M. Purcell, Life at low Reynolds number. *Am. J. Phys.* **45**(1), 3–11 (1977)
120. S. Rafelski, J. Theriot, Crawling toward a unified model of cell motility: spatial and temporal regulation of actin dynamics (English). *Ann. Rev. Biochem.* **73**, 209–239 (2004)
121. J. Ranft, J. Prost, F. Jülicher, J.-F. Joanny, Tissue dynamics with permeation. *Eur. Phys. J. E. Soft Matter* **35**, 9723 (2012)
122. P. Recho, L. Truskinovsky, Asymmetry between pushing and pulling for crawling cells. *Phys. Rev. E* **87**(2), 022720 (2013)
123. P. Recho, L. Truskinovsky, Maximum velocity of self-propulsion for an active segment. *Math. Mech. Solids* (2015). <http://mms.sagepub.com/content/early/2015/07/06/1081286515588675.abstract>

124. P. Recho, T. Putelat, L. Truskinovsky, Contraction-driven cell motility. *Phys. Rev. Lett.* **111**(10), 108102 (2013)
125. P. Recho, J.-F. Joanny, L. Truskinovsky, Optimality of contraction-driven crawling. *Phys. Rev. Lett.* **112**(21), 218101 (2014)
126. P. Recho, T. Putelat, L. Truskinovsky, Mechanics of motility initiation and motility arrest in crawling cells. *J. Mech. Phys. Solids* **84**, 469–505 (2015). Doi:<http://dx.doi.org/10.1016/j.jmps.2015.08.006>. Available at <http://www.sciencedirect.com/science/article/pii/S0022509615300612>
127. A.J. Ridley, M.A. Schwartz, K. Burridge, R.A. Firtel, M.H. Ginsberg, G. Borisy, J.T. Parsons, A.R. Horwitz, Cell migration: integrating signals from front to back. *Science* **302**(5651), 1704–1709 (2003). eprint: <http://www.sciencemag.org/content/302/5651/1704.full.pdf>
128. T. Risler, Cytoskeleton and cell motility. (2011). arXiv:1105.2423 [physics.bio-ph]
129. W. Ronan, V.S. Deshpande, R.M. McMeeking, J.P. McGarry, Cellular contractility and substrate elasticity: a numerical investigation of the actin cytoskeleton and cell adhesion. *Biomech. Model. Mechanobiol.* **13**(2), 417–435 (2014)
130. A. Ros, R. Eichhorn, J. Regtmeier, T. Duong, P. Reimann, D. Anselmetti, Brownian motion - absolute negative particle mobility (English). *Nature* **436**(7053), 928 (2005)
131. B. Rubinstein, M.F. Fournier, K. Jacobson, A.B. Verkhovsky, A. Mogilner, Actin-myosin viscoelastic flow in the keratocyte lamellipod (English). *Biophys. J.* **97**(7), 1853–1863 (2009)
132. D. Saintillan, M.J. Shelley, Emergence of coherent structures and large-scale flows in motile suspensions. *J. R. Soc. Interface* **9**(68), 571–585 (2012)
133. G. Salbreux, J. Prost, J.F. Joanny, Hydrodynamics of cellular cortical flows and the formation of contractile rings. *Phys. Rev. Lett.* **103**(5), 058102 (2009)
134. S. Sankararaman, S. Ramaswamy, Instabilities and waves in thin films of living fluids. *Phys. Rev. Lett.* **102**(11), 118107 (2009)
135. C.H. Schreiber, M. Stewart, T. Duke, Simulation of cell motility that reproduces the force-velocity relationship (English). *Proc. Natl. Acad. Sci. U.S.A.* **107**(20), 9141–9146 (2010)
136. U.S. Schwarz, M.L. Gardel, United we stand - integrating the actin cytoskeleton and cell-matrix adhesions in cellular mechanotransduction. *J. Cell Science* **125**(13), 3051–3060 (2012)
137. U. Schwarz, S. Safran, Elastic interactions of cells. *Phys. Rev. Lett.* **88**(4), 048102 (2002)
138. U. Schwarz, S. Safran, Physics of adherent cells. *Rev. Mod. Phys.* **85**(3), 1327–1381 (2013)
139. J. Sedzinski, M. Biro, A. Oswald, J.-Y. Tinevez, G. Salbreux, E. Paluch, Polar actomyosin contractility destabilizes the position of the cytokinetic furrow. *Nature* **476**(7361), 462–466 (2011)
140. T. Senba, T. Suzuki, Some structures of the solution set for a stationary system of chemotaxis. *Adv. Math. Sci. Appl.* **10**(1), 191–224 (2000)
141. D. Shao, W.-J. Rappel, H. Levine, Computational model for cell morphodynamics (English). *Phys. Rev. Lett.* **105**(10), 108104 (2010)
142. M. Sheetz, J. Sable, H. Dobereiner, Continuous membrane-cytoskeleton adhesion requires continuous accommodation to lipid and cytoskeleton dynamics. *Ann. Rev. Biophys. Biomol. Struct.* **35**, 417–434 (2006)
143. M. Shutova, C. Yang, J.M. Vasiliev, T. Svitkina, Functions of non-muscle myosin II in assembly of the cellular contractile system. *PLoS One* **7**(7), e40814–e40814 (2012)
144. R. Simha, S. Ramaswamy, Hydrodynamic fluctuations and instabilities in ordered suspensions of self-propelled particles. *Phys. Rev. Lett.* **89**(5), 058101_1–058101_4 (2002)
145. M.P. Stewart, J. Helenius, Y. Toyoda, S.P. Ramanathan, D.J. Muller, A.A. Hyman, Hydrostatic pressure and the actomyosin cortex drive mitotic cell rounding. *Nature* **469**(7329), 226–230 (2011)
146. T. Stossel, On the crawling of animal-cells (English). *Science* **260**(5111), 1086–1094 (1993)
147. K.M. Stroka, H. Jiang, S.-H. Chen, Z. Tong, D. Wirtz, S.X. Sun, K. Konstantopoulos, Water permeation drives tumor cell migration in confined microenvironments. *Cell* **157**(3), 611–623 (2014)
148. M. Struwe, G. Tarantello, On multivortex solutions in Chern-Simons gauge theory. *Bollettino della Unione Matematica Italiana-B* **1**, 109–122 (1998)

149. K. Tawada, K. Sekimoto, Protein friction exerted by motor enzymes through a weak-binding interaction. *J. Theor. Biol.* **150**(2), 193–200 (1991)
150. T. Thoresen, M. Lenz, M.L. Gardel, Reconstitution of contractile actomyosin bundles. *Biophys. J.* **100**(11), 2698–2705 (2011)
151. J.-Y. Tinevez, U. Schulze, G. Salbreux, J. Roensch, J.-F. Joanny, E. Paluch, Role of cortical tension in bleb growth. *Proc. Natl. Acad. Sci.* **106**(44), 18581–18586 (2009)
152. E. Tjhung, A. Tiribocchi, D. Marenduzzo, M. Cates, A minimal physical model captures the shapes of crawling cells. *Nat. Commun.* **6** (2015)
153. E. Tjhung, D. Marenduzzo, M.E. Cates, Spontaneous symmetry breaking in active droplets provides a generic route to motility. *Proc. Natl. Acad. Sci. U.S.A.* **109**(31), 12381–12386 (2012)
154. P.G. Torres, K. Doubrovinski, K. Kruse, Filament turnover stabilizes contractile cytoskeletal structures. *Europhys. Lett.* **91**(6), 68003 (2010)
155. X. Trepat, M.R. Wasserman, T.E. Angelini, E. Millet, D.A. Weitz, J.P. Butler, J.J. Fredberg, Physical forces during collective cell migration. *Nat. Phys.* **5**(6), 426–430 (2009)
156. H. Turlier, B. Audoly, J. Prost, J.-F. Joanny, Furrow constriction in animal cell cytokinesis. *Biophys. J.* **106**(1), 114–123 (2014)
157. B. Vanderlei, J.J. Feng, L. Edelstein-Keshet, A computational model of cell polarization and motility coupling mechanics and biochemistry. *Multiscale Model. Simul.* **9**(4), 1420–1443 (2011)
158. S.R.K. Vedula, M.C. Leong, T.L. Lai, P. Hersen, A.J. Kabla, C.T. Lim, B. Ladoux, Emerging modes of collective cell migration induced by geometrical constraints. *Proc. Natl. Acad. Sci. U.S.A.* **109**, 12974–12979 (2012)
159. A. Verkhovsky, T. Svitkina, G. Borisy, Self-polarization and directional motility of cytoplasm. *Curr. Biol.* **9**(1), 11–20 (1999)
160. M. Vicente-Manzanares, D. Webb, A. Horwitz, Cell migration at a glance (English). *J. Cell Sci.* **118**(21), 4917–4919 (2005)
161. M. Vicente-Manzanares, X. Ma, R.S. Adelstein, A.R. Horwitz, Non-muscle myosin II takes centre stage in cell adhesion and migration. *Nat. Rev. Mol. Cell Biol.* **10**(11), 778–790 (2009)
162. Y. Wang, E. Botvinick, Y. Zhao, M. Berns, S. Usami, R. Tsien, S. Chien, Visualizing the mechanical activation of Src. *Nature* **434**(7036), 1040–1045 (2005)
163. Q. Wang, X. Yang, D. Adalsteinsson, T.C. Elston, K. Jacobson, M. Kapustina, M.G. Forest, Computational and modeling strategies for cell motility, in *Biological and Medical Physics, Biomedical Engineering*, ed. by N.V. Dokholyan (Springer, Heidelberg, 2012), pp. 257–296
164. H. Wolfenson, Y.I. Henis, B. Geiger, A.D. Bershadsky, The heel and toe of the cell's foot: a multifaceted approach for understanding the structure and dynamics of focal adhesions. *Cell Motil. Cytoskeleton* **66**(11), 1017–1029 (2009)
165. C. Wolgemuth, Lamellipodial contractions during crawling and spreading. *Biophys. J.* **89**(3), 1643–1649 (2005)
166. C.W. Wolgemuth, J. Stajic, A. Mogilner, Redundant mechanisms for stable cell locomotion revealed by minimal models. *Biophys. J.* **101**(3), 545–553 (2011)
167. P.T. Yam, C.A. Wilson, L. Ji, B. Hebert, E.L. Barnhart, N.A. Dye, P.W. Wiseman, G. Danuser, J.A. Theriot, Actin-myosin network reorganization breaks symmetry at the cell rear to spontaneously initiate polarized cell motility. *J. Cell Biol.* **178**(7), 1207–1221 (2007)
168. F. Ziebert, I.S. Aranson, Effects of adhesion dynamics and substrate compliance on the shape and motility of crawling cells. *PLoS One* **8**(5), e64511 (2013)
169. F. Ziebert, S. Swaminathan, I.S. Aranson, Model for self-polarization and motility of keratocyte fragments. *J. R. Soc. Interface* **9**(70), 1084–1092 (2012)
170. J. Zimmermann, C. Brunner, M. Enculescu, M. Goegler, A. Ehrlacher, J. Kaes, M. Falcke, Actin filament elasticity and retrograde flow shape the force-velocity relation of motile cells. *Biophys. J.* **102**(2), 287–295 (2012)

Index

A

Actin

binding, 7, 35, 73, 119
dynamics, 16–18, 23, 72, 73, 78, 81
filaments, 5, 8, 12, 16, 20, 71, 73, 74, 76,
78, 80, 83, 135, 149, 152
network, 3, 4, 6, 8, 12, 17, 79, 136, 138,
141, 151, 167
polymerization, 2, 5–9, 12, 18, 20, 27, 31,
71, 73–75, 84, 85, 97–99, 101, 103,
104, 115, 119

Active stress

Adenosine-di-phosphate (ADP), 73, 74, 79
Adenosine-triphosphate (ATP), 3, 4, 9, 73, 74,
79, 136, 148, 158, 190

Adhesion

complex, 5, 11, 137, 179, 180, 182, 185,
188
focal, 4, 5, 50, 84, 136, 139, 150, 180, 183,
185, 186, 188, 190
nascent, 4, 20

Amoeba

71, 89, 95

B

Bi-pedal motion, 6, 22, 33–35, 58
Blebbing, 137

C

Catastrophe, 2, 4, 70, 75
Cell
division, 69, 140, 160, 167
fragments, 5, 18, 85, 136
migration, 39, 50, 70, 81, 89, 90, 95, 99,
112

Chemotaxis, 95–97, 117, 119, 125, 151, 152,
154

Collective migration, 39, 45–49, 51
behavior, 43, 48, 51

Collisions

elastic, 43, 44, 47, 48, 50, 51
inelastic, 43, 47, 48, 50, 51

Contractile stress

Contractility, 9, 18, 28, 43, 45, 138, 140, 151,
152, 156, 159–161, 166, 167

Contraction, 3, 4, 6, 7, 9, 11, 12, 17, 18, 23, 28,
40, 70–73, 80, 89, 136–142, 145,
146, 149, 152, 153, 156, 159, 164,
167, 168, 170, 172–174, 176–179,
182, 183, 185–190

Control, 89, 105, 141, 151, 176, 180,
181

Cytoskeletal waves, 70, 75, 79

Cytoskeleton, 2–4, 9, 15, 16, 20, 41, 70, 71,
80–85, 90, 96, 97, 135–137, 140,
142, 162, 174, 190

D

Dictyostelium discoideum, 71, 95

Durotaxis, 7, 22, 35, 38, 39, 50, 58,
59

E

Elasticity, 6, 7, 33, 38, 45, 48, 83, 103, 108,
138, 140, 144, 151, 168, 174

Excitable
behavior, 98–101, 119, 124
media, 71, 78, 98

F

Fiber, stress, 2, 50, 70, 80, 135

Fibronectin, 35, 37

Flow

- actin, 19, 139
- explicit, 19–20
- retrograde, 7, 9, 50, 150, 173
- viscous, 19

Force

- balance, 12, 19–20, 56, 57, 79, 84, 141, 143, 145, 150, 162, 168–170, 172, 173, 180, 181

friction, 146

polymerization, 15, 28

propulsion, 3, 4, 12, 19, 20, 28, 30, 51

Friction, 4, 19, 79, 84, 137, 141, 143, 146, 150, 160, 167, 175

G

Gel, active, 9–11, 17, 52, 79, 136, 137, 139, 141, 145, 149, 170, 180, 189

Gliding motion, 31

Growth factor, 15, 16, 20, 28, 31, 41, 48, 74, 75, 79, 80, 103, 137, 139, 146, 168, 189, 190

I

Instability, 10, 33, 37, 90, 139, 154

Integrin, 4, 5, 35, 41, 190

Interface

moving, 11

sharp, 40, 84

K

Keratocytes, 5, 13, 17, 25, 28, 34, 43, 141

L

Leucocytes, 2, 6, 7, 52, 135

Level set, 10, 11, 81, 101, 102

Ligand, 3, 6, 8, 9, 35, 36, 47, 51, 96

Limit cycle, 32, 120

M

Membrane

proteins, 135

tension, 8, 20

Microtubules

Migration, 39–40, 45–52, 70, 81, 84–90, 95–97, 99, 112–115, 118, 119, 124, 188

Modulation, 35–39

Molecular motors, 4, 16, 75, 79, 80, 86, 140

Motility, 2–8, 10, 11, 20, 24, 28, 30, 31, 33–34, 36–39, 44, 46, 50, 52, 70, 71, 83, 96–98, 104, 108–109, 118, 135–142, 148, 153, 154, 157, 159–162, 165, 167, 173, 179, 182, 183, 185, 186, 188–190

Myosin, 4–7, 9, 11, 16, 17, 25, 28, 45, 70, 135, 136, 138, 139, 141, 151, 153, 154, 158, 159, 164, 179

N

Neutrophils, 24, 25, 50, 70, 71, 87, 95, 97, 104, 128

Nucleators, 16, 75–78, 80, 83, 85

Nullclines, 32, 33, 99, 121

P

Phase

- diagram, 30, 78, 85–86, 159–161, 166
- field, 10–17, 23–25, 31, 39–42, 50–52, 55, 81–85, 87, 137

Polymerization

- depolymerization, 16, 18, 75, 164, 169, 175, 178, 179, 189
- directed, 4, 8, 50, 97
- force, 5, 15, 28, 70, 84
- rate, 16, 18, 178

Protrusion, 3, 11, 37, 70, 86, 96–98, 104, 112, 114, 118, 122, 124, 136–140, 161, 167–168, 172, 173, 176–180, 182, 185–190

Pseudopods, 97, 98, 112, 113, 124

R

Rates

- attachment, 20, 22, 29, 73, 74
- degradation, 16, 18, 178
- detachment, 21, 22, 31
- polymerization, 16, 18, 73, 74

Receptors, 9, 96, 104

Regulation, 3–5, 50, 70, 95, 105, 136, 137, 161

S

Self-propulsion, 135, 137–139, 148, 167, 179, 180, 182, 187–190

Signaling, 11, 50, 71, 98, 106, 116, 119, 124, 136, 141

Solution

- chaotic, 78
- erratic, 88, 89
- linearized, 148, 156
- nonlinear, 10, 20, 22, 43, 46, 54, 136, 158, 165–167
- oscillating, 71, 122
- periodic, 13, 15, 28, 29, 33, 35, 44, 47–49, 52, 53, 55, 56, 70, 87, 96, 100, 101, 108, 111
- stationary, 12–14, 17, 25–27, 45, 46, 49–51, 78, 85, 86, 136, 142, 156

Stick-slip, 6, 28–34, 36, 37, 44, 58

Stimuli, 4–6, 90, 98, 99, 107, 109

Subcritical transition, 25, 26

Substrate, 2–4, 6–13, 15, 20–26, 28–39, 41–43, 45–47, 50–52, 55–57, 70, 71

Symmetry-breaking, 26

T

- Treadmilling, 73–75, 137, 138, 142, 143, 147, 156, 162–164, 169, 176, 177, 181, 186

Tissue, 3, 34, 39, 49, 50, 52, 71

Traction

- force, 7, 12, 20, 22–24, 56, 57
- force microscopy, 7, 24

V

- Viscous drag, 19, 102, 135–137, 141, 144, 150, 151, 171, 180

W

Waves, 9, 11, 50, 69–81, 84–86, 89, 98–100

Wiskott-Aldrich syndrome protein (WASP), 3, 16, 74